AN INVESTIGATION OF DEFECTS IN THE NICKEL-BASED SUPERALLOY IN738LC FABRICATED BY LASER POWDER BED FUSION

By

Chuan Guo

A thesis submitted to the

University of Birmingham

for the degree of

DOCTOR OF PHILOSOPHY

School of Metallurgy and Materials

College of Engineering and Physical Sciences

University of Birmingham

May 2021

UNIVERSITYOF
BIRMINGHAM

University of Birmingham Research Archive

e-theses repository

Abstract

Nickel-based superalloy Inconel 738 LC (IN738LC) can be used for the components in aero-engine due to its excellent high-temperature mechanical properties and oxidation/corrosion resistance. However, this alloy is difficult to be processed due to a high level of defects by laser powder bed fusion (LPBF) technology. Thus, this thesis presents the studies on the formation mechanisms and exposes some potential solutions for the mitigation of these defects during LPBF.

A statistical single variable method of 3 parameters (hatch spacing, scan speed and laser power) in LPBF is applied to understand how processing parameters influence defect formation. It is found that pores can be eliminated using the parameter optimisation method but cracks cannot.

Single-track experiments are performed to study the fluid dynamics and solidification processes during LPBF to explore the pore formation mechanism including lack of fusion and keyholing.

The microstructural characterisation of the as-printed (APed) samples indicates that Zr segregates at the grain boundaries is the main cause of the cracks. And the cracks tend to occur at the grain boundaries with higher misorientation angles.

Different amounts of nanoparticles Y_2O_3 are added into IN738LC powders by powder mixture, and Y_2O_3/IN738LC composite parts are fabricated using LPBF. The addition of 0.05 wt% Y_2O_3 can effectively mitigate the cracks under the current experimental condition, however, further increases of the Y_2O_3 nanoparticles to 0.2 wt% and 0.6 wt% aggravate the cracking phenomenon. In addition, both high-temperature

strength and oxidation resistance are improved by adding 0.05 wt% Y_2O_3 nanoparticles compared to the alloy without Y_2O_3.

Pulsed-wave laser beam also reduces the cracks. Microstructural analysis reveals that the refinement of grains by the application of pulsed-wave mode is the main contributor in reducing the cracks, which results from a higher cooling rate under the pulsed-wave mode.

Acknowledgements

List of Publications

Chuan Guo, Qiang Zhu, Mark Ward, Gan Li, Simulation and experiment investigation on the effect of parameters on crack of as-built IN738LC during SLM process, International Conference on Research Advances in Additive Manufacturing (2019) Nanjing, Jiangsu, China.

Chuan Guo, Sheng Li, Shi Shi, Xinggang Li, Xiaogang Hu, Qiang Zhu, R. Mark Ward, Effect of processing parameters on surface roughness, porosity and cracking of as-built IN738LC parts fabricated by laser powder bed fusion, Journal of Materials Processing Technology 285 (2020) 116788.

Chuan Guo, Zhengrong Yu, Chang Liu, Xinggang Li, Qiang Zhu, R. Mark Ward, Effects of Y_2O_3 nanoparticles on the high-temperature oxidation behaviour of IN738LC manufactured by laser powder bed fusion, Corrosion Science 171 (2020) 108715.

Chuan Guo, Zhen Xu, Yang Zhou, Shi Shi, Gan Li, Hongxing Lu, Qiang Zhu, R. Mark Ward, Single-track investigation of IN738LC superalloy fabricated by laser powder bed fusion: Track morphology, bead characteristics and part quality, Journal of Materials Processing Technology 290 (2021) 117000.

Chuan Guo, Yang Zhou, Xinggang Li, Xiaogang Hu, Zhen Xu, Enjie Dong, Qiang Zhu, R. Mark Ward, A comparing study of defect generation in IN738LC superalloy fabricated by laser powder bed fusion: Continuous-wave mode versus pulsed-wave mode, Journal of Materials Science & Technology 90 (2021) 45-57.

Contents

Nomenclature Symbol

Item	Units	Description
A	N/A	Laser absorptivity of powder
A_M	mol/g	Molar mass of metal atoms
A_s	m^2	Surface area
a	μm	Radius of liquid droplet
a_d	μm	Size of defect at interface
a_γ	Å	Lattice parameter of γ
$a_{\gamma'}$	Å	Lattice parameter of γ'
b	N/A	Burgers vector
C_p	J/g/ºC	Specific heat capacity
D	μm	Diameter of liquid cylinder
D_g	μm	Average size of grains
D_{Al}	m^2/s	Diffusivity of Al atoms
D_o	m^2/s	Diffusivity of O atoms
D_m	μm	Bead depth
D_s	μm	Spot distance
d_O	μm	Thickness of oxide scale
E_O	GPa	Elasticity modulus of oxide scale
f	kHz	Laser frequency
f_g	N/A	Geometric factor
f_i	N/A	Number of cracks that occur at the misorientation angles of i
G	GPa	Shear modulus
G_T	ºC/m	Thermal gradient
h	W/m^2/ºC	Convective heat transfer coefficient
h_s	J/g	Enthalpy at melting
i	N/A	Number
K	N/A	Strengthening coefficient
K_{IC}	MPa·m$^{1/2}$	Fracture toughness
k	W/m·K	Thermal conductivity
k_p	mg^{2}cm^{-4}h^{-1}	Parabolic oxidation rate constant
L	μm	Length of laser beam path
M_O	mol/g	Molar mass of oxide molecules
N_{Al}	N/A	Concentration of Al atoms
N_o	N/A	Concentration of O atoms
n	N/A	Normal vector of powder bed surface
P	W	Laser power

$Q_{conduction}$	J	Energy losses by conduction
$Q_{convection}$	J	Energy losses by convection
$Q_{radiation}$	J	Energy losses by radiation
q	W/m^2	Heat input of laser beam
R	μm	Radius of laser beam
R_T	ºC/s	Cooling rate
r	μm	Radial distance of the target to the centre of laser beam
r_i	mg/cm^2/h	Mass gain rate in the current testing period
r_O	μm	Length of oxide intrusion into matrix for a wavy interface
s	μm	Hatching spacing
T	ºC	Temperature
T_{eq}	ºC	Equicohesive temperature
T_f	K	Fusion temperature
T_m	ºC	Melting point of materials
T_o	ºC	Testing period of oxidation
T_p	ºC	Peak temperature
T_r	K	Room temperature
T_0	ºC	Initial temperature
t	s	Time
t_{cycle}	μs	Time for a pulse
t_{off}	μs	Time that laser is not emitting
t_{on}	μs	Time that laser is emitting
$t_{solidification}$	μs	Solidification time of liquid droplet
t_{spread}	μs	Spread time of liquid droplet
V	m^3	Volume
V_m	cm^3/mol	Molar volume of the alloy
V_{ox}	cm^3/mol	Molar volume of A1$_2$O$_3$
V_T	m/s	Solidification rate
v	mm/s	Scan speed
x	μm	Location of laser beam in x-coordinate
x_0	μm	Starting point of laser beam in x-coordinate
y	μm	Location of laser beam in y-coordinate
y_0	μm	Starting point of laser beam in y-coordinate
z	μm	Location of laser beam in z-coordinate
z_0	μm	Starting point of laser beam in z-coordinate
α	m^2/s	Thermal diffusivity
α_O	10^{-6}/K	Thermal expansion coefficient of substrate
α_S	10^{-6}/K	Thermal expansion coefficient of oxide
γ	N/m	Surface tension
γ_{gb}	J/m	Grain boundary energy

γ_{sl}	J/m^2		Solid/liquid interfacial energy
ΔH	J/g		Deposited energy density
Δm	mg		Mass change
ΔT	ºC		Temperature difference
ΔT_b	ºC		Coalescence undercooling
ΔS_f	J/g/ºC/m^3		Entropy for fusion per unit volume
δ	N/A		Duty ratio
δ_{di}	μm		Thickness of diffuse interface
ε	J/K		Stefan-Boltzmann constant
ε_c	N/A		Critical strain
ζ	N/A		Misfit between precipitate and matrix
η	N/A		Sphericity
θ	º		Contact angle between liquid cylinder and substrate
θ_{gb}	º		Grain boundary misorientation angle
θ_a	º		Solidification angle of liquid droplet
θ_b	º		Spread angle of liquid droplet
θ_m	º		Grain boundary misorientation angle at which grain boundary energy reaches its maximum
λ	μm		Length of liquid cylinder
λ_1	μm		Primary dendrite arm spacing
ξ	μm		Thickness of layer
ρ_M	g/cm^3		Density of metal
ρ_m	kg/m^3		Melt density
ρ_O	g/cm^3		Density of oxide
$\Sigma CGBM_i$	N/A		Total number of the misorientation angles of i around cracks
σ	W/m^2		Emissivity
σ_{CTE}	MPa		Stress related to CET
σ_o	MPa		Starting stress for the movement of dislocation
σ_{PBR}	MPa		Stress related to PBR
σ_{ys}	MPa		Yield stress
υ	N/A		Poisson ratio
υ_O	N/A		Poisson's ratio of oxide scale
ϕ_i	N/A		Fraction of grain boundary misorientation angles
φ_i	N/A		Fraction of the misorientation angles around cracks
ψ	J/mm^3		Volume energy density
ψ_i	N/A		Relative crack rate

Acronyms Description

Item	Description
AM	Additive manufacturing
APB	Anti-phase boundary
APBE	Anti-phase boundary energy
APed	As-printed
APT	Atom probe tomography
BT	Balling track
BTR	Brittle temperature range
CAD	Computer-aided design
CB	Conduction bead
CET	Columnar-to-equiaxed transition
CTEs	Thermal expansion coefficients
CWed	Continuous-wave LPBFed
DDC	Ductility dip cracking
DED	Directed energy deposition
DFT	Density-functional theory
DTR	Ductile dip temperature range
EBSD	Electron backscattered diffraction
EDM	Electro-discharge machining
EDS	Energy dispersive spectrometer
EL	Elongation
fcc	Face-centred cubic
FFT	Fast Fourier Transformation
FIB	Focused ion beam
FT	Fluctuating track
GCP	Geometrically close-packed
HAADF	High angle annular dark-field
HAZ	Heated-affected zone
HAGB	High-misorientation angle grain boundary
HRTEM	High-resolution TEM
HTed	Heat-treated
IN738LC	Inconel 738 LC
IPF	Inverse pole figure
LAGB	Low-misorientation angle grain boundary
LFA	Laser flash apparatus
LPA	Laser particle size analyser
LPBF	Laser powder bed fusion
LSCM	Laser scan confocal microscope

LSW	Slyozov and Wagner
Micro-CT	Micro-computed tomography
MAGB	Medium-misorientation angle grain boundary
NCT	Narrow-continuous track
NKB	Narrow-keyhole bead
ODS	Oxide dispersion strengthened
OM	Optical microscope
PAW	Projection-augmented wave
PBF	Powder bed fusion
PBR	Pilling-Bedworth ratio
PDAS	Primary dendrite arm spacing
PF	Pole figure
PWed	Pulsed-wave LPBFed
REE	Reactive element effect
SBB	Shallow-ball bead
SEM	Scanning electron microscope
SLM	Selective laser melting
SUSTech	Southern University of Science and Technology
TCP	Topologically close-pack
TEM	Transmission electron microscope
UoB	University of Birmingham
UTS	Ultimate tensile strength
VED	Volume energy density
WCT	Wide-continuous track
WKB	Wide-keyhole bead
XRD	X-ray diffraction
YS	Yield strength
2D	Two-dimensional
3D	Three-dimensional

Chapter 1 Introduction: Objectives and Scope

1.1. Research background

Engine materials used at higher temperatures and more corrosion circumstances for both airplane and power generation gas turbines have attracted more and more attention from both industrial and academic communities. Figure 1.1 presents the schematic diagram of a typical single-spool axial flow gas-turbine jet engine. The compressor, comprising compressor blades and discs, plays a role in squeezing entering air and increasing air pressure, presenting a "cold" section of the engine. The compressed air, mixed with fuel, flows into the combustor before igniting in the combustion chamber. The hot gases are allowed to expand through a turbine, extracting the mechanical work required to drive the compressor with a shaft between them, which constitutes the "hot" section of this engine [1]. The "hot" section, especially the turbine, can work at the temperatures as high as 730 ºC-1230 ºC, which requires the application of materials with high strength and excellent oxidation/corrosion resistance at elevated temperatures [2].
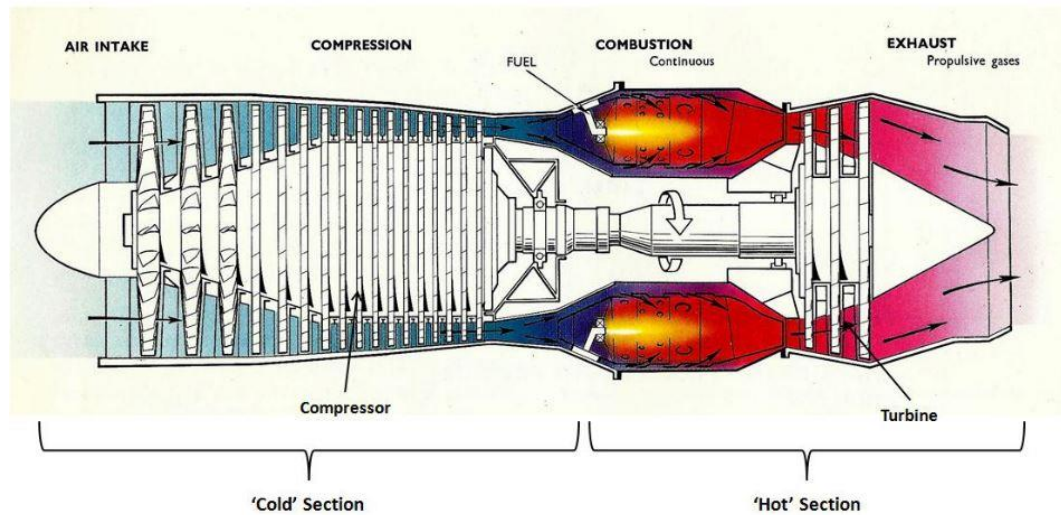
Figure 1.1. Schematic diagram of a simple single spool gas-turbine jet engine with the key stages and components labeled [3].

~ 50 % of the total weight of an aero-engine consists of nickel-based superalloys due to their microstructural stability and excellent properties at elevated temperatures [3]. They are widely used as high-temperature components in the "hot" section such as fuel nozzles (Figure 1.2 (a) [4]) and turbine blades (Figure 1.2 (b) [5]), which have complex internal structures used to transfer fuel, water or cooling air. Here, conventional manufacturing processing is complex such as investment casting, machining and assembling. Additive manufacturing (AM) technology recently developed presents a potential advantage to fabricate components with complex shapes for lower costs, more freedom designs, shorter processes and better qualities. Laser powder bed fusion (LPBF), also known as selective laser melting (SLM), uses metallic powders to make three-dimensional (3D) structures in a layer-by-layer manner and fabricates components with complex geometries in nearly net-shape. Now, LPBF has become the most widely used technology within the metallic AM processes.

LPBF has been widely applied to fabricate components of some weldable superalloys such as Inconel 718 [6] and Inconel 625 [7]. In the manufacturing processes

2

of these alloys, defect-free parts with complex geometries can be built. LPBF provides a prominent reduction of the supply chain and saves both cost and time for the fabrication of parts used in the aerospace field. However, the temperature that these alloys can withstand is generally ~ 700 $^{\circ}$C [6], which greatly limited the usage of LPBFed components made of these alloys at higher temperatures. Therefore, alloys that can be operated at higher temperatures are desired to be applied in the LPBF process to meet the requirements of the aerospace industry for higher temperatures and more severe corrosion/oxidation environments. The Inconel 738 LC (IN738LC) alloy is such a nickel-based superalloy to meet these requirements.

IN738LC is a high-end nickel-based superalloy with an fcc-γ matrix and strengthened by fine γ' precipitations with $Ni_3(Al, Ti)$ chemical composition and $L1_2$ crystal structure. This alloy exhibits excellent creep property and good corrosion resistance at elevated temperatures. The operating temperature can reach as high as 980 $^{\circ}$C [8], which enables the alloy to be used to fabricate turbine discs or blades in the "hot" section. Within the LPBF process, heat transportation phenomena (including heat conduction, convection and radiation), metallurgical phenomena (including melting, solidification, re-melting and re-solidification), laser-matter interaction phenomena (including recoil pressure, vapor and plasma) and melt flowing phenomena (including fluid dynamics and wetting behaviour) determine the complexities of the interaction between powder bed and laser beam [9]. The IN738LC alloy contains a large amount of Al and Ti (Al + Ti > 6 %), indicating the difficulty to be welded and LPBFed due to a strong cracking tendency [10]. Some internal defects such as pores and cracks greatly

restrict its application in fabricating parts that require full densities and excellent performances. Thus, eliminating these defects in IN738LC during LPBF is highly required.
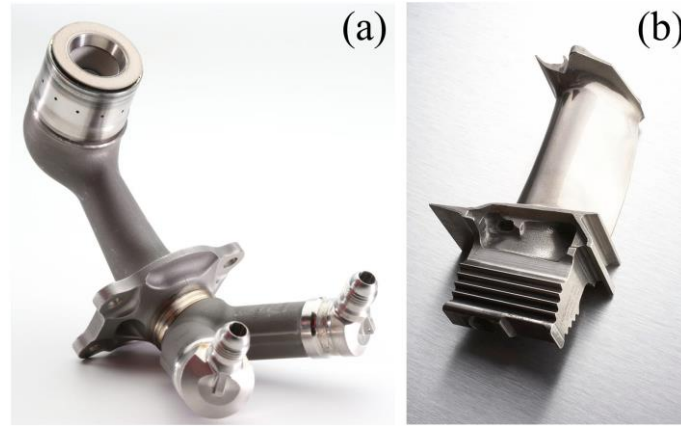
Figure 1.2. Examples of a (a) fuel nozzle [4] and (b) turbine blade [5] in an engine.

1.2. Objectives and scope of this research

Research interest in manufacturing defect-free IN738LC parts using LPBF drives the works of this thesis. The works focus on understanding the defect formation mechanisms and subsequently innovating effective technologies for eliminating these defects in the LPBFed IN738LC alloy. To meet the objectives, the following investigations have been performed in this thesis:

- Firstly, the effects of 3 key processing parameters, i.e., hatch spacing, scan speed and laser power on defects during the LPBF process are studied to understand the forming nature of these defects and optimise the processing parameters for defect-free conditions (Chapter 4).

- Secondly, single-track experiments are performed to study the fluid dynamics and solidification processes during LPBF, focusing on track stability, melt pool

dimensions and bead mode. Bulk samples are fabricated with the same parameters as the single-track testing to associate track behaviour with formation mechanisms of the pore defects (Chapter 5).

- Thirdly, microstructures in the as-printed (APed) and heat-treated (HTed) samples are characterised, and cracking mechanism is particularly investigated (Chapter 6).

- Fourthly, a novel approach of introducing Y_2O_3 nanoparticles to mitigate cracks formed in the IN738LC alloy during LPBF is studied. Tensile properties at both room and elevated temperatures and high-temperature oxidation resistance are measured to evaluate the effectiveness of Y_2O_3 nanoparticles as well (Chapter 7).

- Finally, a pulsed-wave laser beam is also applied as an additional approach to mitigate cracks in IN738LC during LPBF. (Chapter 8).

1.3. References

[1] Roger C. Reed (2006). The Superalloys Fundamentals and Applications. United States of America.

[2] Muzangaza E. (2018). The Effects of Titanium Ti-6Al-4V Powders Manufactured Using Electron Beam Melting (EBM)-Additive Manufacturing on Metallurgical Evaluation. Master Thesis, University of Birmingham.

[3] Wang X. (2017). Improving the microstructure, mechanical properties & process route in selective laser melting of nickel-superalloys. PhD Thesis, University of Birmingham.

[4] GE Aviation (2019). https://blog.geaviation.com/manufacturing/outside-the-box-

how-ge-aviation-entered-the-brave-new-world-of-additive-manufacturing/

[5] Jet Engine Turbine Blade Photograph by Science Photo Library (2018). https://fineartamerica.com/featured/2-jet-engine-turbine-blade-science-photo-library.html

[6] Holland S., Wang X., Fang X., Guo Y., Yan G., Li L. (2018). Grain boundary network evolution in Inconel 718 from selective laser melting to heat treatment. Materials Science & Engineering A, 725, 406-418.

[7] Li C., Guo Y., Zhao J. (2017) Interfacial phenomena and characteristics between the deposited material and substrate in selective laser melting Inconel 625. Journal of Materials Processing Technology, 243, 269-281.

[8] Thakur A. (1997). Microstructural responses of a nickel-based cast IN-738 superalloy to a variety of pre-weld heat-treatments. Master Thesis, University of Manitoba.

[9] Guo C., Xu Z., Zhou Y., Shi S., Li G., Lu H., Zhu Q., Ward R. M. (2021). Single-track investigation of IN738LC superalloy fabricated by laser powder bed fusion: Track morphology, bead characteristics and part quality. Journal of Materials Processing Technology, 290, 117000.

[10] Wang H., Zhang X., Wang G., Shen J., Zhang G., Li Y., Yan M. (2019). Selective laser melting of the hard-to-weld IN738LC superalloy: Efforts to mitigate defects and the resultant microstructural and mechanical properties. Journal of Alloys and Compounds, 807, 151662.

Chapter 2 Literature Review

2.1. Introduction

This chapter presents a review of relevant literature to provide context for the current work. The contents cover the overview of additive manufacturing and laser powder bed fusion technologies including processing parameters and potential defects during this process. In addition, it presents a summary of the fundamental metallurgy of nickel-based superalloys while highlighting the target material, i.e., IN738LC. Lastly, it states the methods for solving the cracking in nickel-based superalloys during LPBF.

2.2. Additive manufacturing overview

Additive manufacturing (AM) technology, also known as "3D printing", has attracted more and more attention from both industrial and research communities, where the object is produced in a layer-by-layer fashion. Computer-aided design (CAD) software or three-dimensional (3D) scanning process prepares a 3D model before sequentially slicing it into a sequence of two-dimensional (2D) layers of profiles with a specific thickness. Each layer represents a cross-section of the objective, with these 2D layers then sent to a 3D printing machine as the source file to control the whole fabrication process. The machine carries out a specific process to produce each layer, which is then stacked from the bottom to the top until its completion [1, 2], as depicted in Figure 2.1.
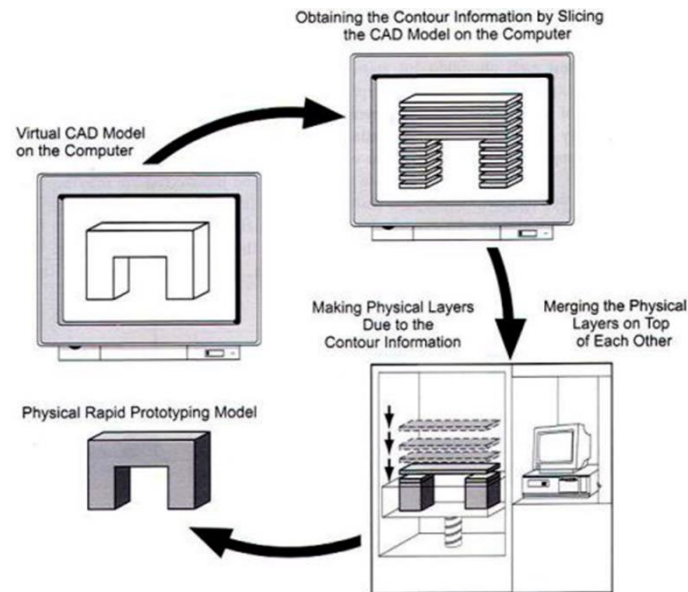
Figure 2.1. Schematic diagram of the AM process [2].

There are 7 types of AM systems identified by the ISO/ASTM52900-15 standard of AM process categorisation including directed energy deposition, powder bed fusion, binder and material jetting, material extrusion, vat photopolymerisation and sheet lamination [3]:

- Directed energy deposition (DED): Metallic powders or wires are the feedstock fed in front of the applied energy source such as laser or electron beam. A multi-axis robotic arm controls the energy source. The metallic feedstock is then melted and deposited in a layer-by-layer manner on the building substrate. The DED process is also an effective approach to repair metallic parts.

- Powder bed fusion (PBF): Energy source such as laser or electron beam, irradiates on the surface of powder bed selectively in the machine's process chamber. Metallic powders are melted, with strong bonds forming between powders within a layer. The stack of layers fabricates the whole part.

- Binder jetting: Powders on the powder bed glued by a liquid bonding agent are

deposited on the building substrate. The process is like PBF, with the materials being in lots of types such as metal, sand, glass and gypsum.

- Material jetting: Unlike the bonding process completed (melt, glue) in the process chamber, a liquid material is sprayed directly by a specialty printhead such as a piezoelectric printhead on the building substrate during the material jetting process. The material is often photosensitive plastic resin, and the layers are formed by hardened using an ultraviolet light.

- Material extrusion: A thermoplastic filament is heated and melted in an extruder. The melt is extruded at the hot end of the extruder and deposited on the building substrate during the material extrusion process.

- Vat photopolymerisation: Photopolymer resin is irradiated by an energy source such as a digital light projector or laser beam. Sequentially, materials are hardened to generate compact layers on the building substrate.

- Sheet lamination: 2D sheets (layers) of material are cut by a laser beam with their desired shapes and fused together to form a 3D objective. The materials are often metal, paper and plastic.

Compared with conventional manufacturing technologies, AM has significant advantages [2]: Material efficiency. Building parts during the AM process are fabricated in a layer-by-layer fashion rather than removing material, where recycling can usually reuse the leftover feedstock; Build and design freedom. Theoretically, even parts with complex geometries can be fabricable due to the layer-by-layer building manner; Resource efficiency. Parts manufactured by AM are usable after simple sandblasting or

9

polishing without or with less post-machine process, which requires fewer auxiliary resources such as fixtures, cutting tools and jigs.

2.3. Laser powder bed fusion

2.3.1. Overview

Laser powder bed fusion (LPBF) is an additive manufacturing method used to fabricate solid metallic components with metallic powders by a high-intensity laser beam [4, 5]. The process of LPBF is shown in Figure 2.2. A 3D CAD model of the objective part is prepared and sliced into 2D profiles with a certain thickness. This sequence of profiles is uploaded to the computer control system as a source file to control the fabrication process. The laser generator emits a high-energy laser beam through a beam expander and a scanning galvanometer. Subsequently, the laser beam irradiates on the powder bed selectively based on the current profile of the input 3D CAD model under the control of a group of lenses. Strong metallurgical bonds are formed between powders within a layer during an extremely fast cooling process. After the presented layer is completed, the build station piston in the building chamber drives the substrate and the LPBFed part to drop a certain distance according to the thickness of the 2D profile. Meanwhile, the supply chamber rises a certain height to replenish powders to a new layer by a recoater. This process repeats until the objective is formed [6]. LPBF can be used in processing Ti-alloys [7], Ni-alloys [8], Fe-alloys [9] and Al-alloys [10].
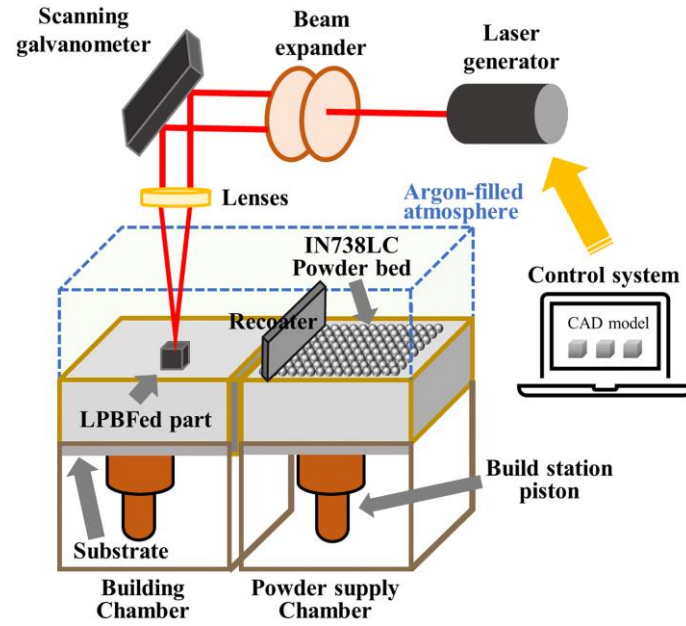
Figure 2.2. Schematic diagram of the LPBF process.

2.3.2. Processing parameters

2.3.2.1. Laser power

Laser power is one of the most important parameters within the LPBF process. Many researchers suggested that the laser power had significant effects on the printing quality of LPBF [11, 12]. The laser power can directly influence the printed part's porosity by changing the energy input densities (laser power/scan speed) [7]. Normally, as the laser power increases, it allows for the full melting of the powders during the LPBF process, which induces a higher relative density in the printed part. By contrast, pores with irregular shapes are formed due to lack of fusion when the laser power is low [13]. Melt pool is the melting trace of the interaction between the laser beam and the powder bed during LPBF. Low laser powers usually lead to a normal-elliptical and shallow melt pool. However, as it applies a considerably high laser power, the excessive

energy input density leads to the formation of a keyhole [14], as shown in Figure 2.3. The keyhole is considered an unstable condition of melt pool and a cause of pores. Later sections will detail the pore formation mechanism and the keyhole.
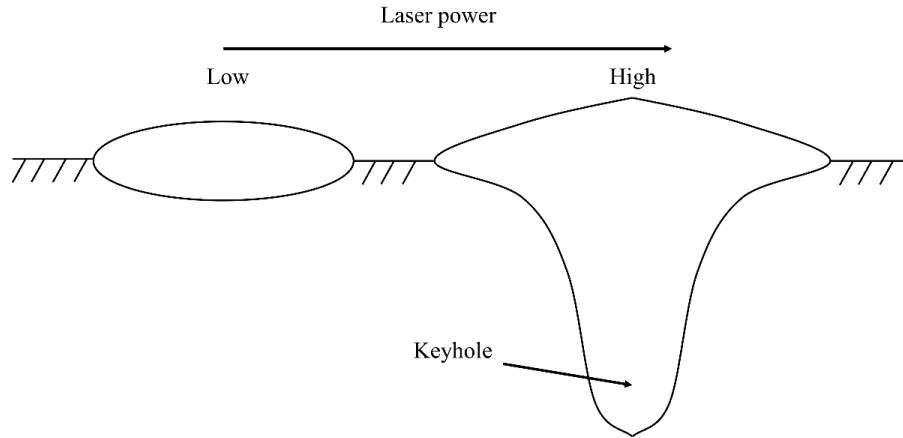
Figure 2.3. Effects of laser power on melt pool interface shape (fixed other parameters) showing a shallow melt pool at low laser powers, while keyhole at high laser powers.

2.3.2.2. Scan speed

Scan speed decides the dwell time that the laser beam stays at a position on the powder bed, which is related to the efficiency of the LPBF process. It also affects the energy input density together with the laser power and further affects the printing quality during the LPBF process. For a given laser power, high scan speeds can lead to low energy input densities, with the porosity in the printed parts increasing accordingly [15, 16]. In addition, it also considers the scan speed as one of the key factors which can influence the fluid dynamics in the LPBF process such as spatter [17] and open pore [18]. When applying a considerably high scan speed, the melt track trends to break up into small droplets, known as Plateau-Rayleigh instability, which is a potential cause of the balling phenomenon in LPBF [19, 20].

2.3.2.3. Hatch spacing

Hatch spacing, also known as hatch space or hatch distance [21, 22], represents the distance of laser tracks within a layer, which directly decides the overlapping of the melt pools between adjacent tracks. Large hatch spacings are unfavourable to build the printed parts with full densities due to the lack of fusion between neighbouring laser tracks [16]. Nevertheless, low hatch spacings lead to the formation of micro-humping, caused by Marangoni convection from the current track to the previously fabricated one [23].

2.3.2.4. Thickness of layer

Thickness of layer is an important parameter that significantly affects the efficiency of the LPBF process and the printing quality. It indicates the thickness of the slice of the input 3D model. For the LPBF process, the thickness of layer is normally between 20 μm and 100 μm [24]. The laser beam cannot entirely penetrate the powder layer that is too thick. As a result, it generates pores due to un-melt powders [25]. In addition, the thickness of layer can influence the spatter behaviour during the LPBF process [26]. As the layer's thickness increases, the spatter becomes more violent, since a relatively thick powder layer can induce more powders melted by the laser beam and more melt surface area, which correspondingly increases the evaporation and the Marangoni force in the LPBF process, thus enhancing the spatter [17].

2.3.2.5. Scan strategy

Scan strategy is the path pattern by which the laser beam scans the powder bed. Figure 2.4 exhibits some typical scan strategies during the LPBF process [27], i.e., parallel scanning, paintbrush scanning, spiral scanning and chessboard scanning.
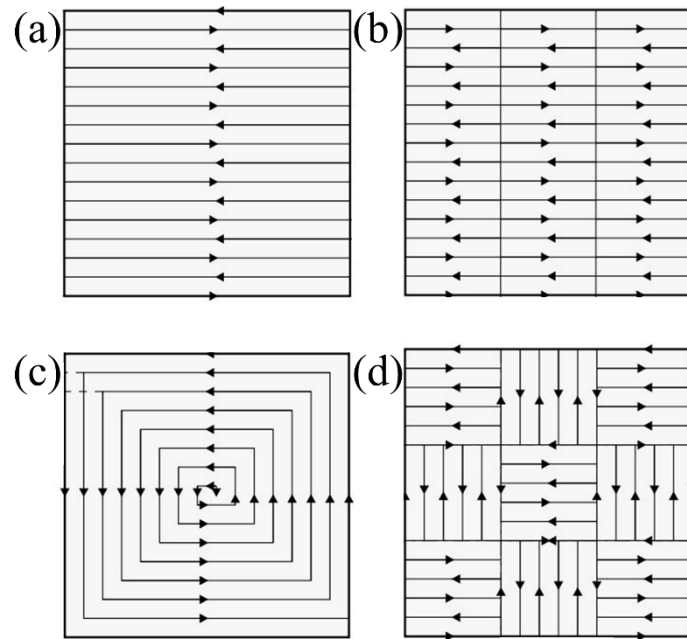
Figure 2.4. Typical scan strategies in the LPBF process, (a) parallel scanning, (b) paintbrush scanning, (c) spiral scanning and (d) chessboard scanning [27].

The scan strategy has a significant effect on the residual stress and the solidification process in LPBF, since it decides the temperature history by changing the thermal input and accumulation [28], which further influences the cracking behaviour and the grain structure during LPBF [29].

2.3.2.6. Other parameters

- Spot size: Spot size is defined as 4Dσ, i.e., the average of 4 times the standard deviation of the energy distribution, evaluated separately in orthogonal directions over the beam intensity profile [30].

14

- Ambient pressure: During the LPBF process, argon and nitrogen often act as shielding gas, preventing materials from reacting with the environment gas in the process chamber, especially oxygen. The pressure of the shielding gas can influence the LPBF performance [31, 32] such as the spatter and denudation phenomena by affecting the gas dynamics surrounding the laser beam.

- Substrate preheating temperature: Preheating temperature is the temperature loaded on the building substrate, which has a significant effect on the grain structure in the printed part [33]. As a method to mitigate the cracking during the LPBF process, preheating the building substrate reduces the thermal stress by decreasing the thermal gradient along the printed part [34].

- Energy input density: Energy input density is widely used to justify the comprehensive effect of the processing parameters on the printing qualities in LPBF. There are 3 different energy input densities, linear (P/v) [35], planar ($P/\pi vs$) [36] and volume ($P/vs\xi$) energy densities (VEDs) [7, 36], where P is the laser power, v is the scan speed, s is the hatch spacing, and ξ is the thickness of layer.

2.3.3. Pore formation

2.3.3.1. Lack of fusion

Lack of fusion is one of the most common defects during the LPBF process [7, 15], attributed to low energy input densities, which are not high enough to melt all the powders within a single layer. The lack of fusion causes un-melt powders to trap in the printed parts, thus forming pores during the melt cooling and shrinking in the

solidification process. The pores caused by the lack of fusion typically exhibit irregular shapes, and the un-melt powders within these pores have no strong metallurgical bonding with the surrounding solidified material and impede the continuity of the whole part, which deteriorates the mechanical properties of the printed components [15]. Figure 2.5 shows an example of the pore attributed to the lack of fusion.
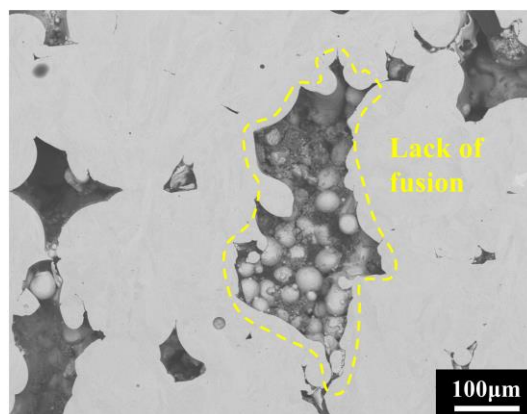
Figure 2.5. An example of a pore attributed to the lack of fusion observed using scanning electron microscope.

2.3.3.2. Metallurgical pore

Metallurgical pores, ascribed to the gases trapped in the melt pool or evolved from the powders during solidification, are sphere-shaped with small sizes [18]. Low scan speeds can eliminate the metallurgical pores, since low scan speeds can increase the convection intensity of the liquid in the melt pool, which favours the gas to escape from the melt and further removes the metallurgical pores [18].

2.3.3.3. Keyhole pore

Keyhole mode is commonly observed during the laser welding process [37] when the energy input density is high enough to cause the evaporation of melt and the formation of plasma [38]. Metal evaporation causes the development of vapour cavities,

which can enhance the powder absorption due to the multiple reflections of the laser beam. It enables the laser beam to "drill" to a considerably deeper melt pool than the normal conduction mode does. However, the evaporation of metal and the collapse of cavity can leave voids in the melt pool after the laser beam leaves the current location [19], as presented in Figure 2.6. Therefore, the keyhole mode is one of the causes of the pores during the LPBF process.
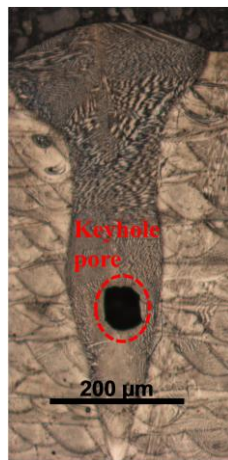
Figure 2.6. An example of a pore attributed to the keyhole observed using optical microscope.

2.3.3.4. Spatter

Spatter phenomenon happens when the laser beam reacts with the powder bed, forced by the gas and melt flow dynamics, considered a factor that can lead to an unstable melt pool and pores in the printed part [39-42]. There are 3 different mechanisms of the spatters in the LPBF process [42], as depicted in Figure 2.7.
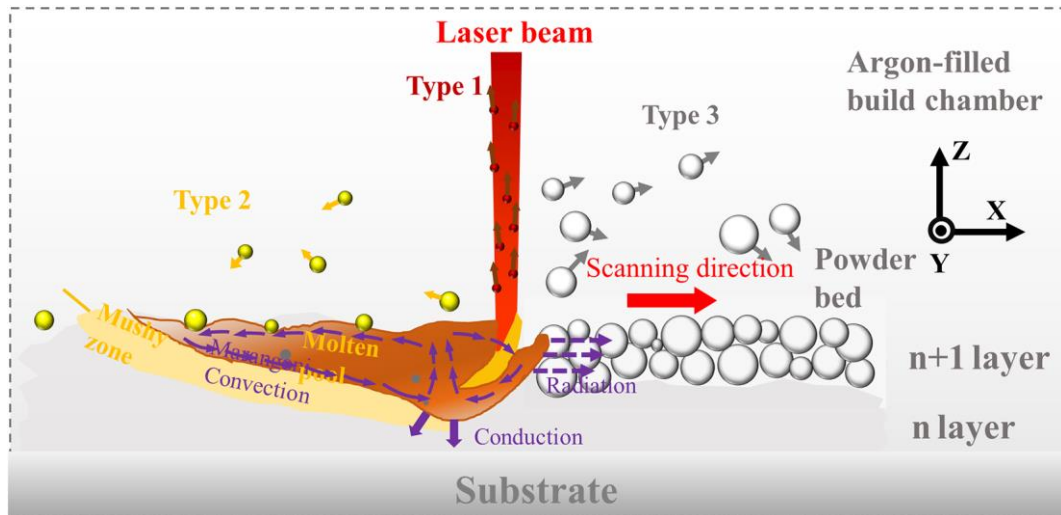
Figure 2.7. Schematic diagram of 3 different types of spatters.

The first type of spatter results from the recoil pressure associated with the extreme expansion of gas phases, inducing a metallic jet along the laser beam. The direction of the spatter in this type is roughly parallel to the laser beam. The second type is droplet spatter, dragged by the melt flowing from the high-temperature bottom of the melt pool to the low-temperature sidewall and edge at the backside due to the Marangoni convection. This type provides the main form of the spatter during the LPBF process. The third type of spatter occurs when blast waves of the laser beam squeeze the un-melted powders, with the splashed powders normally travelling in the direction of the laser beam. Some splashed powders in a large size fall onto the surface of the powder bed, which can affect the powder spreading for the next layer. The splashed powders with considerably large sizes are difficult to fully melt by the laser beam, leading to the pore formation in the printed part.

2.3.4. Cracking formation

2.3.4.1. Solidification cracking

Solidification cracking, also known as hot cracking, is common in the AM and welding processes [43-46]. In the solidification process, liquid films remain at the last stage of solidification due to a large solidification temperature range of the alloy, and the solidification cracking then forms related to the residual stress caused by a high thermal gradient [47, 48]. The solidification cracking occurs at the fusion zone of the melt pool [49, 50], as shown in Figure 2.8 (a), with Figure 2.8 (b) an example of the solidification cracking during the welding process.
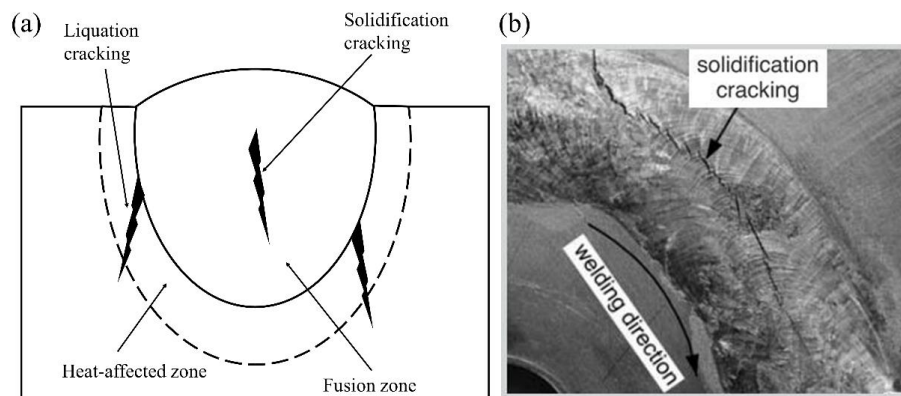
Figure 2.8. (a) Schematic diagram of the solidification crack and the liquation crack, (b) an example of the solidification crack observed using optical microscope [51].

Thermal stress and solidification temperature range are the key factors that can affect the solidification cracking behaviour in the AM and welding processes. The thermal cycle pattern, the heat input, the material shrinkage and expansion property all influence the thermal stress. It is believed that the solidification temperature range is influenced by the segregation behaviour of different elements in alloys. Hu et al. [52] reported the formation of low melting γ + Laves eutectic phase in the inter-dendritic

regions of the Inconel 625 alloy processed by laser solid forming due to the segregation of Nb and Mo, inducing the solidification temperature range to an increased 210 $^{\circ}$C, which was favourable for the solidification cracking. Tomus et al. [53] suggested the content of Mn + Si was the main cause that led to the hot cracking in fabricating Hastelloy-X using LPBF.

2.3.4.2. Liquation cracking

Liquation cracking, primarily attributed to the heat cycle in the laser AM process, where frequent heat inputs lead the low-melting-point phases to re-melt, and the cracking generates under the thermal stress. Unlike the solidification cracking, the liquation cracking occurs at the heated-affected zone (HAZ) of the melt pool [54], as shown in Figure 2.8 (a). Figure 2.9 shows an example of the liquation crack along the grain boundary, with clear re-solidification phases observed.
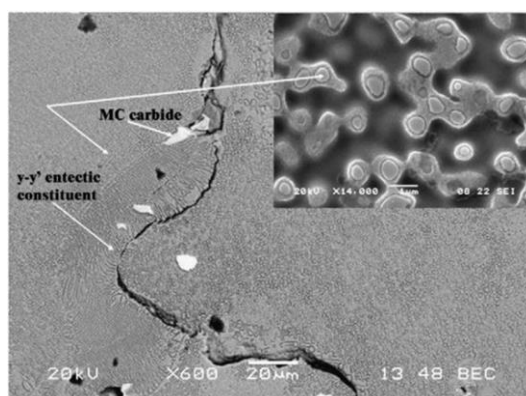
Figure 2.9. An example of the liquation crack observed using scanning electron microscope showing some phases in the cracking region [55].

There are 2 main causes of the liquation cracking: constitutional liquation and low-melting-point phases. During the rapid heating process, the solutes concentrate on the precipitate/matrix interface by the solid-state dissolution of the precipitates. When the

solute concentration and the located temperature meet the equilibrium reaction of the precipitate-matrix eutectic, metastable liquid films form on the precipitate/matrix interface, leading to the constitutional liquation [54]. Pepe et al. [56] first reported secondary phase particle constitutional liquation in 18-Ni steel. Many researchers [57-61] soon found the constitutional liquation of γ' in nickel-based superalloys in the laser AM and welding processes. Tancret [62] used the simulation method to characterise the effect of heating rate and liquidation particle size on the liquation behaviour. He suggested that increasing the heating rate and the liquation particle size aggravated the liquidation. Attallah et al. [63] used confocal laser scanning microscopy to observe the γ' liquation in situ. In addition, borides [64, 65] and carbides [64, 66, 67] are also reported to be the main contributors during the liquidation process. The liquid film migration phenomenon found at grain boundaries [68, 69] suggests that the driving force for the liquid film migration are the diffusional coherency strain and the asymmetry of surface energy due to the curvature on the grain interfaces [69], as depicted in Figure 2.10.
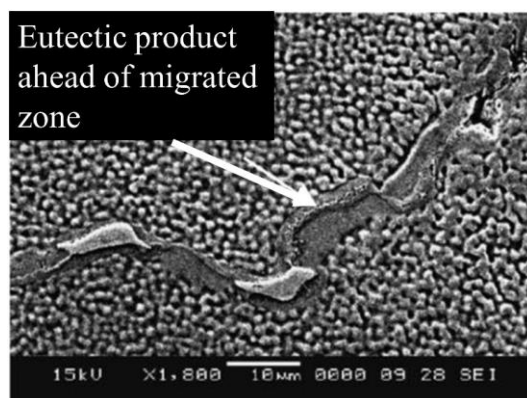
Figure 2.10. An example of the liquid film migration at grain boundary observed using scanning electron microscope [69].

Apart from the constitutional liquation, low-melting-point phases at grain

boundaries also lead to the liquation cracking. The phases such as γ′-γ [70, 71] and γ-Laves [46, 72], melt directly by the rapid heating process.

2.3.4.3. Ductility-dip cracking

Ductility dip cracking (DDC) is a solid-state phenomenon at elevated temperatures, usually observed in austenitic stainless steel and nickel-based superalloys in the multi-pass welding and laser AM processes [6, 73]. The mechanism has been postulated to "ductility exhaustion" along grain boundaries by a "creep-like" mechanism in a certain temperature range [73], as shown in Figure 2.11.
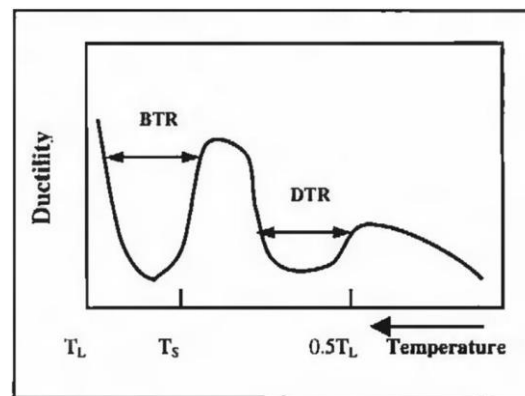
Figure 2.11. Ductility as a function of temperature, where BTR=brittle temperature range and DTR=ductile dip temperature range [73].

Previous works [73-81] reported the DDC's common characteristics. Firstly, the DDC is a characterisation that occurs at the grain boundaries with a long and straight morphology [73, 80]. While some precipitation particles lead to the formation of tortuous grain boundaries, which can effectively hinder the DDC's propagation [75], as depicted in Figure 2.12.
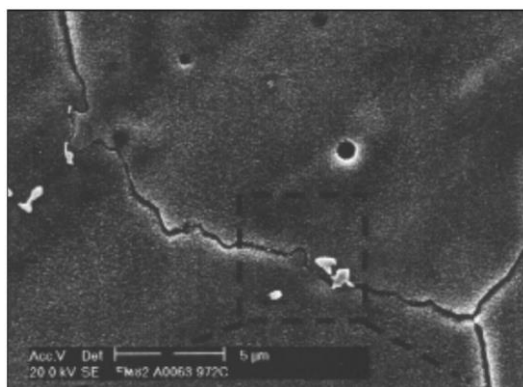
Figure 2.12. Tortuous grain boundary induced by precipitation particles in the Filler Metal 82 alloy observed using scanning electron microscope [75].

The presence of triple-point grain boundary intersections in polycrystalline materials can significantly influence several material properties including ductility, grain boundary migration, sliding and recrystallisation [75]. The triple points are always the DDC's crack initial position, since the stress is favourable to concentrate within these regions [73].

A combination of accumulated deformation and thermal energy can promote recrystallisation at the DDC tips when applying high temperature and stress. High local strain at these crack tips can lower the amount of necessary thermal energy to induce recrystallisation [73], which leads to the particle stimulated nucleation [78]. Therefore, fine grains can be observed in the regions of the DDC tips, as depicted in Figure 2.13.
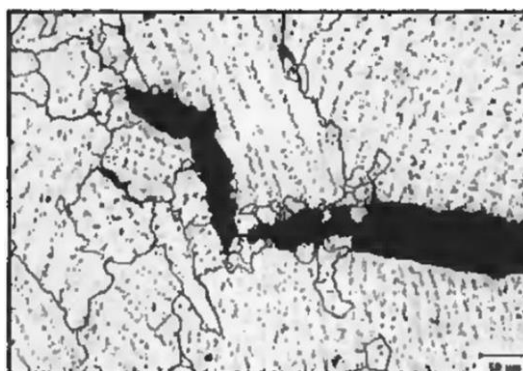
Figure 2.13. Recrystallisation in the region of the DDC crack tips in the Filler Metal 82 alloy (11 % strain and 1147 ºC) observed using scanning electron microscope [73].

23

2.3.4.4. Strain-age cracking

Strain-age cracking occurs during post-fabrication heat treatment of the alloys strengthened by γ′ precipitate, characterised by intergranular micro-cracking in either the HAZ or weld bead [82-85]. During the precipitation process, the ductility of alloy drops to a lower level, with cracks forming when the alloy becomes subjected to the strain which exceeds its available ductility [83]. Because the strain-age cracking relates to γ′ phase, and Ti and Al are important constituent elements of γ′ phase, it is reasonable to infer the compositions of Ti and Al are the main factor which affects strain-age cracking, as demonstrated in Figure 2.14. The alloys with the Al + Ti content greater than 4 wt% are considered a non-weldable alloy due to a large volume fraction of γ′ precipitates existing in the microstructure, leading to the strain-age cracking [84].
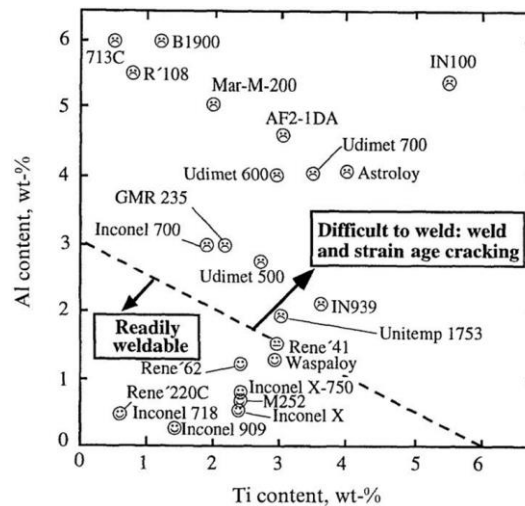
Figure 2.14. Relationship between weldability and (Al + Ti) contents based on strain age cracking susceptibility [84].

2.3.4.5. Residual stress and warping

Previous works [86-90] reported the residual stress during the AM process. Residual stress is the accumulation of material hardening derived from rapid cooling

caused by both phase transformation and temperature gradient, involving the process of solidification and phases changing to a solid-state between crystalline structures [86]. Mercelis et al. [86] suggested a temperature gradient mechanism (TGM) to explain the formation of residual stress, as shown in Figure 2.15 (a). During the laser beam radiates on the top surface of the material, a high heating rate causes a thermal gradient to generate. It also forms a compressive strain due to the expansion of the material in the top layer. When the stress reaches the yield strength of the material at a certain temperature, the material in the top layer becomes plastically compressed, and a counter bending away from the laser beam correspondingly occurs. During the cooling process, the plastic compression in top layers begins to shrink into a relatively small volume, thus dragging the surrounding to a bending angle towards the laser beam [88] and leading to distortion. This also causes cracking to generate in the material. Due to the bending conduction of material towards the laser beam, the edges of the part detach from the building substrate or the subsurface material, thus leading to wrapping. In a worst-case scenario, the part fails to fabricate due to losing the bonding with the building substrate induced by the wrapping phenomenon. Figure 2.15 (b) presents an example of the wrapping during the LPBF process.
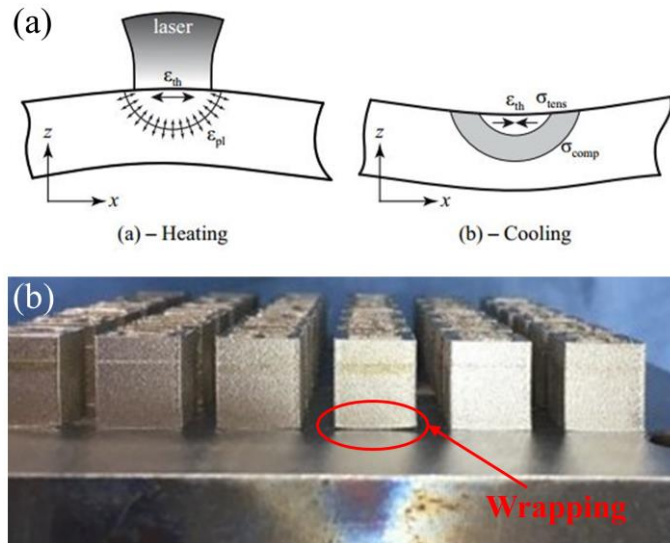
Figure 2.15. (a) Schematic diagram of the residual stresses caused by temperature gradient mechanism [86], (b) an example of the wrapping phenomenon in the LPBF process observed using camera snapshot.

2.4. Nickel-based superalloys

2.4.1. Overview

Aerospace field has a long need for the materials with excellent mechanical performance, good oxidation/corrosion resistance and stability at elevated temperatures [91, 92]. When it requires the properties loaded under static, fatigue and creep conditions, nickel-based superalloys have emerged as the materials of choice for high-temperature applications [93-95]. The operating temperature for nickel-based superalloys is usually beyond 800 °C such as turbine disc and blade. Figure 2.16 (a) shows the Rolls-Royce Trent 800 engine, which powers the Boeing 777 airplane, with Figure 2.16 (b) showing how nickel-based superalloy is one of the most important components of the aero-engine system [92].
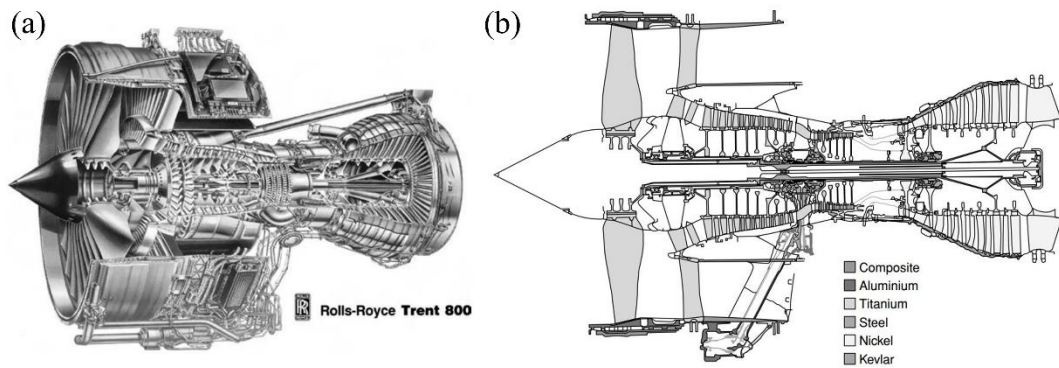
Figure 2.16. (a) A Rolls-Royce's Trent 800 engine, (b) schematic diagram of the major material used in the Trent 800 engine [92].

The basic strengthening mechanism of nickel-based superalloys are divided into the following 3 methods [96-98]:

• Solution strengthening of nickel-based superalloys is achieved by increasing the ability of binding force between atoms, the lattice distortion and the recrystallisation temperature and decreasing the stacking fault energy and the diffusion ability of solution atoms. Typically, the elements with proper solubility, large size effect and high melting point are the main contributors to the solution strengthening effect.

• Precipitation strengthening primarily stems from secondary precipitation particles such as γ', γ'' and carbides, which can prevent grain boundaries from sliding and creating anti-phase boundary energy in the material's microstructure. The strengthening effect significantly depends on the morphology, the size and the volume fraction of the precipitation particles.

• Grain boundary is vulnerable at high temperatures, with cracking also occurring at grain boundaries. Therefore, it is of great significance to strengthen grain boundaries. Some elements diffuse to grain boundaries during solidification, known as internal absorption or equilibrium segregation, which can strengthen or

weaken grain boundaries. It should eliminate the embrittlement element at grain boundaries such as gas and impurity elements. Some rare and alkaline earth elements such as B and Zr, play the role to strengthen grain boundaries by changing grain boundary curvature and purifying grain boundaries.

2.4.2. Phases in nickel-based superalloys

Nickel-based superalloys comprise the austenitic face-centred cubic (fcc) matrix phase γ [99, 100] and a variety of secondary phases, as shown in Figure 2.17. These secondary phases include carbides MC, $M_{23}C_6$, M_6C and M_7C_3 [101, 102], fcc ordered γ' (Ni$_3$(Al,Ti)) [103-105], bct ordered γ'' (Ni$_3$Nb) [106, 107], hexagonal ordered η (Ni$_3$Ti) [108] and the orthorhombic δ (Ni$_3$Nb) [109, 110]. The γ', γ'' and η phases are geometrically close-packed (GCP) phases [91]. In addition, it also forms some detrimental phases in nickel-based superalloys such as Laves, σ and μ, known as topologically close-pack (TCP) phases [97].
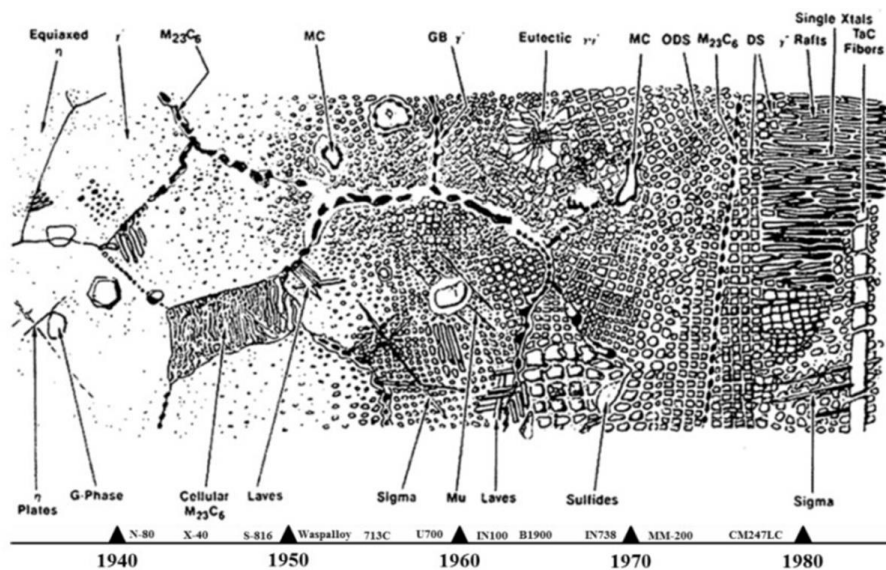
Figure 2.17. Schematic diagram of the phase distributions in nickel-based superalloys [91].

28

2.4.2.1. γ phase

γ phase is the matrix of nickel-based superalloys with the other phases residing within it [92]. It distributes nickel atoms on each corner and the centres of faces in the crystalline cube, as depicted in Figure 2.18. It contains significant concentrations of solution elements such as Co, Cr, Mo and W. These element atoms are solution strengthening solutes residing within the matrix, which can induce the lattice deformation of the crystal. Particularly, some atoms in large sizes are favourable to create strain and stress fields around themselves. As a result, it can impede the crystal slide and the dislocation movement along lattice structure, thus improving the strength of alloys [97].
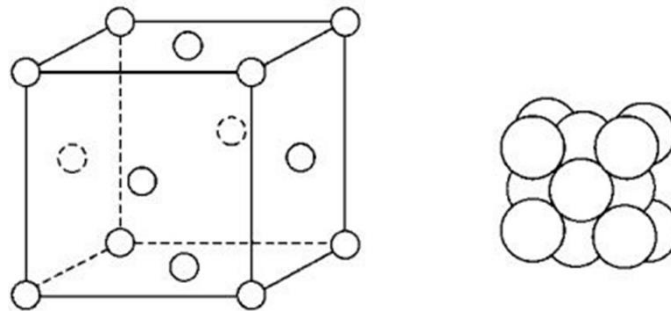
Figure 2.18. Crystal structure of the γ matrix of nickel-based superalloys [91].

2.4.2.2. γ′ phase

γ′ is the main strengthening precipitation phase in the nickel-based superalloys with the stoichiometry A_3B (where A is Ni or Cr, and B is Al, Ti, Ta, V or Nb) like (Ni, Co)$_3$(Al, Ti, Ta) [97]. The lattice structure of γ′ is order $L1_2$ with Al atoms at each corner and Ni on each face centre, as presented in Figure 2.19 (a). Figure 2.19 (b) shows its typical morphology, while the shape and the size vary under different heat treatment conditions such as heating temperature and cooling rate [111].
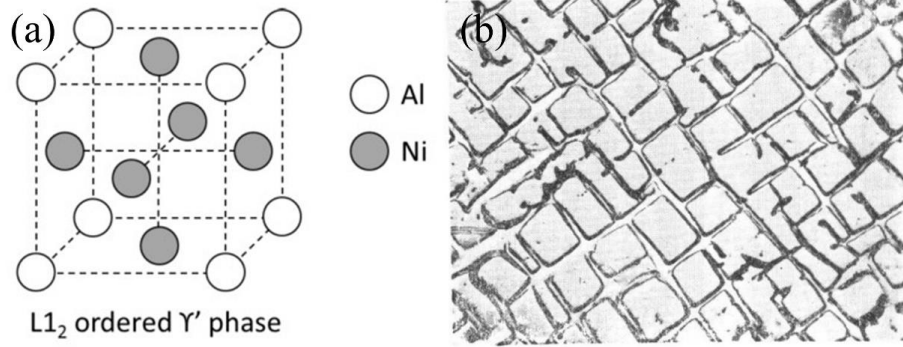
Figure 2.19. (a) Crystal structure of the γ' phase [91], (b) typical γ' morphology in nickel-based superalloys observed using scanning electron microscope [97].

Precipitation strengthening alloys are strengthened by impeding the dislocation motion during plastic deformation. The following lists some principal precipitation hardening characteristics [98]:

- The misfit between the γ' particles and the γ matrix decides the morphology of the precipitates and further the effectiveness of strengthening [112], which are calculated as [113]:

$$\zeta = 2 \times (\frac{a_{\gamma'} - a_{\gamma}}{a_{\gamma'} + a_{\gamma}}) \qquad \text{Equation 2.1}$$

where $a_{\gamma'}$ and a_{γ} are the lattice parameters of γ' and γ phases, respectively. A small lattice misfit normally accompanies coherent precipitates, and a larger misfit gives rise to incoherent precipitates [114]. Spherical γ' particles form at a negligible misfit, while plate-like or cuboidal γ' particles generate with some measurable (> 0.05 %) γ/γ' misfits [115].

- Introducing preferred ordering for single atoms can increase the amount of energy required to pass the dislocation through a precipitation particle. The order of atoms can cause an anti-phase boundary (APB) [116, 117], which can induce extra anti-phase boundary energy (APBE). The lattice with relatively high APBE requires a

greater force to induce deformation, thus strengthening alloys.

- Precipitates hinder the movement of dislocations primarily by 2 mechanisms. In the Orowan mechanism, dislocations bypass the precipitates and form loops around them when the precipitates are larger and incoherent with the matrix. For the shearing mechanism, the dislocations pass through the precipitates by shearing, which is likely to occur when the precipitates are coherent with the matrix with relatively small sizes. [118].

2.4.2.3. Carbides

The presence of carbides has a great impact on the properties of nickel-based superalloys. Carbides at grain boundaries are favourable to prevent grain-boundary sliding, thus strengthening alloys [91]. Carbides can also tie some detrimental elements which form harmful phases in alloys. There are 4 main types of carbides in nickel-based superalloys: MC, $M_{23}C_6$, M_7C_3 and M_6C, where M can be Cr, Mo, Ti, Ta or Hf [92]:

- MC usually exhibits coarse, globular, blocky or script morphology within the microstructure of nickel-based superalloys. M is usually Ti, but is replaceable by Ta, Zr, Nb, Mo, W, Ni and Cr [98]. For example, (Ti, Mo)C is found in Udimet 500 and M-252, and (Ti, Nb, W)C is more common in Mar-M200. The stable temperature of MC ranges from 760 °C to 1150 °C. Under a long-time heating process, MC can dissolve into $M_{23}C_6$ (760 °C-980 °C) or M_6C (815 °C-980 °C) by the reactions:

$$MC + \gamma \rightarrow M_{23}C_6 + \gamma' \qquad \text{Equation 2.2}$$

31

$$MC + \gamma \rightarrow M_6C + \gamma' \qquad\qquad \text{Equation 2.3}$$

- $M_{23}C_6$ is common within the alloys with a composition of Cr larger than 5 %. M is mainly Cr, Fe, Co, W and Mo. $M_{23}C_6$ forms along grain boundaries as a chain morphology, which can impede grain boundaries to slide and further increase the strength of alloys [98].

- Rarely observed in nickel-based superalloys, M_7C_3 is primarily presented in cobalt-based alloys when Ti and Al contents are at low levels [98] such as Nimonic 80A [91]. M is Cr. M_7C_3, known as an unstable carbide, transfers into $M_{23}C_6$ when heating temperatures reach 600 °C-800 °C [97, 98].

- M_6C is more stable than M_7C_3, which decides it is an important grain-boundary precipitate favourable to control the grain size during the wrought process [91]. M can include a large range of elements such as W, Mo, Fe, Co and Ni. M_6C with a chain morphology is beneficial for the strength of alloys, while it is detrimental to the ductility if it exhibits acicular [97].

2.4.2.4. TCP phases

TCP phases include μ, σ and Laves phase, etc., which play an important role in polycrystalline nickel-base superalloys with complex structures and functions:

- Laves phase is in the B_2A type, where A is an element with a bigger atomic radius, and B usually has a smaller atomic radius. Under low-temperature aged, the Laves phase shows as small particles in the microstructure, and these dispersed particles have a strengthening effect on alloys. However, it exhibits bar, leaf and acicular

morphologies under high-temperature aged, which deteriorates the ductility of alloys at room temperature [97].

- σ phase forms at the temperatures ranging from 760 $^{\circ}$C to 980 $^{\circ}$C with the stoichiometric of BA [98]. A is the element on the left of Mn in the periodic table of elements, and B is on the right of Mn. σ phase resides at grain boundaries, showing as small particles or slices. Acicular σ is the channel of crack, which is unfavourable for crack resistance and impact toughness [97]. In addition, it can capture solution strengthening elements from the matrix and further weaken alloys [98].

- μ phase (B_7A_6) forms when a considerable amount of W and Mo exists within alloys. B is the elements in Group VIII in the periodic table of elements, and A is the elements in Groups V and VI. It appears as bar, particle, slice and acicular morphologies in the microstructure. Acicular morphology is detrimental to the strength, and the μ phase with particle morphology is usually big, which has no strengthening effect on alloys [97].

- This research will not mention other TCPs such as χ, β, α' and G.

2.4.2.5. Other phases

Table 2.1 lists other phases in nickel-based superalloys [97, 98].

Table 2.1. Other phases in nickel-based superalloys.

Phase	Structure	Formula	Description and function
γ''	bct	Ni_3Nb	It is known as the primary strengthening phase of Inconel 718. It precipitates as coherent disk-shaped particles on the {100} planes. Generally, it is too small to resolve using scanning electron microscope but observable using dark field transmission electron microscope.
η	hcp	Ni_3Ti	It is commonly found in iron-nickel-, cobalt-, and nickel-based superalloys with a high Ti/Al ratio, which is considered to transfer from metastable $Ni_3(Al, Ti)$.
δ	Orthorhombic	Ni_3Nb	It can be observed in overaged Inconel 718 with an acicular shape, forming by cellular reaction at a low ageing temperature and intragranular precipitation reaction at a high ageing temperature.
M_3B_2	Tetragonal	$(Ta, V, Nb, Mo, Ti, Cr, Ni, Fe)_3B_2$	It is usually found in iron-nickel- and nickel-based superalloys with ~ 0.03 wt% B or greater. The boride with a particle morphology can strengthen the material, but slice morphology increases the brittleness after aged.
MN	Cubic	$(Ti, Nb, Zr)N$	Nitride is observed in the alloys containing Ti, Nb or Zr and always shows as strip or bar if the cooling rate is quite high. While it appears as frame or dendrite at a low cooling rate.
Z	Tetragonal	NbCrN	A small amount of Z phase precipitates after aged with an irregular blocky shape.
Y	Hexagonal	Ti_2SC	When the composition of sulfur is larger than 0.008 wt%, Y phase forms with a long stripe morphology in front of γ' but never participates in the process of heat treatment.

2.4.3. Alloying elements in nickel-based superalloys

Nickel-based superalloys contain over 20 elements, as shown in Figure 2.20.

According to the role of these elements in alloys, they can be divided into 6 categories

[97]:

- The elements which constitute the fcc matrix: Ni, Fe, Co and Mn.

- The elements which can improve oxidation resistance: Cr, Al and Ti.

- The elements which have solution strengthening effect: W, Mo, Cr, N and Al.

- The elements which constitute carbides: Cr, W, Mo, V, Nb, Ta, Hf, Ti, C and N.

- The elements which constitute intermetallic compounds: Al, Ti, Nb, Ta and Hf.

- The elements which have grain boundary strengthening effect: B, Zr, rare and

   alkaline earth elements.

   Table 2.2 presents the elements and corresponding roles in nickel-based
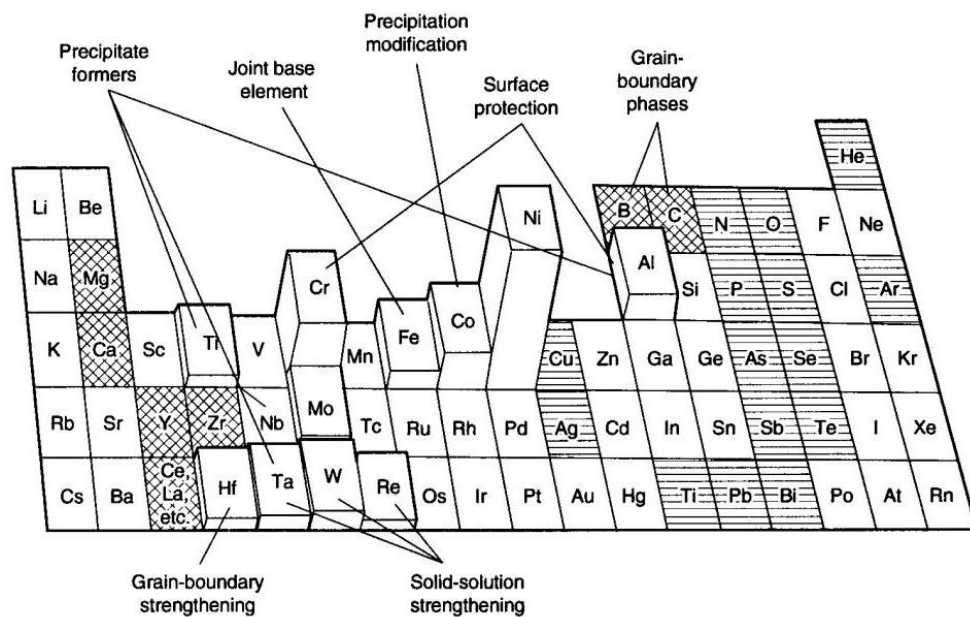
superalloys.

Figure 2.20. Overview of the alloying elements in nickel-based superalloys. The corresponding role of each element is marked beside the table, i.e., beneficial minor elements as marked with crosswires and detrimental elements marked with horizontal lines [97].

Table 2.2. Elements and their roles in nickel-based superalloys.

Element	Description and function
Ni	Ni is the main element forming the fcc austenitic matrix.
Fe	Fe is a solution element forming the fcc austenitic matrix.
Co	Co is a solution element forming the fcc austenitic matrix. It can also reduce stacking fault energy and dislocation motion, which in turn improves the creep property at high temperatures. Furthermore, the presence of Co decreases the solubility of Al and Ti in the matrix, inducing larger volume fractions of γ' precipitates and further strengthening alloys.
Mn	Mn is a solution element forming the fcc austenitic matrix.
Cr	Cr is a solution strengthening element and also favourable for oxidation resistance. In addition, it can form carbides like $M_{23}C_6$ and M_7C_3 at grain boundaries and serve as a carbide strengthening function.
Al	Al is a solution strengthening element and improves oxidation resistance. Al is an important constituent element of ordered $L1_2$ phase γ', which is the main precipitation strengthening phase of nickel-based superalloys.
Ti	Ti can improve high-temperature oxidation resistance of nickel-based superalloys and also replace Al to form γ' phase.
W	W is a solution strengthening element, acting as large size atoms to pin in alloys, which can efficiently impede the dislocation and increase the stability of alloys. It can also form MC, $M_{23}C_6$ and M_6C carbides and dissolve into γ' phase to increase its strengthening effect.
Mo	Mo has the same function as W.
V	V can form MC, $M_{23}C_6$ and M_6C carbides at grain boundaries to strengthen alloys.
Nb	Nb can form NbC carbide and replace Al to form γ' phase.
Ta	Ta has the same function as Nb.
Hf	Hf can form carbides and act as a grain boundary modifier, which refines and redistributes the carbides at grain boundaries to serve the function to strengthen grain boundaries.
Zr	Zr can strengthen grain boundaries and improve creep properties. Moreover, Zr is favourable to refine the grains in the microstructure.
C	C can combine with some metallic elements to form carbides to strengthen alloys. C also tends to catch some metallic elements to reduce the formation of some deleterious phases.
B	B can improve the creep rupture strength of nickel-based superalloys by the formation of tetragonal M_3B_2 borides at grain boundaries, which can impede the migration of grain boundaries and further serve the function to strengthen grain boundaries.

2.4.4. Heat treatment of nickel-based superalloys

Heat treatment is the most common method to modify alloys with low costs. In the process of heat treatment, different temperatures, heating times and cooling rates can lead to variable microstructures and further affect mechanical properties, and it can achieve the purpose of tailoring alloys [96].

Standard heat treatment for nickel-based superalloys can separate into 3 steps [97]:

The first step is solution heat treatment. It aims to dissolve carbides, γ' and other phases into the γ matrix to achieve a homogeneous solid solution and prepare for the next ageing step. The temperature of solution treatment ranges from 1040 ºC to 1230 ºC.

The second step is intermediate treatment. In the early years of heat treatment for nickel-based superalloys, it only included solution treatment at higher temperatures and ageing treatment at lower temperatures. After this heat treatment, although a good mechanical property could be obtainable, it could not last for a long time. For the fabrication of the parts using nickel-based superalloys such as engine blades and turbine disc, a widely used step is adding an intermediate treatment between temperatures ranging from 800 ºC to 1100 ºC, which effectively improves the durability and the plasticity of alloys. It applies an 850 ºC intermediate treatment for some alloys such as U-500, U-700 and X-750, which can increase the alloys' creep life. The intermediate treatment modifies the morphology of carbides and attains the bimodal distribution of γ'. This is beneficial for strength and ductility. The intermediate treatment is favourable to help relieve stress and prevent cracks as well.

The third step is ageing treatment, aiming to precipitate homogeneous strengthening phases such as γ'. The size, the morphology and the distribution of the precipitates vary significantly according to the ageing degree, as depicted in Figure 2.21, and different properties are achievable. The normal temperature for ageing treatment ranges from 700 °C to 1200 °C.
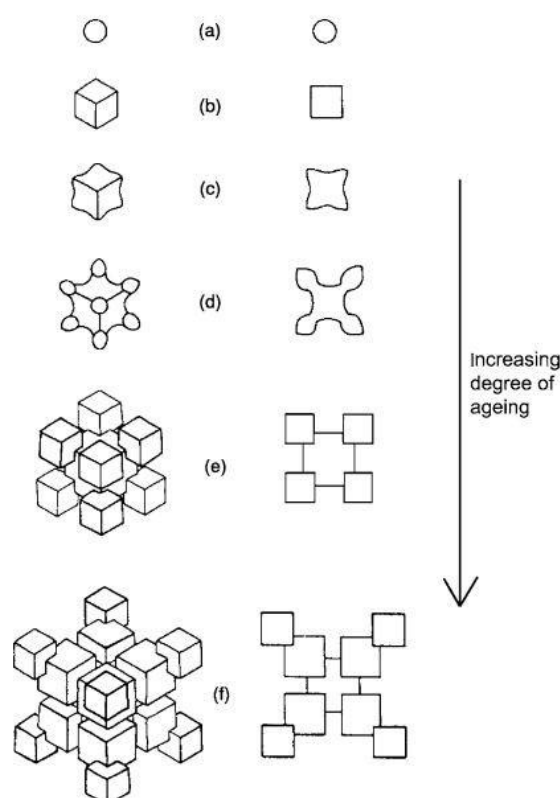
Figure 2.21. Schematic diagrams of the development of a γ' precipitate with increasing ageing time [92].

Many researchers have reported the microstructure and the properties induced by different heat treatment conditions [119-122]. 2 different heat treatments were applied on the nickel-based superalloy 718Plus by Whitmore et al. [123]. The first heat treatment comprised a solution treatment at 980 °C for 30 minutes, followed by quenching directly to room temperature and an ageing treatment at 788 °C for 24 hours. Another comprised a solution treatment at 980 °C for 30 minutes, followed by

quenching to 788 °C and an ageing treatment at 788 °C for 24 hours. The alloy under the former heat treatment condition had higher strength and hardness due to the larger size and volume fraction of γ' phase. The investigation conducted by Zickler et al. [124] showed that the mechanical properties of ATI 718PlusTM were a function of the heat treatment temperature and the ageing time. It also observed 2 types of intermetallic phases, γ' and δ, in the microstructure. γ' particles coarsened with the ageing time range according to a modified Slyozov and Wagner (LSW) theory, which explained the variable mechanical properties of the alloy. It also considered the Orowan and shearing strengthen models to elucidate the strengthening mechanism. Behrouzghaemi et al. [111] discussed the effects of cooling rates on the morphology of γ' in the nickel-based superalloy IN738LC after a sub-solvus heat treatment, as shown in Figure 2.22. It was apparent that the primary γ' changed from spherical (complex flower-like morphology) to cubic with decreasing the cooling rate. This was primarily attributed to the changed stability of γ' particles under different cooling rates, which was related to the misfit of γ/γ' and the corresponding elastic energy during solidification. Due to the considerably high cooling rates (in the magnitude of 10^6 K/s [125]) during the LPBF process, the precipitation of strengthening phases such as γ' and γ", is largely impeded. Therefore, heat treatment is highly required to improve the microstructure and the mechanical properties of as-printed (APed) parts fabricated by LPBF. Zhang et al. [107] applied a standard heat treatment on the Inconel 718 superalloy processed by LPBF and reported that the yield strength (YS) and the ultimate tensile strength (UTS) increased, while the elongation (EL) decreased dramatically due to the fine γ' and γ" precipitates in the γ

39

matrix. Divya et al. [126] found partial recovery and recrystallisation of the microstructure in the CM247LC superalloy using LPBF after the heat treatment. In addition, the γ' precipitates could be also observed, which induced a significant increase of hardness.
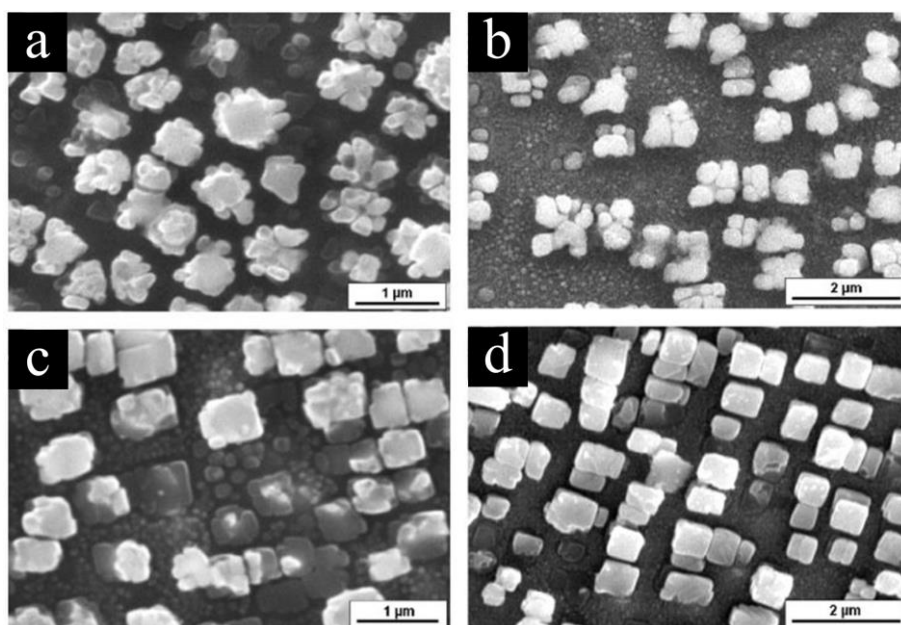
Figure 2.22. Morphologies of γ' precipitates in the IN738LC superalloy after heat treatment of 1120 ºC for 2 hours and cooled with the cooling rates of (a) 247 ºC/s, (b) 98 ºC/s, (c) 72 ºC/s and (d) 11 ºC/s observed using scanning electron microscope [111].

2.4.5. Inconel 738 LC

Nickel-based superalloy Inconel 738 LC (IN738LC), also named 738X, with "LC" meaning low-carbon. IN738LC is a kind of precipitation strengthening alloy by γ' phase [30, 127], widely used in energy and aerospace fields such as the hot gas path for turbines [30] due to its high creep property, excellent oxidation resistance and microstructural stability at elevated temperatures. It can be on long service under 980 ºC, and the endurance property can be comparable with NI713C. Because the content of Cr is high in this alloy, the oxidation resistance of IN738LC is better than NI713C

and can catch up with Udimet 500 [98]. Table 2.3 [128] gives the standard chemical composition of IN738LC. The roles of Cr within this alloy are solution strengthening and the improvement of oxidation resistance at high temperatures. The chemical composition contains relatively high contents of Ti and Al, which are favourable to form a large amount of γ'. High contents of the element atoms in large sizes such as W, Ta and Mo, can pin in the microstructure and hinder the slide of crystal. In addition, Nb, Ta, W and Mo also form carbides and further strengthen the alloy. Moderate amounts of B and Zr can modify grain boundaries and increase the creep resistance of the alloy [96, 98].

Table 2.3. ASTM chemical composition of the IN738LC alloy in wt%.

Element	Ni	Cr	Co	Mo	W	Ta	Al
wt%	Balance	15.7-16.3	8.0-9.0	1.5-2.0	2.4-2.8	1.5-2.0	3.2-3.7
Element	Ti	C	B	Zr	Nb	Fe	Si
wt%	3.2-3.7	0.09-0.15	0.007-0.012	0.02-0.08	0.6-1.1	< 0.05	< 0.3

Figure 2.23 shows the UTS, the YS and the EL of the casting IN738LC tensile bars after a standard heat treatment (a solution treatment at 1120 ^{o}C for 2 hours with air cooling, followed by an ageing treatment at 850 ^{o}C for 24 hours with air cooling) as a function of temperature [98]. There is a big drop of strength when the temperature is ~ 750 ^{o}C, where the lowest EL is also obtained.
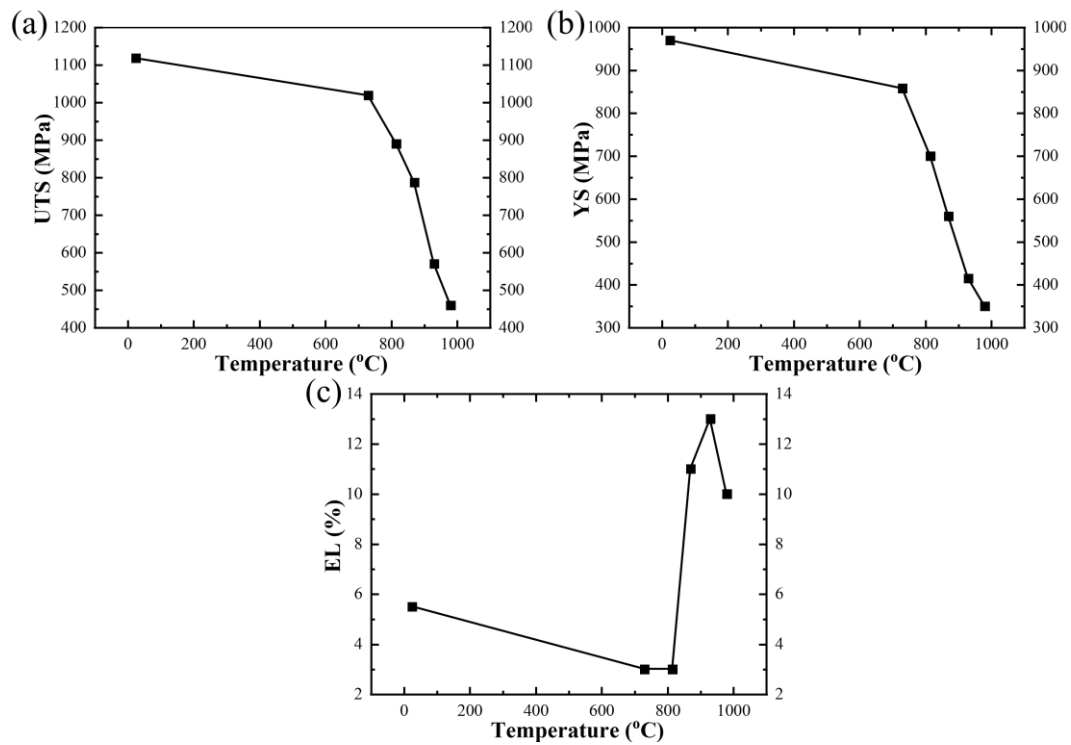
Figure 2.23. Mechanical properties of the IN738LC alloy as a function of temperature, (a) UTS, (b) YS and (c) EL [98].

Figure 2.24 exhibits the creep rupture curves with different initial stress at 1123 K of IN738LC from the work of Stevens et al. [129]. It showed a continuously increasing creep rate, where the strain was proximately proportional to the time, rather than a pronounced primary creep range followed by a classical steady (secondary) range.
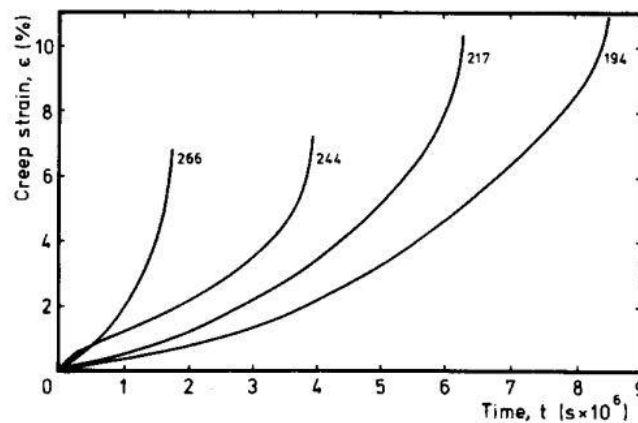
Figure 2.24. Creep rupture curves of the IN738LC alloy at 1123K with different initial stress [129].

Since IN738LC serves at high temperatures, high-temperature oxidation resistance

is a significant property for this alloy. Litz et al. [130] conducted the hot oxidation test on the IN738LC alloy at different temperatures. Figure 2.23 shows the oxide scale of the IN738LC alloy during 1-hour oxidation in air at 1100 ºC. It showed that the main oxidation products were an outer TiO_2 layer, an intermediate layer of Cr_2O_3 with dissolved Ti and an inner layer of (Nb, Ta, Ti)O_2 with a futile structure. Beneath this oxidation scale, there was an internal oxidation zone formed containing Al_2O_3 and TiN into the substrate. Here, Cr_2O_3 and Al_2O_3 were the main protective layers preventing the IN738LC alloy from oxidation at high temperatures.
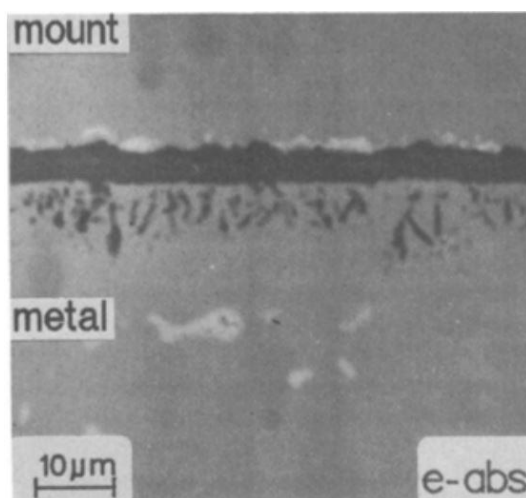
Figure 2.25. Oxide scale of the IN738LC alloy after exposed in the air at 1100 ºC for 1 hour observed using scanning electron microscope [130].

2.5. Laser powder bed fusion fabricated nickel-based superalloys

Nickel-based superalloys have been applied in the fabrication of parts by LPBF such as IN718 [131-133], IN625 [134, 135], CM247LC [136], Hastelloy-X [137-139] and IN738LC [140-142], to meet the high requirement of the complex shape and the design freedom of the components used in aerospace and automobile fields.

43

Figure 2.26 shows the typical microstructure of the APed IN738LC superalloy by LPBF. Figure 2.26 (a) shows that the γ matrix displays cell-like substructures with fine precipitates at the boundaries. This morphology is observable in the plane perpendicular to the building direction during the LPBF process. As shown in Figure 2.26 (b), the cellular dendrites form parallel to the building direction due to the thermal gradient in the rapid cooling process [143]. 2 different structures are visible parallel and perpendicular to the building direction, as depicted in Figure 2.27's electron backscattered diffraction orientation maps [30]. The columnar grains form in the building direction and grow across multiple melt pools and are visible in samples cut parallel to their growth direction, as shown in Figure 2.27 (a). While in Figure 2.27 (b), samples cut transversely to the growth direction show these same grains as cell-like structures.
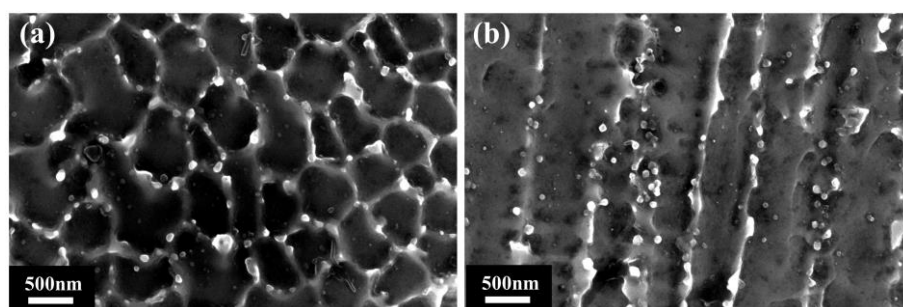
Figure 2.26. Typical microstructures of the IN738LC alloy fabricated using LPBF, (a) cell-like structures visible perpendicular to the growth direction, (b) cellular dendrites parallel to the growth direction observed using scanning electron microscope.
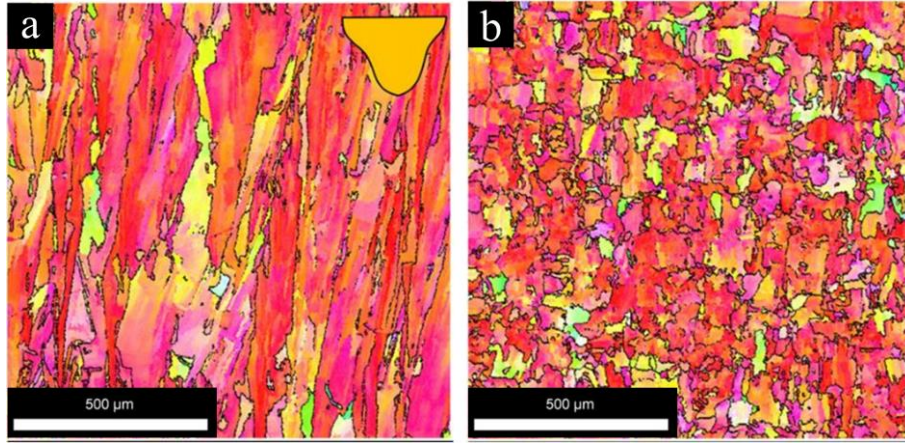
Figure 2.27. Electron backscattered diffraction orientation maps of the IN738LC alloy (a) parallel and (b) perpendicular to the building direction [30].

The corresponding pole figures (PFs) and inverse pole figures (IPFs) in Figures 2.28 (a) and 2.28 (b) demonstrate how most crystals have a preferential growth direction along crystallographic orientation <100> {001} for both of the sections parallel and vertical to the building direction, which is consistent with the preference of red colour in Figures 2.27 (a) and 2.27 (b).
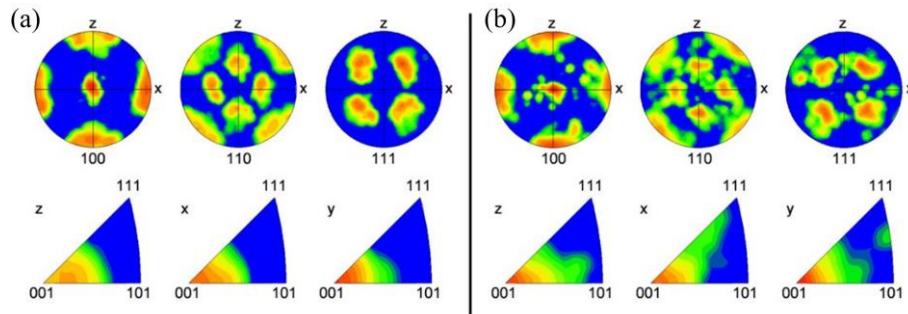
Figure 2.28. Crystal preferred orientations obtained by EBSD with PFs (001, 111, 110) and IPFs of the IN738LC alloy with respect to X, Y and Z directions for the samples (a) parallel and (b) vertical to the building direction [30].

Figure 2.29 exhibits the typical cell-like structures using transmission electron microscope [126]. There are extensive networks of dislocations at the boundaries of these cell-like structures while a lower density of the dislocations inside. It is primarily attributed to that a high cooling rate in the LPBF process causes the development of high residual stress in the sample.

45
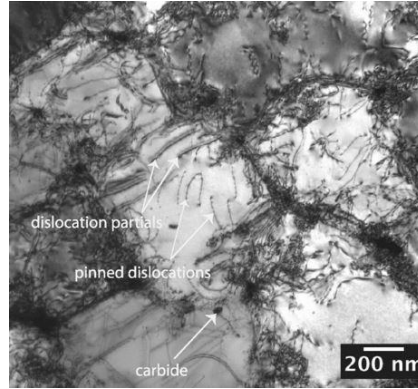
Figure 2.29. Microstructure of the CM247LC alloy showing dislocation distribution observed using transmission electron microscope [126].

Due to the complication of the chemical composition of nickel-based superalloys, the components manufactured by the laser AM process suffer from cracking during the processes of rapid heating and cooling. Section 2.5.2 details the potential mechanisms of cracking in the laser AM and welding processes.

Cloots et al. [30] reported the occurrence of the solidification cracking in the IN738LC alloy fabricated by LPBF. They used atom probe tomography (APT) and Thermo-Calc modelling to identify and characterise the segregation of Zr at grain boundaries, where the content of Zr was ~ 20 times higher when compared to standard proportions within the alloy. The segregation of Zr enlarged the solidification temperature range, inducing the liquid films to remain at the last stage of solidification. In addition, dendrites were visible in the open cracks, as shown in Figure 2.30, which was a typical morphology of the solidification cracking.
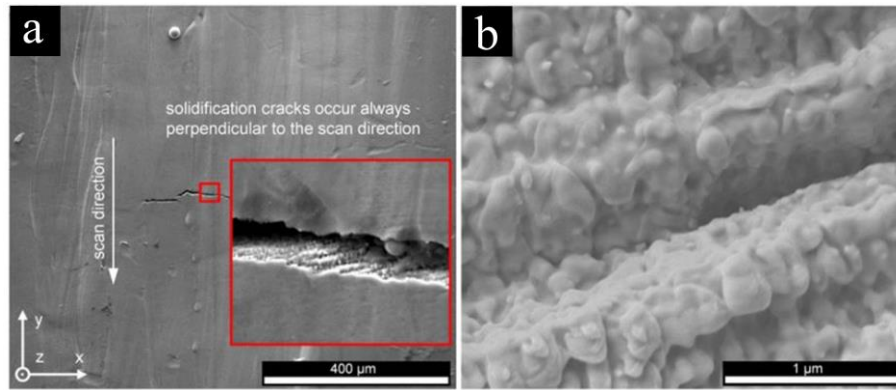
Figure 2.30. (a) Morphology of the crack in the IN738LC alloy processed by LPBF, (b) dendrite morphology in an opening crack at high magnification observed using scanning electron microscope [30].

Marchese et al. [137] attributed the cracks in the Hastelloy X alloy produced by LPBF to the formation of carbides. At grain boundaries, a large amount of sub-micrometric fcc Mo-rich M_nC_m formed due to the segregation of Mo, W and C. In addition, the thermal cycles comprising the re-melting and re-solidification processes also contributed to the formation of new carbides. Therefore, cracks generated with the combination of these intergranular carbides and high thermal stress due to the rapid cooling process in LPBF. Similarly, Han et al. [50] reported that the cracks in Hastelloy X were caused by the liquation cracking due to low-melting Mo-rich carbides lowering the solid/liquid interface energy, and the extensive wetting of the solid dendrites promoted the propagation of cracks. Qiu et al. [144] thought that some oxides such as WO_2, Al_2O_3 and SiO_2 formed firstly, since their melt points were higher than the liquidus temperature of the IN738LC alloy. These oxides showed the morphology as dark, large and elongated particles and gave rise to a significantly higher hardness of grain boundaries in IN738LC fabricated by LPBF. The solidification process generated oxides in the early stage of solidification and dissociated them in the melt. As the temperature decreased, they played the role of inclusion clusters and hindered the

continuity of the liquid films at grain boundaries, which was favourable for the formation of cracking.

2.6. Efforts to solve cracks in nickel-based superalloys during LPBF

Due to the uncontrollability of LPBF and the natural complexities of nickel-based superalloy chemical composition, defects like rough surfaces, pores, undesirable phases, cracks and refractory inclusions become unavoidable in the nickel-based superalloy parts fabricated by LPBF. Compared with some other defects, cracking is the most detrimental, since high stress concentrates at the crack tips, leading to the rapid propagation of cracks. The parts used in aerospace and automobile fields normally require long-term stability and durability, however, the geometries of these parts are relatively complex, which increases the difficulty to process the alloy introducing no cracks using LPBF. Great efforts have been made to mitigate the cracking in nickel-based superalloys during the LPBF process.

2.6.1. Processing parameter control

As detailed in Section 2.4, processing parameters can significantly affect the printing quality of parts by changing, among others, the thermal history, the melting condition and the solidification process. Therefore, processing parameter control is the most direct method to mitigate the defects, including the cracks of the printed parts using LPBF. Normally, laser power, scan speed and hatch spacing are the key

parameters chosen in the parameter control process [145]. Wang et al. [140] studied large ranges of laser powers and scan speeds with 150 W-270 W and 550 mm/s-1100 mm/s, respectively, in the fabrication of IN738LC during LPBF. They suggested that the process window to realise high-quality IN738LC without cracks was narrow. This alloy suffered from a severe cracking condition, and some parameters even failed to fabricate samples due to the wrapping phenomenon. Perevoshchikova et al. [142] used a Doehlert design to optimise the printing quality of IN738LC processed by LPBF with 3 key parameters: laser power, hatch spacing and scan speed. They conducted 14 experiments with both image analysis and Archimedes method and proved that small hatch spacing, medium scanning speed and low laser power could provide a high-quality part with the porosity < 0.5 % and free of cracks. The cracking mitigation by the processing parameter control method can be directly carried out during the LPBF process by operating the machine system [146], which decides its high operability and low costs. However, compared with pores, cracks are difficult to eliminate completely by controlling the parameters with the process window rather limited. In addition, the processing parameters are sensitive to the machines and the powder batches used. The optimised parameters and the process window will deviate once the machine or the powder batch changes.

2.6.2. Substrate preheating

From Section 2.5.2.5, the thermal stress induced by the high thermal gradient in LPBF is the cracking's main driving force. The method of substrate preheating can

significantly increase the temperature of the part bottom, reducing the thermal gradient along the building direction. As a result, the cracking can be mitigated. Risse [147] established a high-temperature preheating system on the 3D printing machine, as shown in Figure 2.31. He preheated the substrate up to 1100 °C in the fabrication of IN738LC during LPBF, which effectively prevented cracking in the printed samples. Due to the thermal expansion characteristics of nickel-based superalloy, the preheating temperature lower than 600 °C normally has no effect in solving cracking in the LPBF process. However, most of the commercially available 3D printing machines typically heat the substrates at temperatures as high as 200 °C, which constrains the substrate preheating method to eliminate the cracking in nickel-based superalloy during LPBF.
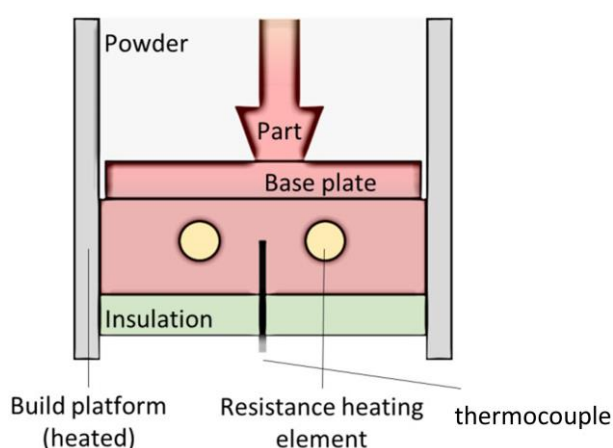
Figure 2.31. Schematic diagram of the preheating system in the LPBF process [147].

2.6.3. Chemical composition design

Due to the differences in the chemical composition of different nickel-based superalloys, the segregation conditions also differ. According to Section 2.5.2, the segregation of elements is the main cause of the solidification crack and the liquation crack. Therefore, reducing the content of the cracking-susceptible elements in alloy

chemical compositions could be an effective method to solve the cracking in nickel-based superalloys processed by LPBF. Tomus et al. [148] printed 2 batches of pre-alloyed Hastelloy-X powder with different C, Mn and Si contents by LPBF. They suggested that the crack initiation generated during the solidification process, and the cracking significantly depended on minor alloying elements such as C and Si. Thus, low C and Si contents could help avoid cracking in the Hastelloy-X alloy during LPBF. Harrison et al. [138] proposed a new theory for the reduction of nickel-based superalloys during LPBF crack susceptibility. They suggested that increasing the contents of substitutional solid solution strengthening elements within the alloy could improve the cracking resistance of materials in LPBF. To prove their hypothesis, they produced a modified composition of Hastelloy X powders. Compared with the nominal composition in Hastelloy X, the contents of some solid solution strengthening elements such as Cr, Co and Mo, increased in the modified one. As a result, they observed an average reduction of 65 % of cracks in the modified Hastelloy X part, and the UTS correspondingly improved at high temperatures. However, the contents of the target elements must be carefully controlled, and typically, this content requires a large amount of trial. Here, many batches of pre-alloyed must be produced. Therefore, high costs make it difficult to commercialise this method.

2.6.4. Metallic matrix composite

Recently, the in-situ fabrication of metallic matrix composite in LPBF with nano/micro-particles has attracted greater attention. This method can modify the

microstructures in printed parts and improve material properties by direct introduction of external particles into commercial alloy powders using ball-milling or powder-mixture while being an approach considered to mitigate cracking development during LPBF. Solving cracking during LPBF using the metallic matrix composite method was first reported in aluminium alloys [149, 150], and the main principle is the columnar-to-equiaxed transition (CET) theory. During the rapid solidification in LPBF, the added particles can act as heterogeneous nucleation sites, refining the grains, and the elongated columnar grains can transfer into equiaxed ones. A homogeneous and equiaxed microstructure accommodates strain more readily and has a better cracking resistance [150]. Figures 2.32 (a) and 2.32 (b) show the process of CET, and Figures 2.32 (c) and 2.32 (d) present the electron backscattered diffraction orientation maps of the microstructures before and after introducing LaB_6 nanoparticles into the AlSi10Mg alloy using LPBF, respectively. The grains are significantly refined with the addition of nanoparticles.
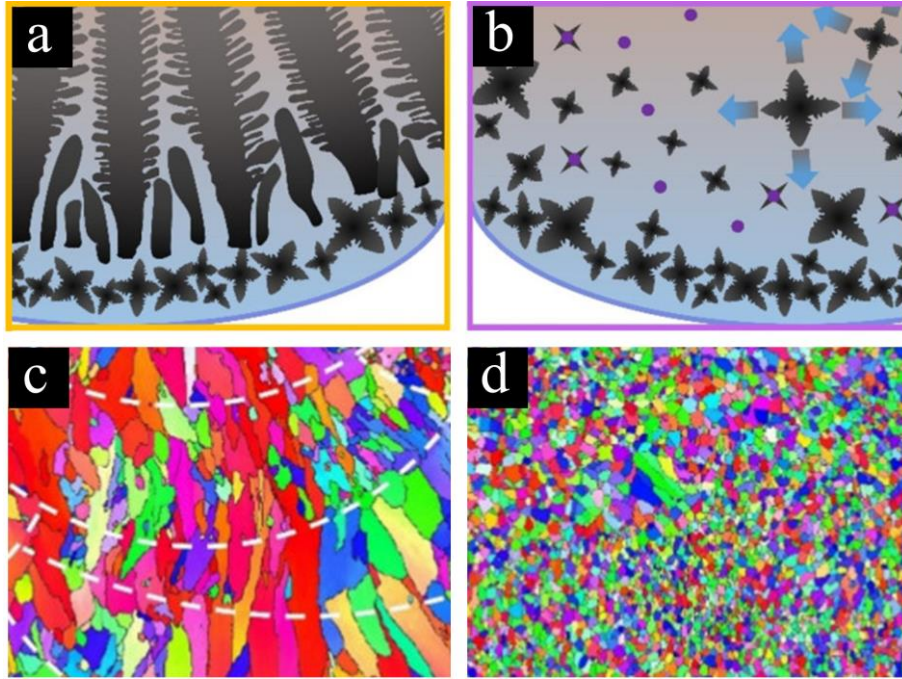
Figure 2.32. Schematic diagram of CET (top) and electron backscattered diffraction orientation maps (bottom) showing the microstructures before (a, c) and after (b, d) adding LaB$_6$ nanoparticles into the AlSi10Mg alloy using LPBF [150].

To remove the cracking, ceramic particles such as TiC and TiB$_2$, are introduced into nickel-matrix during LPBF. Han et al. [151] added 1 wt% TiC nanoparticles into the Hastelloy X superalloy powders and fabricated parts using LPBF. They found that most of the micro-cracks were reduced in the APed sample. They suggested that the increase of low-angle grain boundaries in the microstructure was the main contributor in solving the cracks, indicating that added TiC nanoparticles promoted heterogeneous nucleation during solidification. Zhou et al. [152] also removed the cracks in the LPBFed IN738LC samples using TiC nanoparticles. Unlike the investigation by Han et al. [151], they observed the increase of high-angle grain boundaries after incorporating 2.5 wt% of TiC. Due to the elimination of cracking, the YS, the UTS and the EL improved in the TiC-containing alloy. In addition, using rare earth oxide particles is common in dealing with cracking in nickel-based superalloys during some laser

processes due to their functions in refining grains and purifying grain boundaries. La_2O_3 and Y_2O_3 are the most commonly used rare earth oxides incorporated with Ni alloys in the laser-cladding process. Both favour the formation of crack-free coating and the refinement of microstructure [153, 154]. It is believed the addition of rare earth oxides improves the high-temperature oxidation resistance of materials by refining the grains and promoting the formation of spinel phases [155]. Compared with other methods in solving cracking, the metallic matrix composite is relatively easy to operate with low costs. It cannot only eliminate cracks but also modify the microstructure of alloys and further improve the performances.

2.6.5. Pulsed-wave laser beam

Due to the discontinuous radiation of the laser beam under the pulsed-wave mode, the solidification condition differs compared to the continuous-wave mode during LPBF. As a result, the grain structure, the phase generated and the defect behaviour can be modified in the alloy fabricated using the pulsed-wave laser beam. Therefore, it is considered an approach to solving cracking in nickel-based superalloy in LPBF. Compared with the continuous feature of the Laves phase in the LPBFed IN718 alloy under the continuous-wave laser beam, Tian et al. [125] found discrete Laves phase in pulsed LPBFed arising from high cooling rates induced by the pulsed-wave laser beam. Since the continuous Laves phase at grain boundaries was the primary cause of the liquation cracking in IN718 during LPBF, here, the cracking was effectively removed in their investigation. Muñiz-Lerma et al. [104] also used the pulsed-wave laser beam

to fabricate crack-free Inconel 738 samples, attaining near-equilibrium segregation of elements, since the high solidification rate in LPBF limited the solute trapping. However, the mechanism of action under the pulsed-wave laser mode compared to the continuous laser beam was not fully discussed in their investigation, and the influence of processing parameters on the printing quality must be further discussed. Risse [147] manufactured the IN738LC samples with an area fraction for the lack of fusion less than 0.1 % and free of cracking using the pulsed-wave laser radiation without preheating, finding that the application of the pulsed-wave laser beam could lead to an isotropic grain structure with isotropic mechanical properties. However, the effect of the pulsed-wave laser beam on the cracking formation was not mentioned in his study. The pulsed-wave laser beam method is relatively easy to conduct by controlling the laser beam mode within the machine. Most importantly, cracking can be effectively eliminated without changing the chemical composition of alloys, implying its great practicability in real industrial production.

2.7. Summaries: Key findings of investigation

This chapter reviews some previous works related to the investigation of interest, focusing on the process of LPBF in manufacturing precipitation strengthening nickel-based superalloys. The main concerns of the fabrication of nickel-based superalloy IN738LC using LPBF are the defect generation mechanism and the approach in solving them. The following points summarise the current state of knowledge:

- Great efforts have been made in solving defects using the parameter-design method in IN738LC during LPBF, and the corresponding process windows are developed to give nearly full-density components. However, how these key parameters affect the printing qualities and their action mechanism are not discussed deeply for the objective alloy.

- There are few investigations on the fluid dynamics and the solidification behaviour in bulk printed parts of IN738LC. This is mainly a result of little information revealed due to the overlapping between the previously fabricated tracks and layers. Here, it is even difficult to measure the melt pool's geometry. Therefore, a single-track experiment method needs to be applied to directly reveal the reaction between the powder bed and the laser beam, which is helpful to explain the mechanism of pore formation in depth.

- External particles have been added to the nickel matrix in order to deal with cracking during LPBF. While the mechanism is not clearly stated, and the effect of addition amount on the microstructures and the performances of materials needs to be investigated as well. Moreover, titanium-based ceramic particles such as TiC, TiN and TiB_2 seems to be the only choice in some previous researches.

- Other investigations have focused on the mechanical properties of nickel-based superalloys processed by LPBF. However, some physical properties like oxidation resistance are also important in the process of material service.

- A Pulsed-wave laser beam has been used to fabricate defect-free LPBFed IN738LC components. However, the cracking mitigation mechanism and the effect of pulsed-wave parameters (duty ratio and laser frequency) are not addressed.

Thus, the gaps which are identified from the literature review will be addressed in this thesis are:

- Studying 3 key parameters (hatch spacing, scan speed and laser power) to give a better understanding of how parameters influence defect formation and their action mechanism.

- Performing single-track experiments to study the fluid dynamics and solidification processes during laser powder bed fusion, focusing on track stability, melt pool dimension and bead mode.

- Adding different weight contents of Y_2O_3 nanoparticles by powder mixture in order to mitigate cracking in the printed parts. Simultaneously investigating the mechanical properties and the oxidation resistance of the alloys.

- Applying pulsed-wave laser beam for the fabrication of crack-free IN738LC components using LPBF and studying the mechanism of pulsed-wave laser action and the effects of laser frequency and duty ratio on the printing qualities.

2.8. References

[1] Molitch-Hou M. (2018). Overview of additive manufacturing process. In Additive Manufacturing, 1-38.

[2] Prakash K. S., Nancharaih T., Rao V. V. S. (2018). Additive Manufacturing

Techniques in Manufacturing-An Overview. Materials Today: Proceedings, 5(2), 3873-3882.

[3] ISO/ASTM52900-15 (2015). Standard Terminology for Additive Manufacturing-General. Principles-Terminology. West Conshohocken, PA: ASTM International.

[4] Adeyemi A., Akinlabi E. T., Mahamood R. M. (2018). Powder Bed Based Laser Additive Manufacturing Process of Stainless Steel: A Review. Materials Today: Proceedings, 5(9), 18510-18517.

[5] Schmidt M., Merklei, M., Bourell D., Dimitrov D., Hausotte T., Wegener K., Levy G. N. (2017). Laser based additive manufacturing in industry and academia. CIRP Annals, 66(2), 561-583.

[6] Fousova M., Vojtech D., Kubasek J., Jablonska E., Fojt J. (2017). Promising characteristics of gradient porosity Ti-6Al-4V alloy prepared by SLM process. Journal of the Mechanical Behavior of Biomedical Materials, 69, 368-376.

[7] Kasperovich G., Haubrich J., Gussone J., Requena G. (2016). Correlation between porosity and processing parameters in TiAl6V4 produced by selective laser melting. Materials & Design, 105, 160-170.

[8] Wang X., Carter L. N., Pang B., Attallah M. M., Loretto M. H. (2017). Microstructure and yield strength of SLM-fabricated CM247LC Ni-Superalloy. Acta Materialia, 128, 87-95.

[9] Rombouts M., Kruth J. P., Froyen L., Mercelis P. (2006). Fundamentals of Selective Laser Melting of alloyed steel powders. CIRP Annals, 55(1), 187-192.

[10] Wang L., Wang S., Hong X. (2018). Pulsed SLM-manufactured AlSi10Mg alloy:

Mechanical properties and microstructural effects of designed laser energy densities. Journal of Manufacturing Processes, 35, 492-499.

[11] Gong H., Rafi K., Gu H., Starr T., Stucker B. (2014). Analysis of defect generation in Ti-6Al-4V parts made using powder bed fusion additive manufacturing processes. Additive Manufacturing, 1-4, 87-98.

[12] Koutiri I., Pessard E., Peyre P., Amlou O., De Terris T. (2018). Influence of SLM process parameters on the surface finish, porosity rate and fatigue behavior of as-built Inconel 625 parts. Journal of Materials Processing Technology, 255, 536-546.

[13] Tang M., Pistorius P. C., Beuth J. L. (2017). Prediction of lack-of-fusion porosity for powder bed fusion. Additive Manufacturing, 14, 39-48.

[14] King W. E., Barth H. D., Castillo V. M., Gallegos G. F., Gibbs J. W., Hahn D. E., Rubenchik A. M. (2014). Observation of keyhole-mode laser melting in laser powder-bed fusion additive manufacturing. Journal of Materials Processing Technology, 214(12), 2915-2925.

[15] Carlton H. D., Haboub A., Gallegos G. F., Parkinson D. Y., MacDowell A. A. (2016). Damage evolution and failure mechanisms in additively manufactured stainless steel. Materials Science and Engineering: A, 651, 406-414.

[16] Enneti R. K., Morgan R., Atre S. V. (2018). Effect of process parameters on the Selective Laser Melting (SLM) of tungsten. International Journal of Refractory Metals and Hard Materials, 71, 315-319.

[17] Qiu C., Panwisawas C., Ward M., Basoalto H. C., Brooks J. W., Attallah M. M. (2015). On the role of melt flow into the surface structure and porosity development

during selective laser melting. Acta Materialia, 96, 72-79.

[18] Xia M., Gu D., Yu G., Dai D., Chen H., Shi Q. (2017). Porosity evolution and its thermodynamic mechanism of randomly packed powder-bed during selective laser melting of Inconel 718 alloy. International Journal of Machine Tools and Manufacture, 116, 96-106.

[19] Scipioni B. U., Wolfer A. J., Matthews M. J., Delplanque J. P. R., Schoenung J. M. (2017). On the limitations of Volumetric Energy Density as a design parameter for Selective Laser Melting. Materials & Design, 113, 331-340.

[20] Yadroitsev I., Gusarov A., Yadroitsava I., Smurov I. (2010). Single track formation in selective laser melting of metal powders. Journal of Materials Processing Technology, 210(12), 1624-1631.

[21] Gusarov A. V., Smurov I. (2010). Modeling the interaction of laser radiation with powder bed at selective laser melting. Physics Procedia, 5, 381-394.

[22] Anwar A. B., Pham Q. C. (2018). Study of the spatter distribution on the powder bed during selective laser melting. Additive Manufacturing, 22, 86-97.

[23] Xia M., Gu D., Yu G., Dai D., Chen H., Shi Q. (2016). Influence of hatch spacing on heat and mass transfer, thermodynamics and laser processability during additive manufacturing of Inconel 718 alloy. International Journal of Machine Tools and Manufacture, 109, 147-157.

[24] Herzog D., Seyda V., Wycisk E., Emmelmann C. (2016). Additive manufacturing of metals. Acta Materialia, 117, 371-392.

[25] Yadroitsev I., Smurov I. (2011). Surface Morphology in Selective Laser Melting of

Metal Powders. Physics Procedia, 12, 264-270.

[26] Liu Y., Yang Y., Mai S., Wang D., Song C. (2015). Investigation into spatter behavior during selective laser melting of AISI 316L stainless steel powder. Materials & Design, 87, 797-806.

[27] Jhabvala J., Boillat E., Antignac T., Glardon R. (2010). On the effect of scanning strategies in the selective laser melting process. Virtual and Physical Prototyping, 5(2), 99-109.

[28] Kruth J. P., Froyen L., Van Vaerenbergh J., Mercelis P., Rombouts M., Lauwers B. (2004). Selective laser melting of iron-based powder. Journal of Materials Processing Technology, 149(1-3), 616-622.

[29] Carter L. N., Martin C., Withers P. J., Attallah M. M. (2014). The influence of the laser scan strategy on grain structure and cracking behaviour in SLM powder-bed fabricated nickel superalloy. Journal of Alloys and Compounds, 615, 338-347.

[30] Cloots M., Uggowitzer P. J., Wegener K. (2016). Investigations on the microstructure and crack formation of IN738LC samples processed by selective laser melting using Gaussian and doughnut profiles. Materials & Design, 89, 770-784.

[31] Masmoudi A., Bolot R., Coddet C. (2015). Investigation of the laser-powder-atmosphere interaction zone during the selective laser melting process. Journal of Materials Processing Technology, 225, 122-132.

[32] Matthews M. J., Guss G., Khairallah S. A., Rubenchik,A. M., Depond P. J., King W. E. (2016). Denudation of metal powder layers in laser powder bed fusion

processes. Acta Materialia, 114, 33-42.

[33] Xu J., Lin X., Guo P., Hu Y., Wen X., Xue L., Huang W. (2017). The effect of preheating on microstructure and mechanical properties of laser solid forming IN-738LC alloy. Materials Science and Engineering: A, 691, 71-80.

[34] Kempen K., Vrancken B., Buls S., Thijs L., Humbeeck J. V., Kruth J. P. (2014). Selective Laser Melting of Crack-Free High Density M2 High Speed Steel Parts by Baseplate Preheating, Journal of Manufacturing Science and Engineering, 136, 1-6.

[35] Leung C. L. A., Marussi S., Atwood R. C., Towrie M., Withers P. J., Lee P. D. (2018). In situ X-ray imaging of defect and molten pool dynamics in laser additive manufacturing. Nature Communication, 9(1), 1355, 1-9.

[36] Peng T., Chen C. (2018). Influence of energy density on energy demand and porosity of 316L stainless steel fabricated by selective laser melting. International Journal of Precision Engineering and Manufacturing-Green Technology, 5(1), 55-62.

[37] Fabbro R. (2010). Melt pool and keyhole behaviour analysis for deep penetration laser welding. Journal of Physics D: Applied Physics, 43(44), 1-9.

[38] Ding X., Wang L. (2017). Heat transfer and fluid flow of molten pool during selective laser melting of AlSi10Mg powder: Simulation and experiment. Journal of Manufacturing Processes, 26, 280-289.

[39] Simonelli M., Tuck C., Aboulkhair N. T., Maskery I., Ashcroft I., Wildman R. D., Hague R. (2015). A Study on the Laser Spatter and the Oxidation Reactions During

Selective Laser Melting of 316L Stainless Steel, Al-Si10-Mg, and Ti-6Al-4V. Metallurgical and Materials Transactions A, 46(9), 3842-3851.

[40] Gunenthiram V., Peyre P., Schneider M., Dal M., Coste F., Koutiri I., Fabbro R. (2018). Experimental analysis of spatter generation and melt-pool behavior during the powder bed laser beam melting process. Journal of Materials Processing Technology, 251, 376-386.

[41] Scipioni B. U., Guss G., Wu S., Matthews M. J., Schoenung J. M. (2017). In-situ characterization of laser-powder interaction and cooling rates through high-speed imaging of powder bed fusion additive manufacturing. Materials & Design, 135, 385-396.

[42] Wang D., Wu S., Fu F., Mai S., Yang Y., Liu Y., Song C. (2017). Mechanisms and characteristics of spatter generation in SLM processing and its effect on the properties. Materials & Design, 117, 121-130.

[43] Aucott L., Huang D., Dong H. B., Wen S. W., Marsden J., Rack A., Cocks A. C. F. (2018). A Three-Stage Mechanistic Model for Solidification Cracking During Welding of Steel. Metallurgical and Materials Transactions A, 49(5), 1674-1682.

[44] Chauvet E., Kontis P., Jägle E. A., Gault B., Raabe D., Tassin C., Martin G. (2018). Hot cracking mechanism affecting a non-weldable Ni-based superalloy produced by selective electron Beam Melting. Acta Materialia, 142, 82-94.

[45] Tomus D., Jarvis T., Wu X., Mei J., Rometsch P., Herny E., Vaillant S. (2013). Controlling the Microstructure of Hastelloy-X Components Manufactured by Selective Laser Melting. Physics Procedia, 41, 823-827.

[46] Chen Y., Lu F., Zhang K., Nie P., Elmi H. S. R., Feng K., Li Z. (2016). Dendritic microstructure and hot cracking of laser additive manufactured Inconel 718 under improved base cooling. Journal of Alloys and Compounds, 670, 312-321.

[47] Ghaini F. M., Sheikhi M., Torkamany M. J., Sabbaghzadeh J. (2009). The relation between liquation and solidification cracks in pulsed laser welding of 2024 aluminium alloy. Materials Science and Engineering: A, 519(1-2), 167-171.

[48] Arnold M., Sébastien P., Hervé G. (2017). Study of the suitability of aluminum alloys for additive manufacturing by laser powder bed fusion. U.P.B. Sci. Bull. Series B, 79, 219-238.

[49] Pakniat M., Ghaini F. M., Torkamany M. J. (2016). Hot cracking in laser welding of Hastelloy X with pulsed Nd:YAG and continuous wave fiber lasers. Materials & Design, 106, 177-183.

[50] Han Q., Mertens R., Montero-Sistiaga M. L., Yang S., Setchi R., Vanmeensel K., Fan H. (2018). Laser powder bed fusion of Hastelloy X: Effects of hot isostatic pressing and the hot cracking mechanism. Materials Science and Engineering: A, 732, 228-239.

[51] Kou S. (2003). Solidification and liquation cracking issues in welding. Jom, 55(6), 37-42.

[52] Hu Y. L., Lin X., Yu X. B., Xu J. J., Lei M., Huang W. D. (2017). Effect of Ti addition on cracking and microhardness of Inconel 625 during the laser solid forming processing. Journal of Alloys and Compounds, 711, 267-277.

[53] Tomus D., Rometsch P. A., Heilmaier M., Wu X. (2017). Effect of minor alloying

elements on crack-formation characteristics of Hastelloy-X manufactured by selective laser melting. Additive Manufacturing, 16, 65-72.

[54] Xu J., Lin X., Zhao Y., Guo P., Wen X., Li Q., Huang W. (2018). HAZ Liquation Cracking Mechanism of IN-738LC Superalloy Prepared by Laser Solid Forming. Metallurgical and Materials Transactions A, 49(10), 5118-5136.

[55] Egbewande A. T., Buckson R. A., Ojo O. A. (2010). Analysis of laser beam weldability of Inconel 738 superalloy. Materials Characterization, 61(5), 569-574.

[56] Pepe J. J., Savage W. F. (1967). Effects of Constitutional Liquation in 18-Ni Managing Steel Weldments, Weld Journal, 46, 411-422.

[57] Ojo O. A., Richards N. L., Chaturvedi M. C. (2004). Contribution of constitutional liquation of gamma prime precipitate to weld HAZ cracking of cast Inconel 738 superalloy. Scripta Materialia, 50(5), 641-646.

[58] Hu Y. L., Lin X., Song K., Jiang X. Y., Yang H. O., Huang W. D. (2016). Effect of heat input on cracking in laser solid formed DZ4125 superalloy. Optics & Laser Technology, 86, 1-7.

[59] Ojo O. A., Chaturvedi M. C. (2005). On the role of liquated γ′ precipitates in weld heat affected zone microfissuring of a nickel-based superalloy. Materials Science and Engineering: A, 403(1-2), 77-86.

[60] Danis Y., Arvieu C., Lacoste E., Larrouy T., Quenisset J. M. (2010). An investigation on thermal, metallurgical and mechanical states in weld cracking of Inconel 738LC superalloy. Materials & Design, 31(1), 402-416.

[61] Ojo O. A., Wang Y. L., Chaturvedi M. C. (2008). Heat affected zone liquation

cracking in electron beam welded third generation nickel base superalloys. Materials Science and Engineering: A, 476(1-2), 217-223.

[62] Tancret F. (2007). Thermo-Calc and Dictra simulation of constitutional liquation of gamma prime (γ′) during welding of Ni base superalloys. Computational Materials Science, 41(1), 13-19.

[63] Attallah M. M., Terasaki H., Moat R. J., Bray S. E., Komizo Y., Preuss M. (2011). In-Situ observation of primary γ′ melting in Ni-base superalloy using confocal laser scanning microscopy. Materials Characterization, 62(8), 760-767.

[64] Ren W., Lu F., Yang R., Liu X., Li Z. (2015). Liquation cracking in fiber laser welded joints of inconel 617. Journal of Materials Processing Technology, 226, 214-220.

[65] Montazeri M., Ghaini F. M. (2012). The liquation cracking behavior of IN738LC superalloy during low power Nd:YAG pulsed laser welding. Materials Characterization, 67, 65-73.

[66] West S. L., Baeslack W. A., Kelly T. J. (1989). Morphology of weld heat-affected zone liquation cracking in Ta-modified cast alloy 718. Metallography, 23(3), 219-230.

[67] Radhakrishnan B., Thompson R. G. (1988). A quantitative microstructural study of intergranular liquation and its relationship to hot cracking. Metallography, 21(4), 453-471.

[68] Ren W., Lu F., Yang R., Liu X., Li Z. (2015). Liquid film migration in laser welded joint of Inconel 617. Journal of Materials Research, 30(15), 2340-2347.

[69] Ojo O. A., Richards N. L., Chaturvedi M. C. (2004). Liquid film migration of constitutionally liquated γ′ in weld heat affected zone (HAZ) of Inconel 738LC superalloy. Scripta Materialia, 51(2), 141-146.

[70] Zhong M., Sun H., Liu W., Zhu X., He J. (2005). Boundary liquation and interface cracking characterization in laser deposition of Inconel 738 on directionally solidified Ni-based superalloy. Scripta Materialia, 53(2), 159-164.

[71] Xu J., Lin X., Guo P., Dong H., Wen X., Li Q., Huang W. (2018). The initiation and propagation mechanism of the overlapping zone cracking during laser solid forming of IN-738LC superalloy. Journal of Alloys and Compounds, 749, 859-870.

[72] Chen Y., Zhang K., Huang J., Hosseini S. R. E., Li Z. (2016). Characterization of heat affected zone liquation cracking in laser additive manufacturing of Inconel 718. Materials & Design, 90, 586-594.

[73] Collins M. G., Lippold J. C. (2003). An investigation of ductility dip cracking in nickel-based filler materials-Part I. Welding Journal, 82(10), 288-295.

[74] Collins M. G., Ramirez A. J., Lippold J. C. (2003). An investigation of ductility dip cracking in nickel-based weld metals-Part II: Fracture behavior and fracture surface morphology are related to microstructure, composition, and temperature. Welding journal, 82(12), 348-354.

[75] Collins M. G., Ramirez A. J., Lippold J. C. (2004). An investigation of ductility-dip cracking in nickel-based weld metals-Part III. The characteristics of weld-metal grain boundaries associated with elevated-temperature fracture are investigated. Welding journal, 83(2), 39-49

[76] Hope A. T., Lippold J. C. (2017). Development and testing of a high-chromium, Ni-based filler metal resistant to ductility dip cracking and solidification cracking. Welding in the World, 61(2), 325-332.

[77] Nissley N. E., Lippold J. C. (2008). Ductility-dip cracking susceptibility of nickel-based weld metals part 1: strain-to-fracture testing. Welding journal, 87(10), 257-264.

[78] Nissley N. E., Lippold J. C. (2009). Ductility-dip cracking susceptibility of nickel-based weld metals part 2: microstructural characterization. Welding journal, 88, 131-140.

[79] Mo W., Hu X., Lu S., Li D., Li Y. (2015). Effects of Boron on the Microstructure, Ductility-dip-cracking, and Tensile Properties for NiCrFe-7 Weld Metal. Journal of Materials Science & Technology, 31(12), 1258-1267.

[80] Ramirez A. J., Lippold J. C. (2004). High temperature behavior of Ni-base weld metal. Materials Science and Engineering: A, 380(1-2), 259-271.

[81] Ramirez A. J., Lippold J. C. (2004). High temperature behavior of Ni-base weld metal. Materials Science and Engineering: A, 380(1-2), 245-258.

[82] Carter L. N., Attallah M. M., Reed R. C. (2012). Laser powder bed fabrication of nickel-base superalloys: influence of parameters; characterization, quantification and mitigation of cracking. Superalloys, 2012, 577-586.

[83] Rowe M. D. (2006). Ranking the resistance of wrought superalloys to strain-age cracking. Welding Journal, 85(2), 27-33.

[84] Çam G., Koçak M. (1998). Progress in joining of advanced materials Part 2:

Joining of metal matrix composites and joining of other advanced materials. Science and Technology of Welding and Joining, 3(4), 159-175.

[85] Henderson M. B., Arrell D., Larsson R., Heobel M., Marchant G. (2013). Nickel based superalloy welding practices for industrial gas turbine applications. Science and Technology of Welding and Joining, 9(1), 13-21.

[86] Salmi A., Atzeni E., Iuliano L., Galati M. (2017). Experimental Analysis of Residual Stresses on AlSi10Mg Parts Produced by Means of Selective Laser Melting (SLM). Procedia CIRP, 62, 458-463.

[87] Nadammal N., Cabeza S., Mishurova T., Thiede T., Kromm A., Seyfert C., Bruno G. (2017). Effect of hatch length on the development of microstructure, texture and residual stresses in selective laser melted superalloy Inconel 718. Materials & Design, 134, 139-150.

[88] Mercelis P., Kruth J. P. (2006). Residual stresses in selective laser sintering and selective laser melting. Rapid Prototyping Journal, 12(5), 254-265.

[89] Catchpole-Smith S., Aboulkhair N., Parry L., Tuck C., Ashcroft I. A., Clare A. (2017). Fractal scan strategies for selective laser melting of 'unweldable' nickel superalloys. Additive Manufacturing, 15, 113-122.

[90] Vastola G., Zhang G., Pei Q. X., Zhang Y. W. (2016). Controlling of residual stress in additive manufacturing of Ti6Al4V by finite element modeling. Additive Manufacturing, 12, 231-239.

[91] Matthew J. Donachie, Stephen J. Donachie (2002). SUPERALLOYSA Technical Guide. United States of America.

[92] Roger C. Reed (2006). The Superalloys Fundamentals and Applications. United States of America.

[93] L.E. Murr, E. Martinez, X.M. Pan, S.M. Gaytan, J.A. Castro, C.A. Terrazas, F. Medina, R.B. Wicker, D.H. Abbott (2013). Microstructures of Rene 142 nickel-based superalloy fabricated by electron beam melting. Acta Materialia, 61, 4289-4296.

[94] John L. Everhart P. E. (1971). Engineering Properties of Nickel and Nickel Alloys. United States of America.

[95] D. G. Morris, S. Naka, P. Caron (2000). Intermetallics and Superalloys. Federal Republic of Germany.

[96] China aeronautical materials handbook editorial board (2001). China aeronautical materials handbook. China.

[97] Group of Metallographic pattern of superalloy editorial board (1979). Metallographic pattern of superalloy. China.

[98] Jun Ye (1978). American nickel-based superalloys. China.

[99] Ivanov D., Travyanov A., Petrovskiy P., Cheverikin V., Alekseeve E., Khvan A., Logachev I. (2017). Evolution of structure and properties of the nickel-based alloy EP718 after the SLM growth and after different types of heat and mechanical treatment. Additive Manufacturing, 18, 269-275.

[100] Silva C. C., Miranda H. C., Motta M. F., Farias J. P., Afonso C. R. M., Ramirez A. J. (2013). New insight on the solidification path of an alloy 625 weld overlay. Journal of Materials Research and Technology, 2(3), 228-237.

[101] Tucho W. M., Cuvillier P., Sjolyst-Kverneland A., Hansen V. (2017). Microstructure and hardness studies of Inconel 718 manufactured by selective laser melting before and after solution heat treatment. Materials Science and Engineering: A, 689, 220-232.

[102] Messé O. M. D. M., Muñoz-Moreno R., Illston T., Baker S., Stone H. J. (2018). Metastable carbides and their impact on recrystallisation in IN738LC processed by selective laser melting. Additive Manufacturing, 22, 394-404.

[103] Ramakrishnan A., Dinda G. P. (2019). Direct laser metal deposition of Inconel 738. Materials Science and Engineering: A, 740-741, 1-13.

[104] Muñiz-Lerma J. A., Tian Y., Wang X., Gauvin R., Brochu M. (2018). Microstructure evolution of Inconel 738 fabricated by pulsed laser powder bed fusion. Progress in Additive Manufacturing, 4(2), 97-107.

[105] Chen J., Xue L. (2010). Process-induced microstructural characteristics of laser consolidated IN-738 superalloy. Materials Science and Engineering: A, 527(27-28), 7318-7328.

[106] Liu Y., Kang M., Wu Y., Wang M., Gao H., Wang J. (2017). Effects of microporosity and precipitates on the cracking behavior in polycrystalline superalloy Inconel 718. Materials Characterization, 132, 175-186.

[107] Zhang D., Niu W., Cao X., Liu Z. (2015). Effect of standard heat treatment on the microstructure and mechanical properties of selective laser melting manufactured Inconel 718 superalloy. Materials Science and Engineering: A, 644, 32-40.

[108] Wang M., Du J., Deng Q., Tian Z., Zhu J. (2017). Effect of the precipitation of the

η-Ni3Al0.5Nb0.5 phase on the microstructure and mechanical properties of ATI 718Plus. Journal of Alloys and Compounds, 701, 635-644.

[109] Cao G. H., Sun T. Y., Wang C. H., Li X., Liu M., Zhang Z. X., Chen G. F. (2018). Investigations of γ′, γ″ and δ precipitates in heat-treated Inconel 718 alloy fabricated by selective laser melting. Materials Characterization, 136, 398-406.

[110] You X., Tan Y., Zhao L., You Q., Wang Y., Ye F., Li J. (2018). Effect of solution heat treatment on microstructure and electrochemical behavior of electron beam smelted Inconel 718 superalloy. Journal of Alloys and Compounds, 741, 792-803.

[111] Behrouzghaemi S., Mitchell R. J. (2008). Morphological changes of γ′ precipitates in superalloy IN738LC at various cooling rates. Materials Science and Engineering: A, 498(1-2), 266-271.

[112] Murr L. E., Martinez E., Pan X. M., Gaytan S. M., Castro J. A., Terrazas C. A., Abbott D. H. (2013). Microstructures of Rene 142 nickel-based superalloy fabricated by electron beam melting. Acta Materialia, 61(11), 4289-4296.

[113] Ricks R. A., Porter A. J., Ecob R. C. (1983). Growth of Gamma Prime Precipitates in Nickel-Based Superalloys. Acta Metallurgical, 16, 31-43.

[114] Whitmore L., Leitner H., Povoden-Karadeniz E., Radis R., Stockinger M. (2012). Transmission electron microscopy of single and double aged 718Plus superalloy. Materials Science and Engineering: A, 534, 413-423.

[115] Hornbogen E., Roth M. (1967). DISTRIBUTION OF COHERENT PARTICLES IN NICKEL ALLOYS. Germany.

[116] Bance S., Bittner F., Woodcock T. G., Schultz L., Schrefl T. (2017). Role of twin

and anti-phase defects in MnAl permanent magnets. Acta Materialia, 131, 48-56.

[117] Long H., Liu Y., Kong D., Wei H., Chen Y., Mao S. (2017). Shearing mechanisms of stacking fault and anti-phase-boundary forming dislocation pairs in the γ′ phase in Ni-based single crystal superalloy. Journal of Alloys and Compounds, 724, 287-295.

[118] Whitmore L., Ahmadi M. R., Stockinger M., Povoden-Karadeniz E., Kozeschnik E., Leitner H. (2014). Microstructural investigation of thermally aged nickel-based superalloy 718Plus. Materials Science and Engineering: A, 594, 253-259.

[119] Hosseini S. A., Madar K. Z., Abbasi S. M. (2017). Effect of homogenization heat treatments on the cast structure and tensile properties of nickel-base superalloy ATI 718Plus in the presence of boron and zirconium additions. Materials Science and Engineering: A, 689, 103-114.

[120] Antonov S., Detrois M., Helmink R. C., Tin S. (2015). Precipitate phase stability and compositional dependence on alloying additions in γ-γ′-δ-η Ni-base superalloys. Journal of Alloys and Compounds, 626, 76-86.

[121] Ruan J. J., Ueshima N., Oikawa K. (2018). Phase transformations and grain growth behaviors in superalloy 718. Journal of Alloys and Compounds, 737, 83-91.

[122] Huber D., Sommitsch C., Stockinger M. (2011). Comparison between microstructure evolution in IN718 and ATI Allvac® 718PlusTM-simulation and trial forgings. Advanced Materials Research, 278, 168-173.

[123] Whitmore L., Ahmadi M. R., Guetaz L., Leitner H., Povoden-Karadeniz E., Stockinger M., Kozeschnik E. (2014). The microstructure of heat-treated nickel-

based superalloy 718Plus. Materials Science and Engineering: A, 610, 39-45.

[124] Zickler G. A., Schnitzer R., Radis R., Hochfellner R., Schweins R., Stockinger M., Leitner H. (2009). Microstructure and mechanical properties of the superalloy ATI Allvac® 718Plus™. Materials Science and Engineering: A, 523(1-2), 295-303.

[125] Tian Y., Muñiz-Lerma J. A., Brochu M. (2017). Nickel-based superalloy microstructure obtained by pulsed laser powder bed fusion. Materials Characterization, 131, 306-315.

[126] Divya V. D., Muñoz-Moreno R., Messé O. M. D. M., Barnard J. S., Baker S., Illston T., Stone H. J. (2016). Microstructure of selective laser melted CM247LC nickel-based superalloy and its evolution through heat treatment. Materials Characterization, 114, 62-74.

[127] Balikci E., Mirshams R. A., Raman A. (1999). Fracture behavior of superalloy IN738LC with various precipitate microstructures. Materials Science and Engineering: A, 265(1-2), 50-62.

[128] Engeli R., Etter T., Hövel S., Wegener K. (2016). Processability of different IN738LC powder batches by selective laser melting. Journal of Materials Processing Technology, 229, 484-491.

[129] Stevens R. A., Flewitt P. E. J. (1979). The effects of γ' precipitate coarsening during isothermal aging and creep of the nickel-base superalloy IN-738. Materials Science and Engineering, 37(3), 237-247.

[130] Litz J., Rahmel A., Schorr M., Weiss J. (1989). Scale formation on the ni-base superalloys IN939 and IN738LC. Oxidation of Metals, 32(3), 167-184.

[131] Acharya R., Sharon J. A., Staroselsky A. (2017). Prediction of microstructure in laser powder bed fusion process. Acta Materialia, 124, 360-371.

[132] Pröbstle M., Neumeier S., Hopfenmüller J., Freund L. P., Niendorf T., Schwarze D., Göken M. (2016). Superior creep strength of a nickel-based superalloy produced by selective laser melting. Materials Science and Engineering: A, 674, 299-307.

[133] Sadowski M., Ladani L., Brindley W., Romano J. (2016). Optimizing quality of additively manufactured Inconel 718 using powder bed laser melting process. Additive Manufacturing, 11, 60-70.

[134] Mumtaz K., Hopkinson N. (2009). Top surface and side roughness of Inconel 625 parts processed using selective laser melting. Rapid Prototyping Journal, 15(2), 96-103.

[135] Criales L. E., Arısoy Y. M., Lane B., Moylan S., Donmez A., Özel T. (2017). Laser powder bed fusion of nickel alloy 625: Experimental investigations of effects of process parameters on melt pool size and shape with spatter analysis. International Journal of Machine Tools and Manufacture, 121, 22-36.

[136] Kalentics N., Sohrabi N., Tabasi H. G., Griffiths S., Jhabvala J., Leinenbach C., Loge R. E. (2019). Healing cracks in selective laser melting by 3D laser shock peening. Additive Manufacturing, 30, 100881.

[137] Marchese G., Basile G., Bassini E., Aversa A., Lombardi M., Ugues D., Biamino S. (2018). Study of the Microstructure and Cracking Mechanisms of Hastelloy X Produced by Laser Powder Bed Fusion. Materials, 11(1) 1-12.

[138] Harrison N. J., Todd I., Mumtaz K. (2015). Reduction of micro-cracking in nickel superalloys processed by Selective Laser Melting: A fundamental alloy design approach. Acta Materialia, 94, 59-68.

[139] Tian Y., Tomus D., Rometsch P., Wu X. (2017). Influences of processing parameters on surface roughness of Hastelloy X produced by selective laser melting. Additive Manufacturing, 13, 103-112.

[140] Wang H., Zhang X., Wang G. B., Shen J., Zhang G. Q., Li Y. P., Yan M. (2019). Selective laser melting of the hard-to-weld IN738LC superalloy: Efforts to mitigate defects and the resultant microstructural and mechanical properties. Journal of Alloys and Compounds, 807, 151662.

[141] Kunze K., Etter T., Grässlin J., Shklover V. (2015). Texture, anisotropy in microstructure and mechanical properties of IN738LC alloy processed by selective laser melting (SLM). Materials Science and Engineering: A, 620, 213-222.

[142] Perevoshchikova N., Rigaud J., Sha Y., Heilmaier M., Finnin B., Labelle E., Wu X. (2017). Optimization of selective laser melting parameters for the Ni-based superalloy IN-738 LC using Doehlert's design. Rapid Prototyping Journal, 23(5), 881-892.

[143] Song B., Dong S., Coddet P., Liao H., Coddet C. (2014). Fabrication of NiCr alloy parts by selective laser melting: Columnar microstructure and anisotropic mechanical behavior. Materials & Design, 53, 1-7.

[144] Qiu C., Chen H., Liu Q., Yue S., Wang H. (2019). On the solidification behaviour and cracking origin of a nickel-based superalloy during selective laser melting.

Materials Characterization, 148, 330-344.

[145] Guo C., Li S., Shi S., Li X., Ward, R. M., Zhu Q. (2020). Effect of processing parameters on surface roughness, porosity and cracking of as-built in738lc parts fabricated by laser powder bed fusion. Journal of Materials Processing Technology, 285, 116788.

[146] Guo C., Xu Z., Zhou Y., Shi S., Li G., Lu H., Zhu q., Ward R. M. (2021). Single-track investigation of IN738LC superalloy fabricated by laser powderbed fusion: Track morphology, bead characteristics and part quality. Journal of Materials Processing Technology, 290, 117000.

[147] Risse J. (2019). Additive Manufacturing of Nickel-Base Superalloy IN738LC by Laser Powder Bed Fusion. PhD Thesis, RWTH Aachen University.

[148] Tomus D., Rometsch P. A., Heilmaier M., Wu X. (2017). Effect of minor alloying elements on crack-formation characteristics of Hastelloy-X manufactured by selective laser melting. Additive Manufacturing, 16, 65-72.

[149] Martin J. H., Yahata B. D., Hundley J. M., Mayer J. A., Schaedler, T. A., Pollock T. M. (2017). 3D printing of high-strength aluminium alloys. Nature, 549(7672), 365-369.

[150] Tan Q., Zhang J., Mo N., Fan Z., Zhang M. X. A novel method to 3D-print fine-grained AlSi10Mg alloy with isotropic properties via inoculation with LaB6 nanoparticles. Additive Manufacturing, 32, 101034.

[151] Han Q., Gu Y., Setchi R., Lacan F., Yang S. (2019). Additive manufacturing of high-strength crack-free Ni-based Hastelloy X superalloy. Additive Manufacturing,

30, 100919.

[152] Zhou W., Zhu G., Wang R., Yang C., Sun, B. (2020). Inhibition of cracking by grain boundary modification in a non-weldable nickel-based superalloy processed by laser powder bed fusion. Materials science and Engineering A, 791, 139745.

[153] Li M., Han B., Wang Y., Pu K. (2017). Effects La_2O_3 on the microstructure and property of laser cladding Ni-based ceramic coating. Optik, 130, 1032-1037.

[154] Xu P., Tang X., Yao S., He J., Xu G. (2008). Effect of Y_2O_3 addition on microstructure of Ni-based alloy + Y_2O_3/substrate laser clad. Journal of Materials Processing Technology, 208(1-3), 549-555.

[155] Guo C., Yu Z., Liu C., Li X., Ward R. M., Zhu Q. (2020). Effects of Y_2O_3 nanoparticles on the high-temperature oxidation behavior of IN738LC manufactured by laser powder bed fusion. Corrosion Science, 171, 108715.

Chapter 3 Experimental Methods

3.1. Introduction

This chapter details the materials, the sample preparation processes, the microstructural characterisation, the simulation method and the property tests in this investigation.

3.2. Materials

3.2.1. Raw materials

This research investigated the processability of the nickel-based superalloy Inconel 738 LC (IN738LC). The powders were supplied from 3 different manufacturers separately used for different processes described in the chapters of this research. Y_2O_3 nanoparticles were mechanically blended with the pure IN738LC powders to fabricate a metallic matrix composite. Table 3.1 details the relevant material names, the suppliers, the particle size classifications, the weights supplied, the manufacturing technology and the investigation chapter which used the certain batch. Table 3.2 gives the chemical composition of the IN738LC powders, indicating no significant difference in chemical composition between different suppliers. The morphologies of the powders were observed by scanning electron microscope and shown in Figure 3.1.

Table 3.1. Powder Batch Details.

Material	Supplier	Particle Size (µm)	Weight (kg)	Technology	Chapter
IN738LC	AMC	15-53	20	Argon gas	7
IN738LC	LPW	15-53	10	Argon gas	4, 6
IN738LC	SNDVARY	15-53	10	Argon gas	5, 8
Y_2O_3	Shuitian	0.05-0.1	1	Water	7

Table 3.2. Chemical compositions of the IN738LC powders in wt% (supplies A = AMC, L = LPW, S = SNDVARY).

	Ni	Cr	Co	Ti	Al	W	Ta	Mo	Nb	Zr	C	B
A	Bal.	15.82	8.32	3.48	3.50	2.58	1.78	1.82	0.88	0.06	0.12	0.01
L	Bal.	15.92	8.44	3.33	3.41	2.57	1.73	1.81	0.88	0.04	0.11	0.01
S	Bal.	15.81	8.47	3.41	3.36	2.67	1.63	1.71	0.74	0.03	0.10	0.009
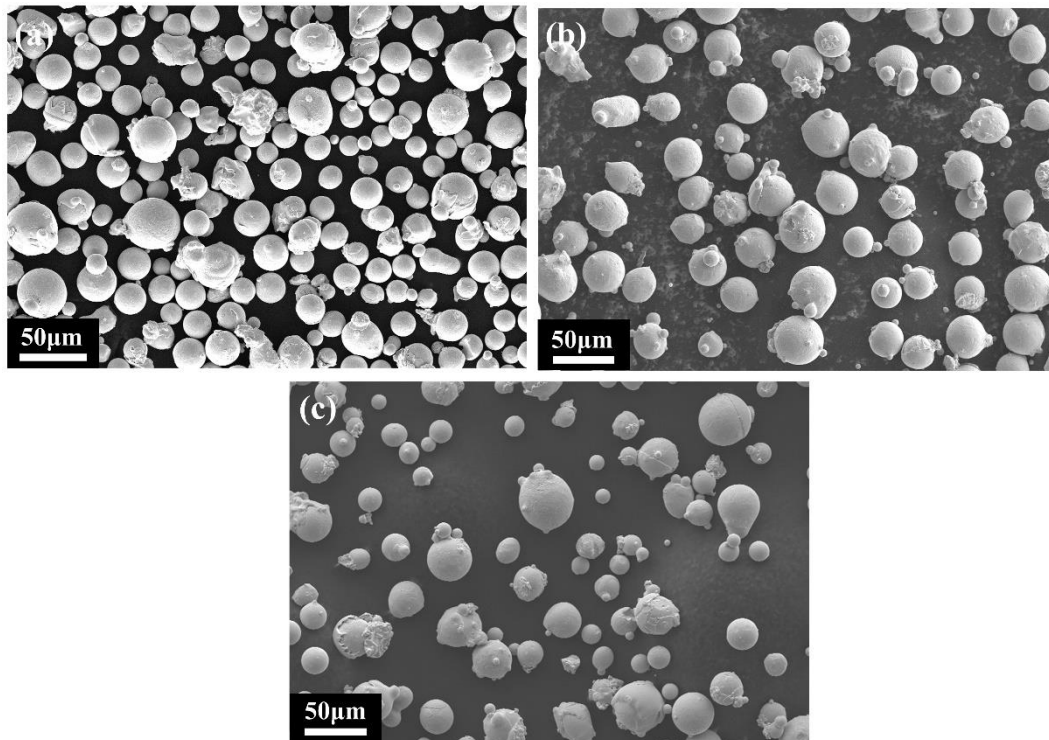
Figure 3.1. Morphologies of the IN738LC powders supplied by (a) LPW, (b) SNDVARY and (c) AMC observed using scanning electron microscopic.

3.2.2. Powder particle size distribution measurement

This research performed a measurement of powder size distribution before the

LPBF process using a CoulterLS230 laser diffraction particle size analyser (LPA)

(Department of Materials Science and Engineering, Southern University of Science and

Technology (SUSTech)). Table 3.3 shows the measurement results of the IN738LC powders. It was reasonable to conclude that the size distributions were similar for the powders supplied by AMC and SNDVARY, while the sizes of the LPW's powders were somehow greater than the other 2 batches.

Table 3.3. Size distributions and flowabilities of the IN738LC powders.

	D10 (μm)	D50 (μm)	D90 (μm)	Flowability (s)
AMC	18.9 ± 0.6	30.1 ± 0.9	47.4 ± 1.1	15.6 ± 0.1
LPW	27.6 ± 0.2	39.1 ± 0.4	49.3 ± 1.9	13.8 ± 0.2
SNDVARY	21.4 ± 1.6	30.7 ± 0.8	42.9 ± 2.5	14.3 ± 0.4

3.2.3. Powder flowability measurement

The powder flowability of the IN738LC powders was measured before the LPBF process. The Hall cup technique, defined as the time for 50 g powders to flow from the Hall cup, was used to perform the measurement. Table 3.3 shows the measured results, and the best flowability of the powders was from LPW.

3.2.4. Powder mixture

The Y_2O_3 nanoparticles of different contents were blended together with the IN738LC powders using a TURBULA T2F 3D swinging powder mixer (Department of Mechanical and Energy Engineering, SUSTech) for 4 hours. Figures 3.2 (a) and 3.2 (b) show the morphologies of the IN738LC and the Y_2O_3 powders observed by scanning electron microscope, while Figures 3.2 (c)-3.2 (f) show the IN738LC powders with the Y_2O_3 nanoparticles inlaid on their surfaces. The inserted images exhibit the details of the powder surfaces at high magnification.

81
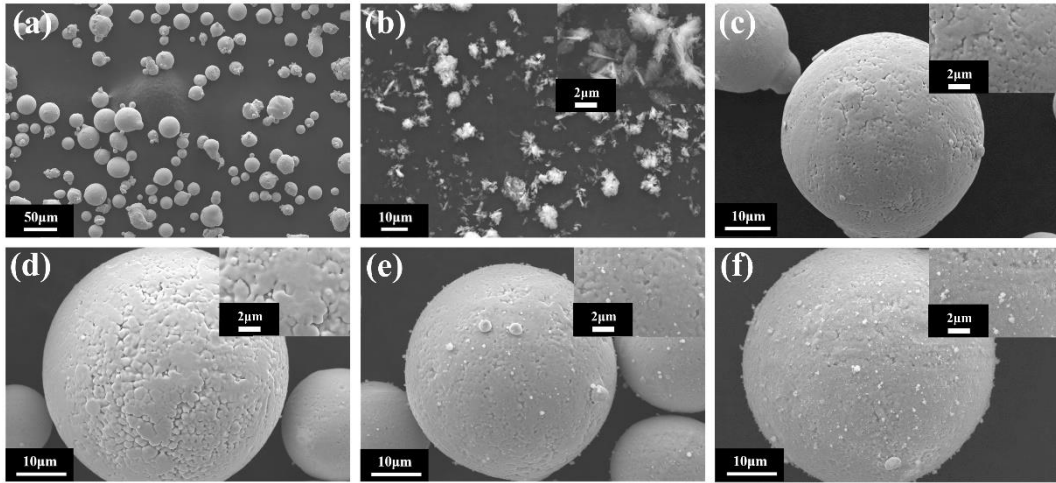
Figure 3.2. Morphologies of (a) the IN738LC powders and (b) the Y$_2$O$_3$ powders as well as the IN738LC powders inlaid with (c) 0 wt% Y$_2$O$_3$, (d) 0.05 wt% Y$_2$O$_3$, (e) 0.2 wt% Y$_2$O$_3$ and (f) 0.6 wt% Y$_2$O$_3$ on the IN738LC powder surfaces observed using scanning electron microscopic. The insert images show the details of the powder surfaces at high magnification.

3.3. Laser powder bed fusion process

3.3.1. Laser powder bed fusion system

A Concept Laser M2 (Netshape, University of Birmingham (UoB)), an SLM Solution 125 (SILENGMAN, Shanghai), a BLT-S210 (GUANGYUNDA, Shenzhen) and a DiMetal-100 (LASERADD, Guangzhou) were used to carry out the Laser powder bed fusion (LPBF) processes. Table 3.4 gives the technical specifications of these LPBF systems. This research defined the surface of the powder bed as the X-Y plane and the movement direction of the recoater as the X-axis. The building direction lied perpendicular to the X-Y plane, defined as the Z-axis.

"Raster" scan mode is a typical scan strategy for the LPBF system, where the laser beam moves back and forth across the whole surface of the current layer, with the direction of the laser beam rotating a certain degree in the latter layers. Figures 3.3 (a)

82

and 3.3 (b) show the schematic diagrams of the "Raster" scan strategy for the rotation angles of 90º and 67º, respectively. A unique scan strategy of the Concept Laser M2 system is an "Island" scan mode. This mode divides the surface of the current layer into several "islands", and the laser beam randomly scans each "island" as the "Raster" mode. The scan directions between the adjacent "islands" are at a 90º angle. The pattern repeats for the next layer but moves a certain distance, as shown in Figure 3.3 (c).

Table 3.4. Technical specifications of the LPBF systems used in this investigation.

LPBF system	Concept Laser	SLM solution	BLT	DiMetal
Laser type	Yb-fiber Continuous Wave	Yb-fiber Continuous Wave	Yb-fiber Continuous Wave	Yb-fiber Continuous/ Pulsed Wave
Max. Laser power (W)	400	400	400	500
Max. Scan speed (mm/s)	4200	10000	7000	7000
Spot size (μm)	150	100	60	100
Scan strategy	Raster & Island	Raster	Raster	Raster
Layer thickness (μm)	20-50	20-100	20-100	20-100
Max. Build height (mm)	280	125	200	100
Plate dimension (mm)	250×250	125×125	105×105	100×100
Pulse frequency (kHz)	N/A	N/A	N/A	1-50
Duty cycle (%)	N/A	N/A	N/A	1-100
Recoater type	Flexible Rubber	Solid Steel/Ceramic	Solid Steel/Ceramic	Solid Steel/Ceramic
Plate material	IN625	SS316	SS316	SS304
Preheat (ºC)	N/A	200	200	N/A
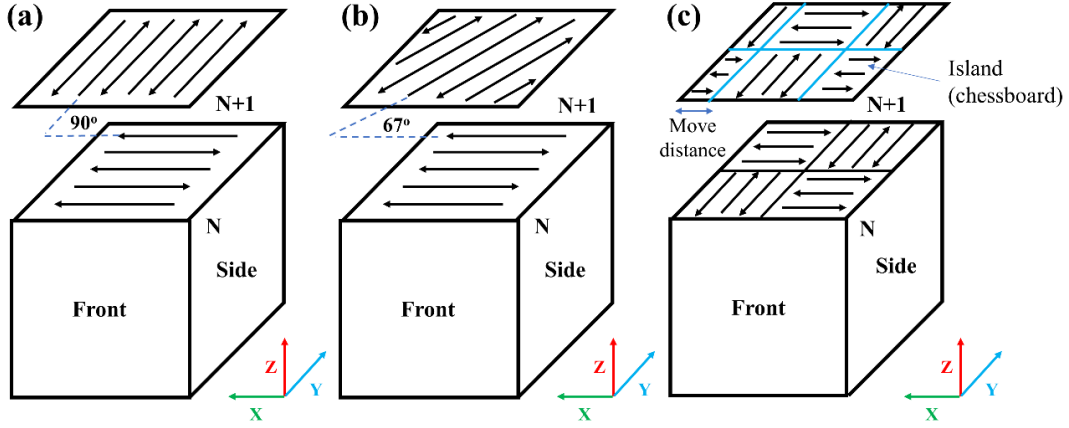
Figure 3.3. Schematic diagrams of the scan strategies of the LPBF systems: (a) Raster 90º, (b) Raster 67º and (c) Island.

In particular, besides the normal continuous-wave laser beam, this research studied pulsed-wave mode using the DiMetal 100 LPBF system. Figure 3.4 shows the typical waveforms of the continuous-wave and pulsed-wave laser emissions, where t_{cycle} is the time for a pulse, so frequency f is $1/t_{cycle}$. t_{on} is the time the laser is emitting, and t_{off} is the time the laser is not emitting. The duty cycle of the pulsed-wave laser emission is:

$$\delta = \frac{t_{on}}{t_{off} + t_{on}} = \frac{t_{on}}{t_{cycle}}$$

Equation 3.1
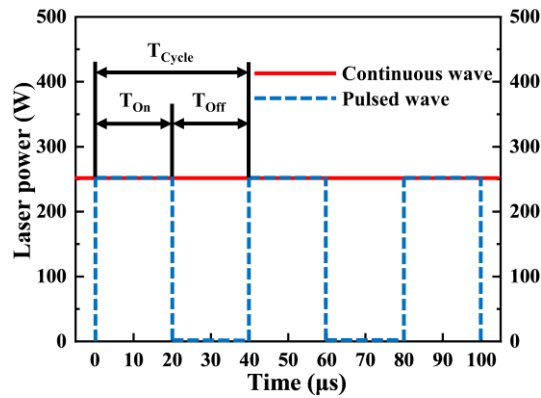
Figure 3.4. Temporal profiles of the power inputs in the continuous-wave and pulsed-wave modes.

3.3.2. Bulk part fabrication

This research fabricated bulk parts with the dimensions of 10 mm × 10 mm × 10

mm for microstructural examination and with the dimensions of 10 mm × 15 mm × 50 mm for property tests. The details of the processing parameters with a fixed layer thickness of 30 μm are shown in Table 3.5.

Table 3.5. Processing parameters used in this investigation.

	Laser power (W)	Scan speed (mm/s)	Hatch spacing (μm)	Scan strategy	Preheat (ºC)	Pulse frequency (kHz)	Duty cycle (%)	Building size (mm)	Chapter
Concept laser	150-350	1000-3000	30-90	Raster 90º	N/A	N/A	N/A	10×10×10 10×15×50	4, 6
SLM solution	250-330	1000-1400	90	Raster 67º	200	N/A	N/A	10×10×10 10×15×50	7
BLT-S200	50-370	500-2500	50	Raster 90º	N/A	N/A	N/A	10×10×10	5
DiMetal 100	220-280	600-1000	50	Raster 67º	N/A	2-8	30-70	10×10×10	8

3.3.3. Single-track testing

3.3.3.1. Effect of laser power and scan speed on track behaviour

This research performed single-track experiments to investigate the effects of laser power and scan speed on track behaviour, i.e., track stability, melt pool dimension and bead mode, using the BLT-S200 system. Since the machine could not directly scan single tracks, it fabricated a basic block to hold the single tracks on its top. The fabricated blocks had the dimensions of 10 mm × 10 mm × 10 mm. All the basic blocks were manufactured using the same parameter of laser power 250 W, scan speed 2000 mm/s, hatching space 50 μm, thickness of layer 30 μm, Raster 90º scan strategy and no preheating. Afterward, a single layer was scanned with a thickness of 30 μm and a track distance of 400 μm on the top of the basic blocks, as shown in Figure 3.5 (a). Figure 3.5 (b) is a schematic diagram of the building part to exhibit the deposited single layer

and tracks.
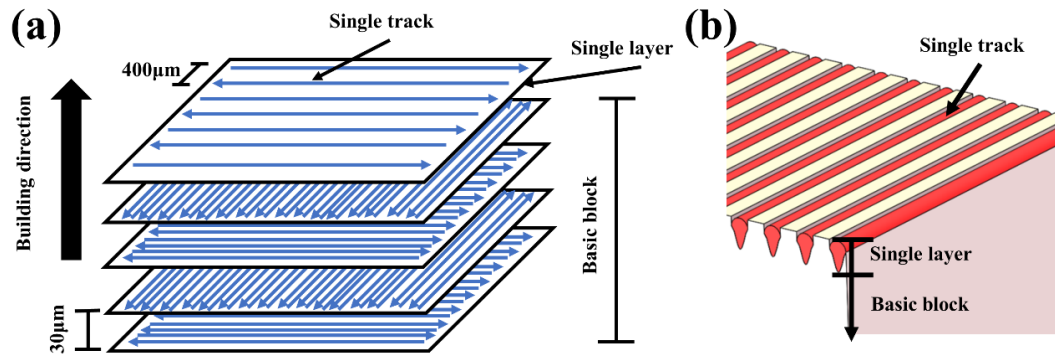
Figure 3.5. Schematic diagrams of (a) the LPBF process to obtain the single tracks and (b) the basic block and the single tracks.

3.3.3.2. Effect of laser beam mode on track behaviour

Single-track experiments were performed to characterise the track morphologies under the continuous and pulsed-wave laser beams using DiMetal100. Unlike BLT-S200, DiMetal100 could directly scan a single track on the substrate under the control of the machine computer system.

3.4. Heat treatment

Standard heat treatment was carried out to optimise the properties of the LPBFed parts using a KSL-1200X furnace (Department of Mechanical and Energy Engineering, SUSTech). In the heat treatment, a solution treatment at 1120 °C for 2 hours, then cooled in air and followed by an ageing treatment at 850 °C for 24 hours, cooled in air were performed [1].

3.5. Metallurgical sample preparation

3.5.1. Grinding and polishing

3.5.1.1. Mechanical polishing

Mechanical polishing is the fundamental step of all metallographic characterisations. Samples were sectioned using a wire electro-discharge machining (EDM) parallel and/or vertical to the building direction, depending on the investigations carried out. After hot-mounted in conductive Bakelite, the samples were ground and polished using auto-polishing machines. Initially, all mounted samples were ground by a coarse abrasive paper (240 p) to obtain relatively level surfaces and remove the contamination from the EDM step. Subsequently, fine grinding steps were applied using abrasive papers with the granulation ranging from 400 p to 3000 p. After grounding, the samples continued being polished in 0.5 μm diamond and 0.04 μm colloidal silica suspension with MD-Dac and MD-Chem polishing cloth, respectively.

3.5.1.2. Vibratory polishing

After the mechanical polishing, a vibratory polisher (Buehler VibroMet 2, Department of Mechanical and Energy Engineering, SUSTech) was subsequently applied to polish the samples with the vibratory frequency of 60 Hz for 2 hours to eliminate the stress on the sample surfaces generated in OPS suspension before electron backscattered diffraction characterisation.

3.5.2. Chemical and electrolytic etching

3.5.2.1. Chemical etching

The samples were etched chemically by submersion in Kalling's No.2 reagent (5 g $CuCl_2$ in 100 mL HCl and 100 mL CH_3CH_2OH [2]) for 2-5 seconds and then rinsed with waterless ethanol and dried out to reveal the microstructural features such as carbides and grain structures.

3.5.2.2. Electrolytic etching

Figure 3.6 depicts the schematic diagram of the electrolytic etching process. This research immersed the polished sample in a glass beaker with the etchant. The anode connected to the surface of the sample, and it submerged the cathode above the sample in the etchant. This research used 2 different electrolytic according to the features of interest. Table 3.6 gives the etching parameters and the corresponding functions of the etchants.
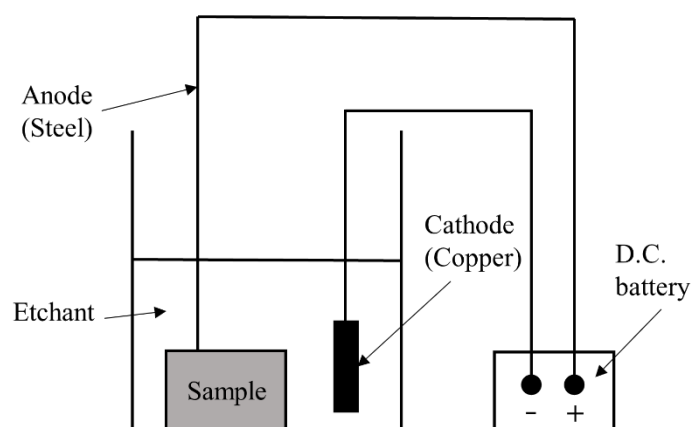
Figure 3.6. Schematic diagram of the electrolytic etching process.

Table 3.6. Etching parameters and functions of the corresponding etchants.

Etchants	Voltage (V)	Time (s)	Function
10% phosphoric acid [3]	4	10	Reveal melt pool and dendrites
70% phosphoric acid [4]	5	5	Reveal γ' phase

3.5.3. Thin foils for transmission electron microscope

3.5.3.1. Focused ion beam

Focused ion beam (FIB) is an ion beam produced by an ion source (most FIBs use Ga, but some devices use He and Ne as the ion source) before accelerated by an ion gun, which is used to strip metallic atoms from the sample surface using a high current beam mode. The advantage of FIB is to be able to thin a foil in a particular location. This research applied FIB (FEI Helios 600i, Core Research Facilities Centre, SUSTech) to prepare a thin foil for the transmission electron microscopic observation. The beam with the voltage of 30 kV and the current from 40 pA to 2.5 nA were conducted to thin the foil under 100 nm. 5 kV and 41 pA were used to eliminate the amorphous layer.

3.5.3.2. Electrolytic twin-jet

Electrolytic twin-jet is favourable to make the samples for transmission electron microscope in large quantities. Initially, a low-speed precision-cutting wheel (Buehler IsoMet LS, Department of Mechanical and Energy Engineering, SUSTech) cut the bulk sample into a slice with the thickness of 0.7 mm, and the slice sample was further ground to the thickness of 100-150 μm by 600 p-1500 p abrasive papers. A punch was used to obtain a φ3 mm disc from the slice. An electrolytic twin-jet thinning system (Struers TenuPol-5, Department of Mechanical and Energy Engineering, SUSTech)

prepared the thin foils for transmission electron microscope in a 10 % perchloric acid ethanol [5] bath under 20 V for 5 minutes below -20 ºC.

3.6. Microstructural characterisation

3.6.1. Optical microscope

An optical microscope (OM) (Axio Observer 3.0, Department of Mechanical and Energy Engineering, SUSTech) equipped with a CCD camera was employed to image the laser track, the melt pools and the defects in the as-printed (APed) LPBFed samples. The Axio Vision SE64 Rel. 4.9 software measured the dimensions (width, depth, height, contact angle) of the melt pools. The final results of the dimensions were the averages by measuring 9 different melt pools. The samples were cut parallel to the building direction into 3 sections for the porosity and crack density measurements, as shown in Figures 3.7 (a) and 3.7 (b). Image threshold techniques (Image J) obtained the porosity and the crack density with optical observations, as shown in Figures 3.7 (c) and 3.7 (d) and Figures 3.7 (f) and 3.7 (g), respectively. Figures 3.7 (e) and 3.7 (h) demonstrate that the porosity is the ratio of the total area of pores to the total measurement area, and the crack density is the ratio of the total length of cracks to the total measurement area. It took 5 different images in each section. And the reported porosity and crack density were the averages from these 3 sections.
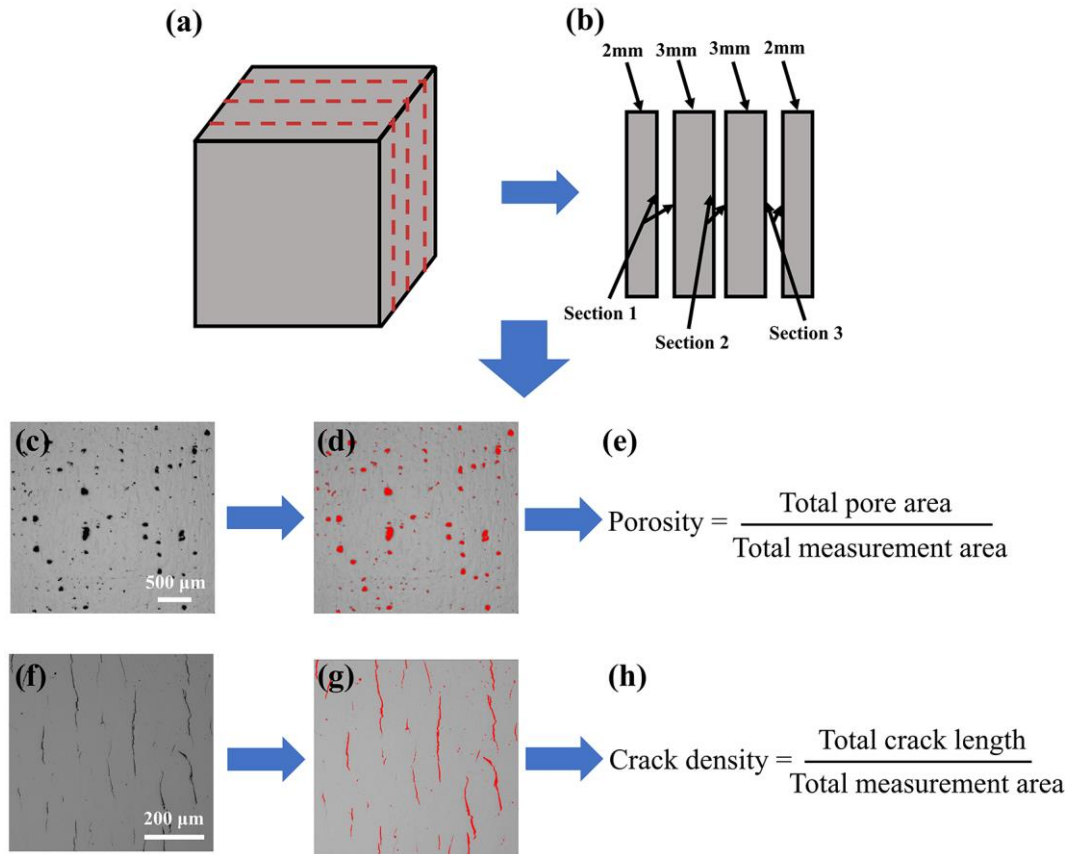
Figure 3.7. (a, b) Schematic diagrams of the sample cutting method, (c-e) analysis procedure for the porosity, (f-h) analysis procedure for the crack density.

3.6.2. Scanning electron microscope

3.6.2.1. Scanning electron microscope observation

This research performed scanning electron microscope (SEM) as the following usages:

- Characterisation of the powders.

- Observation of the details of the defects.

- Observation of the details of the melt pools.

- Observation of the top surfaces of the APed and oxidised parts.

- Observation of the oxidation scales.

- Characterisation of the phases (such as γ′ and carbides) in the APed and heat-treated (HTed) parts.

The reported size and volume fraction of these phases were the averages of the measurements from 5 different view-fields. Table 3.7 shows the technical details of the SEMs, the parameters and the chapters which used in this research.

Table 3.7. Details of the SEMs used in this investigation

Facility	Source	Detector	Current (nA)	Voltage (kV)	Location	Chapter
TM3000	Tungsten Filament	BSE	1	10	UoB	4
Phillips XL30	LaB6	SE2, BSE	5	5	UoB	4
ZEISS Merlin	FEG	SE2, BSE, InLens	0.1/5	5/20	SUSTech	5, 6, 7, 8

3.6.2.2. Energy dispersive spectrometer

The ZEISS Merlin SEM equipped with an EDAX Octane Pro energy dispersive spectrometer (EDS) was used to study the elemental mapping in the cracks and the oxidation scales. This research used the voltage of 10 kV and the current of 1 nA, with the results analysed by the Team software.

3.6.2.3. Electron backscattered diffraction

The ZEISS Merlin SEM equipped with an EDAS Digiview4 electron backscattered diffraction (EBSD) was used to study the microstructural features. It used the voltage of 20 kV and the current of 5 nA and employed the software TSL OIM Analysis 7 64× to analyse the grain size distribution and the misorientation angles by scanning 5 different view-fields for each sample. The corresponding inverse pole figure

(IPF) and pole figure (PF) were used to study the texture. In addition, to investigate the relationship between the crack frequency and the grain boundary misorientation angle, EBSD line scan mode investigated the misorientation angles of 254 cracks.

3.6.3. Transmission electron microscope

A transmission electron microscope (TEM) (Talos F200X, Core Research Facilities Centre, SUSTech) with the acceleration voltage of 200kV was used to identify and characterise the phases in the microstructure by the high-resolution TEM (HRTEM) and high angle annular dark-field (HAADF) scanning TEM (STEM) EDS mode.

3.6.4. X-ray diffraction

To identify the phases on the scanning surface, this research performed an X-ray diffraction (XRD) (ECO D8, Core Research Facilities Centre, SUSTech). It worked with a Cu-K$^\alpha$ source and a ceramic X-ray tube at 40 kV and 25 mA from 20° to 80°/90°.

3.6.5. Laser scan confocal microscope

Figure 3.8 shows the schematic diagram of laser scan confocal microscope (LSCM). When the LSCM works, the laser amplified by the optical lens focuses on the sample through the objective lens under the control of the beam slitting mirror. The fluorescence with a certain wavelength is emitted by the focal point, reaches the detector through the pinhole aperture and presents on the display. 2 LSCMs were employed to measure the surface roughness and re-structure the top surfaces of the APed parts and the oxidised samples. Measuring and averaging 9 different scanning

areas determined the surface roughness. Table 3.8 lists the LSCMs used in this research.
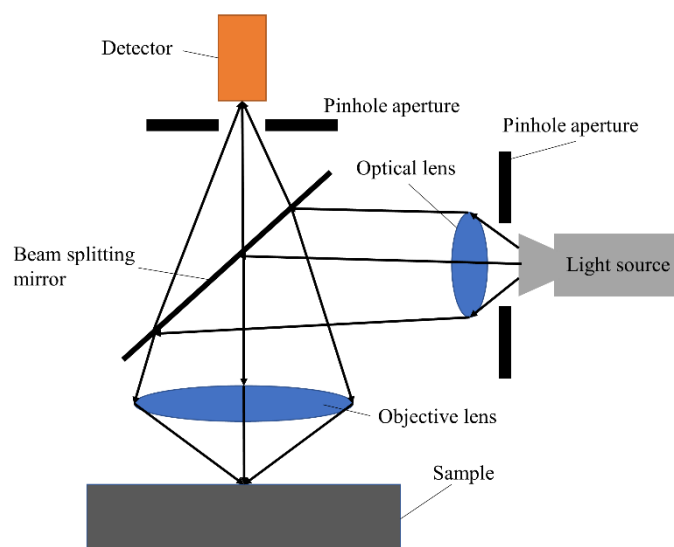
Figure 3.8. Schematic diagram of the LSCM.
Table 3.8. LSCMs used in this investigation

Facility	Location	Chapter
OLYMPUS LEXT	UoB	4
KEYENCE	SUSTech	7, 8

3.6.6. Micro-computed tomography

Figure 3.9 depicts the working process of micro-computed tomography (micro-CT). The sample is rotated 360º within the detection range and irradiated. Each angle collects a two-dimensional (2D) projection image. It reconstructs the acquired 2D projection images through the computer to obtain the three-dimensional (3D) CT volume data, and special software is applied to analyse the data visually. Micro-CT (Diondo d2, ENDI, Shanghai) performed the 3D characterisation of pores with the samples in 3 mm × 3 mm × 3 mm dimensions. In the CT testing, the monochromatic beam volt was 120 kV, and the current was 90 μA with a resolution ratio of 2 μm/pixel. 2040 tomograms reconstruction and data collection were operated by diControl and VG Studio software, respectively.
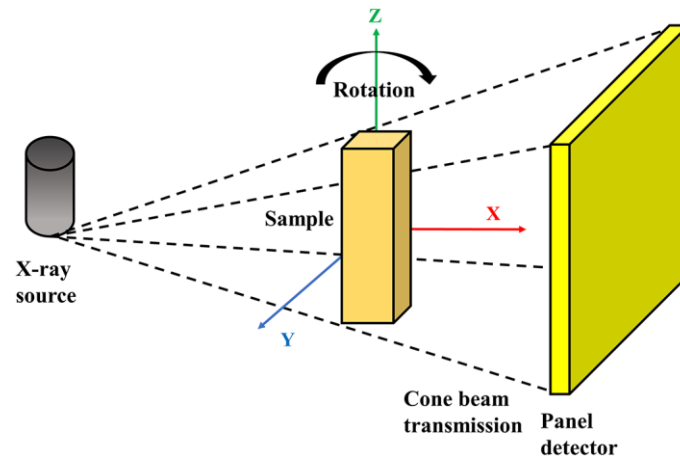
Figure 3.9. Schematic diagram of the micro-CT.

3.7. Simulation

3.7.1. Thermo-Calc solidification patch simulation

Thermo-Calc 2019a was applied to simulate the solidification process of the IN738LC alloy in both equilibrium and Scheil modes. This research also studied the segregation of elements and the solidification temperature range using the Thermo-Calc 2019a software. The simulation temperature range was between 300 ºC and 1500 ºC, and the database used was TCNI8: Ni-Alloys v8.2.

3.7.2. ANSYS Additive Print residual stress simulation

The ANSYS Additive Print 19.2 software was used to simulate the distribution of residual stress during the LPBF process. The ANSYS Additive 19.2 is an advanced finite element analysis software focusing on solving stress distribution problems in LPBF by a thermal-stress coupling method. To reduce the computational cost, the simulation models were simplified into 5 mm × 5 mm × 5 mm dimensions (the real dimensions were 10 mm × 10 mm × 10 mm). Table 3.9 lists the other values involved

in the simulation.

Table 3.9. Constants used in the simulation of the residual stress [6, 7].

Parameter	Value
Powder absorptivity	0.72
Bulk material absorptivity	0.47
Thermal expansion coefficient (K^{-1})	9.78×10^{-6}
Thermal conductivity (W/m·K)	11.85
Specific heat capacity (J/g/K)	0.64
Elastic modulus (GPa)	207
Poisson ratio	0.27
Material yield strength (YS) (MPa)	880

3.7.3. ANSYS 19.2 thermal field simulation

3.7.3.1. Physical model

A 3D thermal model was used to calculate the temperature distribution by the ANSYS 19.2 software, and it achieved the whole process using APDL code input in the Mechanical APDL transient thermal calculation module. Figure 3.10 (a) depicts the 3D finite element model. The dimensions of the top IN738LC layer were 1000 μm × 300 μm × 30 μm and meshed with the size of 10 μm × 10 μm × 10 μm. The bottom substrate (austenitic 304 steel) had the dimensions of 1000 μm × 300 μm × 300 μm with the same mesh size. The simulation loaded the heat source as a single track across the whole surface of the layer, i.e., from P_1 to P_3 with P_2 the midpoint of the track. The moving direction of the heat source was defined as X-axis, and the building direction was Z-axis, as annotated in Figure 3.10 (a).
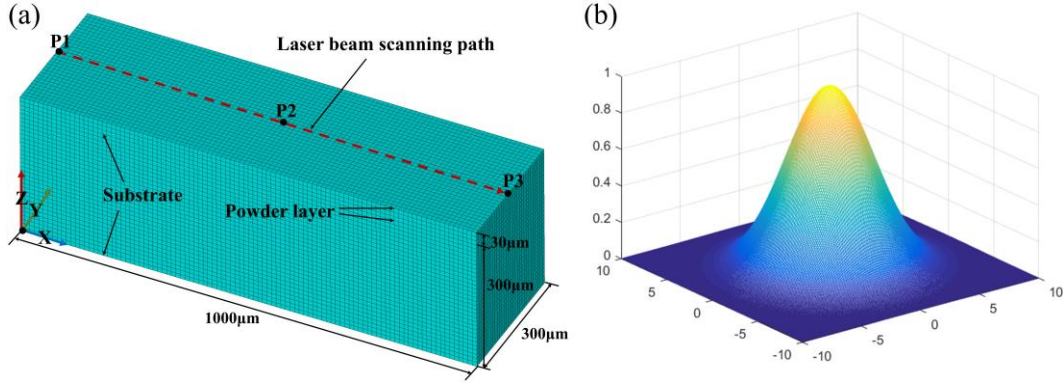
Figure 3.10. (a) 3D thermal finite element model, (b) schematic diagram of the Gaussian laser energy profile.

3.7.3.2. Heat source model

The following equation regards the moving heat source of the laser beam as the Gaussian distribution [8]:

$$q = \frac{2AP}{\pi R^2} \exp(-\frac{2r^2}{R^2})$$ Equation 3.2

where A is the laser absorptivity of the powder (found in Ref. [7]), P is the laser power, R is the radius of the laser beam where the heat flux density falls to its $1/e^2$ at the centre of the laser beam, and r is the radial distance of the target point to the laser beam centre.

Figure 3.10 (b) shows the schematic diagram of the laser beam's pattern. In this simulation, the heat source moved along the X-axis, therefore r could be described as:

$$r^2 = (x - x_0 - vt)^2 + (y - y_0)^2 + (z - z_0)^2$$ Equation 3.3

where (x_0, y_0, z_0) is the starting point of the laser beam, v is the scan speed, and t is the time that the laser beam moves. The loop statements of the ANSYS APDL code achieved the pulse laser action mode. It defined the loops to be equal to the number of cycles in the whole simulation period as:

$$N = \frac{fL}{v}$$ Equation 3.4

97

where f is the frequency, and L is the length of the laser beam path. In a cycle period, the laser on time was δ/f (δ is the duty ratio), and the laser off time was $1/f - \delta/f$. It attained the continuous wave mode as δ was equal to 1.

3.7.3.3. Governing equation

This model considered the powder bed and its surroundings as an adiabatic and closed system, where the energy balance obeys the first law of thermodynamics as [9]:

$$Q_{in} = Q_{conduction} + Q_{convection} + Q_{radiation} \qquad \text{Equation 3.5}$$

where Q_{in} is the heat input, and $Q_{conduction}$, $Q_{convection}$ and $Q_{radiation}$ are the energy losses by conduction, convection and radiation, respectively. The transient spatial temperature field for 3D heat conduction could be described as:

$$\rho \frac{\partial (C_p T)}{\partial t} = \frac{\partial}{\partial x}(k \frac{\partial T}{\partial x}) + \frac{\partial}{\partial y}(k \frac{\partial T}{\partial y}) + \frac{\partial}{\partial z}(k \frac{\partial T}{\partial z}) \qquad \text{Equation 3.6}$$

where r is the density, C_p is the specific heat capacity, T is the surface temperature of the component being fabricating, t is the time of the laser beam-powder bed interaction, k is the thermal conductivity of the material, and x, y and z are the axes. In the simulation, the temperature of the material varied over time, therefore the thermal properties such as C_p and k were also variables with the temperature in the simulation, referred to References [10, 11].

3.7.3.4. Boundary conditions

At the beginning of LPBF, the temperatures of the substrate and the powder bed were equal to the surrounding temperature in the simulation:

$$T(x, y, z, t = 0) = T_0 \qquad \text{Equation 3.7}$$

With boundary conditions potentially described as [9]:

$$k\frac{\partial T}{\partial n} + h(T - T_0) + \sigma\varepsilon(T^4 - T_0^4) = q \qquad \text{Equation 3.8}$$

where k is the thermal conductivity of the material, n is the normal vector of the powder bed surface, h is the convective heat transfer coefficient, σ is the emissivity, and ε is the Stefan-Boltzmann constant. While it could ignore the energy loss related to convection and radiation according to Reference [12].

3.7.4. Matlab R2016b melt pool profile simulation

Matlab code was programmed to describe the profiles of melt pools with different laser frequencies and duty ratios under the pulsed-wave laser mode. The ranges of the simulation field were from -250 μm to 50 μm in the X-axis and -70 μm to 70 μm in the Y-axis. The heat source of the laser beam was in the Gaussian distribution. The governing equation was the point heat source formula [13]. The material properties could be referred to References [6, 7]. The profiles of melt pools exhibited the isotherm of the liquidus of the material.

3.8. Material property tests

3.8.1. Oxidation testing

This research investigated the oxidation behaviour at 1095 °C of the HTed parts. The samples were prepared with the dimensions of 15 mm × 10 mm × 5 mm, polished down to 3000 p and ultrasonically cleaned in ethanol for 5 minutes. Al_2O_3 crucibles

were used to hold the samples for the oxidation tests. To eliminate the effects of moisture in the holder, the Al_2O_3 crucibles were pre-heated at 1000 $^{\circ}$C for 24 hours before cooled to room temperature. Then the preheated Al_2O_3 crucibles were weighted. This process repeated until the weight of crucibles was kept constant. Then the Al_2O_3 crucibles together with the samples were exposed at 1095 $^{\circ}$C in an air atmosphere for 240 hours in a high-temperature furnace (KSL-1200X, Department of Mechanical and Energy Engineering, SUSTech). The furnace had a 5 mm hole connecting to the outside air to guarantee enough oxygen to react with the samples. For every 24 hours, the samples were taken out from the furnace, cooled down to room temperature and measured the total mass together with the crucibles. The mass gain of the samples was used to evaluate the oxidation behaviour over the heated time. There were 3 samples for each alloy, and the measuring results were the average values.

3.8.2. Tensile testing

A tensile testing machine (ZJSY RDL100, Department of Mechanical and Energy Engineering, SUSTech) conducted the tensile tests for the HTed samples at room and 850 $^{\circ}$C at a strain rate of 1.7×10^{-4} /second. The samples were tested perpendicular to the building direction. 3 samples for each condition were tested. The last results were the averages. Figure 3.11 exhibits the dimensions of the tensile sample.
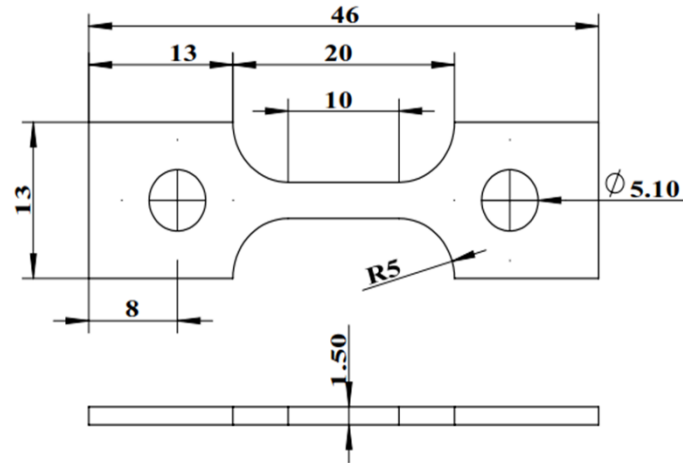
Figure 3.11. Dimensions of the tensile test sample.

3.8.3. Thermal diffusion testing

The thermal diffusivity of the alloys in the APed condition was measured by a NETZSCH LFA 427 laser flash apparatus (LFA). Disc-shaped samples with a thickness of 1.5 mm and a diameter of 10.5 mm were placed in an inert argon gas atmosphere. The samples were heated to 1400 ℃ to a molten condition in a sapphire cell and cooled down to some specified temperatures around the solidus and the liquidus of IN738LC (1360 ℃, 1330 ℃, 1300 ℃, 1270 ℃, 1240 ℃) for the thermal diffusivity measurements. For every temperature, 3 measurements were performed, and the reported results were the averages.

3.9. References

[1] Ramakrishnan A., Dinda G. P. (2019). Direct laser metal deposition of Inconel 738. Materials Science and Engineering: A, 740-741, 1-13.

[2] Marchese G., Basile G., Bassini E., Aversa A., Lombardi M., Ugues D., Biamino S. (2018). Study of the Microstructure and Cracking Mechanisms of Hastelloy X

Produced by Laser Powder Bed Fusion. Materials, 11, 1-12.

[3] Pickering E. J., Mathur H., Bhowmik A., Messé O. M. D. M., Barnard J. S., Hardy M. C., Rae C. M. F. (2012). Grain-boundary precipitation in Allvac 718Plus. Acta Materialia, 60(6-7), 2757-2769.

[4] Peng H., Shi Y., Gong S., Guo, H., Chen B. (2018). Microstructure, mechanical properties and cracking behaviour in a γ′-precipitation strengthened nickel-base superalloy fabricated by electron beam melting. Materials & Design, 159, 155-169.

[5] Krakow R., Johnstone D. N., Eggeman A. S., Hünert D., Hardy M. C., Rae C. M. F., Midgley P. A. (2017). On the crystallography and composition of topologically close-packed phases in ATI 718Plus®. Acta Materialia, 130, 271-280.

[6] X. Yuan (2001). China Aeronautical Materials Handbook. China.

[7] Tolochko N. K., Khlopkov Y. V., Mozzharov S. E., Ignatiev M. B., Laoui Y. (2016). Absorptance of powder materials suitable for laser sintering. Rapid Prototyping Journal, 6(3), 155-161.

[8] Gu D., He B. (2016). Finite element simulation and experimental investigation of residual stresses in selective laser melted Ti-Ni shape memory alloy. Computational Materials Science, 117, 221-232.

[9] Wu J., Wang L., An X. (2017). Numerical analysis of residual stress evolution of AlSi10Mg manufactured by selective laser melting. Optik, 137(137), 65-78.

[10] Quested P. N., Brooks R. F., Chapman L., Morrell R., Youssef Y. M., Mills K. C. (2019). Measurement and estimation of thermophysical properties of nickel based superalloys. Materials Science Technology, 25(2), 154-162.

[11] Mills K. C., Su Y., Li Z., Brooks R. F. (2004). Equations for the Calculation of the Thermo-physical Properties of Stainless Steel. ISIJ International, 44(10), 1661-1668.

[12] Ahsan M. N., Paul C. P., Kukreja L. M., Pinkerton A. J. (2011). Porous structures fabrication by continuous and pulsed laser metal deposition for biomedical applications; modelling and experimental investigation, Journal of Materials Processing Technology, 211(4), 602-609.

[13] Ward M., Guo C. (2020). Programming the Matlab code to describe the profiles of melt pools under the pulsed-wave mode, private communication.

Chapter 4 Parameter Optimisation: Effects of Processing Parameters on Defects

4.1. Introduction

This chapter presents the relationship between the laser powder bed fusion (LPBF) processing parameters and the surface roughness, the porosity and the crack density of the printed parts, while laser power, scan speed and hatch spacing are chosen as the key processing parameters. An experiment with the single variable method is designed among these 3 key parameters, where the primary parameter increases in gradient while the other 2 parameters are fixed. During measurements, it is a challenge to determine the crack density on the sample surface where so many pores co-exist. As the pores may hide the cracks on polished surfaces. In addition, the stress which causes the cracking may be relieved through the pores. These can weaken the responsivity of the parameters on the crack density, implying that the porosity needs to be strictly limited in the samples for the study of cracks. Thus, 2 parallel investigations on parameters versus the porosity (surface roughness) and the crack density are carried out, and parameters are given in Tables 4.1 and 4.2, respectively. In these investigations, the layer thickness is fixed as 30 μm and the scan strategy as Raster 90°, and all the processes are under no preheating condition.

Table 4.1. Parameters used for the investigation on surface roughness and porosity.

Sample	Laser power (W)	Scan speed (mm/s)	Hatch spacing (μm)	VED (J/mm³)
1	200	2000	30	111.1
2	200	2000	45	74.1
3	200	2000	60	55.6
4	200	2000	75	44.4
5	200	2000	90	37.0
6	200	1000	75	88.9
7	200	1500	75	59.3
8	200	2000	75	44.4
9	200	2500	75	35.6
10	200	3000	75	29.6
11	150	2000	90	27.8
12	200	2000	90	37.0
13	250	2000	90	46.3
14	300	2000	90	55.6
15	350	2000	90	64.8

Table 4.2. Parameters used for the investigation on crack density.

Sample	Laser power (W)	Scan speed (mm/s)	Hatch spacing (μm)	VED (J/mm³)
1	250	2000	50	83.3
2	250	2000	60	69.4
3	250	2000	70	59.5
4	250	2000	80	52.1
5	200	1500	60	74.1
6	200	1750	60	63.5
7	200	2000	60	55.6
8	200	2250	60	49.4
9	175	2000	60	48.6
10	200	2000	60	55.6
11	225	2000	60	62.5
12	250	2000	60	69.4

4.2. Results and discussions

4.2.1. Surface roughness

4.2.1.1. Effects of hatch spacing

Figure 4.1 (a) shows the surface roughness as a function of the hatch spacing. The surface roughness decreases initially from 13.9 ± 2.8 μm at the hatch spacing of 30 μm down to 11.5 ± 0.8 μm at 45 μm but then increases up to 21.1 ± 2.3 μm at the hatch spacing of 90 μm.

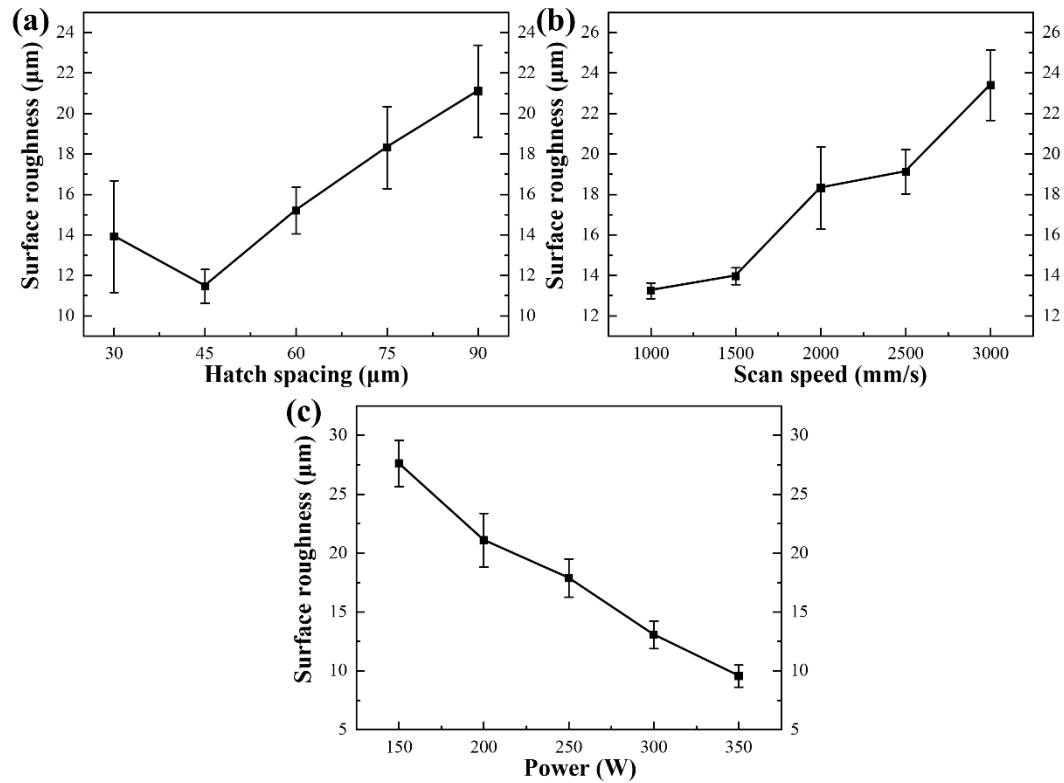**Figure 4.1. Surface roughness as a function of (a) the hatch spacing (laser power 200 W, scan speed 2000 mm/s), (b) the scan speed (laser power 200 W, hatch spacing 75 μm) and (c) the laser power (scan speed 2000 mm/s, hatch spacing 90 μm).**

Figure 4.2 shows the scanning electron microscope (SEM) and reconstruction images of the top surfaces. Figures 4.2 (a) and 4.2 (b) exhibit that the tracks on the top

surface are very close to each other at the hatch spacing of 30 μm. And when the hatch spacing increases to 45 μm, a relatively flat surface is obtained due to the sufficient overlap between tracks, as displayed in Figures 4.2 (c) and 4.2 (d). Figure 4.2 (e) shows that big gaps appear between adjacent laser tracks when the hatch spacing is high. The corresponding reconstruction image (Figure 4.2 (f)) shows a large height difference between the top and the bottom of the tracks, which directly results in high surface roughness. However, when the hatch spacing continues reducing to 30 μm, the surface roughness increases to 13.9 μm with a large deviation (2.8 μm). The humping phenomenon can explain this due to the Marangoni flow as a considerably low hatch spacing is applied during the LPBF process. Figures 4.3 (a) and 4.3 (b) show the schematic diagrams to illustrate the mass transfer of melt between the tracks at high and low hatch spacings, respectively. The Marangoni convection occurs when the melt flows from the regions with low surface tension to the region with high surface tension in the melt pool [1, 2]. Typically, surface tension is negatively related to temperature, implying a high temperature favours a low surface tension. The temperature in the centre of the melt pool is normally higher than that in the edge. Therefore, the direction of the attendant Marangoni flow is from the centre to the edge, resulting in a mass transfer of the melt from the present track to the previously fabricated ones. When the hatch spacing is relatively large, the melt transferred by the Marangoni flow can fill in the gaps between the tracks, which contributes to a flat surface, as shown in Figure 4.3 (a). However, the temperature gradient between the tracks increases at a low hatch spacing [3], thus increasing the Marangoni flow's trend [4]. In addition, low hatch

spacings can increase thermal accumulation, with the melt pool obtaining a resultant high working temperature. The high temperature reduces the viscosity of the melt, which is beneficial for the Marangoni flow. Therefore, the vigorous Marangoni flow increases the mass transfer's intensity to the previously fabricated tracks at low hatch spacings, inducing the stacking of material on the top surface of the tracks, and then the micro-humping occurs after solidification, as shown in Figure 4.3 (b). The micro-humping phenomenon at the hatch spacing of 30 μm is shown in Figures 4.2 (a) and 4.2 (b) by SEM and laser scan confocal microscope (LSCM) (red dotted line), respectively.
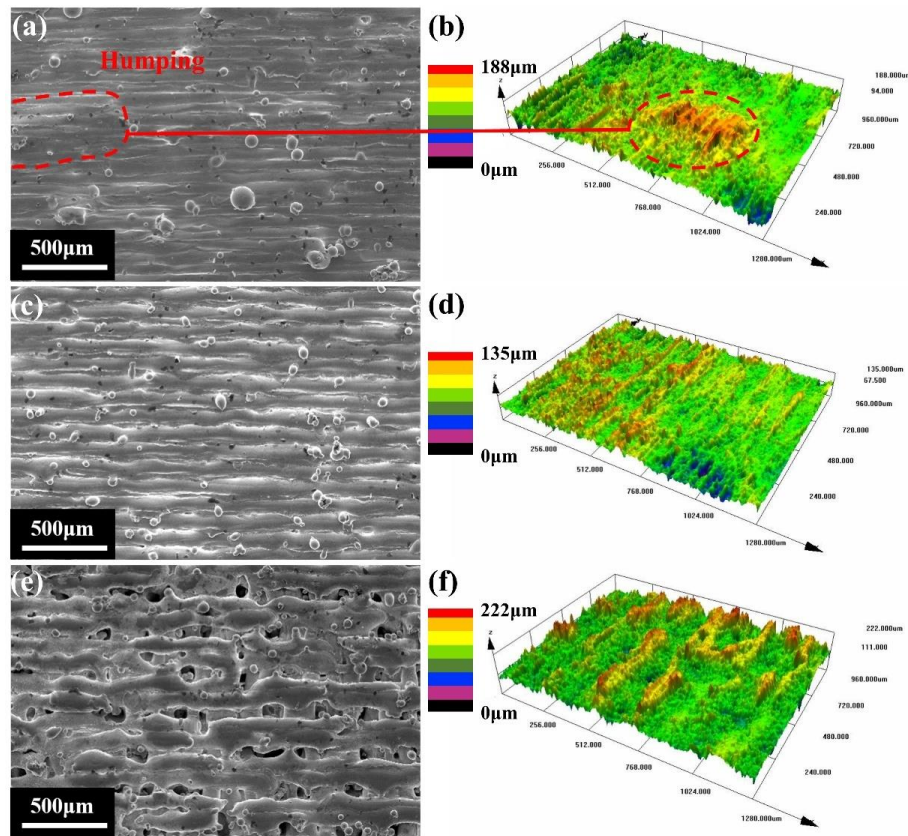

Figure 4.2. SEM and reconstruction images of the top surfaces at the hatch spacings of (a, b) 30 μm, (c, d) 45 μm and (e, f) 90 μm (laser power 200 W, scan speed 2000 mm/s).
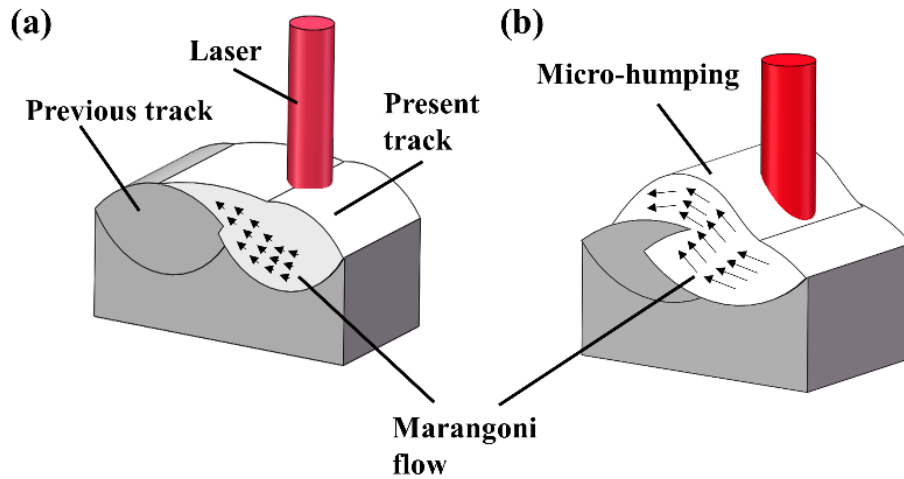
Figure 4.3. Schematic diagram of the mass transfer between the tracks at (a) high and (b) low hatch spacings.

4.2.1.2. Effects of scan speed

Figure 4.1 (b) shows the surface roughness at various scan speeds. The surface roughness has a clear trend of increase with the increase of the scan speed. The scan speed of 1000 mm/s corresponds to a minimum roughness of 13.2 ± 0.4 μm.

When the scan speed is low, high energy input density induces the powders to fully melt, which is beneficial for the formation of a flat surface (Figures 4.4 (a) and 4.4 (b)). As the scan speed increases to 2000 mm/s, the tracks swell, and clear gaps appear between the tracks, as shown in Figure 4.4 (d). When the scan speed reaches 3000 mm/s, the tracks become fluctuant and irregular-shaped, suggesting that an unstable condition occurs. From Figure 4.4 (e), the discontinuity and the instability of the track make it difficult to recognise the scan direction of the laser beam. The Plateau-Rayleigh instability contributes to this unstable condition when applying a considerably high scan speed in LPBF. Scipioni et al. [5] and Li et al. [6] suggested that a molten track could be regarded as a liquid cylinder during the reaction between the laser beam and the

powder bed. λ is the length of the cylinder, and D is the diameter. The instability occurs when the ratio of λ to D is larger than π, as shown in Figure 4.5 (a). Yadroitsev et al. [7] thought that the stability of the melt was related to the contact angle θ between the liquid cylinder and the substrate and suggested that the track stayed stable if $\theta < \pi/2$. During the LPBF process, the top layer is scanned based on the previously fabricated layers, thus $\theta < \pi/2$ is difficult to sustain. Swell and shrinkage result in the necking down and induce the track fluctuation, as shown in Figure 4.5 (b). As a result, the liquid cylinder breaks up into small droplets to lower the surface energy, known as balling phenomenon in LPBF. Rayleigh [8] found that the break time reached its minimum when $\pi D/\lambda = 0.69$, and the time was:

$$t = \{0.3433 \cdot \sqrt{\gamma / [\rho_m \cdot (D/2)^3]}\}^{-1} \qquad \text{Equation 4.1}$$

where γ is the surface tension, and ρ_m is the melt density. When D is 100 μm, γ is 1.88 N/m, and ρ_m is 7324 kg/mm^3 for IN738LC according to the study of Quested et al. [9], the calculated break time is ~ 65 μs, well below the typical solidification time during the LPBF process [1]. The breaking of track happens before it solidifies, implying the bailing phenomenon's occurrence. Rombouts et al. [1] also found that the increase of scan speed led to an increase of the melt pool length, which accordingly induced the ratio's increase of λ to D. Therefore, high scan speeds increase the possibility of Plateau-Rayleigh instability being present.
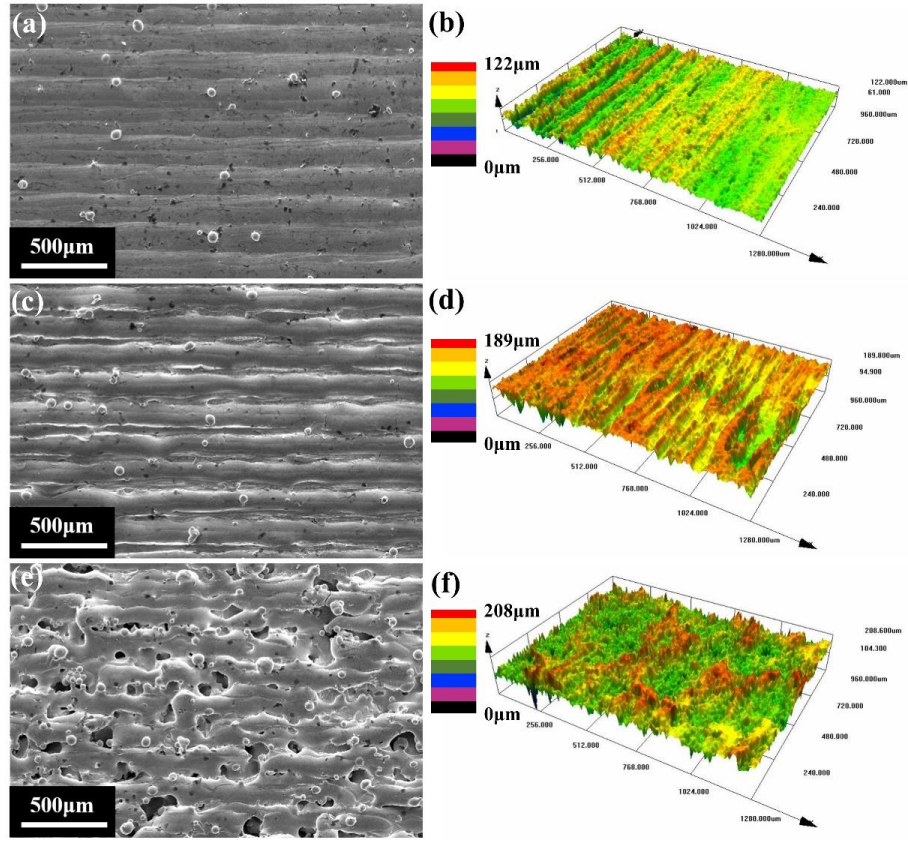
Figure 4.4. SEM and reconstruction images of the top surfaces at the scan speeds of (a, b) 1000 mm/s, (c, d) 2000 mm/s and (e, f) 3000 mm/s (laser power 200 W, hatch spacing 75 μm).
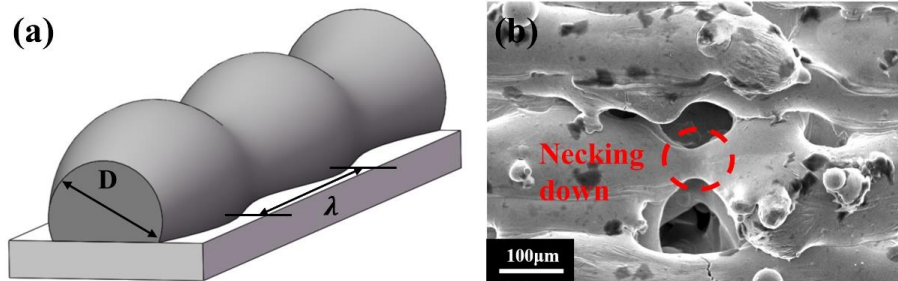
Figure 4.5. (a) Schematic diagram of the disturbance of a liquid cylinder, (b) SEM image of the track fluctuation showing the necking down occurs at the scan speed of 3000 mm/s (laser power 200 W and hatch spacing 75 μm).

Figure 4.6 shows the top surface with different scan speeds at high magnification.

As the scan speed increases, more pores appear. From Figures 4.6 (a)-4.6 (c), the surface

exhibits free pores at the scan speeds of 1000 mm/s-2000 mm/s. However, from Figures

4.6 (d) and 4.6 (e), as the scan speed continues increasing to 2500 mm/s and 3000 mm/s,

the number of pores increases gradually, attributed to the uneven spread of powders and

111

the open pores. The low flowability limits the melt to spread and wet the neighbouring tracks fully during the rapid cooling process at high scan speeds in LPBF, thus causing the open pores. As aforementioned, viscosity is temperature dependent, high scan speeds lower the working temperature and increase the viscosity of melt during solidification. Melt with high viscosity is less likely to migrate toward the adjacent tracks. After solidification and shrinkage, the open pores form, as shown in Figure 4.6 (e). Xia et al. [10] also observed that the number of open pores increased with the increase of the scan speed during LPBF of Inconel 718. Khairallah et al. [11] thought that open pores formed after the laser beam passed through the present location, and accompanying with the increase of surface tension, the pores kept opening due to the depression by the recoil force. Furthermore, numerous un-melted particles caused by the lack of fusion can be observed at the scan speed of 3000 mm/s, as shown in Figure 4.6 (f).

Figure 4.6. SEM images at high magnification of the top surfaces at the scan speeds of (a) 1000 mm/s, (b) 1500 mm/s, (c) 2000 mm/s, (d) 2500 mm/s, (e, f) 3000 mm/s (laser power 200 W, hatch spacing 75 μm).
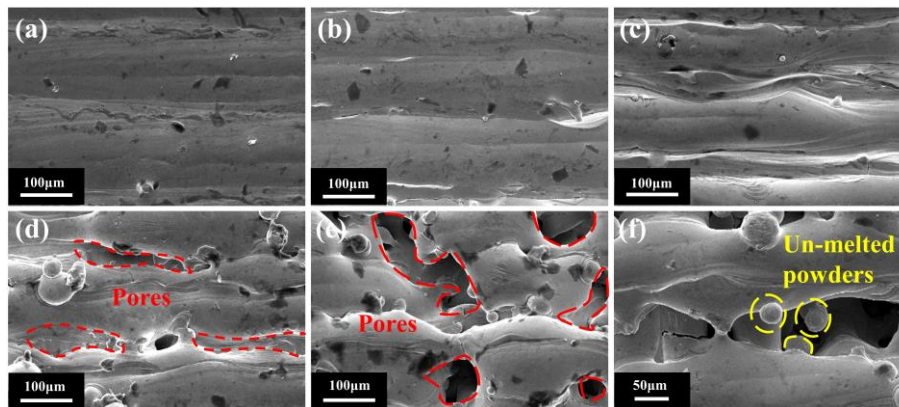
4.2.1.3. Effects of laser power

Figure 4.1 (c) illustrates a linear drop in the surface roughness with increasing the

laser power from 150 W to 350 W. Big gaps form between the tracks due to the lack of overlap at the laser power of 150 W, as shown in Figures 4.7 (a) and 4.7 (b). Although the tracks keep stable along the laser scanning direction, big gaps between the tracks and the intermittent discontinuity induce a poor surface quality. When the laser power increases to 250 W, in contrast, the top surface becomes flat due to the sufficient overlap with an efficient metallurgical bond between the tracks. However, some pores are observable between the tracks, as shown in Figure 4.7 (c). Meanwhile, the discontinuity phenomenon disappears. Continuous elevation of the laser power to 350 W leads to a high-quality surface (Figures 4.7 (e) and 4.7 (f)).
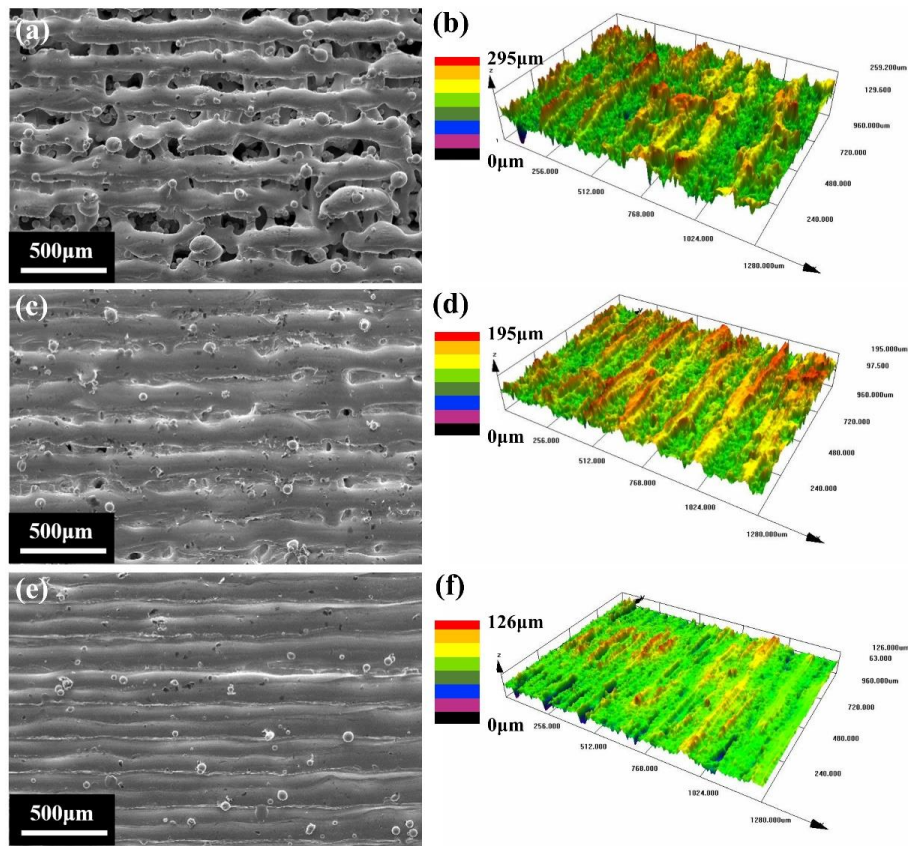

Figure 4.7. SEM and reconstruction images of the top surfaces at the laser powers of (a, b) 150 W, (c, d) 250 W and (e, f) 350 W (scan speed 2000 mm/s, hatch spacing 90 μm).

Figure 4.8 shows another type of balling at the laser powers of 250 W and 300 W.

This type of balling phenomenon is ascribed to the Marangoni convection's reverse flow direction. As mentioned before, the Marangoni convection's normal direction from the melt pool's centre to the edge induces a considerable amount of melt to flow towards neighbouring tracks. However, some elements existing in melt can change the sign of the gradient of surface tension to temperature, i.e., positive correlation between surface tensile and temperature, and the Marangoni convection is dragged from the melt pool's edge to the centre. A large amount of melt comes together and an agglomeration of material forms, exhibiting a ball morphology on the top of the melt pool after solidification, as illustrated in Figure 4.8 (a), and Figure 4.8 (b) shows an example of this type of balling. Rombouts et al. [1] and Zhou et al. [2] found that sulphur and oxygen were the key elements that could induce this type of balling phenomenon in the melt pool. Li et al. [12] thought that the temperature gradient increased significantly at a higher laser power, which could induce a higher surface tension gradient along the building direction and enhance the Marangoni convection. Therefore, this type of balling is more likely to occur at higher laser power. When the laser power reaches its maximum value of 350 W, however, no balling forms, as shown in Figure 4.7 (e). This is attributed to that a high peak temperature induced by the considerably high laser power results in intensive evaporation in the melt pool, promoting recoil pressure. And a strong recoil pressure has the function to detach balls from the solidifying melt pool [13]. Kruth et al. [14] also thought that the application of high laser powers could reduce the trend for the melt pool to undergo the balling phenomenon.
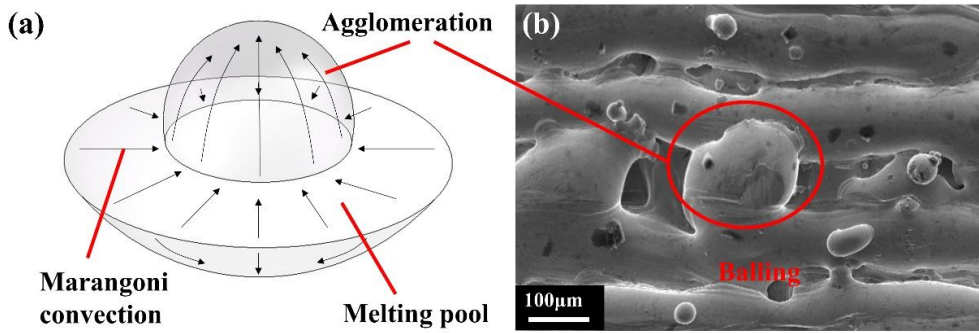
Figure 4.8. (a) Schematic diagram showing the balling mechanism induced by the Marangoni convection, (b) SEM image of a balling morphology at the laser power of 250 W (scan speed 2000 mm/s, hatch spacing 90 μm).

4.2.2. Porosity

4.2.2.1. Effects of hatch spacing

Figure 4.9 shows the porosity as a function of the hatch spacing. The porosity increases gradually from 0.1 ± 0.02 % to 1.1 ± 0.3 %, with the hatch spacing increasing from 45 μm to 75 μm and rapidly up to 11.5 ± 0.6 % at the hatch spacing of 90 μm. The high porosity at the hatch spacing of 90 μm is due to the insufficient overlap between the laser tracks, as shown in Figure 4.2 (e). Figure 4.10 shows that the un-melted powders trap in these irregular-shaped pores due to a lack of fusion. The porosity obviously increases to 5.2 % with a large deviation (0.9 %) at the hatch spacing of 30 μm. This is attributed to the micro-humping phenomenon, which causes the powder layer to unevenly spread across the previously fabricated layers. When the layer is too thick for the laser beam to penetrate, the pores form due to the incomplete bond between layers. Qiu et al. [15] suggested that the thicker layer increased the melt pool's instability and resulted in the track's discontinuity and more spatter. The powder layer's uneven thickness accumulates as the LPBF process continues due to the contingency

of micro-humping. Therefore, the maldistribution of pores appears on the polished

surface, indicating a large data deviation in Figure 4.9 (a).
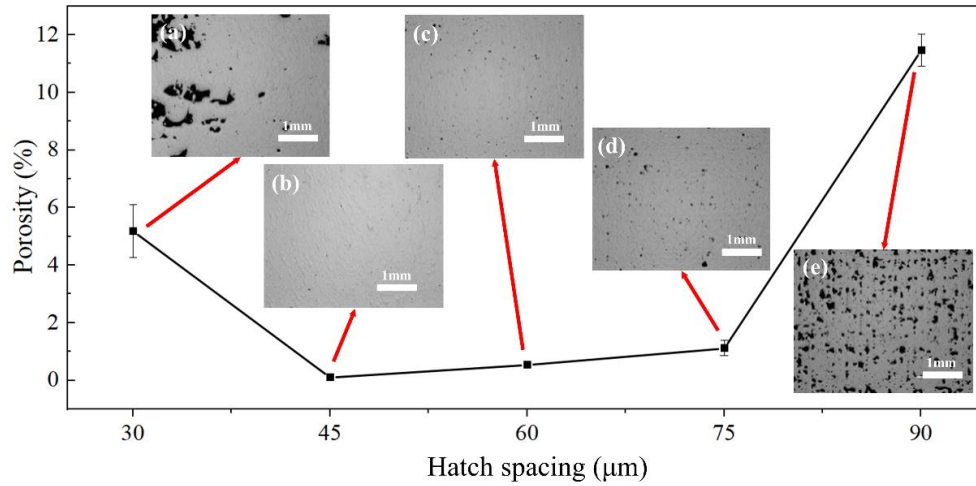
Figure 4.9. Porosity as a function of the hatch spacing, inserted optical microscope (OM) images showing the polished surfaces at the hatch spacings of (a) 30 µm, (b) 45 µm, (c) 60 µm, (d) 75 µm and (e) 90 µm (laser power 200 W, scan speed 2000 mm/s).
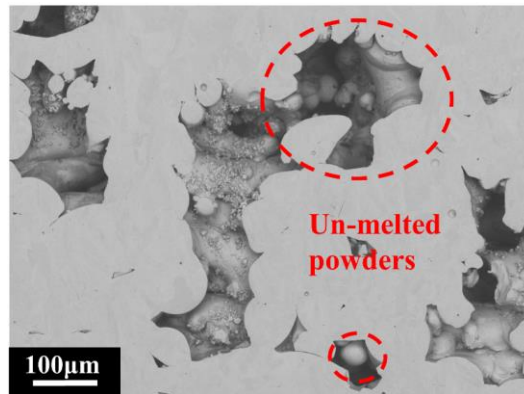
Figure 4.10. SEM image of the polished surface showing the un-melted powders at the hatch spacing of 90 µm (laser power 200 W, scan speed 2000 mm/s).

4.2.2.2. Effects of scan speed

Figure 4.11 shows the porosity as a function of the scan speed. It is apparent that

both high and low scan speeds can cause high porosity. When the scan speed is 1000

mm/s, the corresponding porosity is 3.1 ± 0.2 %, which is higher than that at the scan

speed of 1500 mm/s. As the scan speed increases from 1500 mm/s to 3000 mm/s, the

porosity increases from 0.1 ± 0.01 % to 13.1 ± 0.9 %. The lack of fusion induced by

high scan speeds is the primary cause of high porosity, as shown in Figure 4.12 (a). The

Plateau-Rayleigh instability can be also observed at the scan speed of 3000 mm/s, as

shown in Figure 4.12 (b). The fluctuation causes wave crests and troughs along the laser

scan direction. When the 2 wave crests overlap together, a bridge-like structure with a

dense metallurgical bond forms. While when the 2 wave troughs encounter, a big gap

appears as a pocket with many un-melted powders trapping in it. The insert image of

Figure 4.12 (b) illustrates this process.
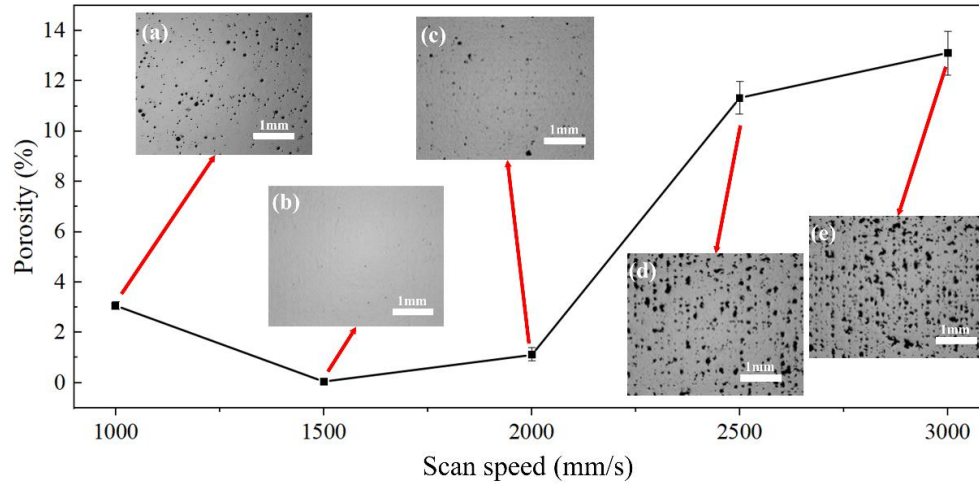
Figure 4.11. Porosity as a function of the scan speed, inserted OM images showing the polished surfaces at the scan speeds of (a) 1000 mm/s, (b) 1500 mm/s, (c) 2000 mm/s, (d) 2500 mm/s and (e) 3000 mm/s (laser power 200 W, hatch spacing 75 μm).
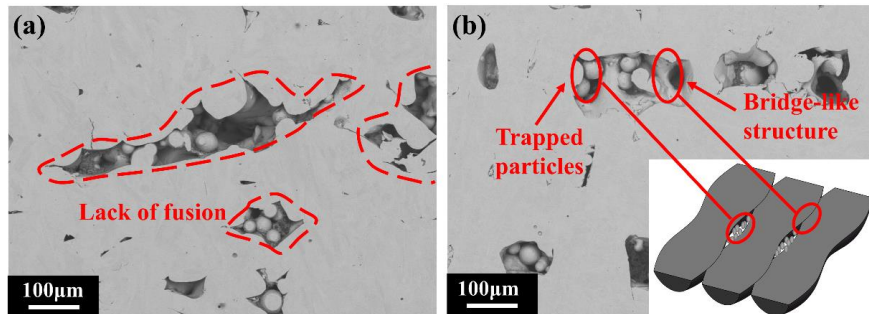
Figure 4.12. SEM images of the polished surfaces showing (a) the lack of fusion and (b) a bridge-like structure and trapping un-melted powders due to the Plateau-Rayleigh instability at the scan speed of 3000 mm/s (laser power 200 W, hatch spacing 75 μm).

Low scan speeds increase the porosity due to another type of pore: keyhole pore, as shown in Figure 4.11 (a). When the combination of scan speed, laser power and laser beam size exceeds a critical value, the normal conduction mode is possible to transfer to the keyhole mode, since the energy input density is high enough to induce evaporation and plasma, which effectively "drills" a deeper depth to form a cavity in the melt pool. King et al. [16] and Fabbro [17] observed a similar behaviour in the LPBF and welding processes. The keyhole pores form due to the gas entrapping and the collapse of these cavities with a more rounded shape [18]. Figure 4.13 shows an example of the keyhole pore.
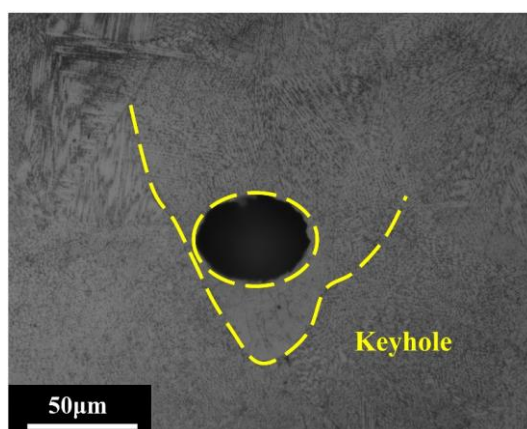
Figure 4.13. OM images showing a keyhole pore at the scan speed of 1000 mm/s (laser power 200 W, hatch spacing 75 μm).

4.2.2.3. Effects of laser power

Figure 4.14 shows a disproportionate decrease of the porosity with the laser power's increase. The maximum porosity is 14.8 ± 0.8 % at the laser power of 150 W and decreases to 11.5 ± 0.6 % as the laser power increases to 200 W. The porosity drops significantly below 1 % with the continuous increase of the laser power. Similarly, the energy input density accordingly decreases when decreasing the laser power, leading to

the lack of fusion and further increasing the porosity.
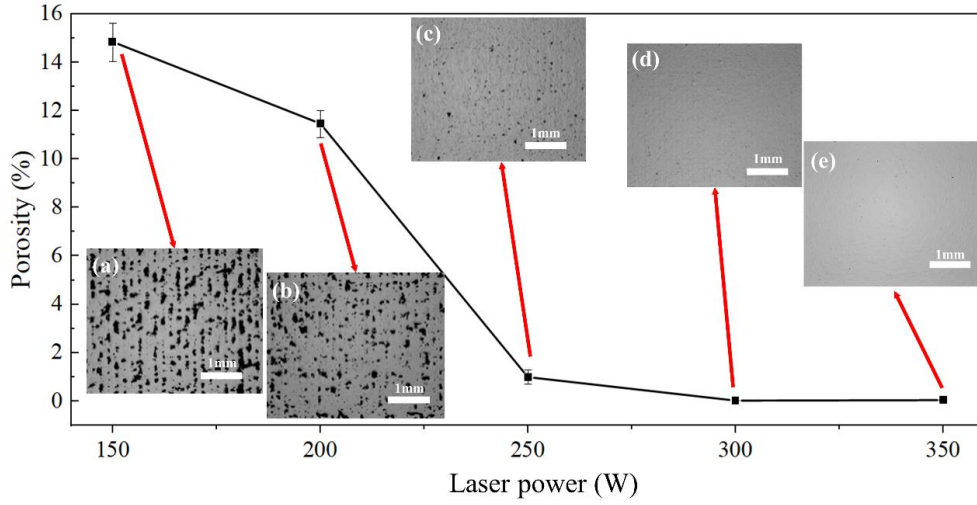
Figure 4.14. Porosity as a function of the laser power, insert OM images showing the polished surfaces at the laser powers of (a) 150 W, (b) 200 W, (c) 250 W, (d) 300 W and (e) 350 W (scan speed 2000 mm/s, hatch spacing 90 μm).

4.2.2.4. Effects of volume energy density

Volume energy density (VED) is widely used to justify the comprehensive effect of processing parameters on printing qualities in LPBF (although other approaches are able to more fully represent the process physics, such as normalised energy density method, see Section 5.3.4), defined as [18]:

$$\psi = \frac{P}{v \cdot s \cdot \xi} \qquad\qquad \text{Equation 4.2}$$

where P is the laser power, v is the scan speed, s is the hatch spacing, and ξ is the layer thickness. Figure 4.15 gives the porosity as a function of the VED, showing that the minimum porosity is obtained at the VED fallen between ~ 55 J/mm^3 and ~ 75 J/mm^3. When the VED increases from ~ 25 J/mm^3 to ~ 60 J/mm^3, the porosity decreases from ~ 15 % to ~ 0.02 %, while when the VED increases further, the porosity increases to ~ 3 % and ~ 5 % at the VEDs of ~ 90 J/mm^3 and ~ 110 J/mm^3, respectively.
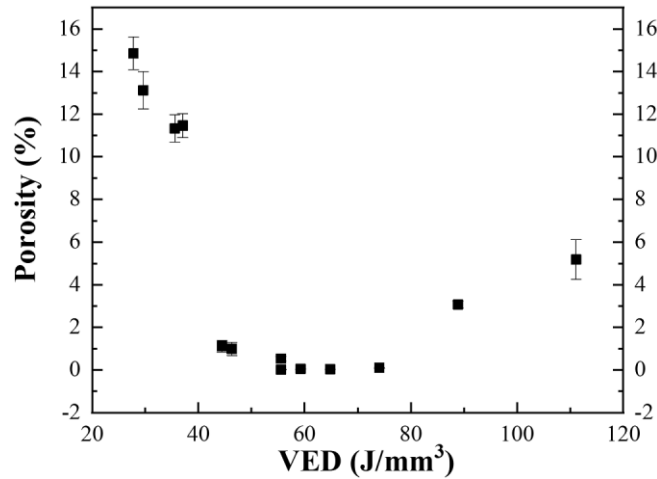
Figure 4.15. Relationship between the VED and the porosity.

To further observe and analyse the morphology of the pores, micro-computed tomography (micro-CT) is performed on 4 samples with different VEDs. Figures 4.16 and 4.17 show the three-dimensional (3D) reconstruction images and the size distribution of the pores, respectively. As shown in the reconstruction image (Figure 4.16 (a)), large and irregular pores occupy the whole measured domain at a lower VED of 29.6 J/mm^3, indicating that the occurrence of insufficient overlap, the melt pool's instability and the lack of fusion. The pores from different layers and tracks are observed to connect, accordingly forming huge hollow spaces and frame-like structures, as shown in the reconstruction image at high magnification (Figure 4.16 (e)), which corresponds to several pores with large size in Figure 4.17 (a). As the VED increases to 44.4 J/mm^3, the porosity decreases to ~ 1 %. A higher VED improves the printing quality drastically, and the increase of the bonds between the layers and the tracks eliminates most large pores. A continuous increase of the VED to 59.3 J/mm^3 allows it to fully melt the powders, leading to a nearly pore-free part manufactured, as shown in Figures 4.16 (c) and 4.17 (c). When the VED further increases to 88.9 J/mm^3, it observes round shape pores scattering all over the measured domain in Figure 4.16 (d),

120

with Figure 4.16 (f) the view at higher magnification, corresponding to the keyhole pores. The size of the keyhole pores distributes concentratedly between 15 μm and 35 μm, as illustrated in Figure 4.17 (d).
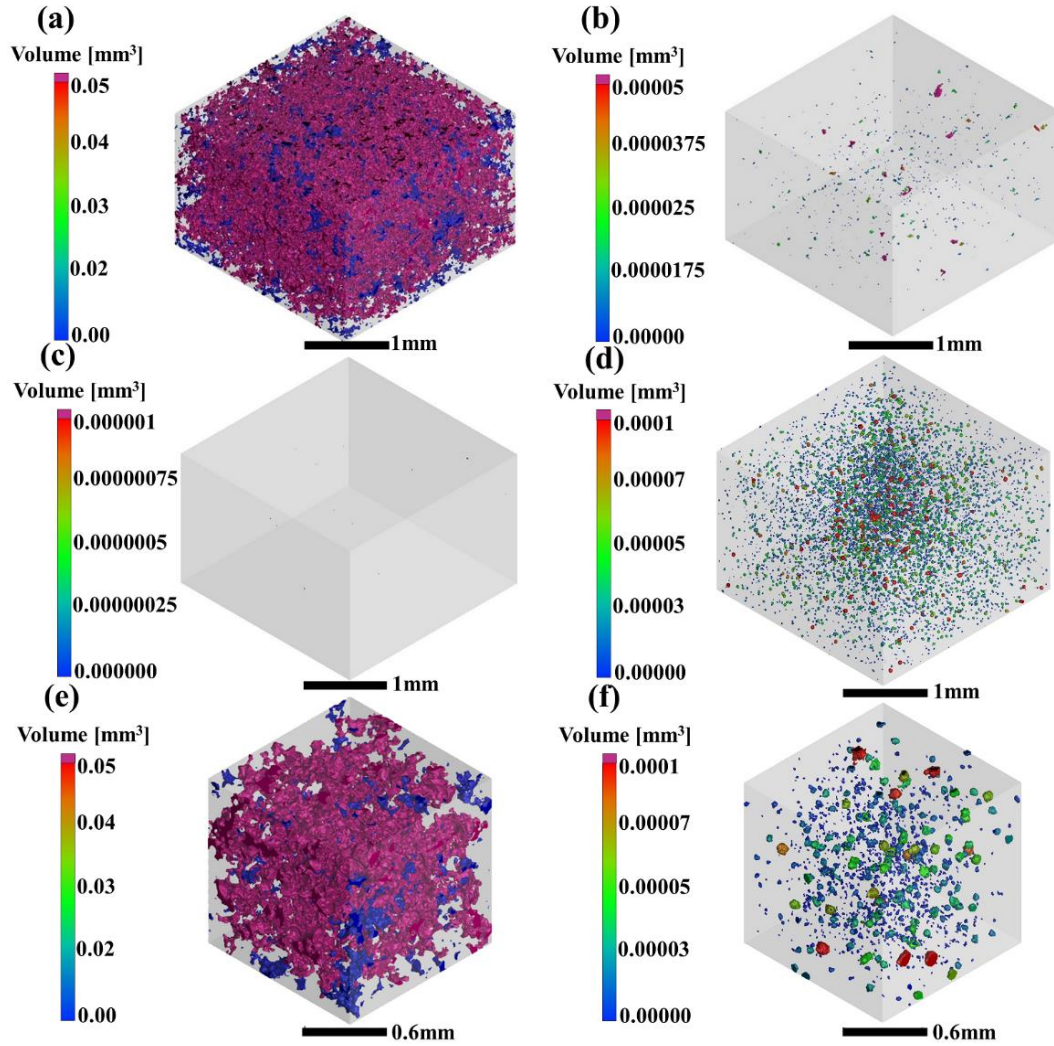
Figure 4.16. 3D reconstruction images of the pores at the VEDs of (a) 29.6 J/mm³, (b) 44.4 J/mm³, (c) 59.3 J/mm³ and (d) 88.9 J/mm³, (e) high magnification of (a), (f) high magnification of (d).

Figure 4.17. Size distributions of the pores at the VEDs of (a) 29.6 J/mm³, (b) 44.4 J/mm³, (c) 59.3 J/mm³ and (d) 88.9 J/mm³.

Figure 4.18 shows the pores' distribution of sphericity. The definition of sphericity is given by Kasperovich et al. [18] as:

$$\eta = \frac{6 \cdot \pi^{1/2} \cdot V}{A_s^{3/2}}$$
<div align="right">Equation 4.3</div>

where V is the volume, and A_s is the object's surface area. As η gets closer to 1, the shape of pore gets closer to a sphere, and $\eta = 1$ for a sphere. As η gets smaller, the pore becomes more concave, elongated or irregular. From Figure 4.18, when the VEDs are 29.6 J/mm³, 44.4 J/mm³ and 59.3 J/mm³, the sphericity mainly distributes between 0.5 and 0.7, and the corresponding frequencies are 74.1 %, 81.2 % and 73.5 %, respectively. At a low VED of 29.6 J/mm³, the sphericity of several pores is lower than 0.4, implying irregular pores at such a low VED. When the VED reaches 88.9 J/mm³, the sphericity of most pores (97.0 %) is larger than 0.7, indicating that the pores with a nearly round shape take the main portion, which is consistent with the observation on metallography
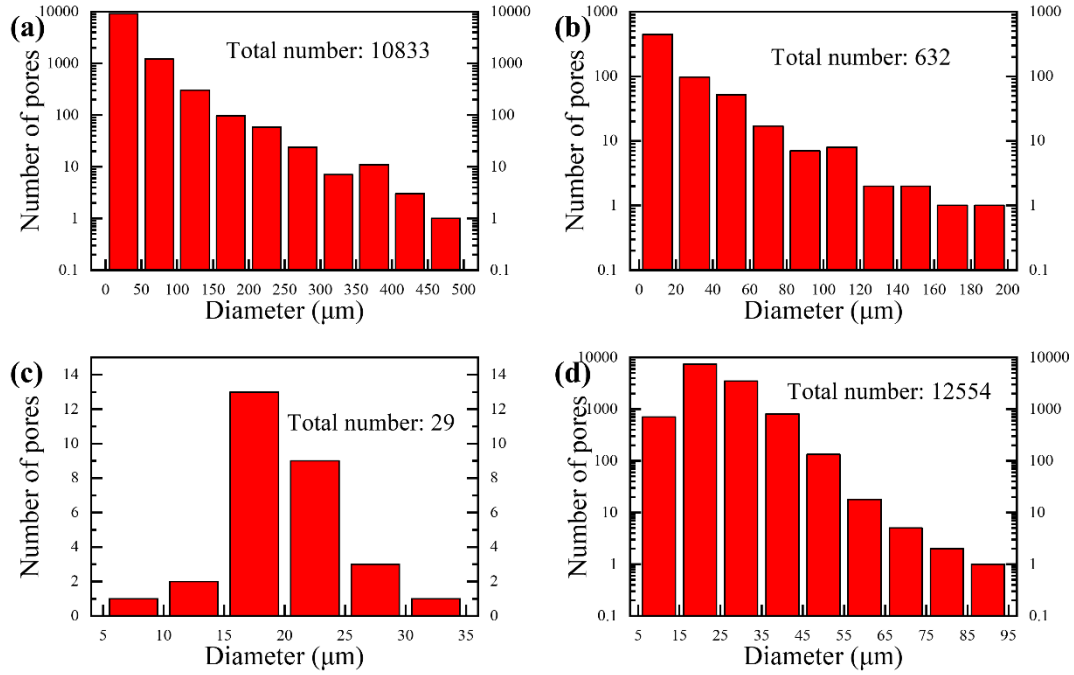
and 3D micro-CT images of the attendant keyhole pores.
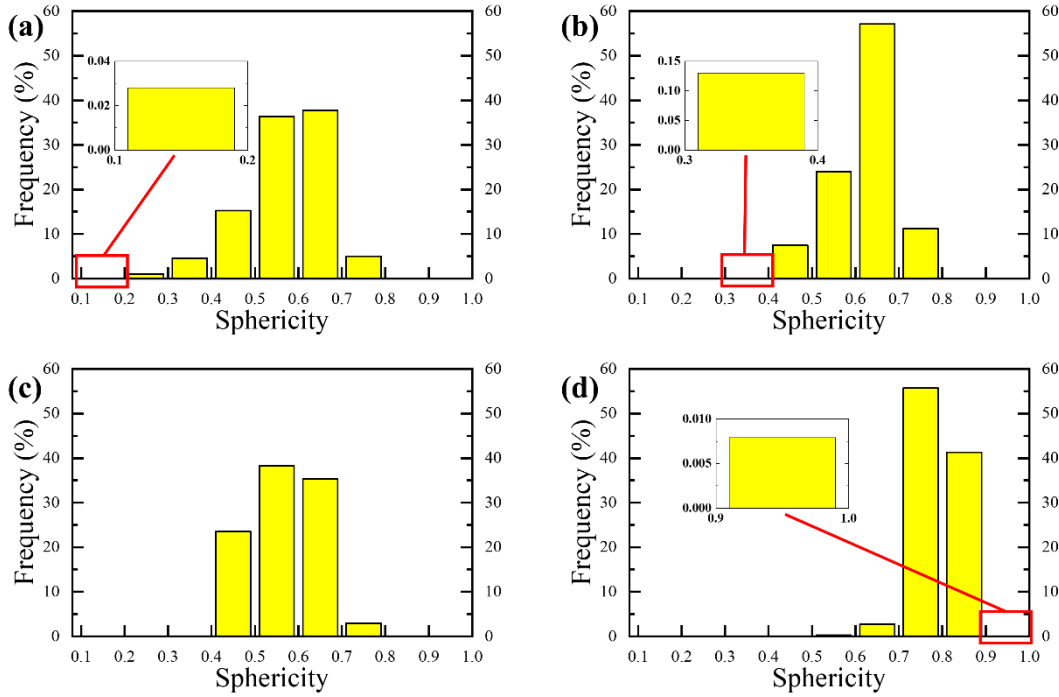
Figure 4.18. Sphericity distributions of the pores at the VEDs of (a) 29.6 J/mm³, (b) 44.4 J/mm³, (c) 59.3 J/mm³ and (d) 88.9 J/mm³.

4.2.3. Crack density

During the LPBF process, residual stress arises from the high thermal gradients induced by the rapid heating and cooling processes [14], and it is considered as the driving force of cracking. Cracks in IN738LC processed by LPBF are known as solidification crack [19]. The IN738LC alloy has a large solidification temperature range, inducing the liquid containing highly concentrated solutes to remain in the grain boundary regions at the last stage of solidification due to the segregation behaviour of solute atoms. The resultant liquid film's presence leads to the weakening of grain boundaries, where cracks occur and propagate under thermal stress. Figure 4.19 (a) shows the Von Mises stress distribution of the whole simulation field created using the method described in Section 3.7.2. It is apparent that the stress attains its maximum at

123

the corner of the contact area between the sample and the substrate. The predicted stress

is well below the alloy nominal yield strength, but their variations with position and

processing parameters are important and meaningful. To analyse how the processing

parameters affect the residual stress, this research investigates the stress distributions

along 2 lines of interest. The first line is the edge of the printed cube, and another is the

contact line between the sample and the substrate, as shown in Figure 4.19 (b). Figure

4.20 shows the distribution of the Von Mises stress along the Z (Line 1) and X directions

(Line 2) with different parameters. For the Z direction, the residual stress reaches its

maximum at the bottom and decreases with the increase of the height until ~ 0 MPa at

the top surface. For the X direction, the maximum stress is obtained at the start and end

points, respectively, and the stress attains its minimum at the middle point. Figure 4.21

depicts the crack density as a function of the processing parameters.
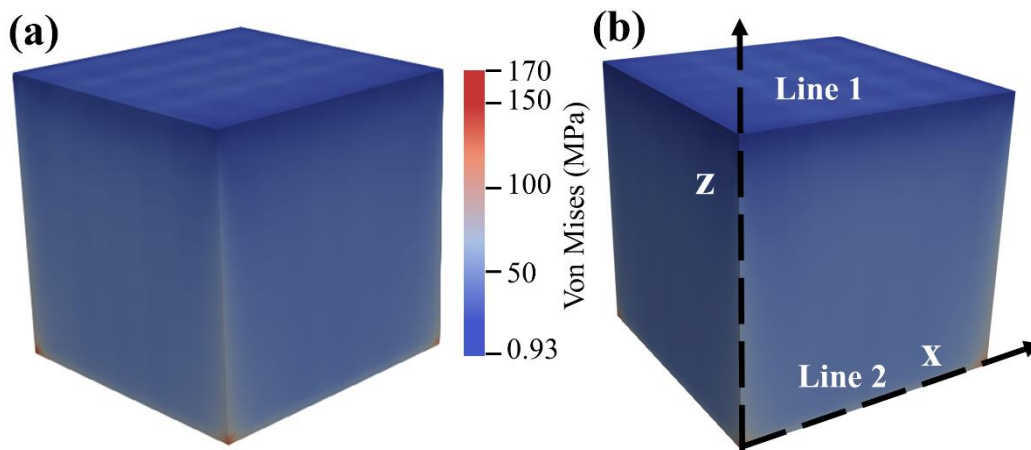
Figure 4.19. (a) Von Mises stress distribution of the printed part, (b) lines of interest for the residual stress analysis.
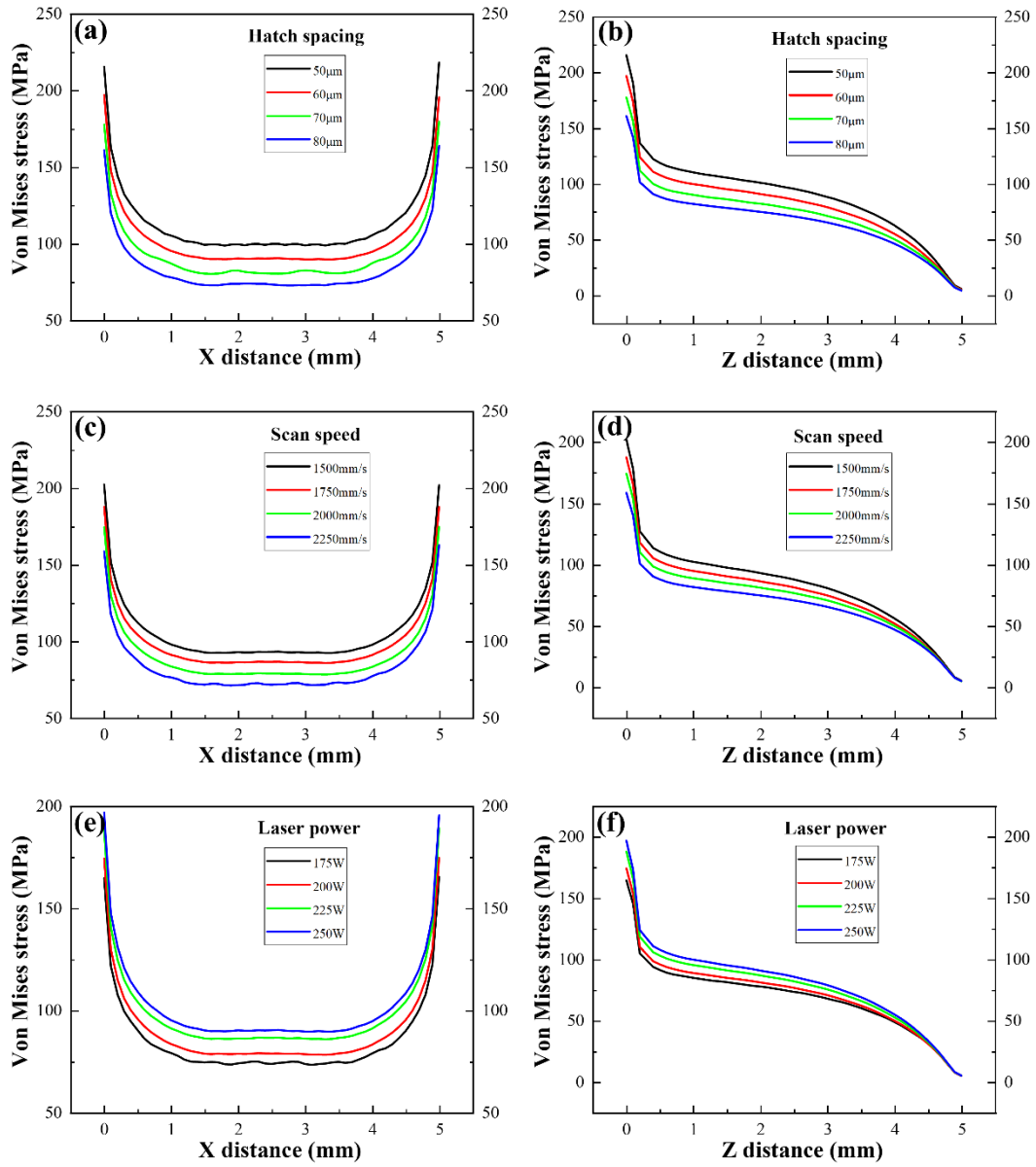
Figure 4.20. Von Mises stress distributions along the X and the Z directions as a function of (a, b) the hatch spacing (laser power 250 W, scan speed 2000 mm/s), (c, d) the scan speed (laser power 200 W, hatch spacing 60 µm), (e, f) the laser power (scan speed 2000 mm/s, hatch spacing 60 µm).
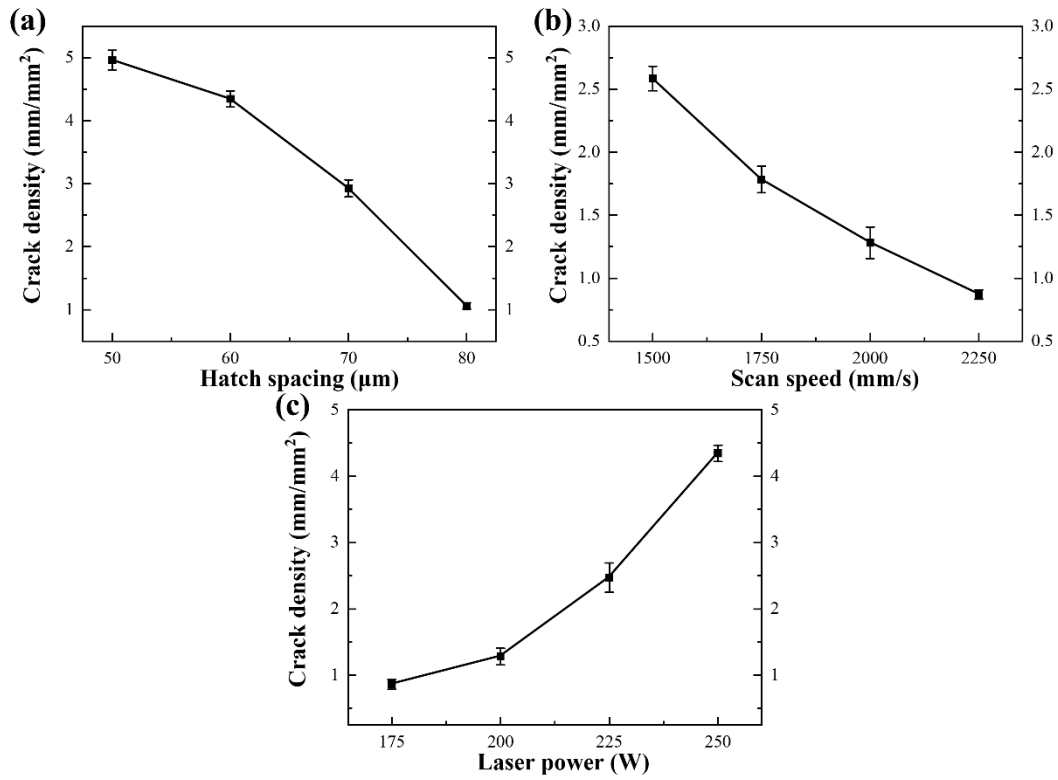
Figure 4.21. Crack density as a function of (a) the hatch spacing (laser power 250 W, scan speed 2000 mm/s), (b) the scan speed (laser power 200 W, hatch spacing 60 μm) and (c) the laser power (scan speed 2000 mm/s, hatch spacing 60 μm).

4.2.3.1. Effects of hatch spacing

Figures 4.20 (a) and 4.20 (b) show that the residual stress decreases in both X and Z directions as the hatch spacing increases. The top stress is 215.7 MPa at the hatch spacing of 50 μm and reduces to 197.1 MPa when the hatch spacing increases to 60 μm. As the hatch spacing increases from 70 μm to 80 μm, the top stress decreases from 177.8 MPa to 161.0 MPa. Similar to the residual stress, the crack density is negatively related to the hatch spacing from Figure 4.21 (a). When the laser power and the scan speed were fixed, Xia et al. [4] suggested that the decrease of the hatch spacing led to an increase of the thermal gradient between tracks, which accordingly increased the residual stress. Low hatch spacings are favourable to increase the working temperature

126

in the melt pool. Solidification behaviour is significantly relative to the melt's temperature. The estimated time for solidification was established by Gao et al. [20] as:

$$t_{solidification} = 2(\frac{a^2}{3\alpha})\ln(\frac{T_p - T_r}{T_f - T_r})$$
<div align="right">Equation 4.4</div>

where a is the radius of droplets, α is the thermal diffusivity, T_p is the melt pool's peak temperature, T_f is the fusion temperature, and T_r is the room temperature. Figure 4.22 depicts the relationship between $t_{solidification}$ and T_p as $a = 50$ μm, $\alpha = 4.87 \times 10^{-6}$ m^2/s, $T_t = 298$ K, and $T_f = 1628$ K for IN738LC [9]. The time for solidification is prolonged by the increase of the working temperature, implying that more liquid remains at grain boundaries within the same time for solidification, which increases the risk of cracking. Therefore, more cracks can be observed in the sample at low hatch spacings.
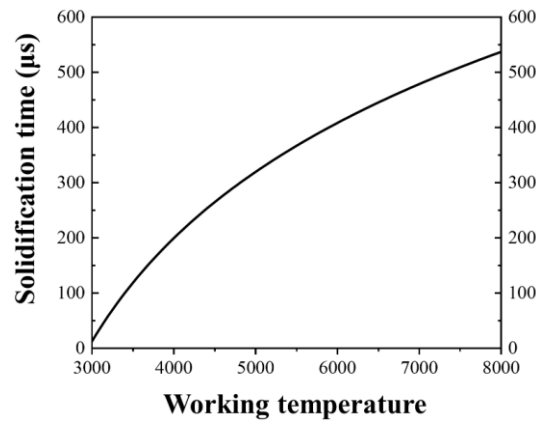
Figure 4.22. Solidification time as a function of working temperature.

4.2.3.2. Effects of scan speed

Figures 4.20 (c) and 4.20 (d) depict the relationship between the residual stress and the distance on the lines of interest in both X and Z directions. As the scan speed successively increases from 1500 mm/s to 2250 mm/s, the top stress decreases from 202.5 MPa to 158.7 MPa. Figure 4.21 (b) demonstrates a continuous decrease of the

crack density with the increase of the scan speed. The crack density decreases from 2.6 $\pm$ 0.1 mm/mm^2 to 0.9 $\pm$ 0.02 mm/mm^2 as the scan speed increases from 1500 mm/s to 2250 mm/s. Xia et al. [10] suggested that a low scan speed could increase the melt pool's working temperature, since the energy input density increased. A higher temperature results in a considerable amount of liquid at the last stage of solidification, unfavourable to the crack resistance. Besides, a high scan speed implies a reduction in the time interval between tracks, which increases the re-heating frequency on previously fabricated tracks and slows the heat transfer from the present track to solidified material, inducing a reduction in the thermal gradient and the resultant residual stress. Therefore, increasing the scan speed can effectively reduce the cracking tendency.

4.2.3.3. Effects of laser power

Figures 4.20 (e) and 4.20 (f) show the Von Mises stress distribution with different laser powers. It is evident that the residual stress increases with the increase of the laser power. The top stress increases from 174.5 MPa to 197.1 MPa as the laser power increases from 200 W to 250 W. The crack density also reaches its maximum value, 4.4 $\pm$ 0.1 mm/mm^2, at the power of 250 W and successively decreases as the laser power decreases. The increase of laser powder is favourable for a higher thermal gradient at a given hatch spacing and scan speed [12, 21], therefore, the attendant residual stress correspondingly increases. The increase of laser power indicates more energy penetration in the powder bed and enhances the thermal accumulation. It obtains a

128

relatively higher working temperature, which induces more remaining liquid in the grain boundary regions at the last stage of solidification. Thus, a relatively higher crack density occurs at high laser powers.

4.2.4. Volume energy density

Figure 4.23 depicts the summary of the effect of the VED on the surface roughness, the porosity and the crack density. Figures 4.23 (a) and 4.23 (b) show that the surface roughness and the porosity are quadratic to the VED, indicating both high and low VEDs can induce high surface roughness and porosity. Equations 4.5 and 4.6 can depict the relationship, and the correlation coefficients (R^2) are 0.9 and 0.8, respectively. A linear relationship between the crack density and the VED shows that the crack density increases with increasing the VED, as illustrated in Figure 4.23 (c). Equation 4.7 shows the corresponding fitting curve, with R^2 being 0.8.

$$\text{Surface roughness} \ = \ 0.005\psi^2 - \ 0.8\psi + \ 44.2 \qquad \text{Equation 4.5}$$

$$\text{Porosity} \ = \ 0.007\psi^2 - 1.1\psi + 38.5 \qquad \text{Equation 4.6}$$

$$\text{Crack density} \ = \ 0.1\psi - 5.2 \qquad \text{Equation 4.7}$$
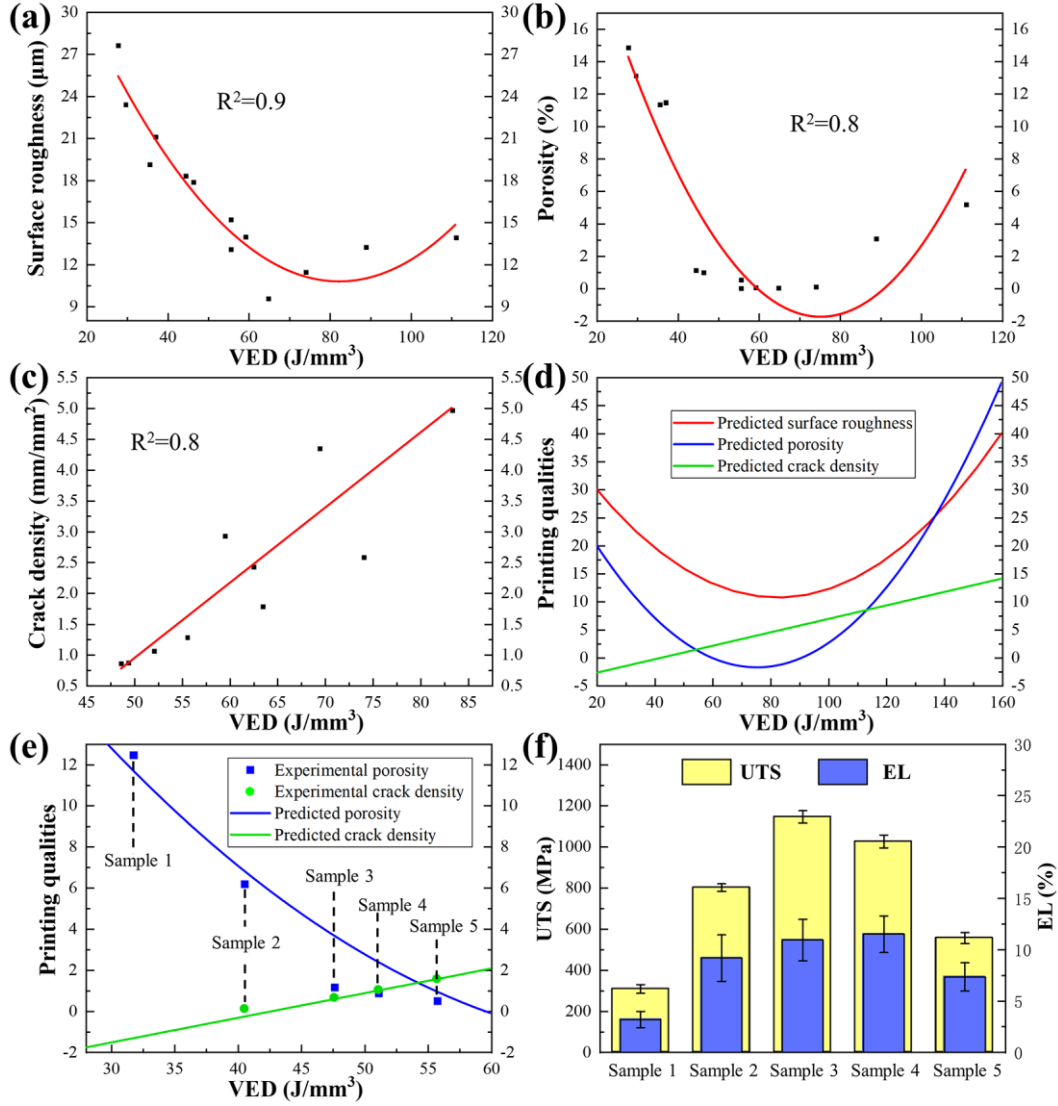
Figure 4.23. Relationship between the VED and (a) the surface roughness, (b) the porosity and (c) the crack density by regression analysis, (d) predicted surface roughness, porosity and crack density as a function of the VED, (e) comparison between the predicted and experimental results, (d) UTS and EL of the samples with different VEDs.

To find the optimal VED for the fabrication of IN738LC components with high properties, Figure 4.23 (d) summarises the predicted results as a function of the VED in terms of regression analysis. Surface roughness is not mentioned alone in the latter part, since it primarily affects the mechanical performances through pores, thus the analysis of porosity includes the effect of surface roughness. According to the experimental results, the porosity reaches the minimal value at the VED of ~ 55 J/mm^3

and keeps at this level until the VED increased to ~ 90 J/mm^3 and ~ 110 J/mm^3. It rises

to 3.1 ± 0.2 % and 5.2 ± 0.9 % due to the keyhole and humping phenomena,

respectively, with Figure 4.23 (d) predicting the crack density to continue increasing.

Therefore, the optimal properties should be obtained at the VED less than ~ 55 J/mm^3.

Another group of parameters is chosen randomly with the VED less than ~ 55 J/mm^3

to print metallographic observation and tensile testing samples, as listed in Table 4.3.

Figure 4.23 (e) shows a comparison between the predicted and experimental results. It

is apparent that the measured crack density fixes well with the predicted curve. The

measured porosity's trend is generally consistent with the predicted results, although

there are slight deviations. However, numerous pores in Sample 1 meant that it is

difficult to measure the crack density.

Table 4.3. Parameters used for the investigations on relationship between the porosity (crack density) and the mechanical properties.

Sample	Laser power (W)	Scan speed (mm/s)	Hatch spacing (μm)	VED (J/mm^3)
1	200	3000	70	31.8
2	175	1800	80	40.5
3	225	1750	90	47.6
4	230	2500	60	51.1
5	250	2300	65	55.7

Figure 4.23 (f) shows the ultimate tensile strength (UTS) and the elongation (EL)

of the testing samples with different VEDs. High porosity induces severe brittleness in

Sample 1, and the UTS and the EL are as low as 309.2 ± 21.6 MPa and 3.2 ± 0.8 %,

respectively. Both UTS and EL of Sample 2 increase as the VED increases from 31.8

J/mm^3 to 40.5 J/mm^3. Compared with Sample 2, the porosity decreases to 1.2 ± 0.1 %,

however, the crack density increases to 0.7 ± 0.03 mm/mm^2 in Sample 3. In this case,

the maximum UTS (1147.4 ± 30.1 MPa) is attained, and the EL also improves (11.1 ±

2.1 %). A further increase of the VED induces the porosity to decrease but the crack

density to increase, as indicated by Figure 4.23 (e). The EL of Sample 4 is 11.5 ± 1.8 %,

slightly higher than Sample 3, and drops to 7.4 ± 1.4 % at the VED of 55.7 J/mm^3

(Sample 5). However, the UTS shows a continuous downward trend for Samples 4

(1026.9 ± 31.3 MPa) and 5 (557.4 ± 26.8 MPa), indicating that cracks within this VED

range dominate the mechanical properties.

Cracks and pores can significantly affect the performances of materials related to

their amount, size and morphology, which must be carefully controlled depending on

the service conditions. In the current experimental condition, the VED of ~ 48 J/mm^3

is optimal for IN738LC during the LPBF process. The laser power and the scan speed

are considered to affect the printed parts by a similar mechanism through the energy

input. Under this VED, relatively high laser powers (~ 300 W) and scan speeds (~ 3000

mm/s) are not recommended due to the balling effect related to the Marangoni flow and

the Plateau-Rayleigh instability. The humping phenomenon induced by low hatch

spacings (~ 30 μm) must be avoided as well.

4.3. Summaries

Surface roughness increases with the increase of the hatch spacing in cases where

the hatch spacing is larger than 45 μm. The maximum surface roughness is 21.1 ± 2.3

μm at the hatch spacing of 90 μm and reaches its minimum (11.5 ± 0.8 μm) when the

hatch spacing is 45 μm. The surface roughness is higher at the hatch spacing of 30 μm

than that at 45 μm due to the micro-humping phenomenon. The surface roughness increases linearly with the scan speed's increase. The scan speed of 1000 mm/s corresponds to the minimum surface roughness, and the value is 13.2 ± 0.4 μm. This research finds a linear drop in the surface roughness with increasing the laser power from 150 W to 350 W.

Porosity increases with the increase of the hatch spacing and the scan speed, while considerably low hatch spacings and scan speeds also lead to increased porosity. High laser powers always induce better printing quality with a lower porosity in the current experimental condition investigated. Micro-CT identifies it can divide the pores into 2 categories: lack of fusion and keyhole. The pores due to the lack of fusion with irregular shapes occur at low VEDs. When the VED is high, it observes round keyhole pores scattering across the measured domain.

The stress distribution through simulation demonstrates that the stress attains its maximum at the corner of the contact area between the sample and the substrate. Both calculated residual stress and crack density increase with the decrease of the hatch spacing and the scan speed and decrease with decreasing the laser power.

Regression analysis indicates that both high and low VEDs can induce high surface roughness and porosity, and the crack density increases linearly with the VED. The VED of ~ 48 J/mm^3 is optimal for building IN738LC components by LPBF according to the mechanical property tests within the current experimental condition.

As mention in Section 2.6.1, the processing parameters are sensitive to the machines and the powder batches used, thus the optimised parameters and the process

window will deviate as the powders and the machines change. Due to the experimental conditions in this research, the optimal parameters are searched many times in the latter chapters using the method mentioned in this chapter since different machines or powder batches are used. In addition, compared with the pores, the cracks cannot be entirely eliminated using the parameter control method, thus some other approaches need to conduct in solving the cracking in IN738LC during LPBF.

4.4. References

[1] Rombouts M., J. P. Kruth, L. Froyen, P. Mercelis. (2006). Fundamentals of Selective Laser Melting of alloyed steel powders. CIRP Annals 55(1), 187-192.

[2] Zhou X., Liu X., Zhang D., Shen Z. and Liu W. (2015). Balling phenomena in selective laser melted tungsten. Journal of Materials Processing Technology, 222, 33-42.

[3] Tan C., K. Zhou, W. Ma, L. Min. (2018). Interfacial characteristic and mechanical performance of maraging steel-copper functional bimetal produced by selective laser melting based hybrid manufacture. Materials and Design, 155, 77-85.

[4] Xia M., D. Gu, G. Yu, D. Dai, H. Chen, Q. Shi. (2016). Influence of hatch spacing on heat and mass transfer, thermodynamics and laser processability during additive manufacturing of Inconel 718 alloy. International Journal of Machine Tools & Manufacture, 109, 147-157.

[5] Scipioni Bertoli, U., A. J. Wolfer, M. J. Matthews, J.-P. R. Delplanque, J. M. Schoenung. (2017). On the limitations of Volumetric Energy Density as a design

parameter for Selective Laser Melting. Materials and Design, 113, 331-340.

[6] Li C., Y. B. Guo, J. B. Zhao. (2017). Interfacial phenomena and characteristics between the deposited material and substrate in selective laser melting Inconel 625. Journal of Materials Processing Technology, 243, 269-281.

[7] Yadroitsev, I., A. Gusarov, I. Yadroitsava, I. Smurov. (2010). Single track formation in selective laser melting of metal powders. Journal of Materials Processing Technology, 210(12), 1624-1631.

[8] Rayleigh, L. (2010). On the instability of a cylinder of viscous liquid under capillary force. The London, Edinburgh, and Dublin Philosophical Magazine and Journal of Science 34(207), 145-154.

[9] Quested, P. N., R. F. Brooks, L. Chapman, R. Morrell, Y. Youssef, K. C. Mills. (2013). Measurement and estimation of thermophysical properties of nickel based superalloys. Journal of Materials Science and Technology, 25(2), 154-162.

[10] Xia M., D. Gu, G. Yu, D. Dai, H. Chen, Q. Shi. (2017). Porosity evolution and its thermodynamic mechanism of randomly packed powder-bed during selective laser melting of Inconel 718 alloy. International Journal of Machine Tools & Manufacture, 116, 96-106.

[11] Khairallah S. A., A. T. Anderson, A. Rubenchik, W. E. King. (2016). Laser powder-bed fusion additive manufacturing: Physics of complex melt flow and formation mechanisms of pores, spatter, and denudation zones. Acta Materialia, 108, 36-45.

[12] Li Y., D. Gu. (2014). Thermal behavior during selective laser melting of commercially pure titanium powder: Numerical simulation and experimental study.

Additive Manufacturing, 1-4, 99-109.

[13] Mumtaz K., N. Hopkinson. (2009). Top surface and side roughness of Inconel 625 parts processed using selective laser melting. Rapid Prototyping Journal, 15(2), 96-103.

[14] Kruth J. P., L. Froyen, J. Van Vaerenbergh, P. Mercelis, M. Rombouts, B. Lauwers. (2004). Selective laser melting of iron-based powder. Journal of Materials Processing Technology, 149(1-3), 616-622.

[15] Qiu C., C. Panwisawas, M. Ward, H. C. Basoalto, J. W. Brooks, M. M. Attallah. (2015). On the role of melt flow into the surface structure and porosity development during selective laser melting. Acta Materialia, 96, 72-79.

[16] King W. E., H. D. Barth, V. M. Castillo, G. F. Gallegos, J. W. Gibbs, D. E. Hahn, C. Kamath, A. M. Rubenchik. (2014). Observation of keyhole-mode laser melting in laser powder-bed fusion additive manufacturing. Journal of Materials Processing Technology, 214(12), 2915-2925.

[17] Fabbro R. (2010). Melt pool and keyhole behaviour analysis for deep penetration laser welding. Journal of Physics D: Applied Physics, 43(44), 1-9.

[18] Kasperovich G., J. Haubrich, J. Gussone, G. Requena. (2016). Correlation between porosity and processing parameters in TiAl6V4 produced by selective laser melting. Materials and Design, 105, 160-170.

[19] Cloots M., P. J. Uggowitzer, K. Wegener. (2016). Investigations on the microstructure and crack formation of IN738LC samples processed by selective laser melting using Gaussian and doughnut profiles. Materials and Design, 89, 770-

784.

[20] Fuquan Gao, Ain A. Sonin. (1994). Precise deposition of molten microdrops: the physics of digital microfabrication. Proceedings of the Royal Society of London A, 444, 533-554.

[21] Parimi L. L., R. G. A, D. Clark, M. M. Attallah. (2014). Microstructural and texture development in direct laser fabricated IN718. Materials Characterization, 89, 102-111.

Chapter 5 Single-track Testing: Pore Formation Mechanism

5.1. Introduction

In this chapter, single tracks of laser powder bed fusion (LPBF) for Inconel 738 LC (IN738LC) with different laser powers and scan speeds are used to investigate how the processing parameters influence the track behaviour such as track morphology, bead dimension and bead mode. In addition, bulk samples are built with the same parameters as the single-track testing to associate the track behaviour with the pore formation mechanism in the IN738LC parts during LPBF. Other parameters used to build the bulk samples are hatching space 50 μm, layer thickness 30 μm and Raster 90° scan strategy under no preheating condition. Table 5.1 presents the details of the parameters for the single-track testing.

Table 5.1. Parameters used for the single-track testing.

	500 mm/s	1000 mm/s	1500 mm/s	2000 mm/s	2500 mm/s
370 W	S21	S22	S23	S24	S25
290 W	S16	S17	S18	S19	S20
210 W	S11	S12	S13	S14	S15
130 W	S6	S7	S8	S9	S10
50 W	S1	S2	S3	S4	S5

5.2. Results

5.2.1. Single-track morphology

Figure 5.1 shows the morphology of the tracks built with different parameters on the basic blocks. According to the morphology, the tracks are classified into 4 types:

the wide-continuous track (WCT), the narrow-continuous track (NCT), the fluctuating track (FT) and the balling track (BT). The summary of the track types vs the processing parameters within the current processing conditions investigated is mapped in Figure 5.2.

The track with a width larger than 200 μm is defined as WCT. It exhibits a continuous and straight morphology, i.e., with almost uniform width along the whole scanning direction. At high magnification, as shown in Figure 5.3, a clear ripple shape going in the opposite direction to the laser beam is visible. The ripple morphology is primarily attributed to the surface tension, exerting a resultant shear force on the melt pool's liquid surface [1], which is affected by the processing parameters and the atmosphere in the building chamber [2]. The WCT appears at high laser powers, i.e., 370 W and 290 W and low scan speeds between 500 mm/s and 1500 mm/s.

The NCT covers a large range of the processing parameters in the upper left of the track type map in Figure 5.2. The track's width in this type is relatively small ~ 100 μm. The track shows a continuous and straight morphology deposited on the basic block with no ripple trace on the surface.

The FT only occurs at the combinations of the laser power of 290 W and the scan speed of 2500 mm/s (S20), the laser power of 210 W and the scan speed of 1500 mm/s (S13). In this type, the track fluctuates with a non-uniform width along the whole track length. Figure 5.4 also observes a discontinuity phenomenon of the track. The track loses its stability due to the track's periodic shrinkage [3] caused by the melt's lateral surface tension.

A low energy input density (laser power/scan speed), i.e., extremely low laser powers and/or high scan speeds, is favourable for the formation of BTs, as shown in the right bottom corner of Figure 5.2. The BT breaks up into small droplets, leading to a severe discontinuity of the track, as shown in Figure 5.1.
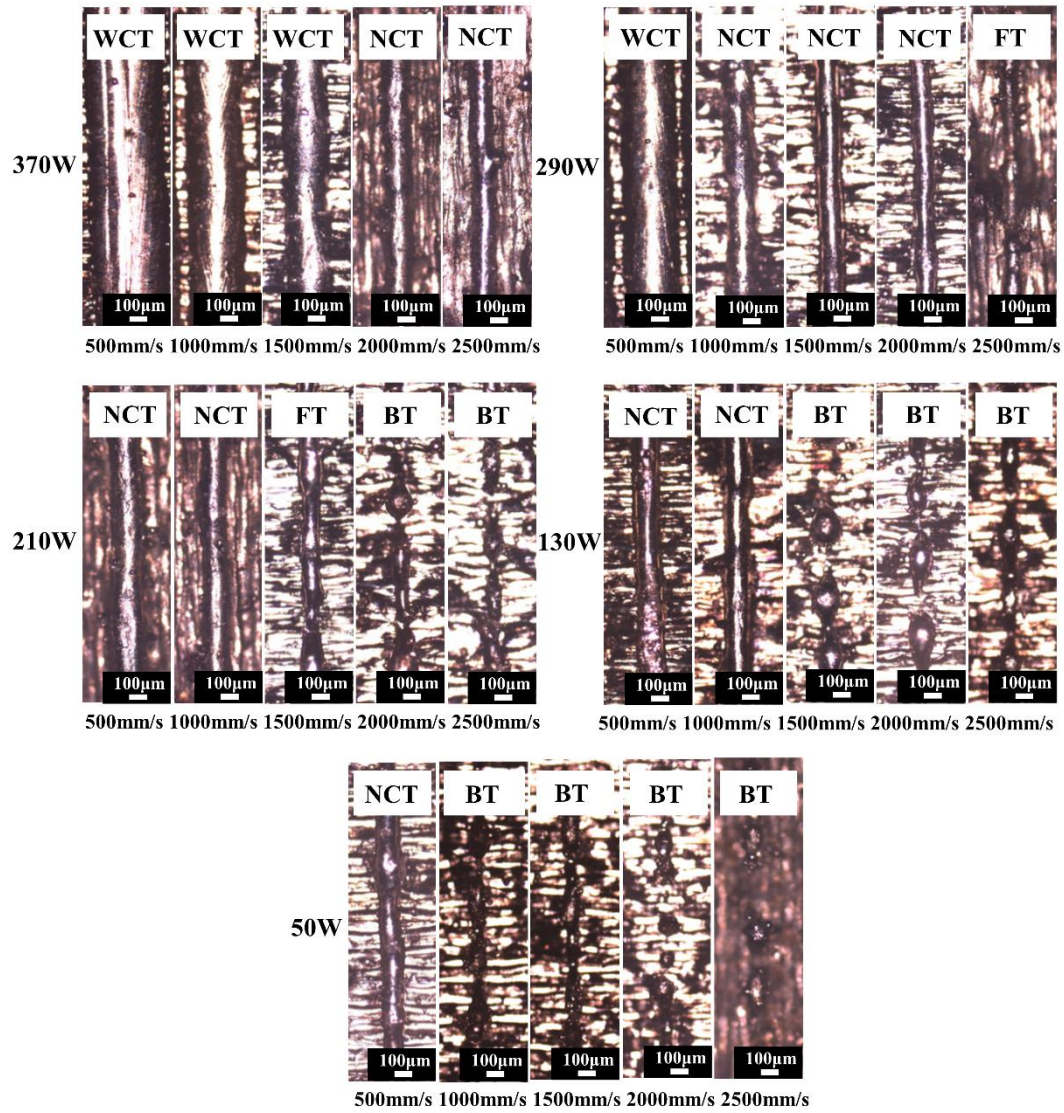
Figure 5.1. Optical microscope (OM) images of the 4 types of tracks, i.e., WCT, NTC, FT and BT in the 25 single-track tests using the laser powers of 50 W-370 W and the scan speeds of 500 mm/s-2500 mm/s.
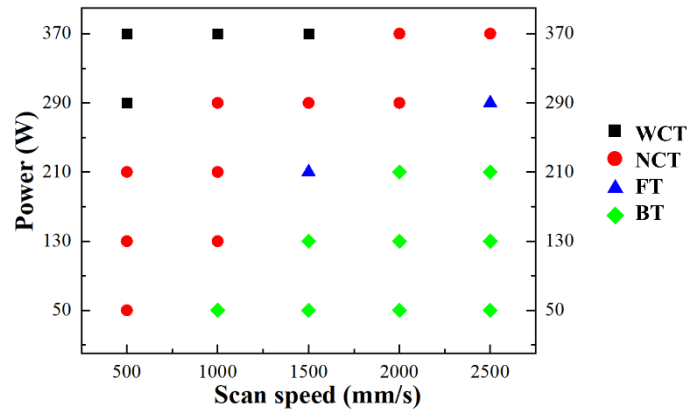
Figure 5.2. Map of the track types vs the processing parameters.
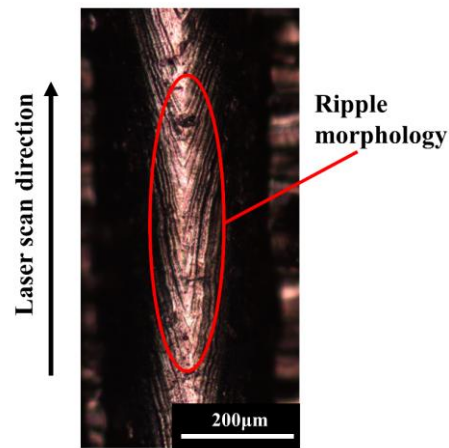
Figure 5.3. OM image of the WCT (S21) at high magnification showing the ripple morphology on the track surface.
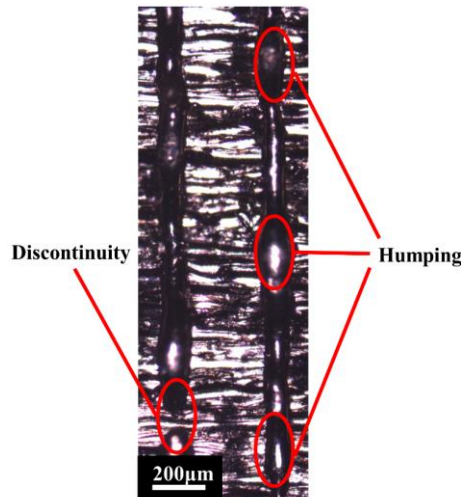
Figure 5.4. OM image of the FT (S13) showing the humping phenomenon and the discontinuity of the track.

141

5.2.2. Bead morphologies

Figure 5.5 shows the bead type's classification according to the track's cross-sections. The shape, the dimension and the wetting behaviour of the beads vary when applying different parameters. With the decrease of the laser power and/or the increase of the scan speed, the bead shape changes from a smooth morphology to necking down, balling, and finally, the bead detaches from the basic block. These beads are classified into 4 types: the wide-keyhole bead (WKB), the narrow-keyhole bead (NKB), the conduction bead (CB) and the shallow-ball bead (SBB), as shown in Figure 5.5. Figures 5.6 and 5.7 summarise the bead type as a function of the laser power and the scan speed within the current processing conditions investigated.
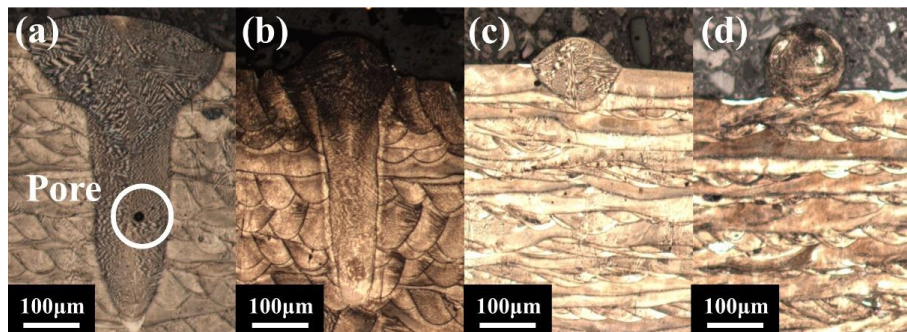
Figure 5.5. OM images of the 4 types of beads, i.e., (a) WKB, (b) NKB, (c) CB and (d) SBB.
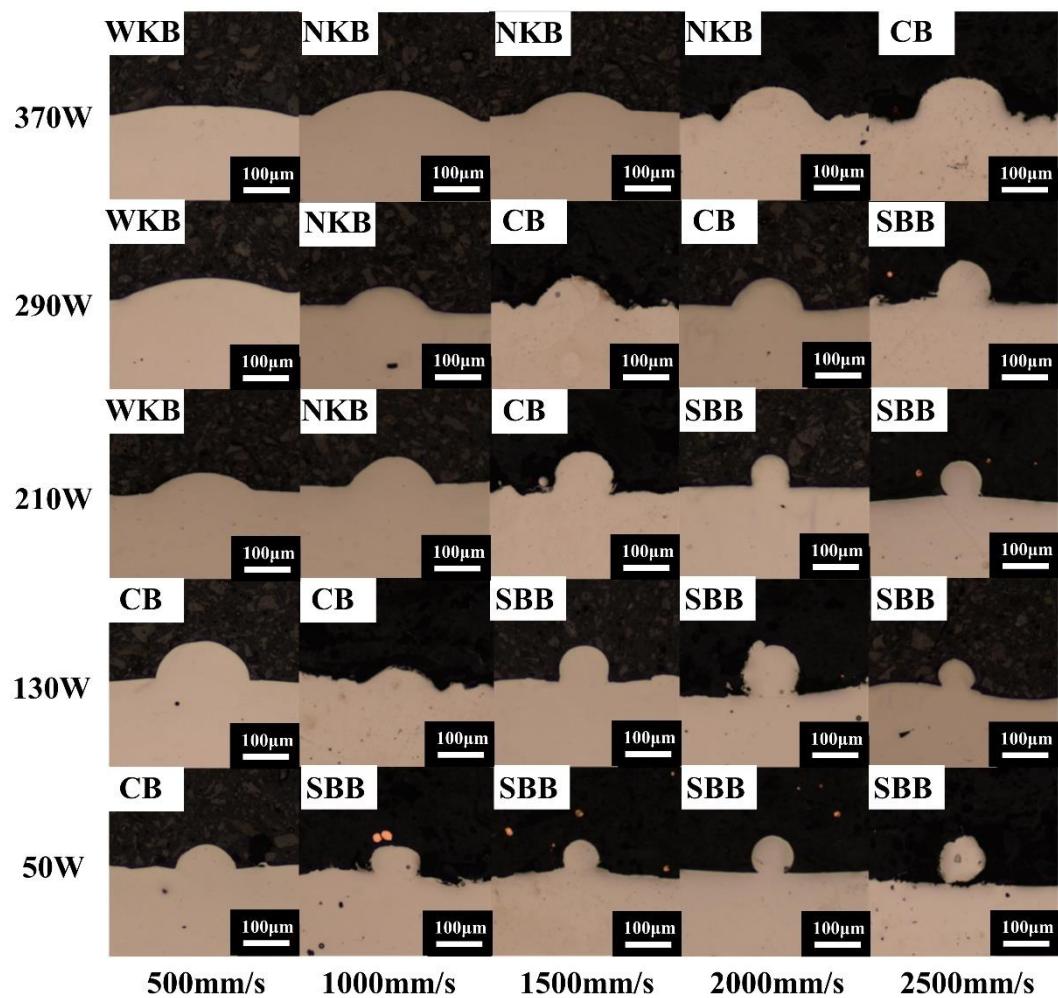
Figure 5.6. OM images of the 25 beads made by the laser powers of 50 W-370 W and the scan speeds of 500 mm/s-2500 mm/s.
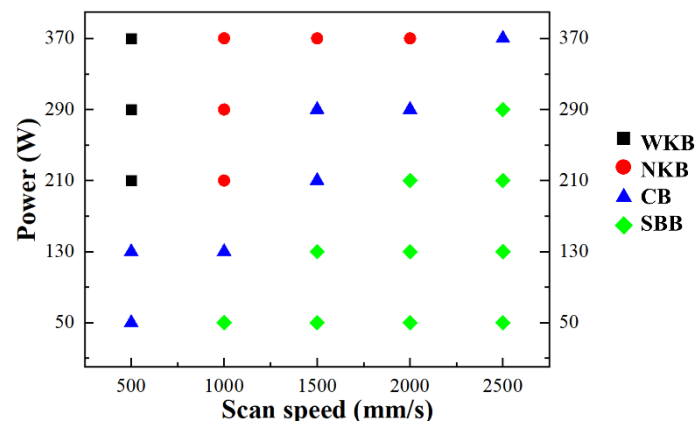
Figure 5.7. Map of the bead types vs the processing parameters.

The WKB occurs at high laser powers, i.e., 210 W-370 W with the minimum scan

speed of 500 mm/s. This type can separate the whole melt pool into 2 parts. The upper

part's width is ~ 150 % greater than that of the lower part, and the lower part is a keyhole

143

with a relatively deep and narrow morphology, as shown in Figure 5.5 (a).

The NKB is observed at the maximum laser power of 370 W with the scan speeds of 1000 mm/s-2000 mm/s, or when the scan speed is low, i.e., 1000 mm/s with the laser powers of 210 W-370 W. The bead in this type has a depth similar to that of the WKB and can also be separated into 2 parts, as shown in Figure 5.5 (b). The difference from the WKB is that the edge of the upper part of the NKB is nearly tangent to the lower part, with the top having a width of no more than 150 % of the lower part.

The CB appears when the scan speed and the laser power combine to give a moderate energy input density, i.e., high laser powers with high scan speeds or low laser powers with low scan speeds. The melt pool in the CB type is nearly elliptic with a short longitudinal length and a large width, as shown in Figure 5.5 (c).

The occurrence of SBB is associated with a relatively low energy input density, i.e., low laser powers with the combination of high scan speeds, as depicted in Figure 5.5 (d). The bead in this type has a round shape with poor wettability with the basic block. The "ball" touches the basic block with a relatively small area, resulting in a rather shallow and narrow melt pool. And the bead breaks away from the basic block at the laser power of 50 W and the scan speed of 2500 mm/s.

5.2.3. Bead dimensions

Figure 5.8 (a) shows the bead width as a function of the processing parameters. The bead width is the distance between the 2 contact points of the melt pool edge and the basic block, indicated by the insert picture of Figure 5.8 (a). It is apparent that the

144

bead width positively correlates to the laser power and negatively correlates to the scan speed. The bead width is considerably large when the laser powers are 290 W and 370 W at the scan speed of 500 mm/s. This is consistent with the WKB, whose upper part is extremely large in width.

The bead depth is the length from the top of the basic block to the bead's deepest point. Figure 5.8 (b) shows that the bead depth increases with the increase of the laser power and decreases with the increase of the scan speed. The bead depths at low scan speeds are larger than those at high scan speeds, especially for the moderate laser powers (210 W and 290 W), attributed to the keyhole formation in the lower part of the WKB and the NKB in these conditions.

The bead height is the length from the top of the basic block to the top of the bead. Figure 5.8 (c) suggests that there is no distinct relationship between the bead height and the processing parameters.

The contact angle is the average of the 2 angles between the basic block surface and the bead edge, as indicated by Figure 5.8 (d)'s insert picture. The contact angle increases with increasing the scan speed and decreases with increasing the laser power. The contact angles are larger than 90° at low laser powers with the combination of high scan speeds, indicating the bead's poor wettability with the occurrence of the SBB type. The maximum contact angle is 180° at the laser power of 50 W and the scan speed of 2500 mm/s, where the bead leaves from the basic block. It attains the smallest contact angle at the laser power of 370 W and the scan speed of 500 mm/s, and the corresponding value is ~ 26°.
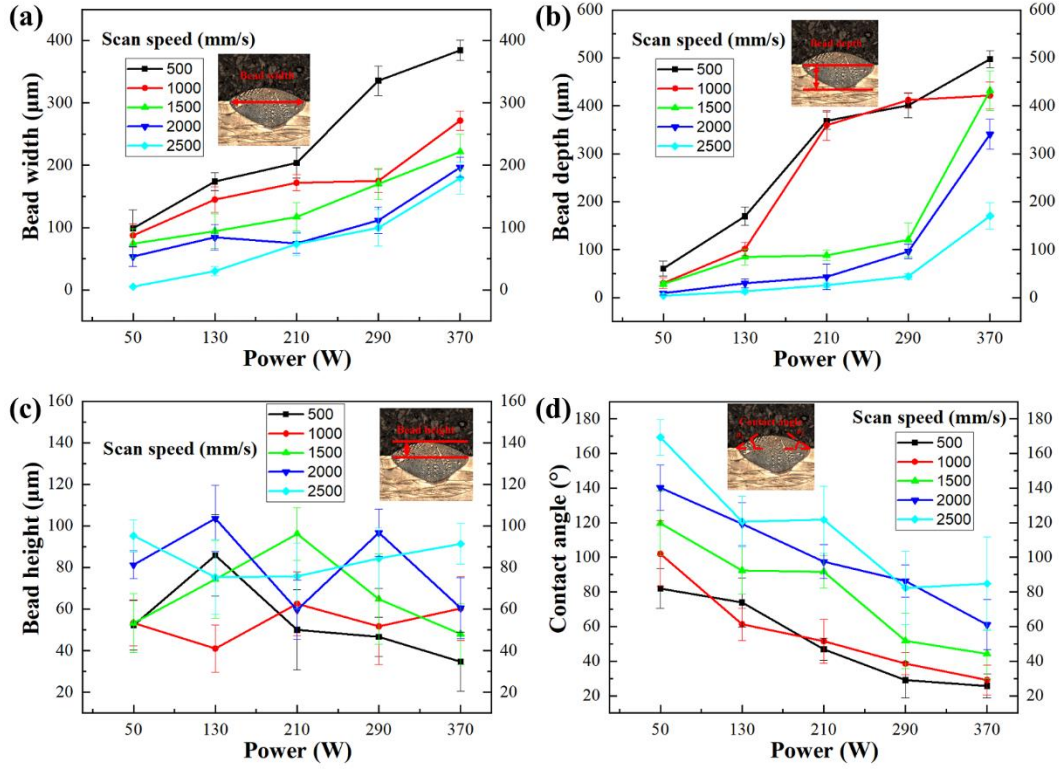
Figure 5.8. (a) The bead width, (b) the bead depth, (c) the bead height and (d) the contact angle as a function of the laser power at various scan speeds.

5.2.4. Pores of bulk samples

Figure 5.9 shows how the processing parameters have a great impact on pore conditions in the printed bulk samples. The pores with regular round shapes appear in the left top corner of the parameter map, i.e., high laser powers combined with low scan speeds (marked with yellow blocks). The sample at the scan speed of 500 mm/s and the laser power of 370 W fails to fabricate due to severe warping on the substrate. The maximum porosity is 11.0 ± 2.0 % at the scan speed of 500 mm/s and the laser power of 290 W among this condition. Green blocks mark off the parts of high quality with nearly full density in Figure 5.9, obtained at relatively moderate energy input densities, i.e., high scan speeds combine with high laser powers or low scan speeds combine with low laser powers. The parts occupy more than half the parameter map with irregular-

shape pores in the right bottom corner (marked with red blocks). Parts cannot be built

at high scan speeds (1500 mm/s-2500 mm/s) with the minimum laser power, i.e., 50 W.

A relatively low porosity of 0.1 ± 0.008 % is attained at 500 mm/s with the combination

of 130 W. While the part density at the scan speed of 1000 mm/s and the laser power of

50 W is almost only half (100 % - 45.7 % = 54.3 %).

Figure 5.9. OM images showing the metallographs of the pores vs the processing parameters and the corresponding porosity.

5.3. Discussions

5.3.1. Effects of parameters on track stability

Track characteristics can reflect the melt's flowing behaviour during the LPBF

process, which can directly determine the quality of the printed components. This

chapter studies a relationship between the track stability and the processing parameters. It is apparent in Figure 5.1 that the straight track becomes fluctuant and breaks into small droplets with the decrease of the laser power and/or the increase of the scan speed. It is described as the balling phenomenon during LPBF. There are 2 potential causes for the balling, known as the Rayleigh instability and the Marangoni convection regarding the melt flow process [4].

In the Rayleigh instability theory, the melt track is regarded as a liquid cylinder, and the critical condition for the instability is described as that the wavelength of the axial harmonic disturbance is larger than the cylinder's circumference, i.e., $\lambda/D > \pi$, as shown in Figure 5.10 (a), where D is the diameter, and λ is the wavelength. Under this unstable condition, Tian et al. [5] found that the cylinder would break up into metallic droplets to reduce the surface energy, leading to the balling phenomenon, as depicted in Figure 5.10 (b). Rombouts et al. [4] remarked that increasing the scan speed could increase the length to width ratio of the melt pool, and the Rayleigh instability's trend was further enhanced [6]. For example, S14 is in the BT type, and its scan speed is higher than that of S13, while S13 is in the FT type. In addition, by comparing S20 (FT, 290 W @ 2500 mm/s) with S15 (BT, 210 W @ 2500 mm/s), it is apparent that decreasing the laser power also favours the Rayleigh instability's formation. This is ascribed to the decrease of the track width D with decreasing the laser power (Figure 5.8 (a)), inducing an increase of λ/D and accordingly aggravating the Rayleigh instability.
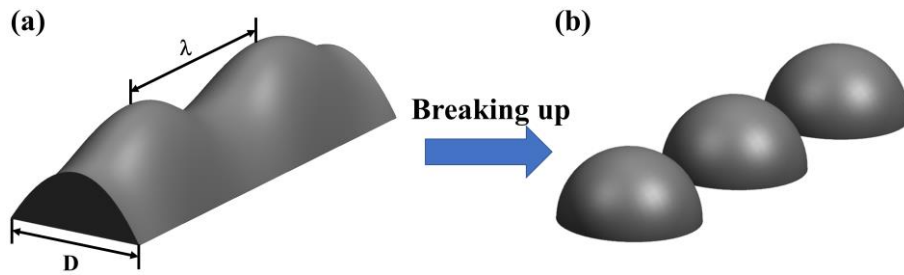
148

Figure 5.10. Schematic diagram showing the development process of the Rayleigh instability.

Apart from the Rayleigh instability, the Marangoni convection in the melt pool also contributes to balling in LPBF [7]. The Marangoni convection happens when the melt flows from the region with low surface tension to the region with high surface tension, driven by the thermal-capillary motion [4]. The Marangoni flow's direction is determined by the surface tension's gradient to the temperature $d\gamma/dT$. Generally, the value of $d\gamma/dT$ is negative, implying that high temperature results in low surface tension. The melt pool's temperature at the centre is always higher than the edge region, inducing the melt to flow from the centre to the edges, and the mass transfer of the melt to the neighbouring tracks forms in most cases. If the Marangoni convection's direction changes from the edge to the centre, the resultant big agglomeration of the melt leads to an obvious stacking on the top surface of the pool, which results in the balling, as depicted in Figure 5.11 (a). The Marangoni flow's directional change results from a high content of surface-active elements, such as oxygen [7] and sulphur [4], which can significantly reduce the surface intension, making $d\gamma/dT$ change to a positive value and relevantly causing the balling phenomenon. And this type of balling is believed to be significantly affected by the processing parameters in LPBF [8] and materials' natural properties like thermal conductivity [9]. Figure 5.11 (b) presents an example showing a clear trace of the Marangoni flow at the bottom of the melt pool (S20, scan speed
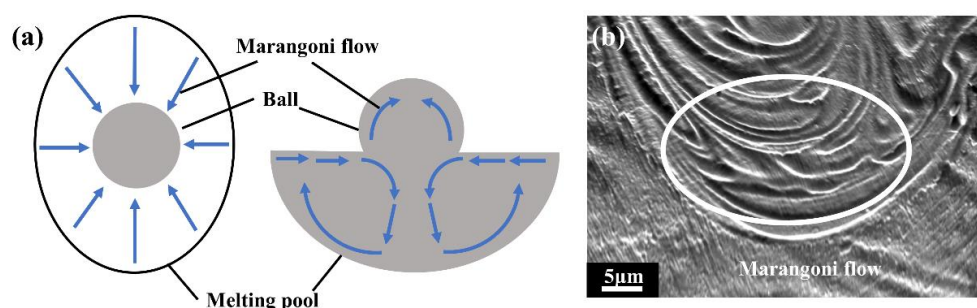
2500 mm/s).

Figure 5.11. (a) Schematic diagram showing the formation mechanism of the balling due to the Marangoni flow, (b) scanning electron microscope (SEM) image of the Marangoni flow trace at the bottom of the melt pool (S20, scan speed 2500 mm/s).

5.3.2. Effects of parameters on bead dimension

Figure 5.6 shows that as the scan speed increases and/or the laser power decreases, the bead's penetration becomes less, and then lateral shrinking happens. Finally, the bead no longer penetrates the basic block at the maximum scan speed combined with the minimum laser power.

As seen in Figures 5.8 (a) and 5.8 (b), both bead depth and width positively correlate to the laser power and negatively correlate to the scan speed. This is ascribed to that the combination of low scan speeds and high laser powers induces a higher energy input per unit length, increasing the working temperature, thus favouring the formation of a broader and deeper melt pool [10].

For bead height, low laser powers and high scan speeds are unfavourable to a good wettability of the bead with the basic block [5], contributing to a large bead height. However, when the laser power is lower and the scan speed is higher, a relatively small number of the powders melt by the laser beam due to the low energy input density,

150

leading to a decrease of the bead height. Due to the opposite effects of these 2 factors, the bead height is independent of the processing parameters.

The contact angle can directly reflect the wettability of the bead. At low laser powers and/or high scan speeds, the contact angle increases, indicating a low wettability of the bead. The working temperature in the melt pool decreases with decreasing the energy input density. The viscosity of the melt in the pool is temperature-dependent, and lower energy input density is likely to lead to cooler liquid with correspondingly higher viscosity [11], which induces a poor flowability of the melt, obtaining a high contact angle. In addition, by comparing Figures 5.2 and 5.7, the BTs always present accompanied by the SBBs with contact angles larger than 90°, implying that the track loses its stability by the balling phenomenon, which is consistent with Davis' theory [12]. Davis suggested that the molten droplet was stable when the contact angle was less than 90° and unstable when it exceeded 90°. The FTs have the contact angles slightly larger than 90°. For instance, the contact angles of S13 and S20 are $91.7 \pm 9.4°$ and $91.3 \pm 21.3°$, respectively, indicating that the track's fluctuation is a transitional condition before the balling.

5.3.3. Spreading vs solidification

The balling phenomenon is considered a competitive process between the spread and solidification processes of molten liquid, controlled by the capillary force and the heat loss during LPBF. Figure 5.12 demonstrates how a droplet attaches to a solid surface with the irradiation of a laser beam. The droplet solidifies with a solidification

angle θ_a and spreads with a spread angle θ_b on a solid basis. As the wetting behaviour continues, θ_b decreases as the droplet spreads on the solid surface, and θ_a correspondingly increases due to that the melt is solidifying. It stops when θ_a is equal to θ_b, and the whole bead forms. It is reasonable to infer that if the melt can spread out on the basic block before it solidifies, then it may avoid balling, thus obtaining a smooth surface and a stable track. It requires the solidification time to be greater than the spread time.
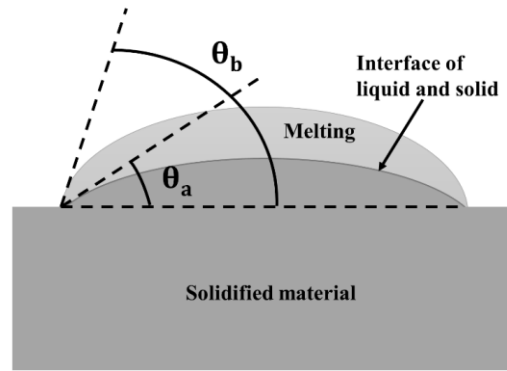

Figure 5.12. Schematic diagram demonstrating the competitive relationship between the spread and the solidification of a droplet.

The model of the time for a droplet to spread on a surface is known as [7]:

$$t_{spread} = (\frac{\rho_m a^3}{\gamma})^{0.5} \qquad \text{Equation 5.1}$$

where ρ_m is the melting density, a is the droplet's radius, and γ is the surface tension.

And the time for solidification was established by Gao et al. in 1994 [13] as:

$$t_{solidification} = 2(\frac{a^2}{3\alpha})\ln(\frac{T_p - T_r}{T_f - T_r}) \qquad \text{Equation 5.2}$$

where a is the droplet's radius, α is the thermal diffusivity, T_p is the peak temperature, T_f is the fusion temperature, also known as liquidus temperature, and T_r is the room temperature. The well-known Rosenthal equation [14, 15] related to different laser

powers and scan speeds for a point heat source to move in the X-direction can obtain T_p:

$$T_p(x,r) = T_0 + \frac{AP}{2\pi k}(\frac{1}{r})\exp[-\frac{v}{2\alpha}(r+x)]$$ Equation 5.3

where T_0 is the initial temperature, A is the absorptivity of powder, k is the thermal conductivity, P is the laser power, v is the scan speed, and r is the distance from the beam location to the point of interest as $r = \sqrt{x^2 + y^2 + z^2}$. In this model, a is usually ~ 50 μm. It selects the average peak temperature point right between the laser beam and droplet edge, i.e., $r = x = 25$ μm. T_0 is equal to T_f, showing that the laser beam irradiates on melt as it moves in the scanning direction during the wetting process. Table 5.2 gives other relevant material properties and temperatures. Figure 5.13 shows the calculated solidification time versus the contact angle.

Table 5.2. Constants used in the calculation of the solidification time and the spread time [16-18].

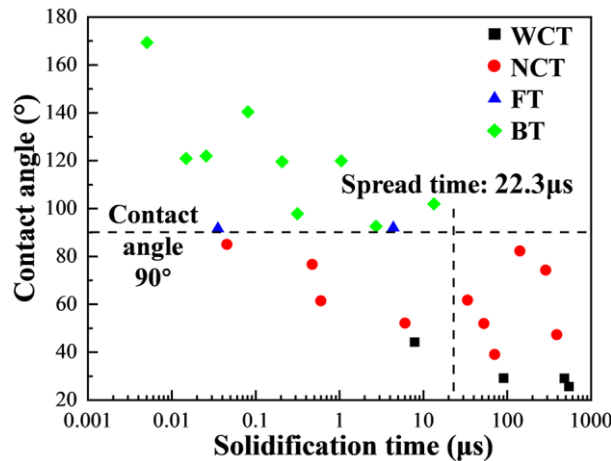| ρ_m (kg/m^3)	γ (N/m)	α (m^2/s)	k (W/m·K)	A	T_f(K)	T_r (K)
7324	1.85	4.87×10^{-6}	24.9	0.72	1628	298

Figure 5.13. Relationship between the contact angle and the solidification time. The spread time and the critical contact angle are marked with dotted lines.

The contact angle increases with the decrease of the solidification time. The decrease of the solidification time implies that the time for molten droplets to spread

on the basic block correspondingly reduces, leading to an increased contact angle. Equation 5.1 calculates the spread time to be 22.3 μs. Figure 5.13 demonstrates that the predicted solidification times of the FTs and the BTs are less than 22.3 μs, therefore the droplets with these parameters solidify before they spread on the basic block, thus losing their stability by fluctuating and balling. The solidification time and the contact angle are significantly influenced by the temperature and the fluid dynamic behaviour in the melt pool. By carefully selecting the processing parameters, a stable track is obtainable to avoid defects such as balling, low overlap and pores in printed components.

5.3.4. Keyhole and conduction mode transition

Keyhole mode has been widely studied in the welding process of metals [19]. The keyhole occurs when the energy input densities are high enough to induce material vaporisation, and a recoil force is exerted on the molten material to form a cavity [20, 21]. The keyhole's formation improves the laser beam's efficiency due to the multiple reflections in the cavity [22]. However, it is considered as an unstable condition of the melt pool and a cause of pores, as indicated by the circle in Figure 5.5 (a), which should be prevented in this case [20]. Figure 5.14 presents the formation mechanism of the keyhole pore. A considerably high working temperature induced by a high energy density causes substantial metallic vaporisation and generates recoil pressure towards the melt pool, as shown in Figure 5.14 (a). Once the recoil pressure exceeds the hydrostatic pressure and the surface tension, it presses downward the molten liquid to

154

the melt pool's bottom. As a result, the melt pool is relatively deep and narrow, as depicted in Figure 5.14 (b). Subsequently, the downwards flow driven by the recoil pressure, the gravity and the upwards flow driven by the surface tension collide and induce inward collapse to generate with the participation of the hydrostatic pressure at the keyhole's waists, as shown in Figure 5.14 (c). The collapsed molten liquid on both sides joints together, and strong metallic bonding forms after solidification, leaving a large void with vapour entrapping at the bottom of the keyhole, see Figure 5.14 (d).
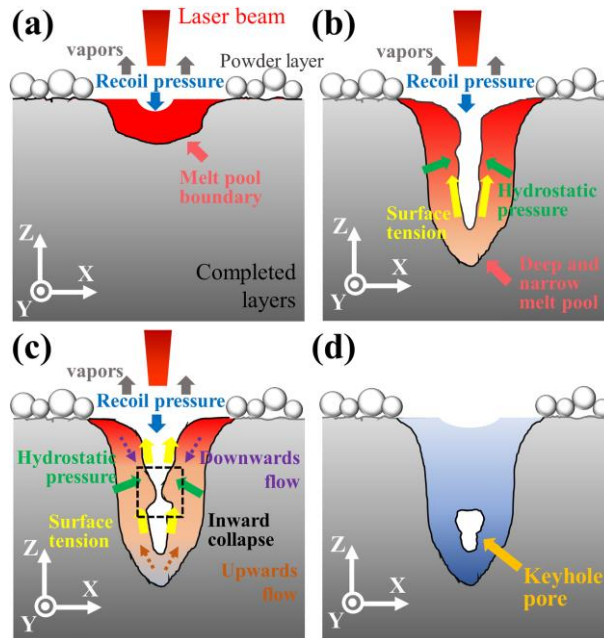
Figure 5.14. Schematic diagram showing the formation mechanism of a keyhole pore.

Previous studies explore the physical basis of the keyhole mode and the conduction mode transition [20]. By investigating different materials and welding parameters, Hann et al. [23] found that the bead depth normalised by the beam radius was a function only of the ratio of the deposited energy density to the enthalpy for melting. They calculate the normalised energy density as [24]:

$$\frac{\Delta H}{h_s} = \frac{2^{3/4} AP}{h_s \sqrt{\pi \alpha v R^3}}$$

Equation 5.4

where ΔH is the deposited energy density, A is the absorptivity of powder, α is the thermal diffusivity, P is the laser power, v is the scan speed, R is the radius of the laser beam, and h_s is the enthalpy at melting. The bead depth normalised by the beam radius is $D_m / \sqrt{\alpha R / v}$, and D_m is the bead depth. Table 5.3 lists other relevant material properties and the laser beam sizes. Similar to Hann et al. [22], Figure 5.15 shows the bead depth normalised by the beam size against the normalised enthalpy. The SBBs have a relatively low normalised bead depth below 10. The corresponding normalised enthalpy is also at a low level. When the value of normalised enthalpy increases gradually to ~ 50, the bead type changes from the conduction mode to the keyhole mode. Hence, when the deposited energy is ~ 50 times larger than the enthalpy for melting, the keyhole mode occurs for IN738LC during the LPBF process.

Table 5.3. Constants used in the calculation of the normalized enthalpy [15, 17, 25].

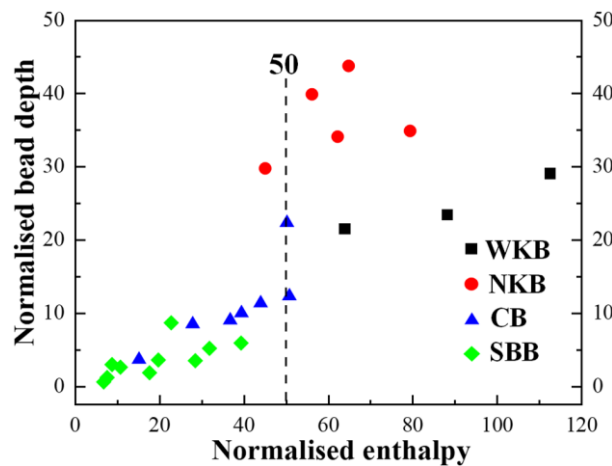| ρ (kg/m³)	α (m²/s)	h_s (J/g)	A	R (µm)
8177	4.87×10⁻⁶	1071.8	0.72	30

Figure 5.15. Relationship between the bead depth normalized by beam size and the normalized enthalpy. The critical value for the occurrence of the keyhole is marked with a dotted line.

5.3.5. Track behaviour vs pore

Stability is achieved in the condition of continuous tracks (WCTs and NCTs), as shown in Figure 5.1, and the overlapping between tracks is adequate, ensuring the full melt of powders. However, Figures 5.2 and 5.7 show that a large proportion of the continuous tracks occur accompanying with the keyhole beads (WKBs, NKBs). Here, many keyhole pores appear, as shown in Figure 5.9. On the contrary, the low energy input density results in BTs and SBBs. On the one hand, low bead width and the track instability can induce low overlapping between tracks, on the other hand, the balling hinders the continuity of the melt within a single laser track, both of which lead to irregular-shape pores attributed to un-melted powders or lack of fusion. The parts with high quality are obtained in the overlap of NCTs and CBs in Figures 5.2 and 5.7, such as S6 and S18. Among these parameters, moderate energy input density favours the stability of the melt track, and the keyhole pores and the lack of fusion are effectively avoided. Considering the part quality and the fabrication efficiency, the parameters with high scan speeds such as S19 (290 W @ 2000 mm/s) and S25 (370 W @ 2500 mm/s), are believed to be more desirable for the part fabrication in the current LPBF system.

5.4. Summaries

The tracks are classified into 4 types: WCT, NCT, FT and BT, regarding their morphology and stability. The continuous (stable) tracks appear at high energy input densities. When energy input densities are low, the track fluctuates and breaks into metallic droplets.

The bead width and depth increase with the increase of the laser power and decrease with the increase of the scan speed due to different energy input densities. The bead height is independent of the processing parameters. The contact angle decreases with increasing the energy input density, indicating a good wettability. The contact angle for the fluctuating and balling tracks is greater than 90°.

It proposes a model for a competitive process between the spread and the solidification of the melt to justify the relationship between the balling and the processing parameters. It suggests that if the solidification time is less than the spread time, i.e., the molten droplet solidifies before it spreads out on the basic block, the balling correspondingly forms.

It classifies the beads into 4 types: WKB, NKB, CB and SBB. The normalised bead depth increases with the normalised enthalpy. When the deposited energy is ~ 50 times greater than the enthalpy for melting, the bead changes from the conduction mode to the keyhole mode.

Both high and low energy densities can lead to high porosity in bulk samples due to the keyhole pores and the un-melted powders, respectively.

5.5. References

[1] Mumtaz K., N. Hopkinson. (2009). Top surface and side roughness of Inconel 625 parts processed using selective laser melting. Rapid Prototyping Journal, 15(2), 96-103.

[2] Masmoudi A., R. Bolot, C. Coddet. (2015). Investigation of the laser–powder–

atmosphere interaction zone during the selective laser melting process, Journal of Materials Processing Technology, 225, 122-132.

[3] Gunenthiram V., P. Peyre, M. Schneider, M. Dal, F. Coste, R. Fabbro. (2017). Analysis of laser-melt pool-powder bed interaction during the selective laser melting of a stainless steel, Journal of Laser Applications, 29(2), 1-8.

[4] Rombouts M., J. P. Kruth, L. Froyen, P. Mercelis. (2006). Fundamentals of Selective Laser Melting of alloyed steel powders, cirp annals-manufacturing technology, 55(1), 187-192.

[5] Tian Y., D. Tomus, P. Rometsch, X. Wu. (2017). Influences of processing parameters on surface roughness of Hastelloy X produced by selective laser melting, Additive Manufacturing, 13, 103-112.

[6] Tomus D., T. Jarvis, X. Wu, J. Mei, P. Rometsch, E. Herny, J. F. Rideau, S. Vaillant. (2013). Controlling the Microstructure of Hastelloy-X Components Manufactured by Selective Laser Melting, Physics Procedia, 41, 823-827.

[7] Zhou X., X. Liu, D. Zhang, Z. Shen, W. Liu. (2015). Balling phenomena in selective laser melted tungsten, Journal of Materials Processing Technology, 222, 33-42.

[8] Li Y., Gu D. (2014). Thermal behavior during selective laser melting of commercially pure titanium powder: Numerical simulation and experimental study, Additive Manufacturing, 1-4, 99-109.

[9] Tan C., K. Zhou, W. Ma, L. Min. (2018). Interfacial characteristic and mechanical performance of maraging steel-copper functional bimetal produced by selective

laser melting based hybrid manufacture, Materials and Design, 155, 77-85.

[10] Li C., Y. B. Guo, J. B. Zhao. (2017). Interfacial phenomena and characteristics between the deposited material and substrate in selective laser melting Inconel 625, Journal of Materials Processing Technology, 243, 269-281.

[11] Xia M., D. Gu, G. Yu, D. Dai, H. Chen, Q. Shi. (2017). Porosity evolution and its thermodynamic mechanism of randomly packed powder-bed during selective laser melting of Inconel 718 alloy, International Journal of Machine Tools & Manufacture, 116, 96-106.

[12] Schiaffino S., A. A. Sonin. (1997). Formation and stability of liquid and molten beads on a solid surface, Journal of Fluid Mechanics, 343, 95-110.

[13] Gao F., Ain A. Sonin. (1994). Precise deposition of molten micro drops: the physics of digital microfabrication, Proceedings of the Royal Society of London A, 444, 533-554

[14] D. Rosenthal. (1946). The theory of moving source of heat and its application to metal treatments, Transactions of the American Society of Mechanical Engineering Nov 1964, 849-866

[15] Plotkowski A., M. M. Kirka, S. S. Babu. (2017). Verification and validation of a rapid heat transfer calculation methodology for transient melt pool solidification conditions in powder bed metal additive manufacturing, Materials and Design, 18, 256-268.

[16] Tolochko N. K., Y. V. Khlopkov, S. E. Mozzharov, M. B. Ignatiev, T. Laoui, V. I. Titov. (2000). Absorptance of powder materials suitable for laser sintering, Rapid

Prototyping Journal, 6(3), 155-161.

[17] Quested P. N., R. F. Brooks, L. Chapman, R. Morrell, Y. Youssef, K. C. Mills. (2013). Measurement and estimation of thermophysical properties of nickel-based superalloys, Journal of Materials Science and Technology, 25(2), 154-162.

[18] Ragnhild E. Aune, Livio Battezzati, Robert Brooks, Ivan Egry, Hans-Jörg Fecht, Jean-Paul Garandet, Miyuki Hayashi1, Ken C. Mills, Alberto Passerone, Peter N. Quested, Enrica Ricci, Frank Schmidt-Hohagen, Seshadri Seetharaman, Bernard Vinet, Rainer K. Wunderlich. (2005). Thermophysical properties of IN738LC, MM247LC and CMSX-4 in the liquid and high temperature solid phase. 6th International Symposium on Superalloys 718, 625, 706, 625-706.

[19] Fabbro R. (2010). Melt pool and keyhole behavior analysis for deep penetration laser welding, Journal of Physics D: Applied Physics, 43, (44), 1-9.

[20] King W. E., H. D. Barth, V. M. Castillo, G. F. Gallegos, J. W. Gibbs, D. E. Hahn, C. Kamath, A. M. Rubenchik. (2014). Observation of keyhole-mode laser melting in laser powder-bed fusion additive manufacturing, Journal of Materials Processing Technology, 214(12), 2915-2925.

[21] Kasperovich G., J. Haubrich, J. Gussone, G. Requena. (2016). Correlation between porosity and processing parameters in TiAl6V4 produced by selective laser melting, Materials and Design, 105, 160-170.

[22] Rai R., J. W. Elmer, T. A. Palmer, T. DebRoy. (2007). Heat transfer and fluid flow during keyhole mode laser welding of tantalum, Ti–6Al–4V, 304L stainless steel and vanadium, Journal of Physics D: Applied Physics, 40(18) 5753-5766.

[23] Hann D. B., J. Iammi, J. Folkes. (2011). A simple methodology for predicting laser-weld properties from material and laser parameters. Journal of Physics D: Applied Physics, 44(44), 445401.

[24] Rubenchik A. M., W. E. King, S. S. Wu. (2018). Scaling laws for the additive manufacturing, Journal of Materials Processing Technology, 257, 234-243.

[25] Chapman L., R Morrell, P N Quested, R F Brooks. (2008). Properties of Alloys and Moulds Relevant to Investment Casting. NPL Report MATC (D), 141-156.

Chapter 6 Microstructural Characteristics: Crack Formation Mechanism

6.1. Introduction

This chapter studies the microstructures in the (as-printed) APed and (heat-treated) HTed conditions and the cracking behaviour in the APed condition of the Inconel 738 LC (IN738LC) alloy processed by laser powder bed fusion (LPBF). The processing parameters of the parts in this chapter are fixed as laser power 200 W, scan speed 1500 mm/s, hatch spacing 75 μm, thickness of layer 30 μm, Raster 90º scan strategy under no preheating condition.

6.2. Results and discussions

6.2.1. Microstructure

6.2.1.1. As-printed condition

Figure 6.1 shows the X-ray diffraction (XRD) patterns of the IN738LC powders and the printed part on the longitude section. It reveals that the main phase in the IN738LC powders is the γ/γ' phase. The XRD result of the IN738LC sample processed by LPBF shows the same locations of the peaks but significantly different heights in the APed condition. The strong diffraction peaks of (111) are detectable in the powders with an intensity ratio of $I_{(111)}/I_{(100)} \sim 2.5$, while ~ 0.1 in the APed sample, indicating a conversion of the crystal orientation from (111) to (100) during the LPBF process. This

is due to the strong texture arising from the heat flow during a rapid cooling process.
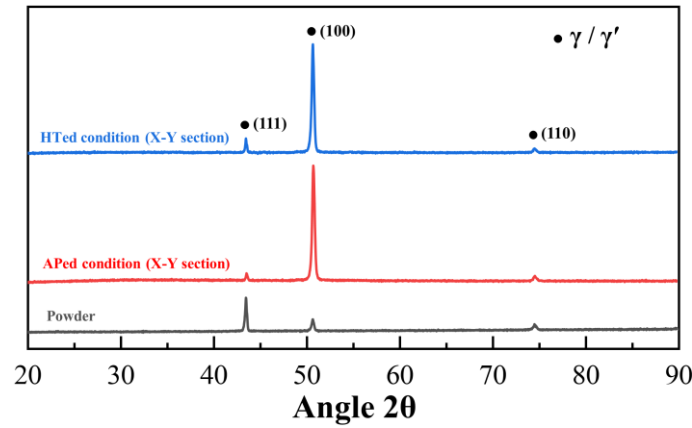

Figure 6.1. XRD patterns of the IN738LC powders and the X-Z sections of the parts in the APed and HTed conditions.

Figure 6.2 shows the scanning electron microscope (SEM) images of the APed sample on the longitude (X-Z) and cross (X-Y) sections at different magnifications. For the X-Z direction, the shape of the melt pool is clearly visible, exhibiting a curvature morphology towards the part bottom, as shown in Figure 6.2 (a), while Figure 6.2 (d) presents the boundary of the laser bath in the X-Y section. In the melt pool, refined cellular dendrites grow nearly parallel to the building direction (Z-axis), as presented in Figure 6.2 (b). In the X-Y section, cell-like morphology appears when the grain growth orientation is at a certain angle to the cutting section, which is considered to be the cross sections of the cellular dendrites. The sizes of these cell-like structures are ranged from ~ 0.3 μm to ~ 0.9 μm in diameter. In the high magnification image (Figure 6.2 (e)), the primary dendrite arm spacing (PDAS) λ_1 can be measured, and then the cooling rate ($\partial T/\partial t$) can be further calculated using [1, 2]:

$$\lambda_1 = 97 \pm 5 (\frac{\partial T}{\partial t})^{-0.36 \pm 0.01} \qquad \text{Equation 6.1}$$

The reported PDAS is the average from the measurements of 9 different view-fields. The result is 0.7 ± 0.04 μm, and then the corresponding cooling rate is calculated to be

164

$\sim 1.6 \times 10^6$ °C/s according to Equation 6.1. At higher magnification shown in Figures 6.2 (c) and 6.2 (f), particles with a blocky morphology (white arrows) exist between the dendrites in both the X-Z and X-Y sections. This is normally observed in the APed condition of the LPBFed IN738LC alloy [3]. These particles are considered to be MC-type carbides. Fine γ′ precipitates are difficultly observed due to the rapid cooling process, in which the alloy undergoes an immediate quenching after a high-temperature solution process [4]. As a result, the γ matrix keeps the condition of a supersaturated solid solution with no γ′ precipitating from it.
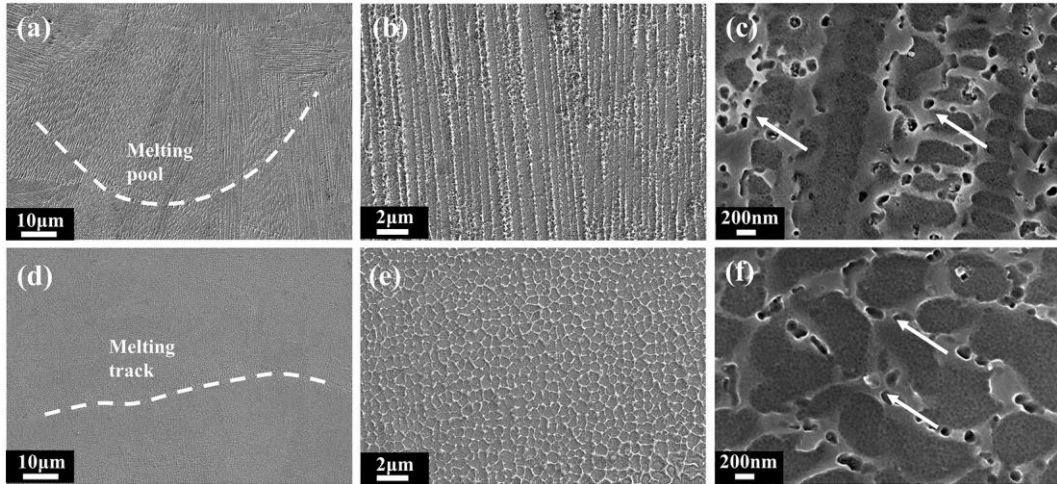

Figure 6.2. SEM images of the microstructures in the APed condition on (a, b, c) the X-Z and (d, e, f) the X-Y sections.

Columnar grains are the main grain structures in the X-Z section, as presented in the orientation maps by electron backscattered diffraction (EBSD) in Figure 6.3 (a). These grains extend along the building direction over more than 15 layers, and the maximum length can reach ~ 600 μm. Fine grain structure, corresponding to the cell-like morphology, appears in the X-Y section, as shown in Figure 6.3 (b). The average grain sizes are 19.6 ± 1.0 μm and 9.3 ± 0.8 μm for the X-Z and X-Y sections, respectively. The corresponding inverse pole figures (PFs) and inverse pole figures

(IPFs) in Figures 6.3 (c) and 6.3 (d) show that most crystals have a preferential growth direction along the crystallographic orientation <100> {001} for both sections, being consistent with the red colour in Figures 6.3 (a) and 6.3 (b) and the XRD analysis results.
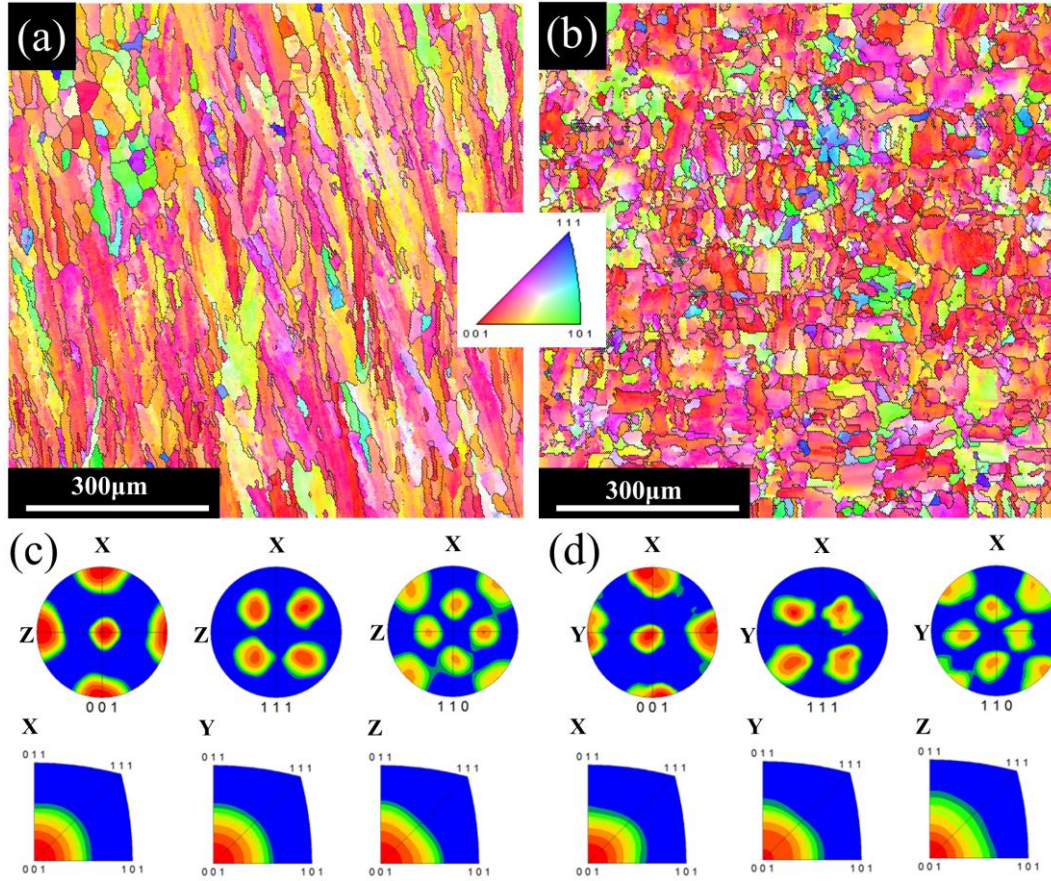

Figure 6.3. EBSD maps of the (a) X-Z and (b) X-Y sections for the part, PFs at (001), (111) and (110) and IPFs at X, Y and Z directions of the (c) X-Z and (d) X-Y sections in the APed condition.

Transmission electron microscope (TEM) is performed to study the constituents in the APed IN738LC alloy during LPBF. Figure 6.4 shows the bright field TEM micrographs of the X-Z and X-Y sections. Figure 6.4 (a) shows entangled dislocations in the inter-dendrite regions for the sample in the X-Z section. Similarly, Figure 6.4 (b) illustrates lots of dislocation at the boundaries between the cell-like structures in the X-Y section. As presented in both images, dislocation density exhibits higher at the sub-grain boundaries than that in the matrix [5, 6].

Figure 6.5 presents the energy dispersive spectrometer (EDS) mapping result of the cell-like structure under the scanning TEM (STEM) mode. Cr and Al exhibit almost uniform distribution overall the regions, attributed to the unit partition coefficients of Cr and Al in the IN738LC alloy during solidification [1]. The elements of Ni, Co and W, however, are depleted in the boundary region, similar to the findings of Wang et al. [7]. The blocky particles in the boundary region are identified to be enrichments of Ti, Ta, Nb, which are typical elements of the MC carbides in nickel-based superalloys [8]. In addition, it also observes the segregation of Zr at the boundaries.
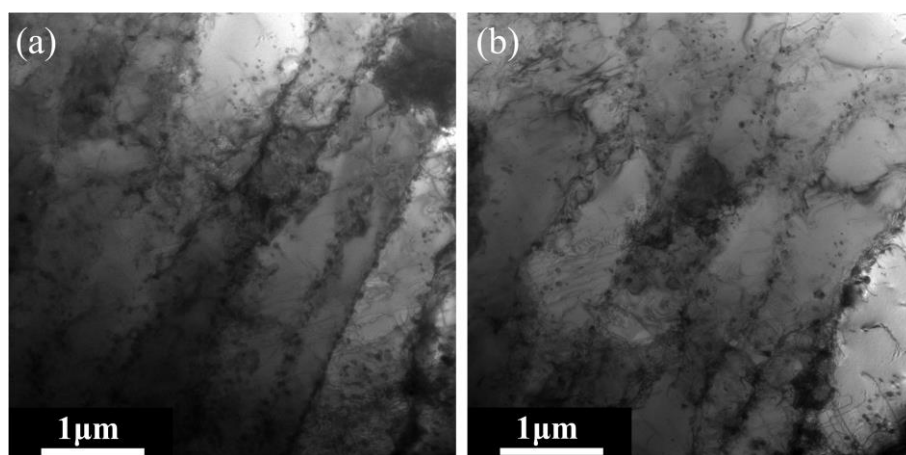

Figure 6.4. Bright field TEM images of the (a) X-Z and (b) X-Y sections of the part in the APed condition showing local dislocation substructures.

6.2.1.2. Heat-treated condition

Compared with the microstructures in the samples before and after heat treatment shown in Figures 6.3 (a) and 6.6 (a), the grain structure, i.e., the columnar grains are not changed in the X-Z section. The compensation between the recrystallisation and the grain growth induces the average size to slight increase from 19.6 ± 1.0 μm for the X-Z section and 9.3 ± 0.8 μm for the X-Y section to 21.9 ± 2.1 μm and 10.1 ± 1.1 μm, respectively [9]. The strong cube texture dominated by a preferential alignment of <100>

is unchanged during heat treatment, proven by the PFs and IPFs in Figures 6.6 (c) and

6.6 (d) compared with Figures 6.3 (c) and 6.3 (d) and the XRD pattern in Figure 6.1.
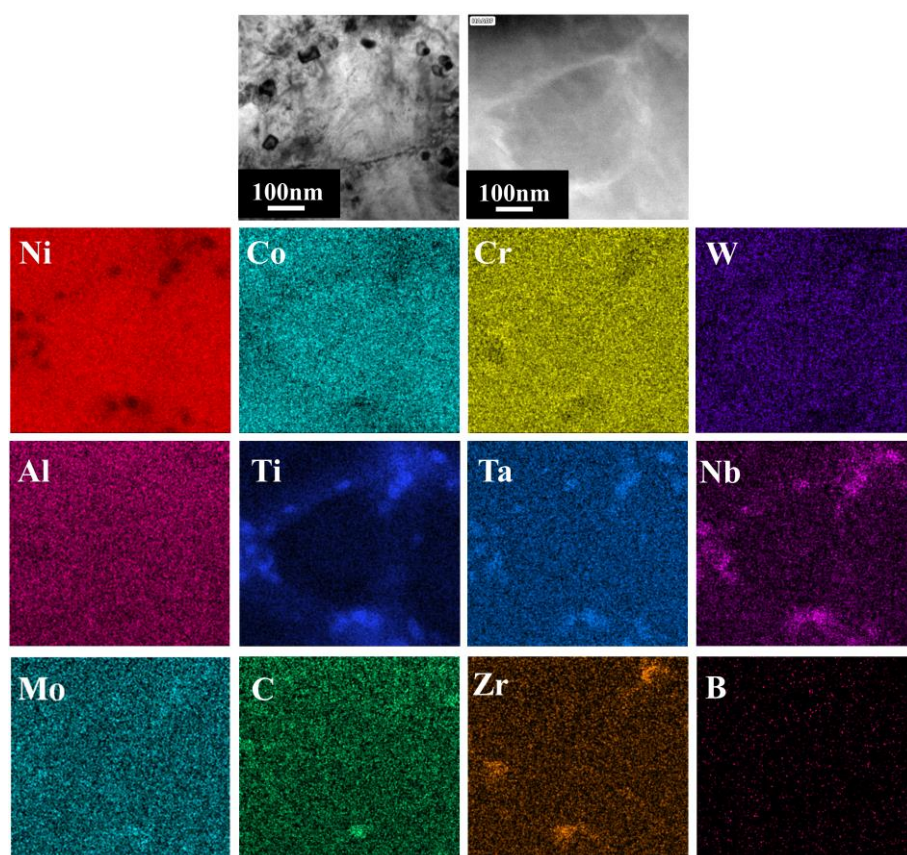

**Figure 6.5. TEM and STEM images (top) and EDS chemical mapping (bottom)
for the cell-like structure in the APed condition.**

Figure 6.7 (a) shows the SEM images of IN738LC processed by LPBF after heat

treatment, and Figure 6.7 (b) is the view at high magnification. These observations

demonstrate 2 groups of precipitates, i.e., coarse (red arrow) and fine precipitates

(yellow arrow) [10, 11]. The coarse precipitates are considered primary γ′ with an

average size of 423.5 ± 45.4 nm, while the fine precipitates are the secondary γ′, and

the average size is 52.0 ± 13.1 nm. Volume fractions of the primary and secondary γ′

are 37.1 ± 1.3 vol% and 25.3 ± 2.3 vol%, respectively. Carbides that change into chain-

like morphology (white arrow) are found at the grain boundary, as presented in Figure

6.7 (c).
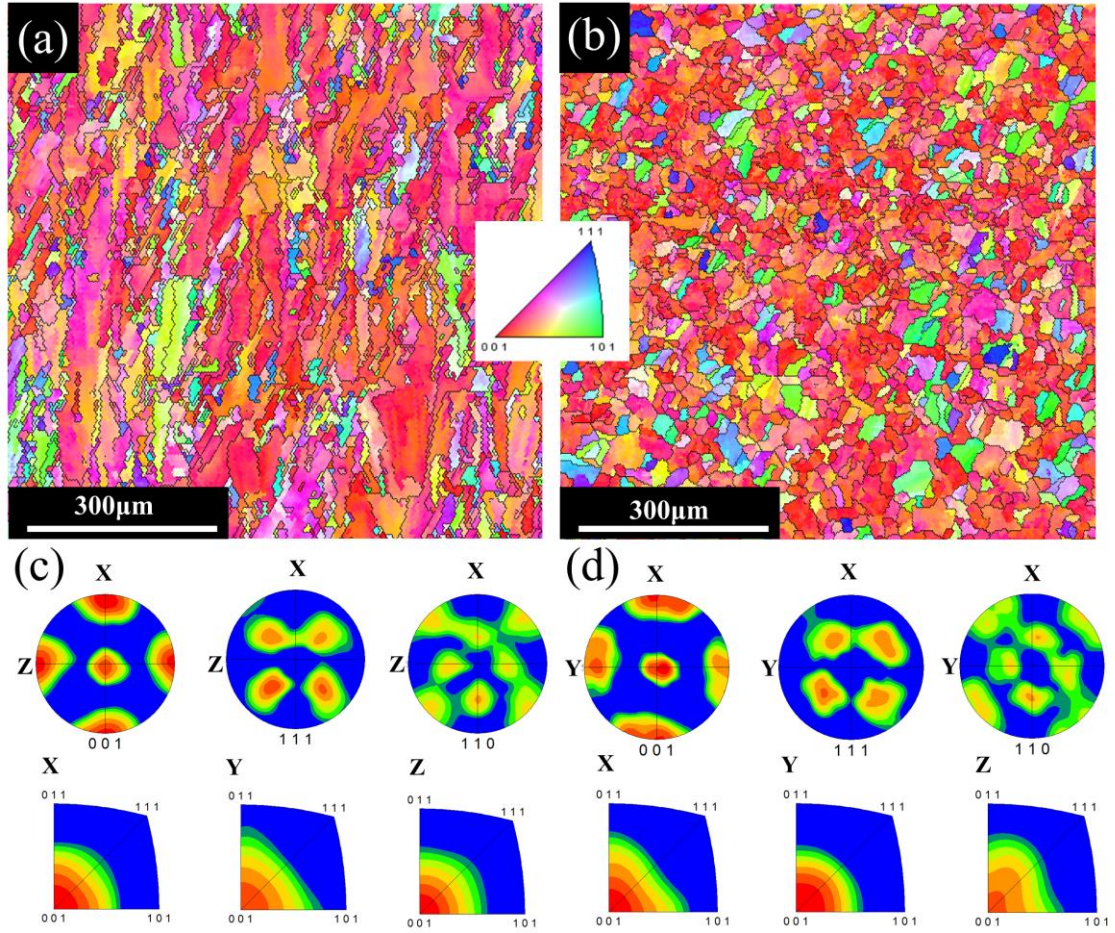
Figure 6.6. EBSD maps of the (a) X-Z and (b) X-Y sections for the part, PFs at (001), (111) and (110) and IPFs at X, Y and Z directions of the (c) X-Z and (d) X-Y sections in the HTed condition.

Figure 6.7. (a) SEM images showing (a, b) bimodal distribution of the primary and secondary γ′ phases and (c) chain morphology of carbides at the grain boundary in the HTed condition.

6.2.2. Cracking

6.2.2.1. Cracking mechanism

Figure 6.8 shows that cracking is associated with several inclusions and/or micro-

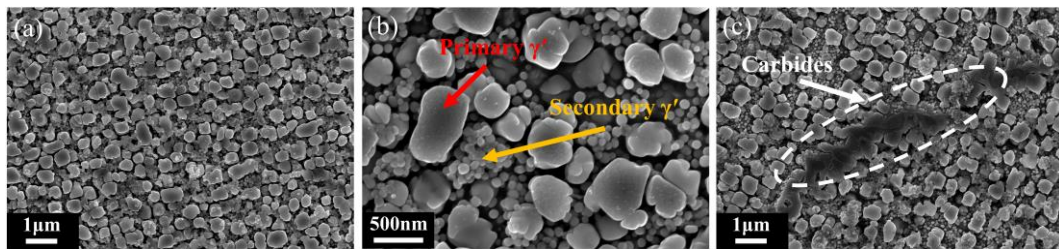segregation of alloying elements in the APed IN738LC alloy during the LPBF process. Some relatively dark and blocky particles enriched in Ta, W and Si are trapped into the cracks. The presence of these particles can lead to cracking during solidification due to the characteristic of loose bonding with the surrounding matrix. The enriched C at the crack attributes to the existence of MC-type carbides. Xu et al. [12] reported that the distribution of carbides at grain boundaries was liable for the stress concentration and interrupted the liquid film's continuity, which also promoted the formation of cracks. Meanwhile, the segregation of Zr is apparent in this crack region, noted in the IN738LC alloy during LPBF in a previous investigation [13].
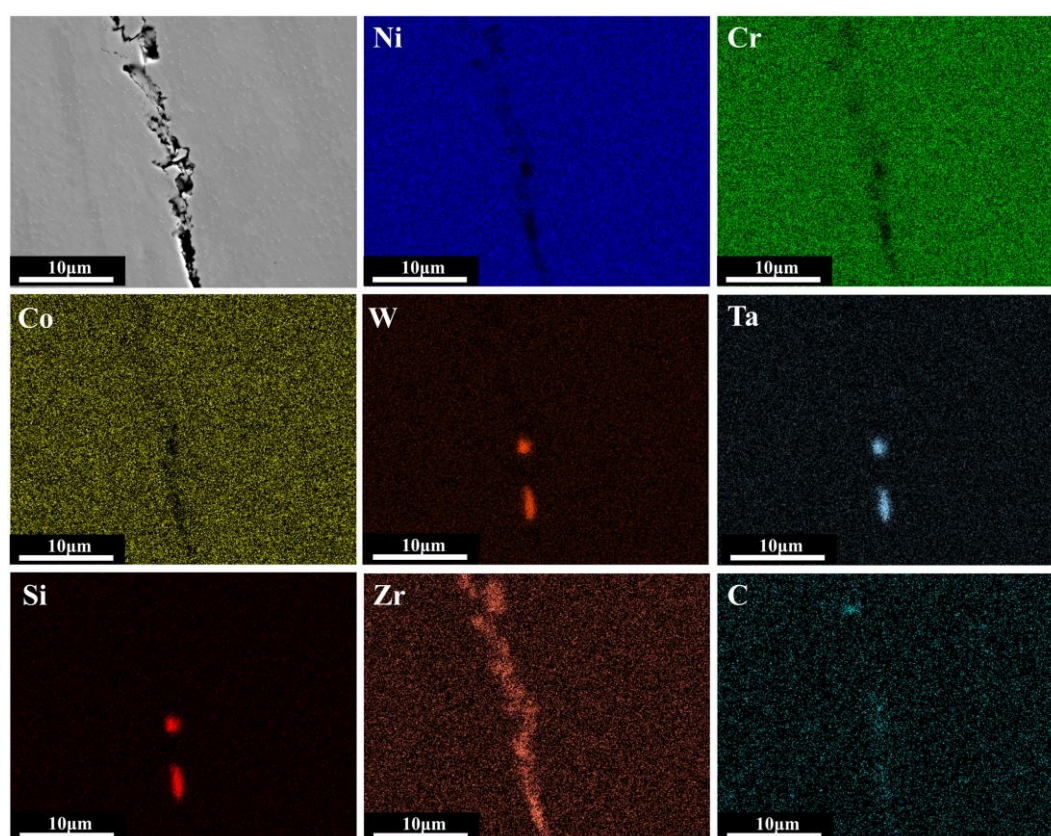

Figure 6.8. EDS chemical mapping showing the inclusions enriched in W, Ta, Si and the segregations of C, Zr along a crack in the IN738LC part processed by LPBF in the APed condition.

The cracking phenomenon has been well investigated in casting and welding

170

processes of the IN738LC alloy, e.g., a hot tearing phenomenon in a polycrystalline Ni-based IN738LC superalloy [14]. In their research, it detected the presences of eutectic phase and isolated carbides in intergranular zones, which hindered the liquid flowing to feed into the mushy zone. In this process, Zr segregated at grain boundaries and elevated the solid-liquid interfacial energy, thus correspondingly increasing the undercooling of the dendrite coalescence. Consequently, the material displayed a lower hot cracking resistance. Ojo et al. [15] believed that the main cause of heat affected zone (HAZ) cracking of casting IN738 in the welding process was attributed to the constitutional liquation of γ/γ′ precipitations. Influenced by the thermal cycle in HAZ, alloying solutes were enriched at the interface between precipitates and matrix by solid-state diffusion. When solute concentration and temperature met the γ′-γ eutectic reaction, a metastable liquid film formed on the interface. Xu et al. [16] reported a similar phenomenon in the IN738LC part manufactured by laser solid forming. Apart from the constitutional liquation of the γ/γ′ phase, they suggested that segregation of solute B contributed to a decline in liquidus temperature at grain boundaries, which increased the tendency of hot cracking as well. The mechanism of solidification cracking in IN738LC processed by LPBF was elucidated by Cloots et al. [13]. They used atom probe tomography (APT) to identify and characterise the enrichment of Zr at grain boundaries, which favoured the crack formation. Figure 6.9 (a) presents a longitudinal section of an open crack in the APed IN738LC alloy processed by LPBF. Clear blunt dendrites are observed on the crack at high magnification (Figure 6.9 (b)). This is a typical morphology of a solidification crack surface, identifying the wetting

behaviour between the dendrites and liquation films. The segregation of Zr at grain boundaries can be proven in the thermodynamic calculation, as shown in Figure 6.9 (c). Within the liquid phase at the last stage of solidification (grain boundaries), the amount of Zr is ~ 60 times higher than the mean chemical composition of the alloy. Calculation results by Scheil mode in Figure 6.9 (d) demonstrates that the solidus is significantly lowered due to the micro-segregations, and the solidification temperature range is enlarged by nearly 600 $^{\circ}$C compared to the equilibrium mode.

In addition, silicide particles, presumably $TaSi_2$ and WSi_2, are also associated with the cracks in Figure 6.9 (b) (yellow dotted line). The $TaSi_2$ and WSi_2 particles form at the early stage during the solidification as their high melting points (2200 $^{\circ}$C and 2160 $^{\circ}$C [17], respectively), thus hindering the liquid flow in the mushy zone and causing the discontinuity of last solidified liquid channel and stress concentration. Accompanying with the segregation of Zr, solidification cracking occurs, as shown in Figure 6.8. Qiu et al. [18] found the particles enriched in Si, W and Al at the cracks in IN738LC manufactured by LPBF and believed that the presence of WO_2, Al_2O_3 and SiO_2 particles along grain boundaries also contributed to cracking.
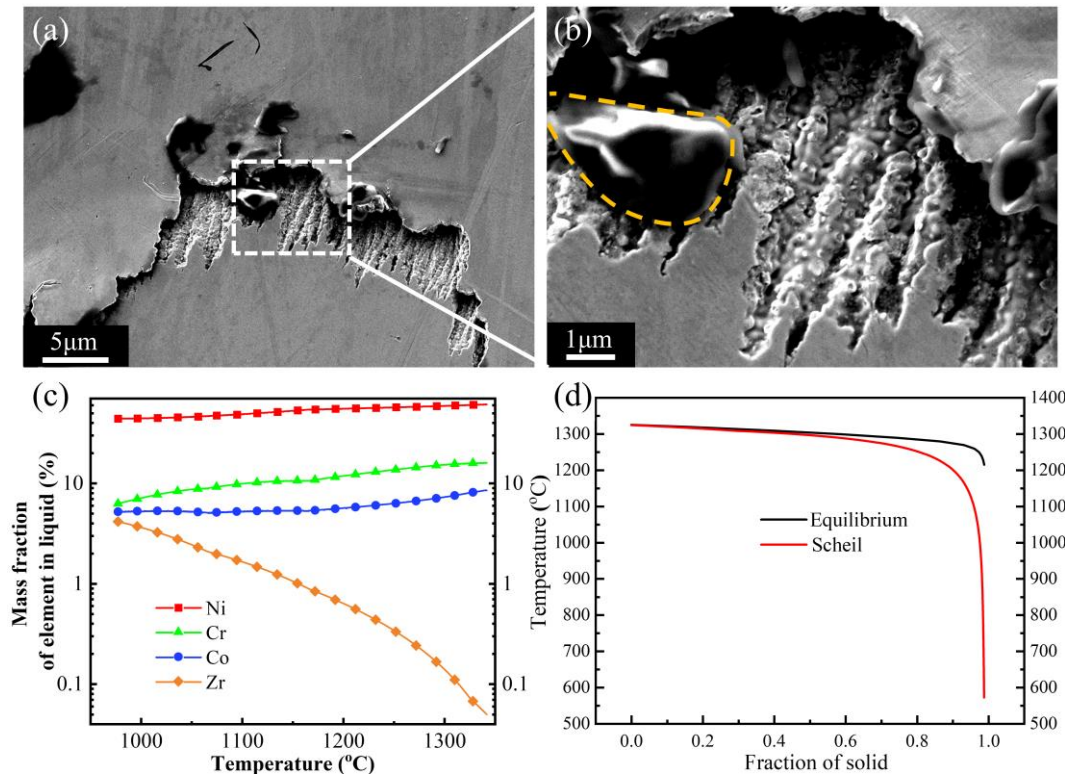
Figure 6.9. (a) SEM image of a crack, (b) high magnification of the crack showing the details of the dendrite structures and the silicide marked with yellow dotted line on the crack surface, (c) the fraction of alloy elements in the liquid phase during solidification and (d) the solidification path of the IN738LC alloy based respectively in the equilibrium and Scheil modes in the thermodynamic calculations.

Figure 6.10 illustrates the whole process of the solidification cracking in the APed IN738LC alloy during LPBF. Silicide particles form firstly due to their high melting point and scattered in the solidifying liquid (Step 1). Dendrites develop and grow at the front of the solid-liquid interface. Alloying elements with the partition coefficients less than 1 like Zr discharge into the liquid phase (Step 2). As the solidification process continues, the adjacent dendrites connect with each other with some silicide particles between them, with the liquid film being enriched in Zr (Step 3). Subsequently, the material almost solidifies, while a low-melting-point liquid film remains at the last stage of solidification between dendrites (Step 4). The silicide particles prevent molten liquid from flowing to the narrow path between dendrites, so isolated liquid films form. These

173

isolated liquid films have very weak strength. Meanwhile, residual stress increases as temperature decreases. As soon as the residual stress is greater than the strength of the isolated liquid film region, cracking starts and propagates along the inter-dendrite regions as the LPBF progress (Step 5).
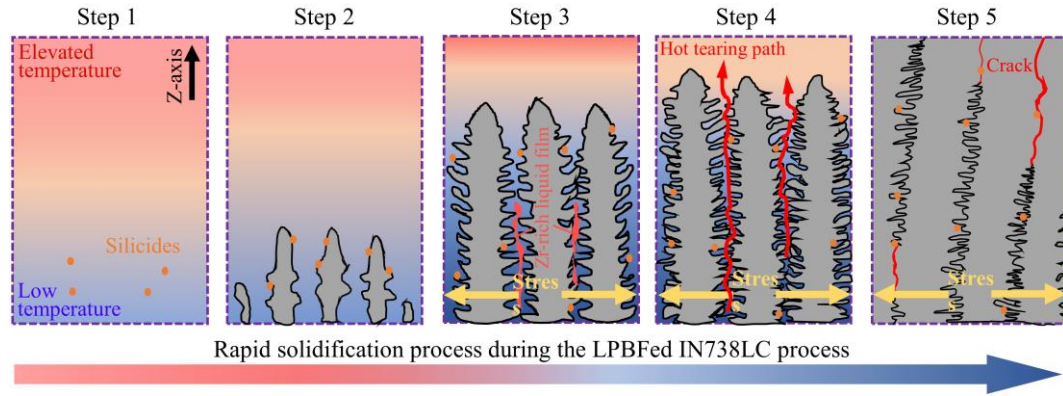

Figure 6.10. Schematic diagram showing the cracking starting and propagation processes of the APed IN738LC alloy during LPBF.

6.2.2.2. Cracking vs grain boundary misorientation

Figure 6.11 shows the misorientation angle distributions of general grain boundaries and the grain boundaries around the cracks, which is calculated using Equation 6.2 [19], as well as the relative cracking rate in the APed IN738LC alloy fabricated by LPBF.

$$\varphi_i = \frac{\Sigma CGBM_i}{\Sigma CGBM_1 + \Sigma CGBM_2 + ...\Sigma CGBM_i + ...\Sigma CGBM_n} \quad \text{Equation 6.2}$$

where $\Sigma CGBM_i$ is the total number of the misorientation angles of i around the cracks. There are ~ 42 % of the general grain boundaries with the misorientation angles lower than 10°, while ~ 44 % between 10° and 40° and ~ 14 % greater than 40°. Compared Figures 6.11 (a) and 6.11 (b), the distribution of misorientation angles of the grain boundaries around the cracks is distinguishably different from the general grain

boundaries. Only ~ 6 % of the cracking grain boundaries have the misorientation angles lower than 10°, ~ 57 % between 10° and 40° and ~ 37 % greater than 40°. This difference indicates that there is a correlation between the possibility of cracking and the misorientation angles of grain boundaries. Figure 6.11 (c) shows the relationship between the relative cracking rate and the misorientation angles. The relative cracking rate ψ_i is defined as [20]:

$$f_i = \frac{\varphi_i}{\phi_i}$$
Equation 6.3

$$\psi_i = \frac{f_i}{f_1 + f_2 + f_3 + f_4 \ldots \ldots \ldots f_n}$$
Equation 6.4

where φ_i is the fraction of the misorientation angles around the cracks, ϕ_i is the fraction of the general grain boundary misorientation angles, and f_i is the number of the cracks which occur at the misorientation angles of i. Figure 6.11 (c) shows that the relative cracking rate generally increases with increasing the grain boundary misorientation angle, indicating that the grain boundaries with high misorientation angles are susceptible to cracking.

Rappaz et al. [21] established a relationship between coalescence undercooling and grain boundary energy during solidification as:

$$\Delta T_b = \frac{\gamma_{gb} - 2\gamma_{sl}}{\Delta S_f \delta_{di}}$$
Equation 6.5

where γ_{gb} is the grain boundary energy, γ_{sl} is the solid/liquid interfacial energy, ΔS_f is the entropy for fusion per unit volume, and δ_{di} is the thickness of the diffuse interface. If $\gamma_{gb} < 2\gamma_{sl}$, the 2 interfaces of solid/liquid are "attractive", indicating that the liquid film remaining cannot stay stable. The dendrites around the liquid will coalesce with

each other once the distance of these 2 interfaces is lower than δ_{di}, and the liquid between dendrites will solidify. However, the condition of $\gamma_{gb} > 2\gamma_{sl}$ favours the formation of "repulsive" grain boundaries, where the liquid film stays stable unless the temperature reaches the corresponding undercooling ΔT_b, which further increases the solidification temperature range and the risk of cracking. The Read-Shockley equation [22] interpreted the relationship between grain boundary energy and grain boundary misorientation angle as:

$$\gamma_{gb} = \frac{Gb\theta_{gb}}{4\pi(1-\upsilon)}(1-\ln\frac{\theta_{gb}}{\theta_m}) \qquad \text{Equation 6.6}$$

where G is the shear modulus, b is the Burgers vector, υ is the Poisson ratio, θ_{gb} is the grain boundary misorientation angle, and θ_m is the angle at which γ_{gb} reaches its maximum. This equation is applied when $\theta_{gb} < \theta_m$, and when $\theta_{gb} > \theta_m$, γ_{gb} will keep the constant of its maximum value. According to Equation 6.6, γ_{gb} increases with increasing the misorientation angles of grain boundaries, and accordingly, the coalescence undercooling ΔT_b expressed in Equation 6.5 increases as well. As a result, the liquid film will keep stable at the last stage of solidification with an undercooling of ΔT_b. Therefore, it expects cracks to occur at the grain boundaries with high misorientation angles, as shown in Figure 6.11 (c).
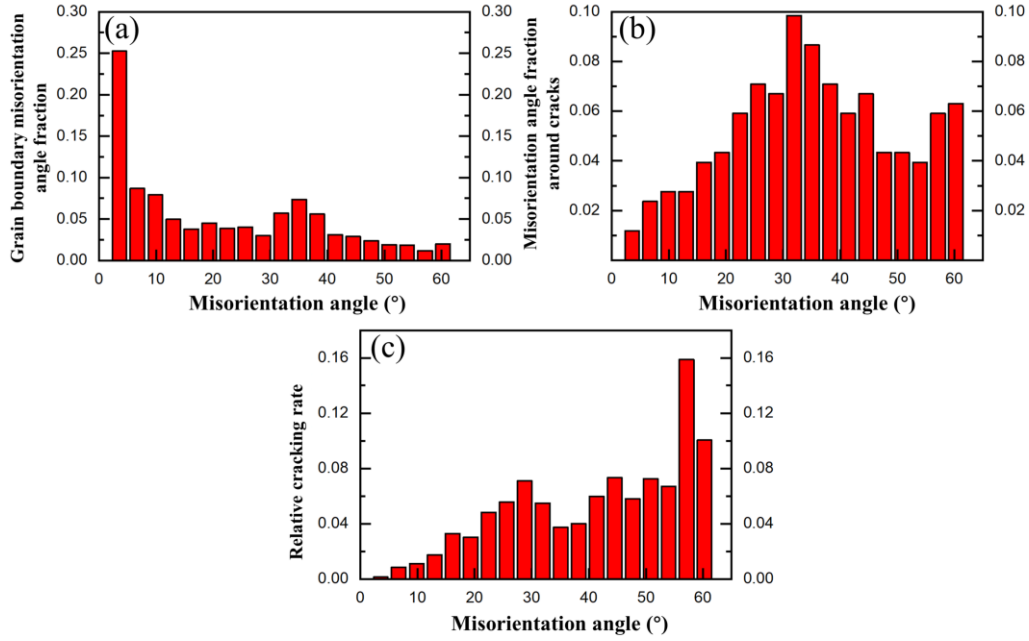
Figure 6.11. (a) Misorientation angle distribution of grain boundaries, (b) misorientation angle distribution around the cracks, (c) relative cracking rate of the IN738LC part in the APed condition.

6.3. Summaries

The average grain sizes of the APed IN738LC alloy are 19.6 ± 1.0 μm and 9.3 ± 0.8 μm for the X-Z and X-Y sections, respectively. Coarse (primary) γ′ precipitates with an average size of 423.5 ± 45.4 nm and fine (secondary) precipitates with an average size of 52.0 ± 13.1 nm are identified in the HTed sample. Both fractions of grains with the sizes less than 10 μm and larger than 100 μm increase after heat treatment, arising from the occurrence of recrystallisation and the grain growth. The average sizes slightly increase to 21.9 ± 2.1 μm from 19.6 ± 1.0 μm for the X-Z section and 10.1 ± 1.1 μm from 9.3 ± 0.8 μm for the X-Y section. Whatever the APed and HTed conditions, the parts exhibit a strong cubic texture dominated by a preferential alignment of <100>.

During rapid heating and cooling processes in LPBF, Zr segregates in the grain boundary regions, reducing the solidus at grain boundaries, and the solidification cracks

177

occur due to the remaining liquid at grain boundaries at the last stage of solidification. Silicide particles form at the early stage of solidification can hinder the liquid film's continuity once they are trapped in the mushy zone and cause stress concentration, promoting the origin of cracks. Furthermore, it expects the cracks to occur at the grain boundaries with high misorientation angles due to the increased solidification temperature range.

6.4. References

[1] Muñiz-Lerma J. A., Tian Y., Wang X., Gauvin R., Brochu, M. (2018). Microstructure evolution of Inconel 738 fabricated by pulsed laser powder bed fusion. Progress in Additive Manufacturing, 4(2), 97-107.

[2] Harrison N. J., Todd I., Mumtaz K. (2015). Reduction of micro-cracking in nickel superalloys processed by selective laser melting: a fundamental alloy design approach. Acta Materialia, 94, 59-68.

[3] Messé O. M. D. M., Muñoz-Moreno R., Illston T., Baker S., Stone H. J. (2018). Metastable carbides and their impact on recrystallisation in IN738LC processed by selective laser melting. Additive Manufacturing, 22, 394-404.

[4] Chen J., Xue L. (2010). Process-induced microstructural characteristics of laser consolidated IN-738 superalloy. Materials Science and Engineering: A, 527(27-28), 7318-7328.

[5] Tucho W. M., Cuvillier P., Sjolyst-Kverneland A., Hansen V. (2017). Microstructure and hardness studies of Inconel 718 manufactured by selective laser

melting before and after solution heat treatment. Materials Science and Engineering: A, 689, 220-232.

[6] Tian Y., Muñiz-Lerma J. A., Brochu M. (2017). Nickel-based superalloy microstructure obtained by pulsed laser powder bed fusion. Materials Characterization, 131, 306-315

[7] Wang X., Carter L. N., Pang B., Attallah M. M., Loretto M. H. (2017). Microstructure and yield strength of slm-fabricated CM247LC Ni-superalloy. Acta Materialia, 128, 87-95.

[8] Group of Metallographic pattern of superalloy editorial board (1979). Metallographic pattern of superalloy. China.

[9] Holland S., Wang X., Fang X. Y., Guo Y. B., Yan F., Li, L. (2018). Grain boundary network evolution in Inconel 718 from selective laser melting to heat treatment. Materials Science & Engineering A, 725, 406-418.

[10] Rickenbacher L., Etter T., S. Hövel, Wegener K. (2013). High temperature material properties of IN738LC processed by selective laser melting (SLM) technology. Rapid Prototyping Journal, 9(4), 282-290.

[11] Ramakrishnan A., Dinda G. P. (2019). Direct laser metal deposition of Inconel 738. Materials Science and Engineering: A, 740-741, 1-13.

[12] Xu J., Lin X., Guo P., Dong H., Wen X., Li Q., Huang W. (2018). The initiation and propagation mechanism of the overlapping zone cracking during laser solid forming of IN-738LC superalloy. Journal of Alloys and Compounds, 749, 859-870.

[13] Cloots M., Uggowitzer P. J., Wegener K. (2016). Investigations on the

microstructure and crack formation of IN738LC samples processed by selective laser melting using Gaussian and doughnut profiles. Materials & Design, 89, 770-784.

[14] Heydari D., Fard A. S., Bakhshi A., Drezet J. M. (2014). Hot tearing in polycrystalline Ni-based IN738LC superalloy: Influence of Zr content. Journal of Materials Processing Technology, 214(3), 681-687.

[15] Ojo O. A., Richards N. L., Chaturvedi M. C. (2004). Contribution of constitutional liquation of gamma prime precipitate to weld HAZ cracking of cast Inconel 738 superalloy. Scripta Materialia, 50(5), 641-646.

[16] Xu J., Lin X., Zhao Y., Guo P., Wen X., Li Q., Huang W. (2018). HAZ Liquation Cracking Mechanism of IN-738LC Superalloy Prepared by Laser Solid Forming. Metallurgical and Materials Transactions A, 49(10), 5118-5136.

[17] Mat Web Material property data (1996). http://www.matweb.com/index.aspx

[18] Qiu C., Chen H., Liu Q., Yue S., Wang H. (2019). On the solidification behaviour and cracking origin of a nickel-based superalloy during selective laser melting. Materials Characterization, 148, 330-344.

[19] Chen Y., Zhang K., Huang J., Hosseini S. R. E., Li Z. (2016). Characterization of heat affected zone liquation cracking in laser additive manufacturing of Inconel 718. Materials & Design, 90, 586-594.

[20] Chen Y., Lu F., Zhang K., Nie P., Elmi Hosseini S. R., Feng K., Li Z. (2016). Dendritic microstructure and hot cracking of laser additive manufactured Inconel 718 under improved base cooling. Journal of Alloys and Compounds, 670, 312-

321.

[21] Rappaz M., Jacot A., Boettinger W. J. (2003). Last-stage solidification of alloys: theoretical model of dendrite-arm and grain coalescence. Metallurgical and Materials Transactions A, 34(3), 467-479.

[22] Read W. T., Shockley, W. (1950). Dislocation Models of Crystal Grain Boundaries. Physical Review, 78(3), 275-289.

Chapter 7 Cracking Mitigation Method: Y₂O₃ Nanoparticles Decoration

7.1. Introduction

In this chapter, the effects of adding Y_2O_3 nanoparticles into the Inconel 738 LC (IN738LC) powders for the laser powder bed fusion (LPBF) process are studied. The added levels of Y_2O_3 nanoparticle are 0.05 wt%, 0.2 wt% and 0.6 wt%. Cracking behaviours, microstructures, tensile mechanical properties and oxidation resistance of the IN738LC/nanoparticles Y_2O_3 composites are examined. Table 7.1 lists the laser powers and the scan speeds used in this chapter. Other parameters are fixed as the hatch spacing 90 μm, the thickness of layer 30 μm, the Raster 67º scan strategy under the preheating at 200 ºC.

Table 7.1. Parameters used in the LPBF process.

Sample	Laser power (W)	Scan speed (mm/s)
1	250	1000
2	250	1200
3	250	1400
4	290	1000
5	290	1200
6	290	1400
7	330	1000
8	330	1200
9	330	1400

7.2. Results

7.2.1. Process window

Optical microscope (OM) observations show that the scan speeds and the laser

powers have a great impact on the defect behaviour in the IN738LC alloy without Y_2O_3 in the current processing condition, as shown in Figure 7.1. A nearly defect-free sample is produced under a combination of the laser power of 290 W and the scan speed of 1200 mm/s, while defects appear at both higher and lower laser powers, i.e., 250 W and 330 W at this scan speed. The crack density on the polished surface increases with the decrease of the scan speed when the laser power is fixed. The defects change from pores to cracks with the increase of the energy density, i.e., the decrease of the scan speed and/or the increase of the laser power, similar to the findings in Section 4.2.4. An optimal condition is attained at a medium energy density. Insufficient energy input can lead to the lack of fusion, inducing un-melted powders [1]. At a high energy density, however, the improper closure of keyhole forms [2], resulting in the keyhole pores, as shown in Figure 7.1 (white circle) under the laser power of 330 W and the scan speed of 1000 mm/s. With adding 0.05 wt% nanoparticles Y_2O_3, the processed IN738LC alloy contains approaching free defects for most of the parameters and achieves nearly 100 % density under the condition of moderate energy density, i.e., the combination of the laser power of 290 W and the scan speed of 1200 mm/s. At low and/or high energy inputs, however, a few defects, mainly pores, can be seen. It is apparent that the addition of 0.05 wt% Y_2O_3 nanoparticles significantly reduces the defects, especially the cracks in the samples, implying that adding 0.05 wt% Y_2O_3 nanoparticles enlarges the process window for the defect-free condition in the IN738LC alloy fabricated by LPBF. However, more defects appear with the increase of Y_2O_3 nanoparticle addition to 0.2 wt%, as shown in Figure 7.3. The samples contain cracks under most of the parameters,

and even the medium energy density (290 W @ 1200 mm/s) cannot build a crack-free part. With further increase of Y_2O_3 addition to 0.6 wt%, the process window of getting optimal quality samples becomes further smaller, comparing Figure 7.4 with Figures 7.2 and 7.3. As a result, the following investigations on the microstructures and the properties will be concentrated on the processing parameters of the laser power of 290 W and the scan speed of 1200 mm/s, with which the defects are at a relatively low level for all the alloys with different additions of Y_2O_3 nanoparticles.
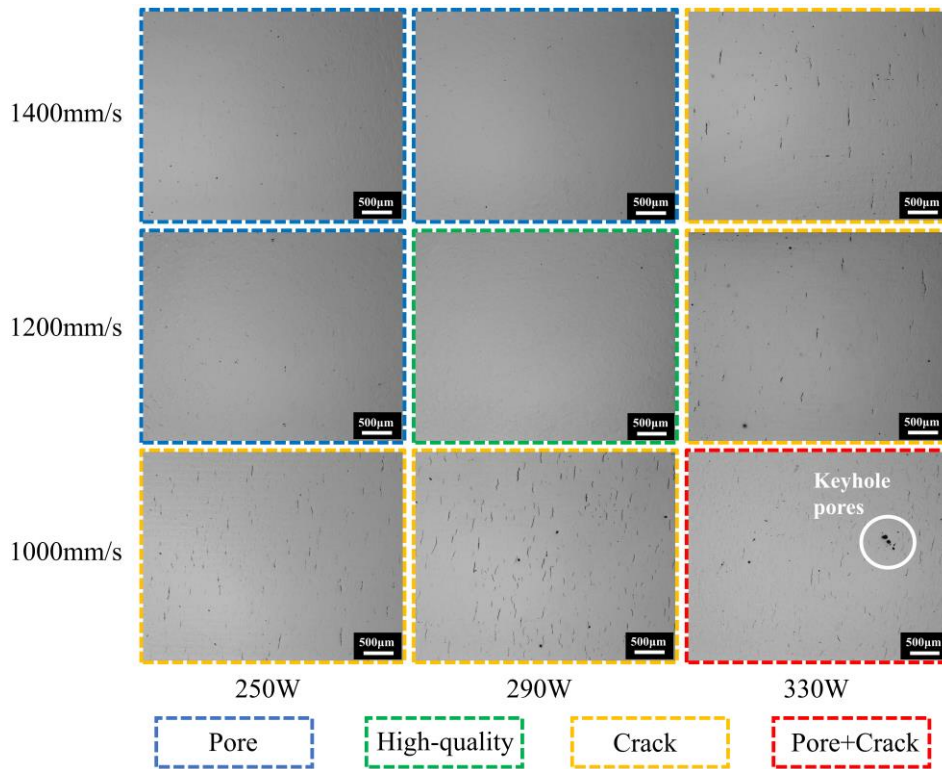

Figure 7.1. OM images on the polished surfaces of the as-printed (APed) alloy without Y_2O_3 fabricated by LPBF with different laser powers and scan speeds showing the defects.
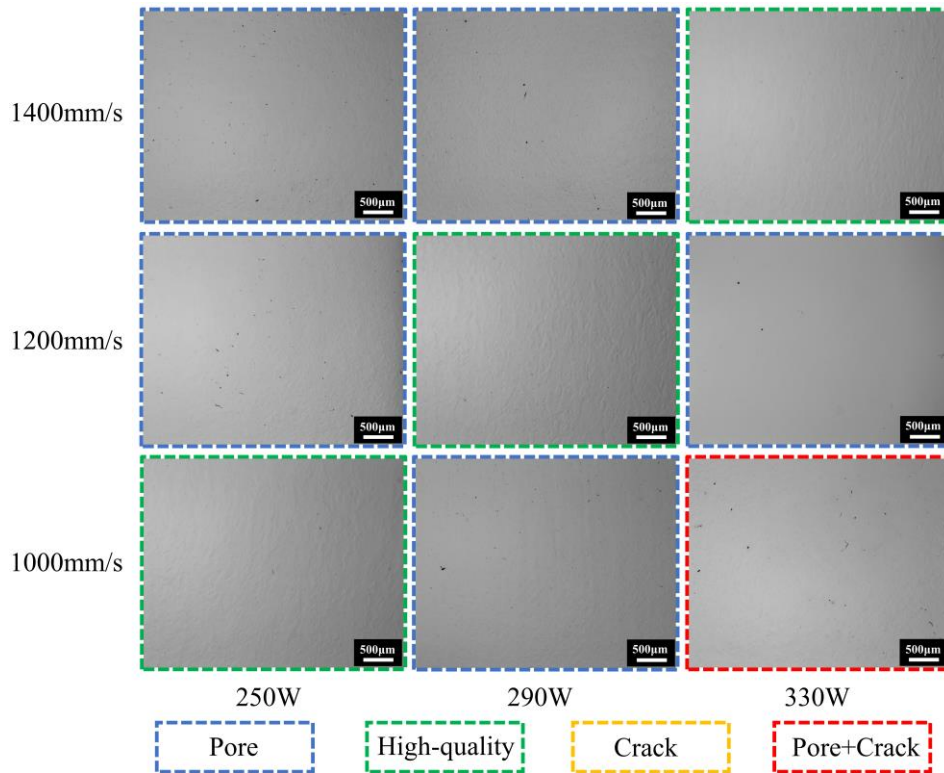
Figure 7.2. OM images on the polished surfaces of the APed alloy containing 0.05 wt% Y₂O₃ fabricated by LPBF with different laser powers and scan speeds showing the defects.

Figure 7.3. OM images on the polished surfaces of the APed alloy containing 0.2 wt% Y₂O₃ fabricated by LPBF with different laser powers and scan speeds showing the defects.

185

Figure 7.4. OM images on the polished surfaces of the APed alloy containing 0.6 wt% Y$_2$O$_3$ fabricated by LPBF with different laser powers and scan speeds showing the defects.
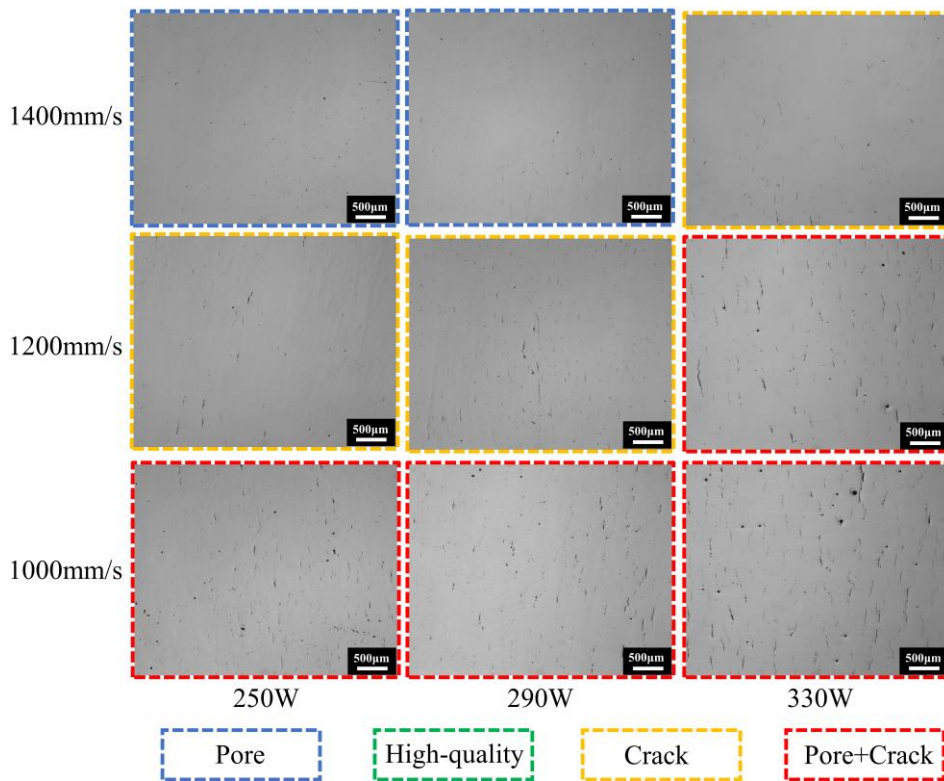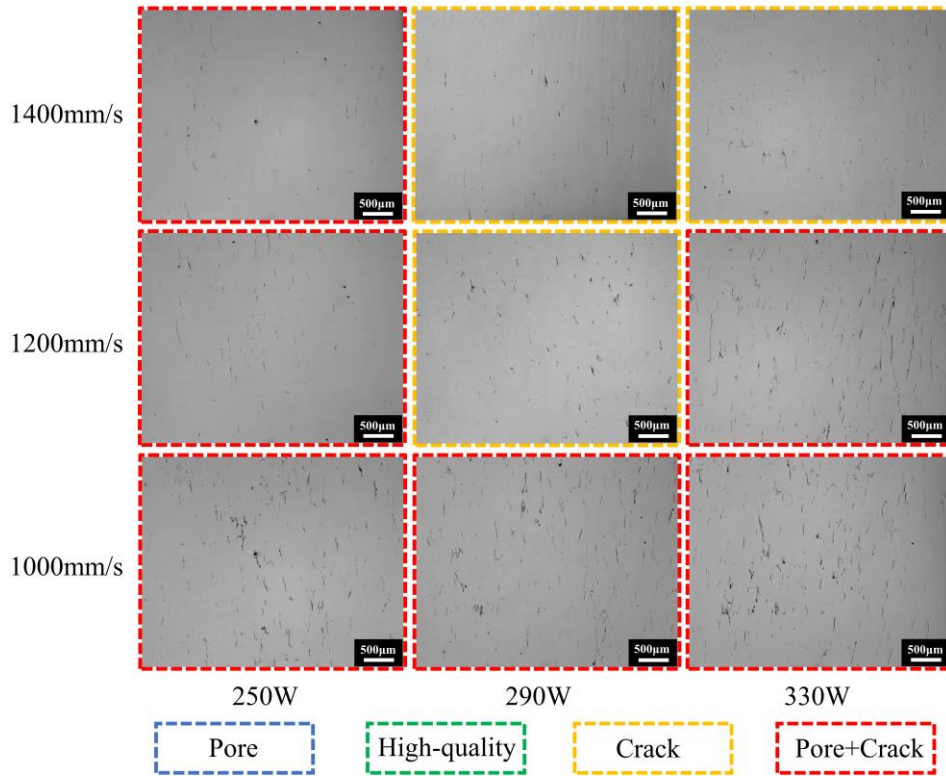
7.2.2. Microstructure

Figure 7.5 shows the inverse pole figures (IPFs) and the grain size distribution regarding the building direction for the IN738LC alloys containing various amounts of Y$_2$O$_3$ nanoparticles. Similar to the findings in Section 6.2.1.1, the columnar grains grow parallel to the building direction, crossing multiple layers. This columnar grain structure is attributed to the highly directional laser-induced temperature gradient during the LPBF process. In particular, the tendency of columnar grain growth is more obvious for the alloy without Y$_2$O$_3$, in which the length-width ratio of the grains is ~ 11 : 1, while ~ 6 : 1 for the alloys containing Y$_2$O$_3$. In addition, the grain sizes vary noticeably between these alloys, as shown in Figure 7.5 (e). The average size for the alloy without

the addition of Y_2O_3 nanoparticles is 16.7 ± 1.4 μm. It contains more grains with the size smaller than 30 μm, and the total fraction is 82.9 %. While the grains with the size greater than 100 μm accounts for only 0.3 %. For the alloy containing 0.05 wt % Y_2O_3, a significant number of the grains have the size greater than 100 μm (2.4 %), leading to a relatively larger average size (27.5 ± 1.7 μm) compared to the alloy without Y_2O_3. With increasing the contents of Y_2O_3 to 0.2 wt% and 0.6 wt%, the fractions of the grains with small size (less than 30 μm) decrease continuously down to 64.9 % and 59.5 %, respectively, while the fractions of large size grains (greater than 100 μm) increase to 3.4 % and 5.1 %, and the average grain sizes are 29.7 ± 1.4 μm and 36.8 ± 2.5 μm, respectively.

Transmission electron microscope (TEM) observes fine disperse particles in the nickel matrix of the alloy containing 0.05 wt% Y_2O_3. The bright-field TEM image in Figure 7.6 (a) shows the typical morphology of these fine particles (white arrows) with a size ranging from 50 nm to 100 nm, and the mean diameter is $\sim$ 60 nm. A few dislocations around the particles are also visible. The homogeneous distribution and the spherical morphology of these particles are more obvious in the high angle annular dark-field (HAADF) image in Figure 7.6 (b) (black arrows).
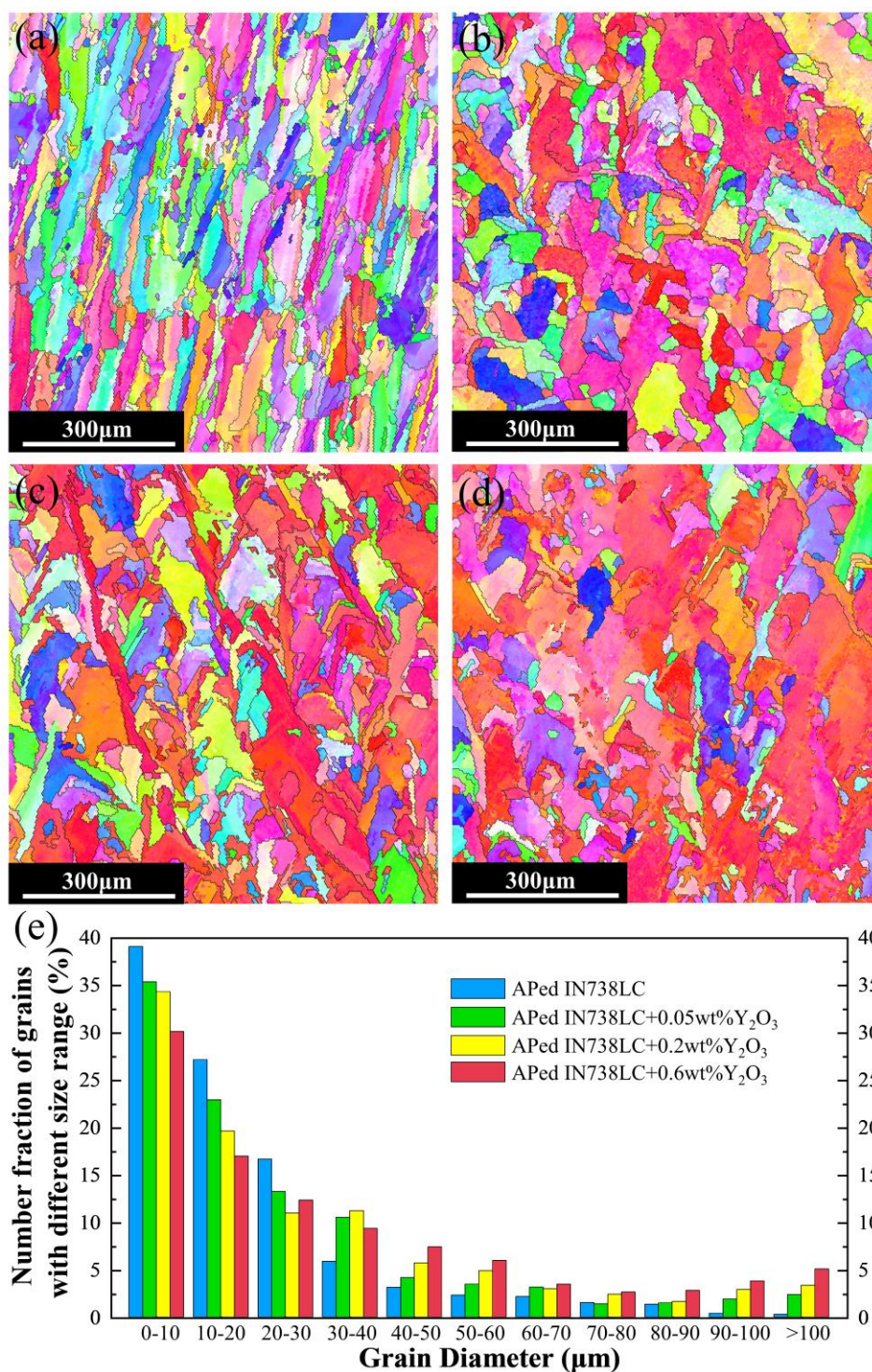
Figure 7.5. Electron backscattered diffraction (EBSD) mapping of the samples in the X-Z section showing the grain structures of the APed alloys (a) without and containing (b) 0.05 wt%, (c) 0.2 wt% and (d) 0.6 wt% Y_2O_3, (e) the grain size distribution.

Detailed morphology of a fine nanoparticle is shown in Figure 7.6 (c), and its high-

resolution TEM (HRTEM) lattice image is shown in Figure 7.6 (d). 2 measured atomic

planes have the lattice parameters of 2.1 Å and 2.0 Å in an angle of 107.4°. The Fast

Fourier Transformation (FFT) test is conducted in the area shown in Figure 7.6 (c) (red

rectangle), with Figure 7.6 (e) presenting the corresponding filtered image. This result

is in good agreement with the monoclinic crystal structure YAM-phase $Y_4Al_2O_9$ at the

zone axis of [-2 3 0], which has a space group: $P2_{1/c}$, C_{2h}, a = 7.26 Å, b = 10.31 Å, c =

10.94 Å, $\alpha = \gamma = 90°$, $\beta = 108.61°$ [3]. Figure 7.6 (f) shows the energy dispersive

spectrometer (EDS) results of the nanoparticle and proves the particles as being of the
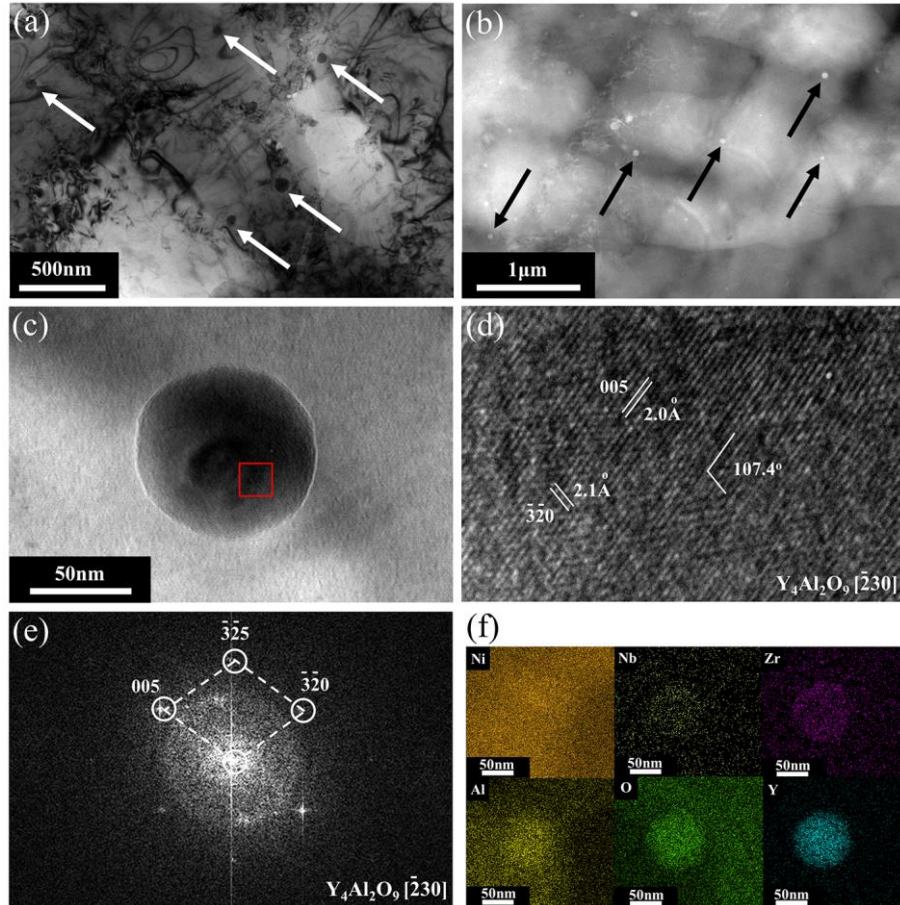
Y-Al-O type.

Figure 7.6. (a) Bright-field TEM image, (b) HAADF scanning TEM (STEM) image, (c) high magnification bright-field TEM image, (d) HRTEM, (e) FFT filtered image from the red-framed area in (c), (f) EDS mapping of the fine disperse particle in the APed alloy containing 0.05 wt% Y_2O_3.

Figure 7.7 shows the IPFs and the grain size distribution for the alloys with various

amounts of Y_2O_3 after heat treatment. Compared with the grain structure in the alloys before heat treatment, as shown in Figure 7.5, the heat treatment does not change the distribution of grain size qualitatively (Figure 7.7 (e)). The average sizes of the grains are 19.9 ± 0.8 μm, 29.3 ± 2.4 μm, 32.2 ± 1.8 μm and 34.8 ± 2.7 μm for the alloys without and containing 0.05 wt%, 0.2 wt% and 0.6 wt% Y_2O_3, respectively. The fraction of the grains with sizes smaller than 10 μm increases after heat treatment for all the alloys, arising from the occurrence of recrystallisation [4]. The number of large size grains (greater than 100 μm) also increases due to the grain growth during heat treatment, as mentioned in Section 6.2.1.2.

7.2.3. Mechanical properties

Figure 7.8 shows the tensile properties at room temperature and 850 °C of the samples with various amounts of Y_2O_3 after heat treatment. At room temperature, the alloy without Y_2O_3 has a superior yield strength (YS) of 1049.6 ± 48.2 MPa and ultimate tensile strength (UTS) of 1190.3 ± 19.1 MPa compared to the alloy containing 0.05 wt% Y_2O_3, where the corresponding values are 1003.8 ± 35.4 MPa and 1148.2 ± 14.7 MPa. For the alloys without and containing 0.05 wt% Y_2O_3, the elongations (ELs) are almost the same (6.7 ± 0.5 % vs 7.2 ± 0.6 %). With further increase of Y_2O_3 nanoparticles, the YS, the UTS and the EL decrease to 526.1 ± 25.6 MPa, 782.7 ± 16.1 MPa and 3.6 ± 0.5 % for the alloy containing 0.2 wt% Y_2O_3 nanoparticles and 476.5 ± 31.6 MPa, 685.3 ± 19.4 MPa and 2.5 ± 0.7 % for the alloy containing 0.6 wt% Y_2O_3 nanoparticles, respectively.
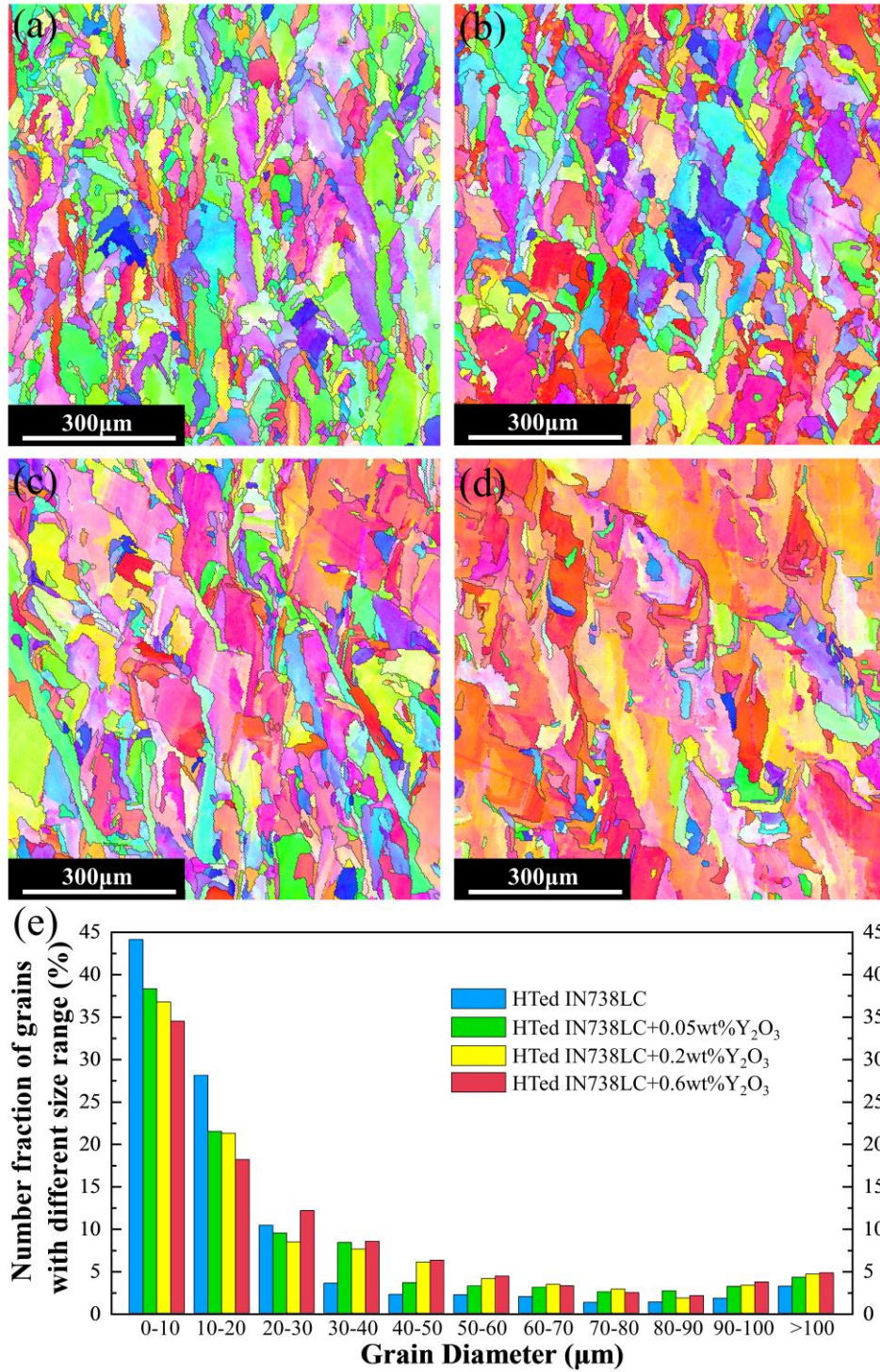
Figure 7.7. EBSD mapping of the samples in the X-Z section showing the grain structures of the heat-treated (HTed) alloys (a) without and containing (b) 0.05 wt%, (c) 0.2 wt% and (d) 0.6 wt% Y_2O_3, (e) the grain size distribution.

For the tensile properties at 850 $^{\circ}$C, however, the YS and the UTS are somewhat

improved with the addition of 0.05 wt% Y_2O_3 with 633.1 ± 8.9 MPa and 773.3 ± 5.2

MPa compare to 615.4 ± 13.5 MPa and 714.3 ± 11.3 MPa for the alloy without Y_2O_3,

while the EL is ~ 23 % lower. Further increasing the Y_2O_3 contents to 0.2 wt% and 0.6

wt%, the YS, the UTS and EL are 419.6 ± 17.4 MPa and 338.4 ± 20.9 MPa, 539.4 ±

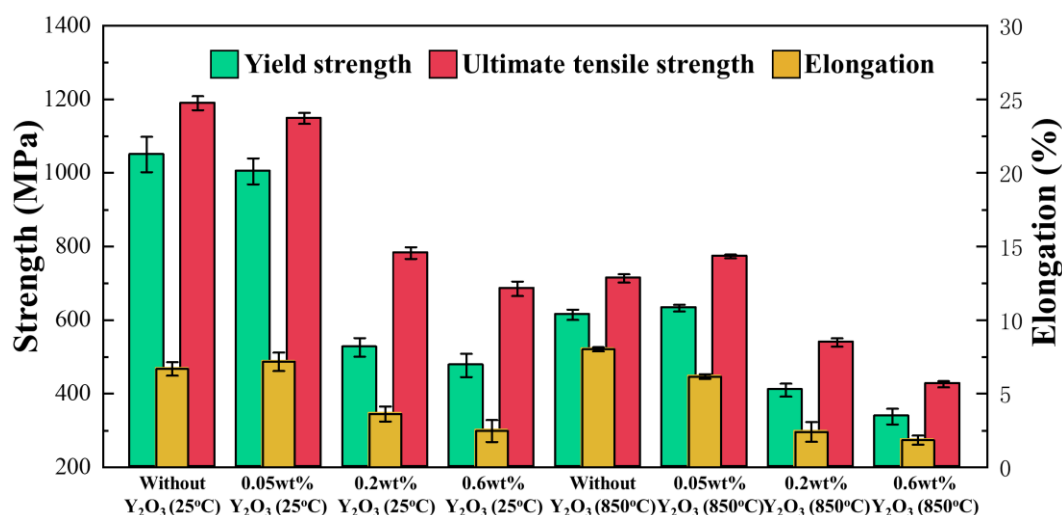11.3 MPa and 425.7 ± 8.1 MPa, 2.4 ± 0.7 % and 1.9 ± 0.3 %, respectively.

Figure 7.8. Tensile properties of the HTed alloys without and containing Y_2O_3 at room and high temperatures.

7.2.4. Oxidation resistance

7.2.4.1 Oxidation kinetics

Figure 7.9 (a) shows the mass gain of the alloys after heat treatment under the

conditions for adding various amounts of Y_2O_3 as a function of the exposure time at

1095 °C in the air atmosphere. The mass gain increases continuously with time for all

samples. The alloy containing 0.6 wt% Y_2O_3 exhibits the highest oxidation rate among

these alloys, followed by the alloy containing 0.2 wt% Y_2O_3 and the alloy without Y_2O_3.

The alloy containing 0.05 wt% Y_2O_3 has the best oxidation resistance. Figure 7.9 (b)

shows the mass gain rate as a function of the exposure time. The mass gain rate is

calculated as:

192

$$r_i = \frac{(\Delta m / A_s)_i - (\Delta m / A_s)_{i-1}}{T_o}$$
<div align="right">Equation 7.1</div>

where r_i is the mass gain rate in the current testing period, Δm is the mass change, A_s is the surface area, $(\Delta m/A_s)_i$ is the mass change per unit area in the current testing period, $(\Delta m/A_s)_{i-1}$ is the mass change per unit area in the previous testing period, and T_o is the testing period, i.e. 24 hours in the current experimental condition. For all the samples, the mass gain rate shows a gradual downward trend with the exposure time, implying that the oxidation rate gradually slows down with the progress of the oxidation tests. The oxidation kinetics curve in Figure 7.9 (a) can be described as a parabolic shape like [5]:

$$(\frac{\Delta m}{A_s})^2 = k_p t$$
<div align="right">Equation 7.2</div>

where k_p is the parabolic oxidation rate constant. The lower the k_p value is, the better the oxidation resistance. Table 7.2 lists the summary of the fitting results, and all the coefficients of determination R^2 are close to 1, indicating that the results fit well with a parabolic curve described in Equation 7.2. The addition of 0.05 wt% Y_2O_3 improves the oxidation resistance significantly. Compared with the alloy without Y_2O_3, the oxidation rate constant k_p decreases from 0.6 $mg^2cm^{-4}h^{-1}$ to 0.4 $mg^2cm^{-4}h^{-1}$. However, with further increase of the Y_2O_3 content, the oxidation resistance decreases, and the k_p values increase to 0.7 $mg^2cm^{-4}h^{-1}$ and 1.2 $mg^2cm^{-4}h^{-1}$ for the alloys containing 0.2 wt% and 0.6 wt% Y_2O_3, respectively.
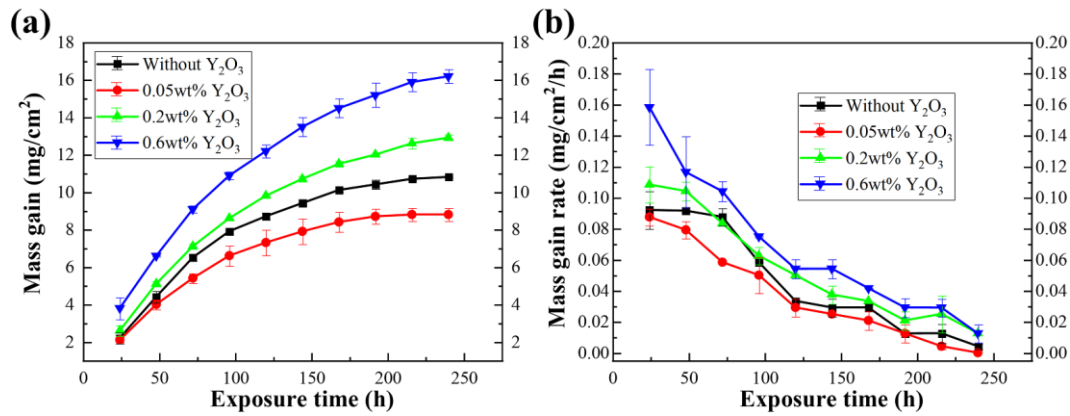
Figure 7.9. (a) Mass gain and (b) mass gain rate as a function of the exposure time for the HTed alloys without and containing Y$_2$O$_3$.

Table 7.2. Oxidation rate constant k_p in Equation 7.1 by fitting the experimental results.

Y$_2$O$_3$ content (wt%)	0	0.05	0.2	0.6
k_p (mg^{2}cm^{-4}h^{-1})	0.6	0.4	0.7	1.2
R^2	0.9	0.9	0.9	0.9

7.2.4.2 Oxide scale surface

Figure 7.10 shows the surface roughness and the three-dimensional (3D) reconstruction images of the oxide scale surfaces by laser scan confocal microscope (LSCM) of the alloys with various amounts of Y$_2$O$_3$ after the oxidation tests at 1095 ^{o}C for 240 hours. The alloy without Y$_2$O$_3$ has a surface roughness of 7.6 ± 0.2 μm, and a small nodular morphology is visible on the oxide scale surface (Figure 7.10 (a)). For the alloy containing 0.05 wt% Y$_2$O$_3$, it attains a relatively flat surface, and the surface roughness decreases to 5.5 ± 0.3 μm. With increasing the Y$_2$O$_3$ content, the oxide scale surfaces become rougher and more irregular with a surface roughness of 11.1 ± 0.2 μm for the alloy containing 0.2 wt% Y$_2$O$_3$ and 13.7 ± 0.3 μm for the alloy containing 0.6 wt% Y$_2$O$_3$. Large nodular structures appear on these oxide scale surfaces, as shown in Figures 7.10 (c) and 7.10 (d), leading to higher surface roughness. For the alloys, spalled zones are detectable on the oxide scale surfaces, which reduces the surface

quality as well. From the surface reconstruction images, the spallation phenomenon is more severe for the alloys containing 0.2 wt% and 0.6 wt% Y_2O_3.
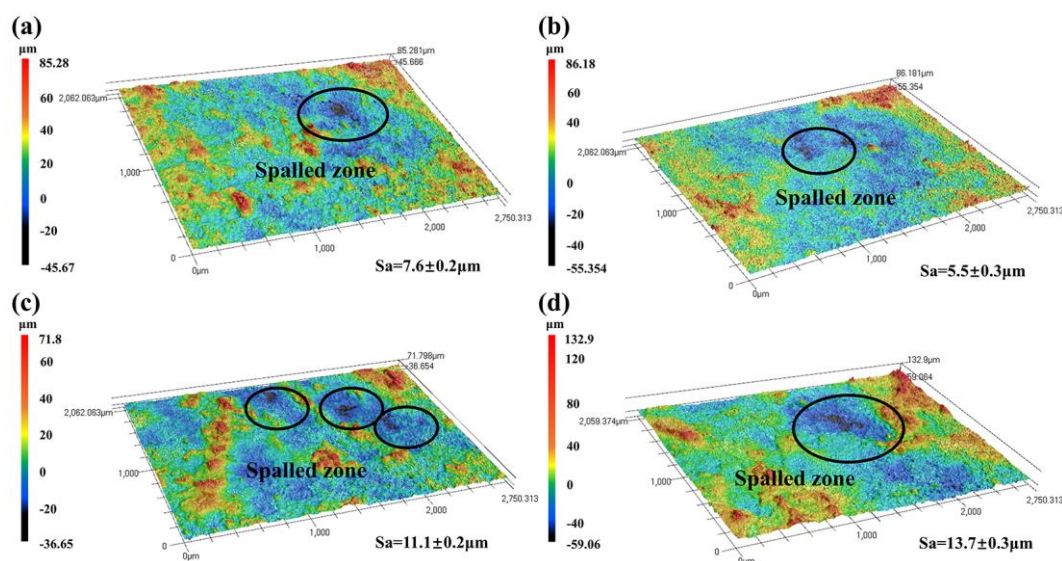

Figure 7.10. 3D reconstruction images of the oxide scale surfaces after the oxidation tests at 1095 °C for 240 hours of (a) the alloy without Y_2O_3 and the alloys containing (b) 0.05 wt%, (c) 0.2 wt% and (d) 0.6 wt% Y_2O_3 by LSCM and the corresponding surface roughness.

Figure 7.11 illustrates the oxide scale surface morphologies observed by scanning electron microscope (SEM) of the alloy samples at both low and high magnifications after the oxidation tests at 1095 °C for 240 hours. It is apparent that the addition of Y_2O_3 affects the morphology of the oxide scale surfaces of IN738LC fabricated by LPBF. A reasonably flat oxide scale is observed on the surfaces of the alloy without Y_2O_3 (Figure 7.11(a)) and the alloy with 0.05 wt% Y_2O_3 (Figure 7.11(c)). While the additions of 0.2 wt% and 0.6 wt% Y_2O_3 lead to many nodular structures on the oxide scale surfaces, as shown in Figures 7.11 (e)-7.11 (h).
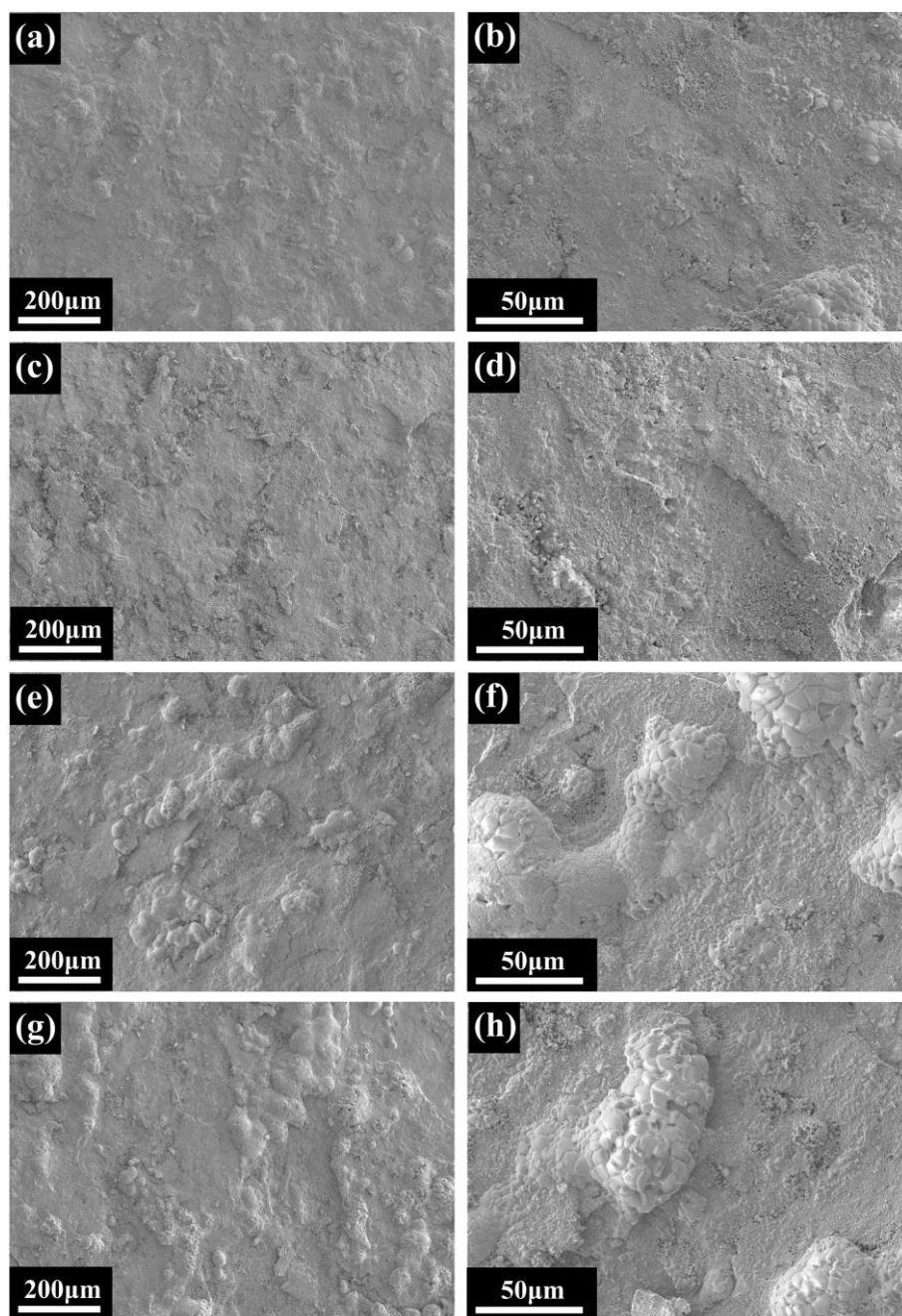
Figure 7.11. SEM images of the oxide scale surfaces after the oxidation tests at 1095 ºC for 240 hours of (a, b) the alloy without Y₂O₃ and the alloys containing (c, d) 0.05 wt%, (e, f) 0.2 wt% and (g, h) 0.6 wt% Y₂O₃ at low and high magnifications.

7.2.4.3 Oxidation product

Figure 7.12 shows the X-ray diffraction (XRD) analysis results of the alloys with various amounts of Y_2O_3 after the oxidation tests at 1095 ºC for 240 hours. It shows

196

that the main oxidation products are Al_2O_3, Cr_2O_3, NiO, $NiCr_2O_4$ and $CoCr_2O_4$. From the signal intensity in the XRD results, a large amount of Al_2O_3 forms in the oxide scale for the alloys without Y_2O_3 and containing 0.05 wt% Y_2O_3. With increasing the Y_2O_3 content, the diffraction peaks of Cr-rich oxides become stronger, considering $NiCr_2O_4$, $CoCr_2O_4$ and Cr_2O_3 as the primary oxidation products in the alloys containing 0.2 wt% and 0.6 wt% Y_2O_3. On the contrary, the intensity levels of Al_2O_3 are lower than those for the alloys without Y_2O_3 and containing 0.05 wt% Y_2O_3.
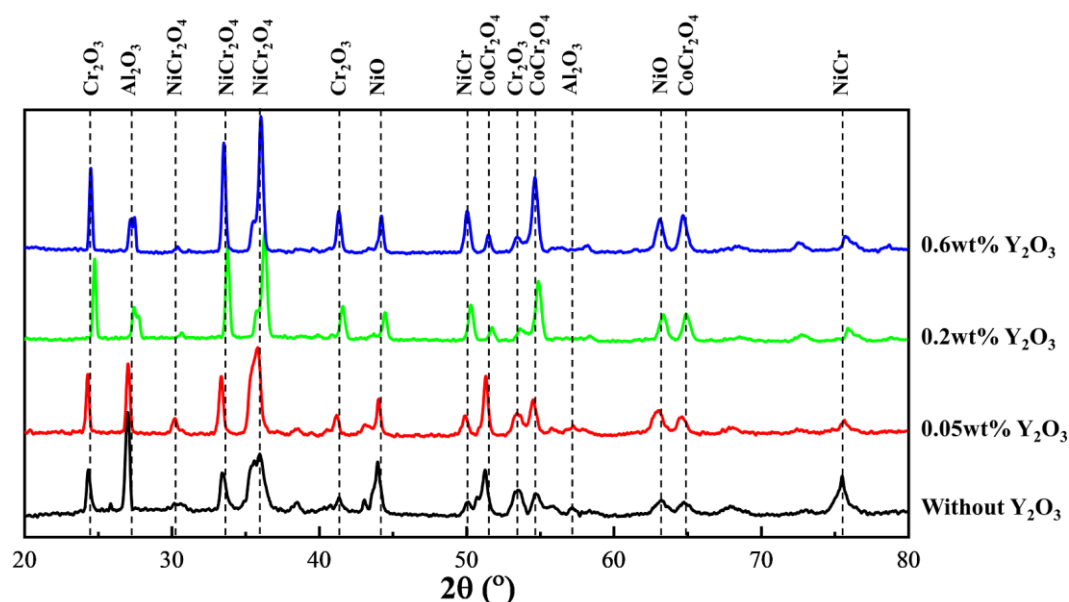

Figure 7.12. XRD patterns of the oxide scale surfaces after the oxidation tests at 1095 °C for 240 hours of the alloys with different contents of Y_2O_3 nanoparticles.

Figure 7.13 presents 3 different morphologies observed on the oxide scale surfaces, namely crystalline, lamellar and nodular structures. The crystalline structure contains Cr, O, Ni, Ti and Co, as shown in Figure 7.13 (g), considered a type of Cr-rich oxide. This research observes this kind of oxide in all samples among the 4 alloys. Figure 7.13 (h) shows that the lamellar oxide mainly contains Al and O. Combined with the results of XRD, it indicates the presence of Al_2O_3. Al_2O_3 is visible in the alloy without Y_2O_3 and the alloy containing 0.05 wt% Y_2O_3, but only rarely in the alloys containing 0.2 wt%

197

and 0.6 wt% Y_2O_3. EDS detects a large amount of Ni and O, implying that the nodular structure primarily comprises NiO, as shown in Figure 7.13 (i). These nodular structures scattering on the oxide scale surfaces are commonly observed in the alloy without Y_2O_3 and the alloys containing 0.2 wt% and 0.6 wt% Y_2O_3. Detailed observation, however, shows that NiO exists in the alloy containing 0.05 wt% Y_2O_3 as a blocky morphology (black arrows) ranging from 0.5 μm to 5 μm, as shown in Figure 7.14 (a), with Figure 7.14 (b) the EDS result.

Figure 7.15 shows the EDS chemical mapping analysis results of the oxide scale for the alloy without Y_2O_3 after the oxidation tests at 1095 ºC for 240 hours. The oxidation products compose of O, Al and Cr but heterogeneously distribute in the oxide scale. The Al_2O_3 and Cr-rich oxides compete with each other, i.e., little Cr-rich oxide found in the regions rich in Al_2O_3 and vice versa. As Al_2O_3 is the main constituent that occupies a large part of the oxide scale, this scale is defined as an Al-type scale. This research observes the enrichment of Cr to be associated with O in the oxide scale, considered as Cr-rich oxide. A thin layer rich in Cr is visible in the outer layer of the oxide scale. Combined with the XRD results, it is reasonable to infer that this layer is spinel oxide such as $CoCr_2O_4$ and $NiCr_2O_4$. However, the microstructure and the chemical composition distribution are quite different for the alloy containing 0.6 wt% Y_2O_3, as shown in Figure 7.16. This scale composes largely of oxides with a high concentration of Cr. In this Cr-type oxide scale, however, the formation of Al_2O_3 is found underneath the Cr-rich layer with an irregular and discontinuous morphology extending down into the parent metal.
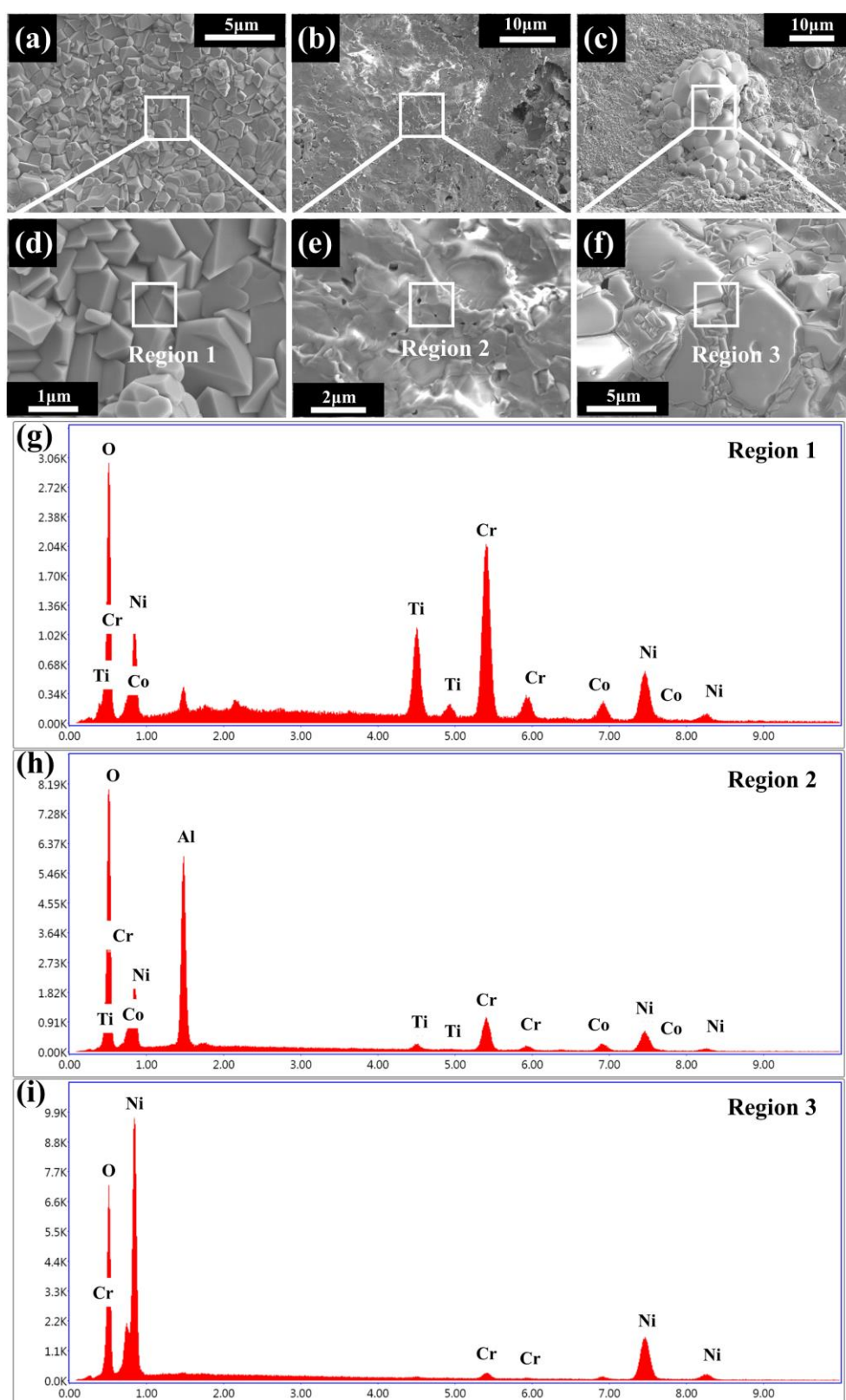
Figure 7.13. SEM images of the oxide scale surfaces after the oxidation tests at 1095 °C for 240 hours of the alloy without Y₂O₃, indicating 3 different morphologies, i.e., (a, d) crystalline, (b, e) lamellar and (c, f) nodular, (g), (h) and (i) showing the EDS analysis on the corresponding morphological regions.
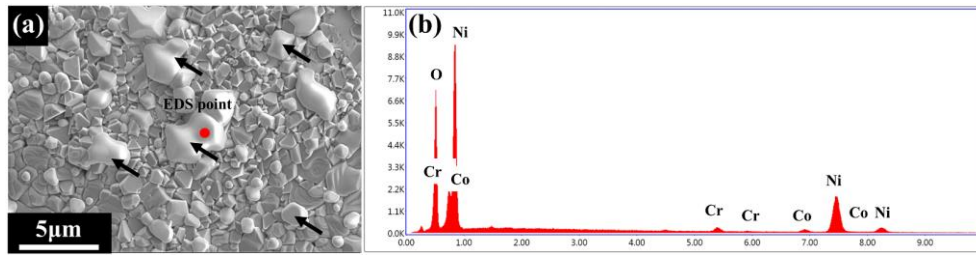
Figure 7.14. (a) SEM image of the nodular structures after the oxidation tests at 1095 °C for 240 hours of the alloy containing 0.05 wt% Y_2O_3 and (b) the corresponding EDS result.
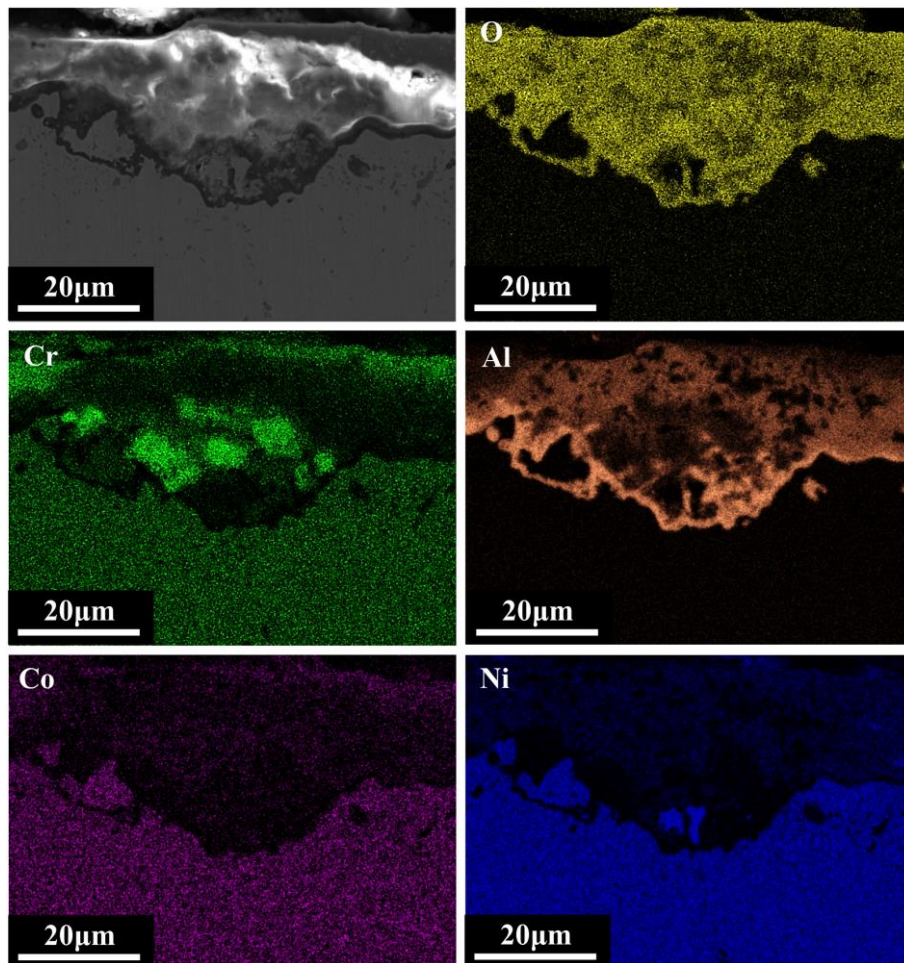

Figure 7.15. EDS chemical composition mapping of the oxide scale after the oxidation tests at 1095 °C for 240 hours of the alloy without Y_2O_3.
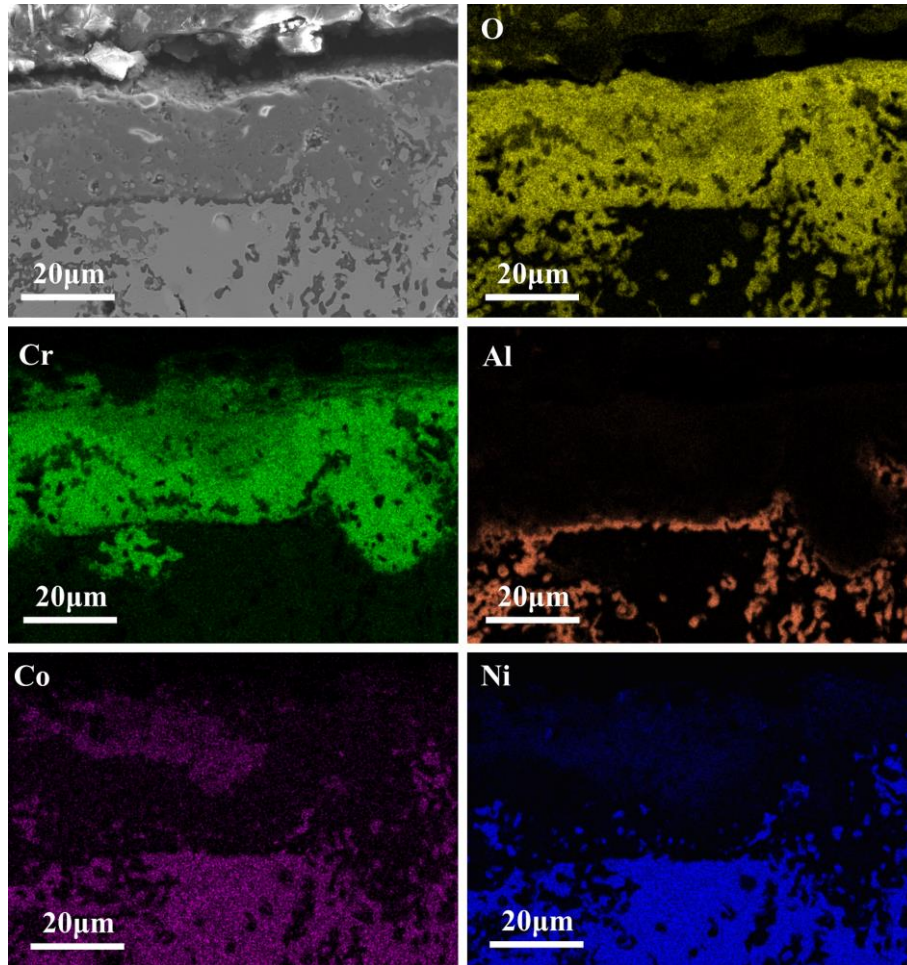
Figure 7.16. EDS chemical composition mapping of the oxide scale after the oxidation tests at 1095 ºC for 240 hours of the alloy containing 0.6 wt% Y$_2$O$_3$.

Figure 7.17 shows the SEM cross-sections of the oxide scales for the alloys without and containing 0.05 wt% Y$_2$O$_3$ at both low and high magnifications after the oxidation tests at 1095 ºC for 240 hours. Similar to Figure 7.15, the oxide scale comprises a thin upper Cr-rich layer (5-10 μm typically) and a thicker Al$_2$O$_3$ sublayer (15-25 μm typically). Figures 7.17 (e) and 7.17 (f) show the compositions from EDS analysis. Both layers are mostly continuous. The parent metal beneath these layers is fully continuous as well. In Figure 7.18, for the alloys containing 0.2 wt% and 0.6 wt% Y$_2$O$_3$, the parent metal beneath the oxide scales is strongly discontinuous with significant jagged lines of Al$_2$O$_3$ presence (Figure 7.18 (e)). But now there is no longer

a mostly continuous Al_2O_3 layer near the surface, just a Cr-rich layer (Figure 7.18 (f)).

These observations are consistent with the high-magnification results shown in Figure

7.16.

Figure 7.17. SEM images of the oxide scales after the oxidation tests at 1095 ºC for 240 hours of the alloys (a, b) without and (c, d) containing 0.05 wt% Y_2O_3 at low and high magnifications, (e) EDS result of Region 1 and (f) EDS result of Region 2.
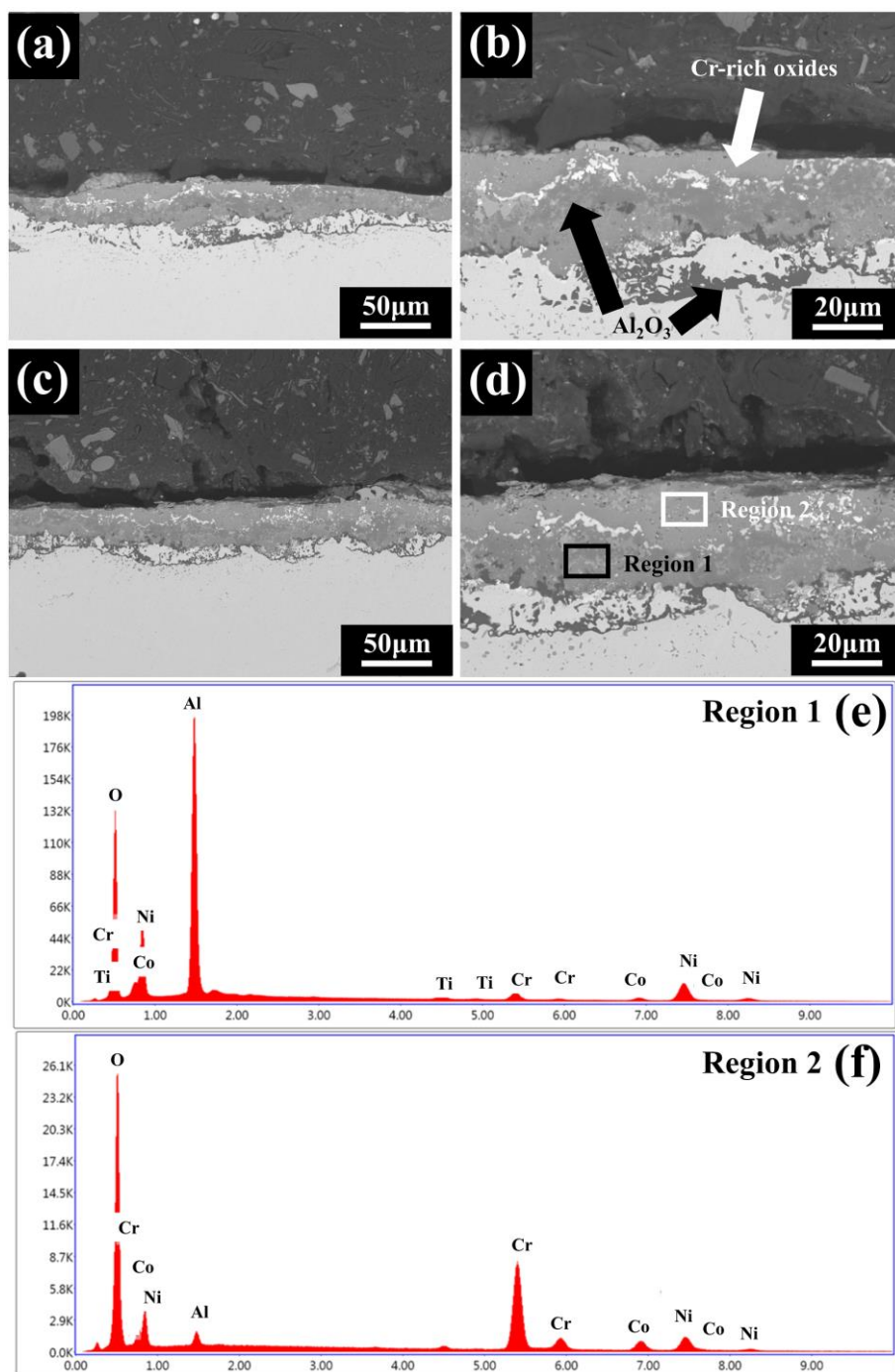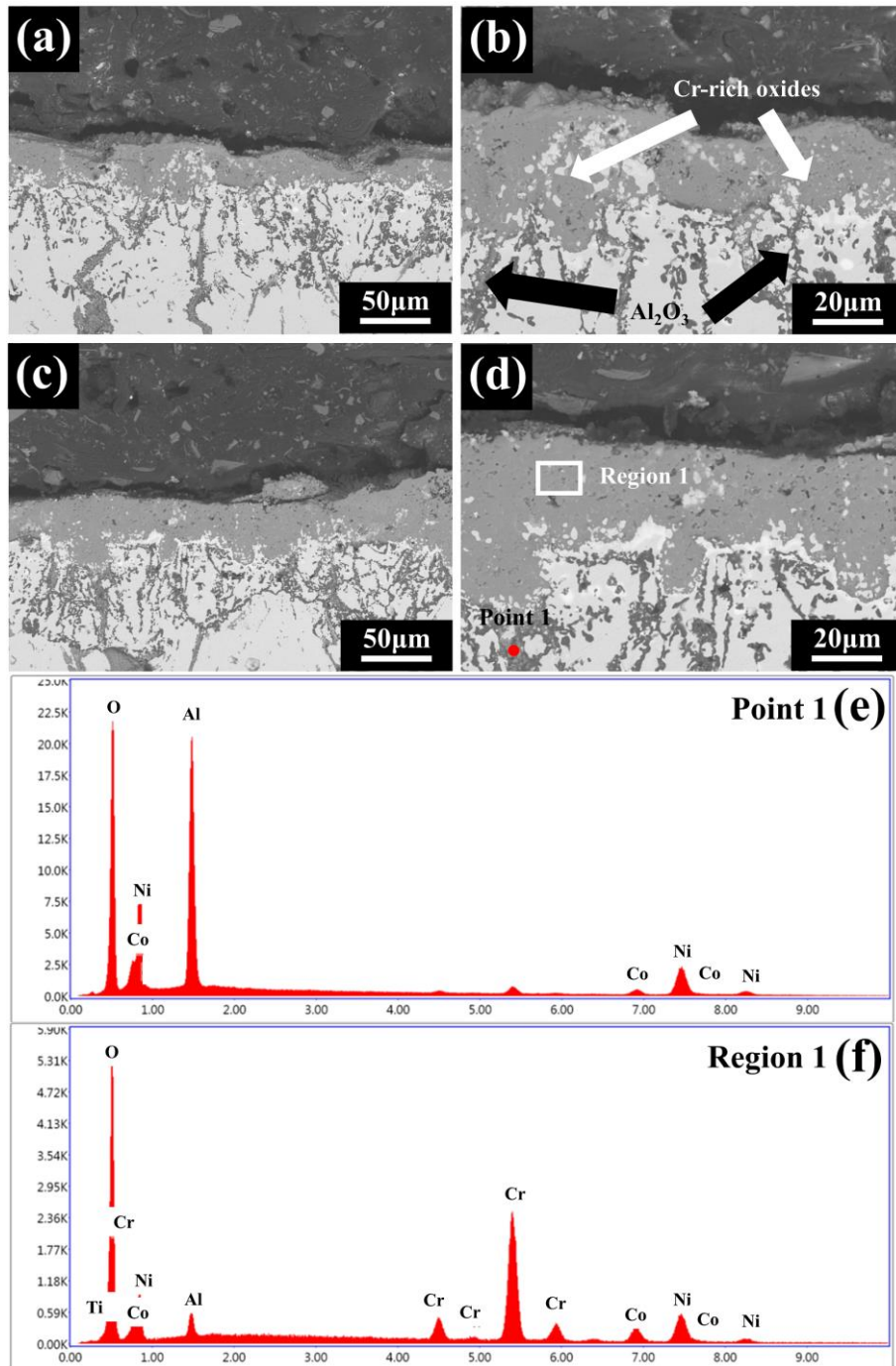
Figure 7.18. SEM images of the oxide scales after the oxidation tests at 1095 ºC for 240 hours of the alloys containing (a, b) 0.2 wt% and (c, d) 0.6 wt% Y₂O₃ at low and high magnifications, (e) EDS result of Point 1 and (f) EDS result of Region 1.
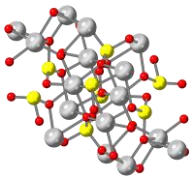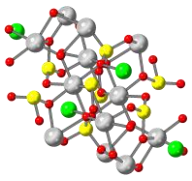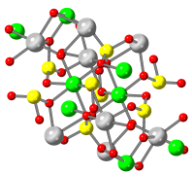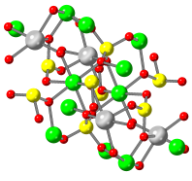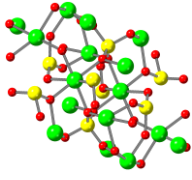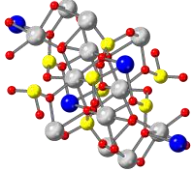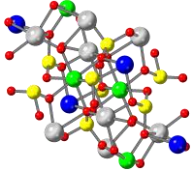
7.3. Discussions
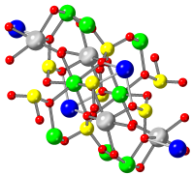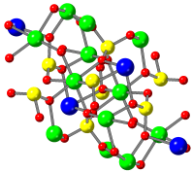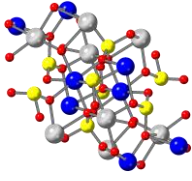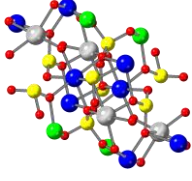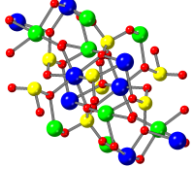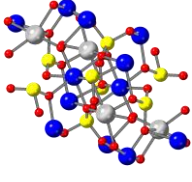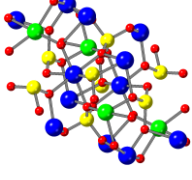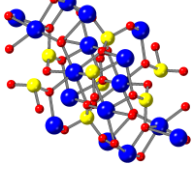
7.3.1. Effects of Y_2O_3 on cracking behaviour

The cracking mechanism has been discussed in Section 6.2.2.1. Segregation of Zr in the grain boundary regions reduces the solidus of the alloy and promotes the formation of solidification cracking due to the remaining liquid at the last stage of solidification under high thermal stress. Adding 0.05 wt% Y_2O_3 nanoparticles promotes Zr and Nb atoms to segregate into the YAM-particles, as shown in Figure 7.6 (f), thus reducing the residual Zr's concentration in the last solidified liquid and correspondingly mitigating the cracking in the LPBFed IN738LC samples. Previous researches have reported the reaction between Zr and Y_2O_3. Zhang et al. [6] added 0.9 wt% Zr into 14Cr-Y_2O_3-oxide dispersion strengthened (ODS) alloy. The UTS and the EL of the alloy were improved by fine $Y_4Zr_3O_{12}$ particles due to their strong pinning effect and interface bonding force with the matrix. Similarly, Xu et al. [7] studied hot isostatic pressed the Fe-15Cr-2W-0.3Y_2O_3 alloy with the addition of 0.3 wt% Zr and detected the formation of trigonal δ-$Y_4Zr_3O_{12}$ phase. This research finds no $Y_4Zr_3O_{12}$ through the FFT analysis in the microstructure, implying that $Y_4Al_2O_9$ may preferentially form in the alloy containing Al. Zr and Nb have similar ionic radiuses to Y and locate next to Y in the periodic table of the elements (ionic radiuses are 0.9 Å, 1.1 Å, 1.0 Å, and atomic numbers are 39, 40, 41 for Y, Zr and Nb, respectively) [8], indicating that Zr and Nb have similar chemical characteristics with Y and may thermodynamically occupy the crystallographic sites of Y atoms in the $Y_4Al_2O_9$ particles. To prove the possibility

of this reaction, density-functional theory (DFT) calculations are conducted using the projection-augmented wave (PAW) method, where the crystal lattices fully relax until the total force on each atom is less than 0.02 eV/Å [9]. Table 7.3 displays the formation energy and the corresponding crystal structure. The values of the formation energy for all the structures are negative, indicating that Zr and Nb atoms have thermodynamical potential to replace Y in the YAM lattice. Presumably, $Y_4Al_2O_9$ forms at the early stage of solidification due to its high melting point (melting point 2020 $^{\circ}$C [10]), and a considerable amount of Zr dissolves into the $Y_4Al_2O_9$ particles. As a result, the segregation of Zr is effectively hindered, and the risk of cracking correspondingly decreases. As a result, the process window of the IN738LC alloy processed by LPBF is enlarged due to the mitigation of cracking by avoiding the segregation of Zr. However, Figures 7.3 and 7.4 show that more Y_2O_3 additions induce more cracks in the alloys. In the process of solidification, the formation of $Y_4Al_2O_9$ particles at the early stage of solidification may lead to huge clusters in the grain boundary regions. As a result, the strength of grain boundaries is further impaired due to the poor bonding between the particle clusters and the material matrix. Therefore, excessive Y_2O_3 additions (0.2 wt% and 0.6 wt%) adversely affect the cracking resistance of the IN738LC alloy processed by LPBF.

Table 7.3. DFT calculation results of the formation energy of the possible crystal structures, where Zr and Nb occupy the crystallographic sites of Y atoms in the $Y_4Al_2O_9$ lattice and the schematic diagrams of the corresponding crystal structures.

Chemical formula	Total energy (eV)	Formation energy (eV)	Formation energy/atom (eV/atom)	Crystal structure[a]
$Y_4Al_2O_9$	-517.3	-300.4	-5.0	
$Y_3NbAl_2O_9$	-514.9	-270.0	-4.5	
$Y_2Nb_2Al_2O_9$	-514.8	-242.0	-4.0	
$YNb_3Al_2O_9$	-512.2	-211.4	-3.5	
$Nb_4Al_2O_9$	-519.4	-190.7	-3.2	
$Y_3ZrAl_2O_9$	-514.5	-276.4	-4.1	
$Y_2ZrNbAl_2O_9$	-513.4	-247.4	-4.1	

YZrNb$_2$Al$_2$O$_9$	-515.0	-221.0	-3.7	
ZrNb$_3$Al$_2$O$_9$	-516.2	-194.2	-3.2	
Y$_2$Zr$_2$Al$_2$O$_9$	-518.3	-259.0	-4.3	
YZr$_2$NbAl$_2$O$_9$	-520.3	-233.0	-3.9	
Zr$_2$Nb$_2$Al$_2$O$_9$	-518.1	-202.9	-3.4	
YZr$_3$Al$_2$O$_9$	-519.2	-238.8	-4.0	
Zr$_3$NbAl$_2$O$_9$	-518.5	-210.1	-3.5	
Zr$_4$Al$_2$O$_9$	-520.0	-218.3	-3.6	

[a] ⬤Y ⬤Al ⬤O ⬤Zr ⬤Nb

207

7.3.2. Effects of Y_2O_3 on microstructure

Emerging grain morphology is determined by cooling rate R_T (ºC/s), solidification rate V_T (m/s) and thermal gradient G_T (ºC/m) during solidification [11]. As depicted in Figure 7.19 (a), with the decrease of G_T/V_T, grain structure gradually changes from planar grain to cellular grain and columnar grain, and finally equiaxed grain with processing. The decrease of $G_T V_T$ (= R_T) leads to an increase of the grain size within the corresponding grain mode [12]. Figure 7.5 exhibits that the columnar grains dominate the microstructure of IN738LC fabricated by LPBF, primarily attributed to the considerably high thermal gradient in the solidification process, as schematically shown in Figure 7.19 (c). Moreover, it is apparent that the addition of Y_2O_3 causes the grain size to increase from 16.7 ± 1.4 μm to 27.5 ± 1.7 μm, 29.7 ± 1.4 μm and 36.8 ± 2.5 μm for the addition of 0.05 wt%, 0.2 wt% and 0.6 wt% Y_2O_3 nanoparticles, respectively. There is a traditional theory and practice that the added nanoparticles can be heterogeneous nucleus to refine grains [13-16]. In this research, however, the grain structure is actually coarsened by incorporating Y_2O_3. $Y_4Al_2O_9$ is a type of thermal barrier material due to its low thermal conductivity at high temperatures [10]. The thermal conductivity of $Y_4Al_2O_9$ is only ~ 1/16 of that of IN738LC at the same temperature levels [17, 18], thus effectively impeding the thermal diffusion in the alloy during solidification. To evaluate the effects of the $Y_4Al_2O_9$ particles on the thermal diffusion in the melt during solidification, a laser flash method is used to measure the thermal diffusivity at 5 different temperatures between the solidus and the liquidus of the samples in the APed condition. The results are presented in Figure 7.19 (b), showing

that the thermal diffusivities are lower for the alloys containing Y_2O_3 than the alloy without Y_2O_3 in the whole measured temperature range. The thermal diffusion coefficient decreases continuously with the increase of the Y_2O_3 nanoparticle amount. Therefore, this research makes a speculative hypothesis that these dispersed $Y_4Al_2O_9$ nanoparticles can significantly retard the heat dissipation from the current location to the surrounding material during solidification due to their low thermal conductivity characteristic and decrease the cooling rate of solidifying melt [19], accordingly leading to coarser microstructures. Figure 7.19 (d) schematically shows this mechanism. However, since the additional amounts are at such a low level, it is worth investigating deeply in the latter research the effects of Y_2O_3 on the thermal diffusion as well as the grain structure during such a rapid cooling process.
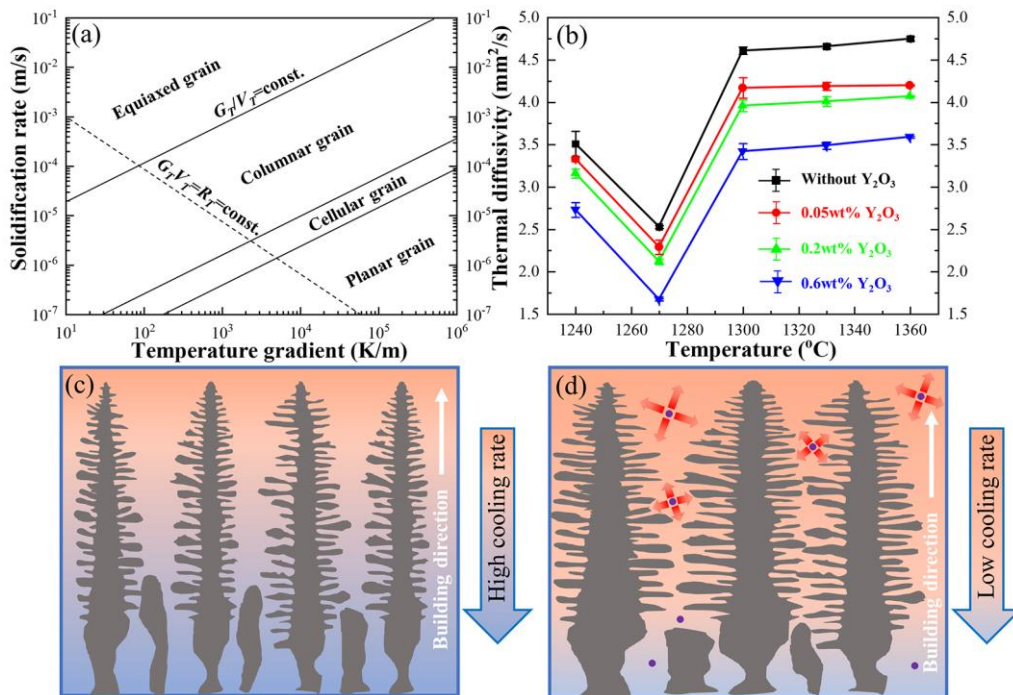
Figure 7.19. (a) Schematic diagram of the grain mode related to cooling rate, solidification rate and temperature gradient, (b) thermal diffusivity as a function of temperature for the APed alloys without and containing Y_2O_3, schematic diagrams of the solidification process in the APed alloys (c) without and (d) containing Y_2O_3 during LPBF.

7.3.3. Effects of Y_2O_3 on mechanical properties

The strength of IN738LC is degraded by adding 0.05 wt% Y_2O_3 nanoparticles at room temperature. This can be explained by the Hall-Petch relationship [20] shown in the equation:

$$\sigma_{ys} = \sigma_o + K \times D_g^{-1/2}$$
<div align="right">Equation 7.3</div>

where σ_{ys} is the yield stress, σ_o is the constants corresponding to the starting stress for the movement of dislocation, K is the strengthening coefficient, and D_g is the average grain size. In the process of tensile testing, dislocations glide along the movement of the dislocation line on its slip surface under the action of external force, leading to plastic deformation. High dislocation densities in the grain boundary regions indicate stress concentration in these regions due to that dislocations pile up at front of grain boundaries, which determines the yield stress of materials [21]. The average grain size of the alloy containing 0.05 wt% Y_2O_3 is significantly greater than the alloy without Y_2O_3 in both APed and HTed conditions, leading to fewer grain boundaries and reducing the strength of the 0.05 wt% Y_2O_3-containing alloy. At the temperatures higher than the equicohesive temperature (T_{eq}), the plastic deformation of crystal can be promoted by grain boundary sliding, migration and accelerated diffusion of elements, therefore, grain boundary strength is lower than the grain interior strength [22]. Figure 7.20 illustrates the strength evolution with temperature change [23]. It is reasonable to assume that the T_{eq} for IN738LC is well below the testing temperature (850 ℃), thus the grain interior strength becomes higher than the grain boundary strength in the high-temperature tensile testing, implying that a relatively coarse microstructure is beneficial

for tensile strength. Therefore, the strength of the alloy containing 0.05 wt% Y_2O_3 is superior to that of the alloy without Y_2O_3 at 850 ºC, as shown in Figure 7.8. Effects of grain size on creep behaviour may be more obvious than tensile properties, and the grain coarsening by adding 0.05 wt% Y_2O_3 may be more beneficial on the creep property. Xu et al. [24] in their recent investigation proved that the short-term creep behaviour of nickel-based superalloys could be evaluated by slow-strain-rate tensile testing as well. That is to say, grain size is still a key factor affecting the tensile properties at both room and elevated temperatures in the current investigation. For the inferior mechanical properties in the alloys with 0.2 wt% and 0.6 wt% Y_2O_3, it can be explained by the high crack density in these samples, as presented in Figures 7.3 and 7.4.
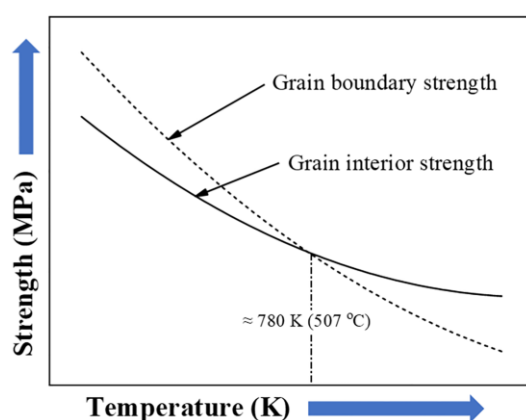
Figure 7.20. Schematic illustration of the strength as function of temperature for the IN738LC alloy, the approximate equicohesive temperature is marked with a dotted line. [23].

7.3.4 Effects of Y_2O_3 on oxidation behaviour

Effects of grain size on oxidation behaviour have been widely investigated among metallic and ceramic materials [25, 26]. Jo et al. [27] examined the internal oxidation behaviour of as-received and grain-refined Alloy 617 at 950 ºC up to 2000 hours. They

found that the internal oxidation rate of the grain-refined alloy increased rapidly at the testing initial stage and gradually decreased during prolonged exposure, while the as-received alloy exhibited a constant oxidation rate during the whole oxidation process. Besides, they observed large cracks due to the high stress concentration from the longer internal oxides in the as-received alloy. Short cracks in the grain-refined sample scattered near the surface due to relatively low stress concentration related to more densely stretched internal oxides. Pérez [28] suggested that fine grains were beneficial for oxidation resistance due to increased nucleation of Al_2O_3 particles, which led to the formation of a pure Al_2O_3 scale and increased the oxidation resistance. The improvement of oxidation resistance by refined grains is widely reported [29, 30], which is primarily due to the acceleration of diffusion of protective elements to form oxide scales related to more grain boundaries. In this research, the addition of Y_2O_3 leads to coarser grains and then potentially causes the increase of oxidation rate, as shown in Figure 7.9. However, 0.05 wt% Y_2O_3 is favourable to improve the oxidation resistance. Therefore, the effects of Y_2O_3 need to be discussed in further details.

Based on the XRD and EDS results in Figures 7.12 and 7.13, the main oxides found are Al_2O_3, Cr_2O_3, NiO, $NiCr_2O_4$ and $CoCr_2O_4$. According to typical oxidation theory, the more stable the oxide is, the more preferentially the corresponding element is oxidised. In the alloy systems of Ni-Cr-Al such as IN738LC, the oxidation priority of the main elements is Al > Cr > Ni according to both thermodynamic and kinetic potentials, indicating Al_2O_3 forms firstly followed by Cr and Ni oxides. However, the affinity with O_2 is not the only factor deciding the oxidation behaviour [31]. The

formation of Al_2O_3 has an important effect of hindering O_2 diffusion through it and prevents the oxidation progress with other elements in the parent alloy. Cr_2O_3 can react with NiO and CoO to form $NiCr_2O_4$ and $CoCr_2O_4$ by the reactions:

$$Cr_2O_3 + NiO \text{ (or } Ni + 1/2O_2) = NiCr_2O_4 \qquad \text{Equation 7.4}$$

$$Cr_2O_3 + CoO \text{ (or } Co + 1/2O_2) = CoCr_2O_4 \qquad \text{Equation 7.5}$$

XRD also indicates the formation of $NiCr_2O_4$ and $CoCr_2O_4$, as shown in Figure 7.12. $NiCr_2O_4$ and $CoCr_2O_4$ belong to the group of spinel oxide [31, 32], and Figures 7.13 (a) and 7.13 (d) show its typical morphology. Zhou et al. [33] proposed that Ni cations diffused slowly in the structure of $NiCr_2O_4$, indicating that $NiCr_2O_4$ could inhibit the diffusion of Ni cations and thus improve the oxidation resistance. Sun et al. [31] believed that $NiCr_2O_4$ improved the oxide scale's compactness and further prevented the alloy from reacting with O_2.

Previous studies [31] found $YCrO_3$ in the alloy containing Y_2O_3 during the oxidation tests. $YCrO_3$ forms according to the reaction:

$$Cr_2O_3 + Y_2O_3 = 2YCrO_3 \qquad \text{Equation 7.6}$$

$YCrO_3$ is a type of perovskite structure with symmetric P*bnm* space. The melting point of $YCrO_3$ is ~ 2290 °C [34]. High thermal and structural stabilities of $YCrO_3$ lead it to be inclusions in the oxide scale, which deteriorates the exfoliation resistance. Moreover, Sun et al. [31] reported that $YCrO_3$ favoured creating compressive stress on crystal grains of the matrix phase, and then the oxide scale cracked and peeled off with the accumulation of stress. However, the $YCrO_3$ peak is not found in the XRD analysis in this research, since it is difficult to produce a complete diffraction pattern for XRD to

213

detect when the content of a phase is too low in the multiphase mixture.

From Figure 7.9, adding 0.05 wt% Y_2O_3 reduces the oxidation rate of the LPBF-processed IN738LC component. The result is consistent with previous reports for Fe-Cr alloy [35] and austenitic stainless steel [36]. In the study of Stringer et al. [37], rare earth element oxide particles such as Y_2O_3 and CeO_2, acted as nucleation centres for oxides, especially Cr_2O_3, promoting the formation of Cr_2O_3. It is possible that more spinel oxides, i.e., $NiCr_2O_4$ and $CoCr_2O_4$, form in the oxidation cycle in the alloy containing 0.05 wt% Y_2O_3, related to the observation in Figure 7.17 and the XRD analysis in Figure 7.12. As a result, it reduces the oxidation rate due to the formation of more spinel oxides. Moreover, Bautista et al. [38] believed that Y_2O_3 improved the adherence and the resistance of oxide scales to spallation, which was also favourable to improve the oxidation resistance of alloys. However, a further increase of Y_2O_3 up to 0.2 wt% has a negative effect on the oxidation resistance. This is ascribed to the low amount of Al_2O_3 in the oxide scales of the alloys containing 0.2 wt% and 0.6 wt% Y_2O_3, as Al_2O_3 is believed to be more effective to prevent materials from being oxidised than Cr_2O_3 [39].

The oxides are mainly composed of Al_2O_3 for the alloy without Y_2O_3 and the alloy containing 0.05 wt% Y_2O_3, as depicted in Figure 7.17. When more Y_2O_3 nanoparticles are added to the IN738LC alloy, Cr_2O_3 and other Cr-rich oxides become the dominant oxides in the scale, and the formation of Al_2O_3 is largely limited to the jagged regions penetrating down into the parent metal. The finding of Giggins et al. [40] in 1971 can explain the change of the oxide scale from Al-type to Cr-type by the addition of Y_2O_3.

They argued that there were 3 different mechanisms of oxidation in the system of Ni-Cr-Al according to the alloy's different compositions. The oxide scale in the first mechanism (I) comprises a layer of NiO with a subscale of Al_2O_3 and Cr_2O_3 in the matrix, while the second (II) type is a layer of Cr_2O_3 with an Al_2O_3 subscale in the matrix, and the third (III) one is a continuous layer of Al_2O_3. Figure 7.21 presents the isothermal diagram exhibiting the compositional limits for these 3 mechanisms of oxidation in the Ni-Cr-Al system. The chemical composition of IN738LC is almost at the borderline between Mechanism II and Mechanism III, indicating even a slight reduction in Al content can completely change the oxidation behaviour of the IN738LC alloy. The added Y_2O_3 can react with Al to form $Y_4Al_2O_9$, which effectively consumes Al in the alloy's composition, as shown in Figure 7.6 (f). Presumably, the addition of Y_2O_3 reduces the amount of Al in the microstructure, inducing the change of the oxide scale from a continuous layer of Al_2O_3 (Mechanism III, Figure 7.17) to a layer of Cr_2O_3 with an Al_2O_3 subscale in the parent alloy (Mechanism II, Figure 7.18).
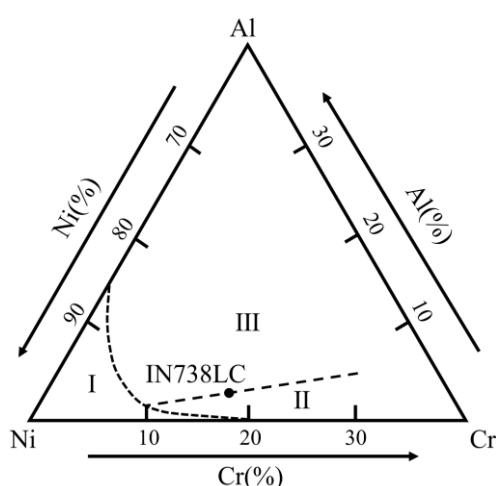
Figure 7.21. Isothermal diagram showing the compositional limits for 3 mechanisms of oxidation in the Ni-Cr-Al system [40].

Furthermore, Lou et al. [41] suggested that the increase of grain size altered the

oxide scale formed on the surface from Al-type into Cr-type, where the diffusion of Al atoms was delayed due to the relatively small number of grain boundaries in the coarse microstructure. The minimum Al concentration N_{Al} required to form an Al_2O_3 scale in the pure oxidising condition is given by Wagner [42, 43]:

$$N_{Al} = (\frac{0.3\pi V_m N_o D_o}{3V_{ox}D_{Al}})^{0.5}$$
Equation 7.7

where V_m is the alloy's molar volume, N_o is the concentration of O atoms, D_o is the diffusivity of O atoms in the alloy, V_{ox} is the molar volume of Al_2O_3, and D_{Al} is the diffusivity of Al atoms in the alloy. The diffusion at grain boundaries is more rapid than that inside the grains. The addition of Y_2O_3 leads to coarse grains and a relatively small number of grain boundaries, which decreases the diffusivity of Al atoms and further increases N_{Al}. Therefore, the critical Al concentration required for the formation of the Al_2O_3 scale increases, indicating the Al_2O_3 scale is suppressed. On the contrary, the formation of Al_2O_3 is facilitated by a relatively fine microstructure in the alloy without Y_2O_3.

From Figures 7.10 and 7.11, the high surface roughness is attributed to the spallation phenomenon and the nodule structures on the oxide scale surfaces. Spallation occurs when the stress is larger than the adhesion between the parent alloy and the oxide scale in materials [44]. Severe spallation of the oxide scales for the alloys containing 0.2 wt% and 0.6 wt% Y_2O_3 after the oxidation tests at 1095 °C for 240 hours is found in Figures 7.22 (a)-7.22 (d). The oxide scales crack and peel off from the parent alloy, which plays an important role in leading to a high oxidation rate.
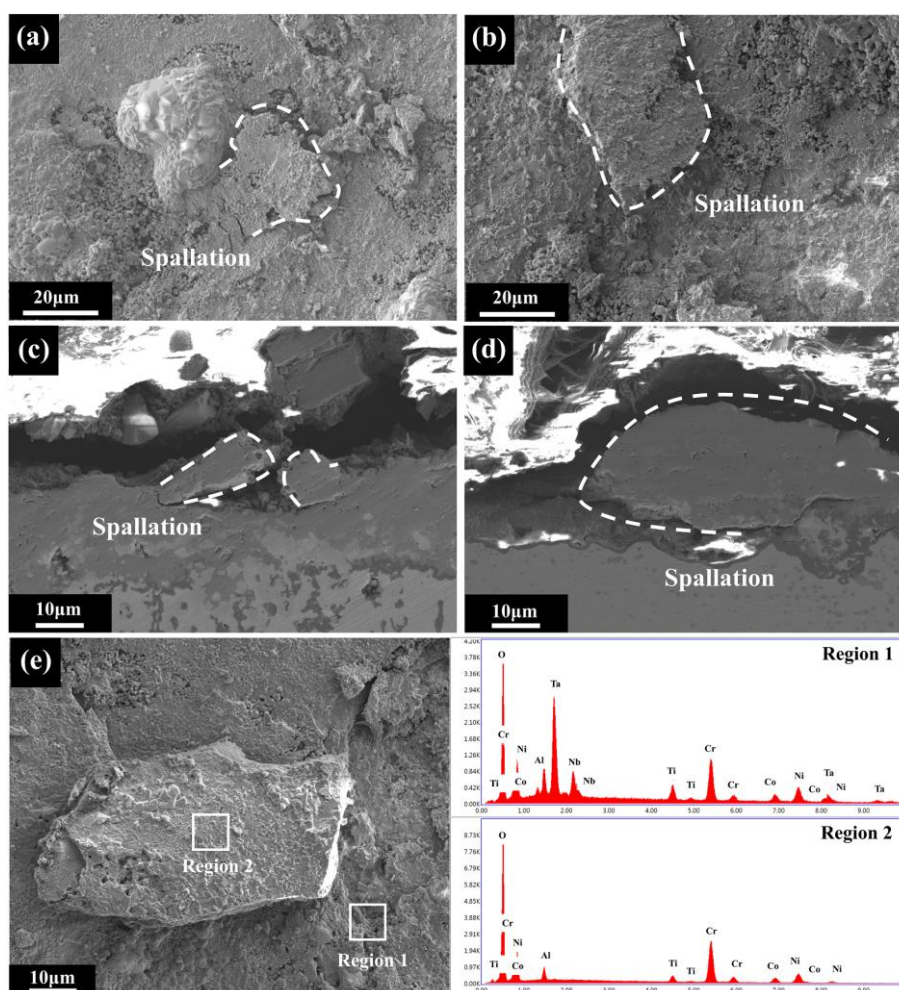
Figure 7.22. SEM images of the spallation phenomenon after the oxidation tests at 1095 ºC for 240 hours observed from the oxide scale surfaces of the alloys containing (a) 0.2 wt% and (b) 0.6 wt% Y_2O_3 and from the oxide scale cross-sections of the alloys containing (c) 0.2 wt% and (d) 0.6 wt% Y_2O_3, (e) an example of the oxide scale spallation and the corresponding EDS results.

In addition, as aforementioned, more cracks generate in the alloys containing 0.2 wt% and 0.6 wt% Y_2O_3. Sun et al. [31] suggested that defects were generated due to the development of a weak nanoparticle-matrix bonding when excess nanoparticles were added, related to the grain boundary segregation and the capillary force. Evans et al. [45] reported that the oxide scale wrapped first at the "pre-existing interfacial flaw" under the action of compressive or tensile stress perpendicular to the interface generated on the periphery of warping, leading to expansion of warping and cracks in the oxide scale. Spallation occurs when the cracks go through the oxide scale. Similarly, Rahmel

217

et al. [46] summarised the critical strain equation for the oxide scale rupture:

$$-\varepsilon_c = \frac{K_{IC}}{f_g(\pi a_d)^{1/2}} \cdot \frac{1 + r_O/d_O}{2E_O/(1 + \upsilon_O)}$$ Equation 7.8

where $-\varepsilon_c$ is the critical strain, K_{IC} is the fracture toughness, f_g is the geometric factor, a_d is the size of defect at the interface, r_O is the length of oxide intrusion into the matrix for a wavy interface, d_O is the thickness of oxide scale, E_O is the elasticity modulus of oxide scale, and υ_O is the Poisson's ratio of oxide scale. According to Equation 7.8, large defects and thick oxide scales in the alloys containing 0.2 wt% and 0.6 wt% Y_2O_3 are favourable to reduce the value of $-\varepsilon_c$ and directly increase the risk of spallation.

The Pilling-Bedworth ratio (PBR) [47] is the ratio of oxide volume to metal volume, as determined in Equation 7.9:

$$PBR = \frac{M_O \times \rho_M}{A_M \times i \times \rho_O}$$ Equation 7.9

where M_O is the molar mass of oxide molecules, ρ_M is the density of metal, A_M is the molar mass of metal atoms, ρ_O is the density of oxide, and i is the number of metal atoms in the corresponding oxide molecule. PBR is useful in determining the integrity of an oxide scale. The higher the PBR value, the more easily the oxide scale peels off. Table 7.4 [8] shows the values used to calculate PBRs. Using Equation 7.9, the calculated PBRs of Al_2O_3, NiO and Cr_2O_3 are 1.3, 1.7 and 2.0, respectively, indicating that Cr_2O_3 is more likely to peel off due to its high internal stress during the repeated heating and cooling processes in the oxidation cycle. The stress related to PBR in the oxidation process is determined as [48, 49]:

$$\sigma_{PBR} = \frac{E_O}{1-\upsilon_O}(1-(PBR)^{1/3}) \qquad \text{Equation 7.10}$$

where E_O is the Young's modulus of the oxide, υ_O is the Poisson's ratio of the oxide, and the σ_{PBR} for Al_2O_3 and Cr_2O_3 are 42.0 GPa and 102.2 GPa (Table 7.4 lists the relative values used in the calculation), respectively, implying the stress generated in Cr_2O_3 scale is larger than that in Al_2O_3 scale.

Table 7.4. Values used to calculate PBR, σ_{PBR} and σ_{CTE} [8, 50].

	M_O (mol/g)	ρ_M (g/cm^3)	A_M (mol/g)	i	ρ_O (g/cm^3)	E_o (GPa)	υ_o	α_o ($\times 10^{-6}$ /K)
Al_2O_3	101.96	2.7	26.98	2	3.96	370	0.22	9.6
NiO	74.69	8.88	58.69	1	6.72	N/A	N/A	N/A
Cr_2O_3	151.99	7.19	52	2	5.22	273	0.3	5.7

Cracking also results from the large difference in thermal expansion coefficients (CTEs) between oxide scales and alloys [50]. The following equation can calculate the corresponding stress in the oxide scale [51]:

$$\sigma_{CTE} = \frac{E_O}{1-v_O}(\alpha_O - \alpha_S)\Delta T \qquad \text{Equation 7.11}$$

where α is the thermal expansion coefficient, the subscripts s and o refer to the substrate and the oxide, and ΔT is the temperature difference between the oxidation temperature and room temperature (1095 °C – 25 °C = 1070 °C). The thermal expansion coefficients of the parent alloy and the oxides can be found in Reference [18] and Table 7.4, respectively. Using Equation 7.11, the σ_{CTE} values are 3.2 GPa and 4.3 GPa for Al_2O_3 and Cr_2O_3, respectively. Although the σ_{CTE} of Cr_2O_3 is larger than that of Al_2O_3, the difference is small compared to that in σ_{PBR}. In addition, σ_{PBR} is noticeably larger than σ_{CTE}. Actually, there are 2 assumptions about using PBR to estimate the stress generated in oxide scales during the oxidation process. Firstly, all new oxides form

within or beneath the scale (since there is no stress on free surfaces if these oxides form at the external). It also ignores the stress relief mechanism. Here, the stress calculated by Equation 7.10 is the maximum value. Therefore, the σ_{PBR} is unrealistically large in this research.

In conclusion, more spallation occurs in the Cr-type scale, i.e., the alloys containing 0.2 wt% and 0.6 wt% Y_2O_3, due to the relatively large stress in the oxide scale, thus increasing the oxidation rate. From Figure 22 (e), the EDS result in Region 2 proves that the spallation layer is Cr-rich, and the peaks of Ta and Nb can be observed in Region 1 beside the spallation layer, indicating that the parent alloy is exposed to air due to the spallation.

The effects of rare earth elements and/or their oxides on oxidation behaviour have been reported in Al_2O_3-forming and Cr_2O_3-forming alloys and termed the "reactive element effect" (REE) [52]. It is based on 2 effects from reactive elements on oxidation behaviour, i.e., the ability to change the structure of oxide scales by affecting oxidation mechanism and the ability to improve oxide scales' adhesion [53]. Hou et al. [52] suggested that the reactive elements and their oxides could promote the formation of Cr_2O_3 scales on alloys by developing Cr_2O_3 scales with less Cr in chemical composition and suppressing further oxidation process of base metal in the presence of a stable Cr_2O_3 scale, related to the enhancement of Cr diffusion in microstructure and oxide nucleation theory [37]. For the improvement of scale adhesion, 3 mechanisms [52] are proposed as (I) reducing internal stress by modifying scale growth mechanism, (II) enhancing the bonds at alloy-scale interfaces and (III) increasing the toughness of

existing scale, thus improving oxide scales' exfoliation resistance.

According to the formation mechanism of multilayer oxides in previous studies [54], a schematic diagram of the scale formation process of the LPBF-processed IN738LC components with various amounts of Y_2O_3 is proposed in Figure 7.23. In the first stage, O_2 adsorbs onto the surface of the alloy. Cr cations initially diffuse towards the metal/oxide interface and react with O_2. Cr_2O_3 nucleates on the surface as the outer oxide, and more Cr_2O_3 forms in Cr-type oxide scales when adding 0.2 wt% and 0.6 wt% Y_2O_3. Subsequently, Ni cations migrate to the continuous Cr_2O_3 film and participate in the reaction between O_2 and Cr_2O_3 to form spinel $NiCr_2O_4$. Simultaneously, the oxidation reaction of Ni takes place when the parent alloy exposes itself to O_2 due to the spallation of Cr_2O_3 and/or $NiCr_2O_4$, and the nodular NiO accordingly grows to the top surface of the oxide scale, as depicted in Step 2. In the Al-type scale, many Al cations diffuse towards the top surface, inducing Al_2O_3 to nearly occupy the whole sublayer (in the alloy without Y_2O_3 and the alloy containing 0.05 wt% Y_2O_3). However, the formation of Al_2O_3 is suppressed in the alloys containing 0.2 wt% and 0.6 wt% Y_2O_3, which is attributed to the thick Cr-rich layer hindering the reaction of O_2 and Al atoms [52]. Furthermore, the coarse grains in the Y_2O_3-containing alloys also inhibit the rapid formation of Al_2O_3 by slowing the diffusion of Al atoms due to the reduced grain boundaries in the microstructure, as aforementioned.
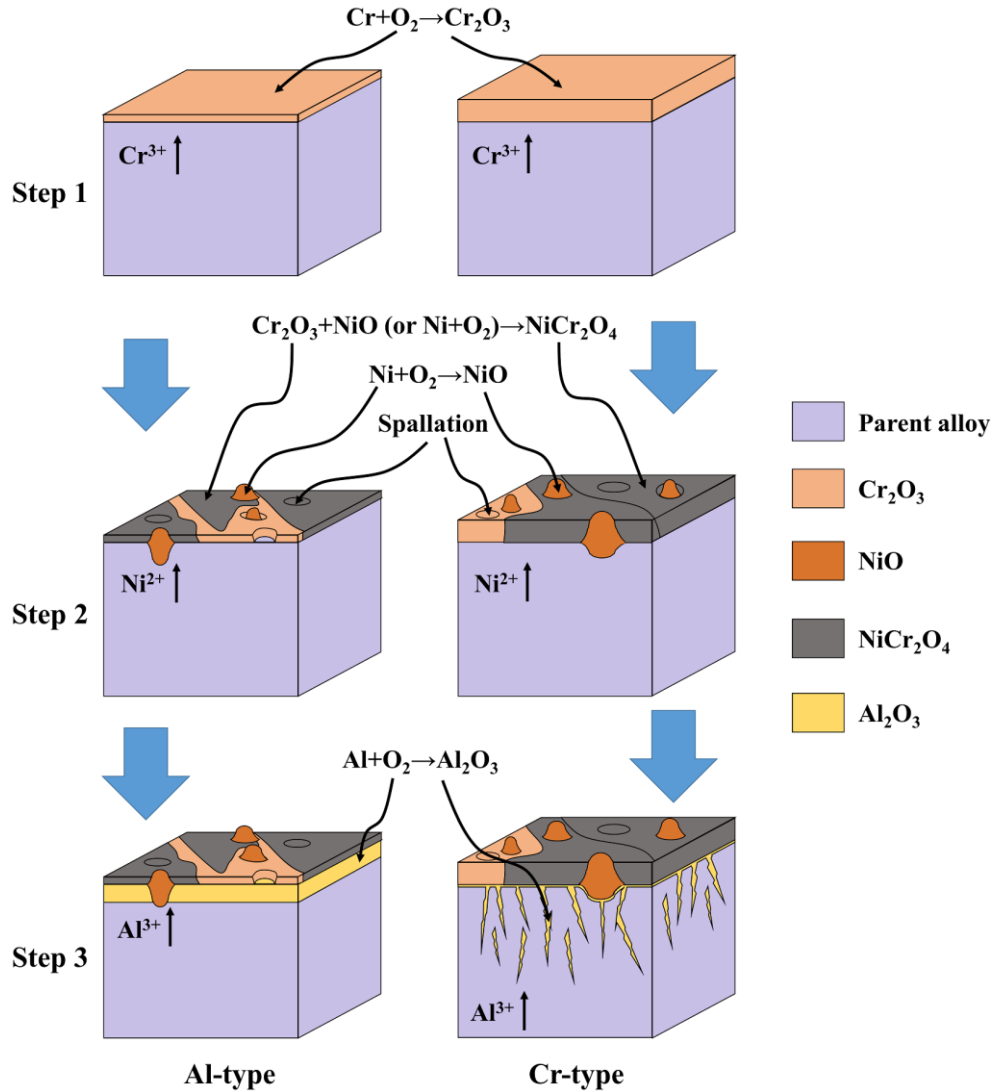
Figure 7.23. Schematic diagrams showing the oxidation mechanisms of the LPBF-processed IN738LC components at 1095 ºC with the oxide scale in Al-type and Cr-type.

7.4. Summaries

The addition of 0.05 wt% Y_2O_3 nanoparticles significantly enlarges the process window by mitigating the cracks in the APed condition of IN738LC processed by LPBF. While excessive Y_2O_3 addition (0.2 wt% and 0.6 wt%) adversely affects the cracking resistance. Well-dispersed $Y_4Al_2O_9$ particles form in the Y_2O_3-containing alloy, and Zr is found to be enriched in these particles. Here, it avoids the segregation of Zr at grain

boundaries, considered the main contributor in eliminating the cracks. However, excessive $Y_4Al_2O_9$ particles formed impair the strength of grain boundaries due to huge clusters of these particles trapped, leading to high crack density.

The gains significantly coarsen with incorporating Y_2O_3 nanoparticles before and after heat treatment. As a result, the 0.05 wt% Y_2O_3-inoculated IN738LC exhibits an improved strength compared to the alloy without Y_2O_3 at elevated temperature. Nevertheless, the alloys with 0.2 wt% and 0.6 wt% Y_2O_3 have inferior mechanical properties at both room and higher temperature due to the severe cracking condition.

Adding 0.05 wt% Y_2O_3 improves the oxidation resistance, causing the oxidation rate constant k_p to decrease from 0.6 $mg^2cm^{-4}h^{-1}$ to 0.4 $mg^2cm^{-4}h^{-1}$. However, further additions to 0.2 wt% and 0.6 wt% Y_2O_3 increase the oxidation rate, and the k_p values are then 0.7 $mg^2cm^{-4}h^{-1}$ and 1.2 $mg^2cm^{-4}h^{-1}$, respectively.

The main oxidation products are Al_2O_3, Cr_2O_3, NiO, $NiCr_2O_4$ and $CoCr_2O_4$. The addition of sufficient Y_2O_3 causes the oxide scale to become dominated by Cr-rich oxides, pushing the Al_2O_3 sublayer found in the oxide scale into jagged regions in the parent alloy. It finds the oxidation resistance of the LPBFed IN738LC components to be affected by many factors such as the characteristics of oxide scale, the chemical composition of alloy and the microstructure (grain sizes and defects).

7.5. References

[1] Guo C., Li S., Shi S., Li X., Zhu Q., Ward R. M. (2020). Effect of processing parameters on surface roughness, porosity and cracking of as-built IN738LC parts

fabricated by laser powder bed fusion. Journal of Materials Processing Technology, 285, 116788.

[2] Guraya T., Singamneni S., Chen Z. W. (2019). Microstructure formed during selective laser melting of IN738LC in keyhole mode. Journal of Alloys and Compounds, 792, 151-160.

[3] Zhan X., Li Z., Liu B., Wang J., Zhou Y., Hu Z. (2009). Theoretical Prediction of Elastic Stiffness and Minimum Lattice Thermal Conductivity of $Y_3Al_5O_{12}$, $YAlO_3$ and $Y_4Al_2O_9$. Journal of the American Ceramic Society, 95(4), 1429-1434.

[4] Messé O. M. D. M., Muñoz-Moreno R., Illston T., Baker S., Stone H. J. (2018). Metastable carbides and their impact on recrystallisation in IN738LC processed by selective laser melting. Additive Manufacturing, 22, 394-404.

[5] Arnold K., Tatlock G., Kenel C., Colella A., Matteazzi P. (2017). High temperature isothermal oxidation behaviour of an oxide dispersion strengthened derivative of IN625. Materials at High Temperatures, 35(1-3), 141-150.

[6] Zhang L., Yu L., Liu Y., Liu C., Li H., Wu J. (2017). Influence of Zr addition on the microstructures and mechanical properties of 14Cr ODS steels. Materials Science and Engineering: A, 695, 66-73.

[7] Xu H., Lu Z., Wang D., Liu C. (2017). Effect of zirconium addition on the microstructure and mechanical properties of 15Cr-ODS ferritic Steels consolidated by hot isostatic pressing. Fusion Engineering and Design, 114, 33-39.

[8] Mat Web, Material property data, http://www.matweb.com/index.aspx

[9] Zhongjingkeyi company (2020). Conducting the first-principles calculations using

density-functional theory, private communication.

[10] Zhou Y., Lu X., Xiang H., Feng Z. (2015). Preparation, mechanical, and thermal properties of a promising thermal barrier material: $Y_4Al_2O_9$. Journal of Advanced Ceramics, 4(2), 94-102

[11] Tan Q., Zhang J., Mo N., Fan Z., Yin Y., Bermingham M., Zhang M. X. (2020). A novel method to 3D-print fine-grained AlSi10Mg alloy with isotropic properties via inoculation with LaB_6 nanoparticles. Additive Manufacturing, 32, 101034.

[12] Risse J., Additive Manufacturing of Nickel-Base Superalloy IN738LC by Laser Powder Bed Fusion, PhD Thesis, RWTH Aachen University (2019).

[13] Martin J. H., Yahata B. D., Hundley J. M., Mayer J. A., Schaedler T. A., Pollock T. M. (2017). 3D printing of high-strength aluminium alloys. Nature, 549(7672), 365-369.

[14] Hong C., Gu D., Dai D., Alkhayat M., Urban W., Yuan P., Poprawe R. (2015). Laser additive manufacturing of ultrafine TiC particle reinforced Inconel 625 based composite parts: Tailored microstructures and enhanced performance. Materials Science and Engineering: A, 635, 118-128.

[15] Gu D., Wang H., Dai D., Yuan P., Meiners W., Poprawe R. (2015). Rapid fabrication of Al-based bulk-form nanocomposites with novel reinforcement and enhanced performance by selective laser melting. Scripta Materialia, 96, 25-28.

[16] Wilms M. B., Streubel R., Fömel F., Weisheit A., Tenkamp J., Walther F., Barcikowski S., Schleifenbaum J. H., Gökce. B. (2018). Laser additive manufacturing of oxide dispersion strengthened steels using laser-generated

nanoparticle-metal composite powders. Procedia CIRP, 74, 196-200.

[17] Zhan X., Li Z., Liu B., Wang J., Zhou Y., Hu Z. (2009). Theoretical Prediction of Elastic Stiffness and Minimum Lattice Thermal Conductivity of $Y_3Al_5O_{12}$, $YAlO_3$ and $Y_4Al_2O_9$. Journal of the American Ceramic Society, 95(4), 1429-1434.

[18] Quested P. N., Brooks R. F., Chapman L., Morrell R., Youssef Y., Mills K. C. (2013). Measurement and estimation of thermophysical properties of nickel-based superalloys. Materials Science and Technology, 25(2), 154-162.

[19] Wang Y., Microstructure and Mechanical Properties of Laser Additively Manufactured Nickle based Alloy with External Nano Reinforcement: A Feasibility Study, PhD Thesis, University of Cincinnati (2018).

[20] Zhang D., Niu W., Cao X., Liu Z. (2015). Effect of standard heat treatment on the microstructure and mechanical properties of selective laser melting manufactured Inconel 718 superalloy. Materials Science and Technology, 644, 32-40.

[21] Zhu L., Xu Z., Gu Y. (2018). Effect of laser power on the microstructure and mechanical properties of heat treated Inconel 718 superalloy by laser solid forming. Journal of Alloys and Compounds, 746, 159-167.

[22] Fei W., Yue H., Wang L. (2010). Equicohesive temperature of the interface and matrix and its effect on the tensile plasticity of $Al_{18}B_4O_{33}$ whiskers reinforced aluminum composite at elevated temperatures. Materials Chemistry and Physics, 119(3), 515-518.

[23] Kong Q., Dai Y. (1988). The role of grain boundaries in creep and creep fracture of metals, Materials Science and processing, 2(2), 1-8.

[24] Xu J., Gruber H., Deng D., Peng R. L., Moverare J. J. (2019). Short-term creep behavior of an additive manufactured non-weldable nickel-base superalloy evaluated by slow strain rate testing. Acta Materialia, 179, 142-157.

[25] Li S., Chen X., Zhou Y., Song G. (2013). Influence of grain size on high temperature oxidation behavior of Cr2AlC ceramics. Ceramics International, 39(3), 2715-2721.

[26] Trindade V., Christ H. J., Krupp U. (2010). Grain-Size Effects on the High-Temperature Oxidation Behaviour of Chromium Steels. Oxidation of Metals, 73(5-6), 551-563.

[27] Jo T. S., Kim S. H., Kim D. G., Park J. Y., Kim Y. D. (2010). Effects of grain refinement on internal oxidation of Alloy 617, Journal of Nuclear Materials 402(2-3) 162-166.

[28] Perez P. (2002). Influence of the alloy grain size on the oxidation behaviour of PM2000 alloy. Corrosion Science, 44(8), 1793-1808.

[29] Kim J. H., Kim K. M., Byun T. S., Lee D. W., Park C. H. (2014). High-temperature oxidation behavior of nano-structured ferritic oxide dispersion-strengthened alloys. Thermochimica Acta, 579, 1-8.

[30] Zheng H. Z., Lu S. Q., Huang Y. (2009). Influence of grain size on the oxidation behavior of NbCr2 alloys at 950-1200°C. Corrosion Science, 51(2), 434-438.

[31] Sun D., Liang C., Shang J., Yin J., Song Y., Li W., Liang T., Zhang X. (2016). Effect of Y_2O_3 contents on oxidation resistance at 1150 °C and mechanical properties at room temperature of ODS Ni-20Cr-5Al alloy. Applied Surface Science, 3855, 87-

96.

[32] Wang Y., Yong L., Tang H., Li W., Han C. (2017). Oxidation behavior and mechanism of porous nickel-based alloy between 850 and 1000 °C. Transactions of Nonferrous Metals Society of China., 277, 1558-1568.

[33] Zhou T., Yuan T., Li Y., Zhou K. (2006). Comparison of oxidation-resistance property between two kinds of Ni-Fe alloys. Mining and Metallurgical Engineering, 2668-2671.

[34] Su Y., Guo J., Cheng X., Feng S., Yang Y. (2019). Intrinsic anharmonicity effect in $YCrO_3$: pressure and temperature dependent Raman spectra studies. Journal of Alloys and Compounds, 805, 489-495.

[35] Kim J. H., Kyong M. K., Thak S. B., Dong W. L., Chan H. P. (2014). High-temperature oxidation behavior of nano-structured ferritic oxide dispersion-strengthened alloys. Thermochimica Acta, 579, 1-8.

[36] Peruzzo M., Beux T. D., Ordoñez M. F. C., Souza R. M., Farias M. C. M. (2017). High-temperature oxidation of sintered austenitic stainless steel containing boron or yttria. Corrosion Science, 129, 26-37.

[37] Stringer J., Wilcox B. A., Jaffee R. I. (1972). The high-temperature oxidation of nickel-20 wt% chromium alloys containing dispersed oxide phases. Oxidation of Metals, 5.1, 11-47.

[38] Bautista A., Velasco F., Abenojar J. (2003). Oxidation resistance of sintered stainless steels: effect of yttria additions. Corrosion Science, 45, 1343-1354.

[39] Wang E., Sun D., Liu H., Lu M., Guo W., Zheng B., Zhang X. (2019). The

Oxidation Behavior of Ni–15Cr–5Al–xSi (x = 0, 1, 3, 5 wt%) Alloys in Air at 1100 °C. Oxidation of Metals, 92, 3-4.

[40] Giggins C. S., Pettit F. S. (1971). Oxidation of NiCrAl Alloys Between 1000° and 1200°C. Journal of the Electrochemical Society, 118, 1-9.

[41] Lou H., Wang F., Zhu S., Xia B., Zhang L. (1994). Oxide formation of K38G superalloy and its sputtered micro-grained coating. Surface and Coatings Technology, 63(1-2), 105-114.

[42] Zhao W., Gleeson B. (2015). Assessment of the detrimental effects of steam on Al_2O_3-scale establishment. Oxidation of Metals, 83(5-6), 607-627.

[43] Leblond, J. B., Pignol, M., Huin D. (2013). Predicting the transition from internal to external oxidation of alloys using an extended Wagner model. Comptes Rendus Mécanique, 341(3), 314-322.

[44] Chou K., Qun L., Qian L., Zhang J. Y. (2014). Influence of the density of oxide on oxidation kinetics. Intermetallics, 47, 17-22.

[45] Evans H. E., Lobb R. C. (1984). Conditions for the initiation of oxide-scale cracking and spallation. Corrosion Science, 24.3, 0-222.

[46] Stott F. H., Wood G. C., Stringer J. (1995). The influence of alloying elements on the development and maintenance of protective scales. Oxidation of Metals. 44.1-2. 113-145.

[47] Pilling N.B., Bedworth R.E. (1923). The oxidation of metals at high temperatures. The Journal of the Institute of Metals, 29529, 1-12.

[48] Huntz A.M. (1995). Stresses in NiO, Cr_2O_3 and Al_2O_3 oxide scales. Materials

Science and Engineering: A, 201(1-2), 211-228.

[49] Evans H.E. (1995). Stress effects in high temperature oxidation of metals. International Materials Reviews, 40, 1-40.

[50] Barnes J. J., Goedjen J. G., Shores D. A. (1989). A Model for stress generation and relief in oxide-Metal systems during a temperature change. Oxidation of Metals, 32(5-6), 449-469.

[51] Li N., Xiao J., Prud'homme N., Chen Z., Ji V. (2014). Residual stresses in oxide scale formed on Fe-17Cr stainless steel. Applied Surface Science, 316, 108-113.

[52] Hou P. Y., Stringer J. (1995). The effect of reactive element additions on the selective oxidation, growth and adhesion of chromia scales. Materials Science and Engineering: A, 202(1-2), 1-10.

[53] Stringer J. (1989). The reactive element effect in high-temperature corrosion. Materials Science and Engineering: A, 120-121(part-P1), 129-137.

[54] Seal S., Kuiry S. C., Bracho L. A. (2002). Surface chemistry of oxide scale on in-738lc superalloy: effect of long-term exposure in air at 1173 k. Oxidation of Metals, 57(3-4), 297-322.

Chapter 8 Cracking Mitigation Method: Pulsed Wave Laser Mode

8.1. Introduction

This chapter presents the investigation using a pulsed-wave laser beam during the laser powder bed fusion (LPBF) process to mitigate the cracking in Inconel 738 LC (IN738LC). 2 groups of parameters are applied in this chapter. The parameters focusing on the laser frequency and the duty ratio in the first group are given in Table 8.1, with fixed laser power and scan speed. which is designed to determine the optimum pulsed-wave parameters (laser frequency and duty ratio). Parameters used to compare the printing quality between the continuous-wave and the optimised pulsed-wave laser beams are given in Table 8.2, with fixed the hatch spacing of 50 μm, the thickness of layer 30 μm, the Raster 67$^{\mathrm{o}}$ scan strategy under no preheating condition.

Table 8.1. Parameters used for searching the optimum pulsed-wave parameters (laser frequency and duty ratio).

Sample	Laser power (W)	Scan speed (mm/s)	Laser Frequency (kHz)	Duty ratio (%)
1	250	800	2	30
2	250	800	5	30
3	250	800	8	30
4	250	800	2	50
5	250	800	5	50
6	250	800	8	50
7	250	800	2	70
8	250	800	5	70
9	250	800	8	70

Table 8.2. Parameters used for comparing the continuous-wave and optimized pulsed-wave (laser frequency 5kHz and duty ratio 70 %) laser beams.

Sample	Laser power (W)	Scan speed (mm/s)	Laser Frequency (kHz)	Duty ratio (%)	Laser mode
1	220	600	N/A	N/A	Continuous
2	250	600	N/A	N/A	Continuous
3	280	600	N/A	N/A	Continuous
4	220	800	N/A	N/A	Continuous
5	250	800	N/A	N/A	Continuous
6	280	800	N/A	N/A	Continuous
7	220	1000	N/A	N/A	Continuous
8	250	1000	N/A	N/A	Continuous
9	280	1000	N/A	N/A	Continuous
10	220	600	5	70	Pulsed
11	250	600	5	70	Pulsed
12	280	600	5	70	Pulsed
13	220	800	5	70	Pulsed
14	250	800	5	70	Pulsed
15	280	800	5	70	Pulsed
16	220	1000	5	70	Pulsed
17	250	1000	5	70	Pulsed
18	280	1000	5	70	Pulsed

8.2. Results

8.2.1. Process window

Optical microscope (OM) observations show the pores on the polished surfaces with different laser frequencies and duty ratios, as shown in Figure 8.1. The pores with different sizes and morphologies are observed under almost all the parameters except the duty ratio of 70 % and the laser frequencies of 5 kHz and 8 kHz. The porosity increases with decreasing the duty ratio, while the lowest porosity is attained at the laser frequency of 5 kHz and worsens again at both 8 kHz and 2 kHz. It is worthy to note that the sample cannot be built under the condition of the laser frequency 2 kHz and the
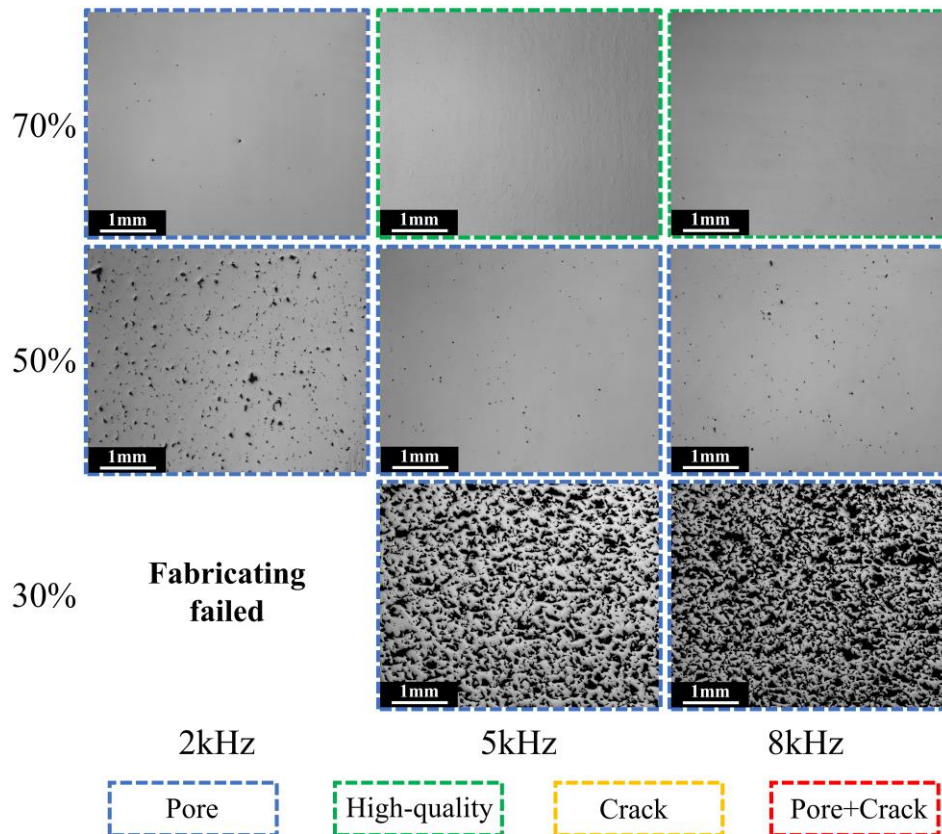
duty ratio 30 %.

Figure 8.1. OM images of the polished surfaces of the as-printed (APed) alloy fabricated by LPBF showing the defects under the pulsed laser mode with different laser frequencies and duty ratios.

Figures 8.2 and 8.3 show the defects under various laser powers and scan speeds in the continuous-wave LPBFed (CWed) and optimised pulsed-wave LPBFed (PWed) IN738LC samples, respectively. As presented in Section 7.2.1, pores are formed at lower energy densities, i.e., low laser powers and/or high scan speeds, and the defects change from pores to cracks with an increase of energy density, as shown in the CWed samples (Figure 8.2). Figure 8.3 presents that little cracking is visually detected in the PWed samples at almost all the parameters, except the laser power of 280 W and the scan speed of 600 mm/s. However, more pores scatter in the view fields of the PWed samples compared to the CWed samples, especially at low energy densities, e.g., the laser power of 220 W and the scan speed of 1000 mm/s. Since the defect rate is at a

233

relatively low level at the laser power of 290 W and the scan speed of 1200 mm/s for both continuous-wave and pulsed-wave laser beams, it conducts the latter investigations on the printed surfaces and the microstructures using the samples under this group of parameters.
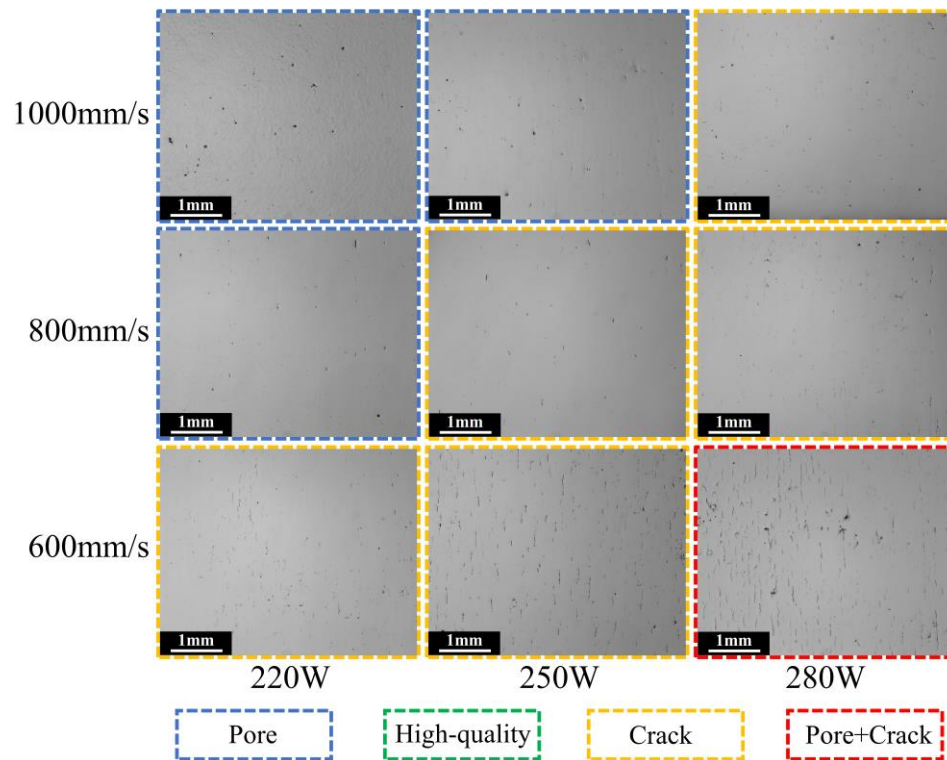

Figure 8.2. OM images of the polished surfaces of the APed alloy fabricated by LPBF showing the defects under the continuous-wave mode with different laser powers and scan speeds.
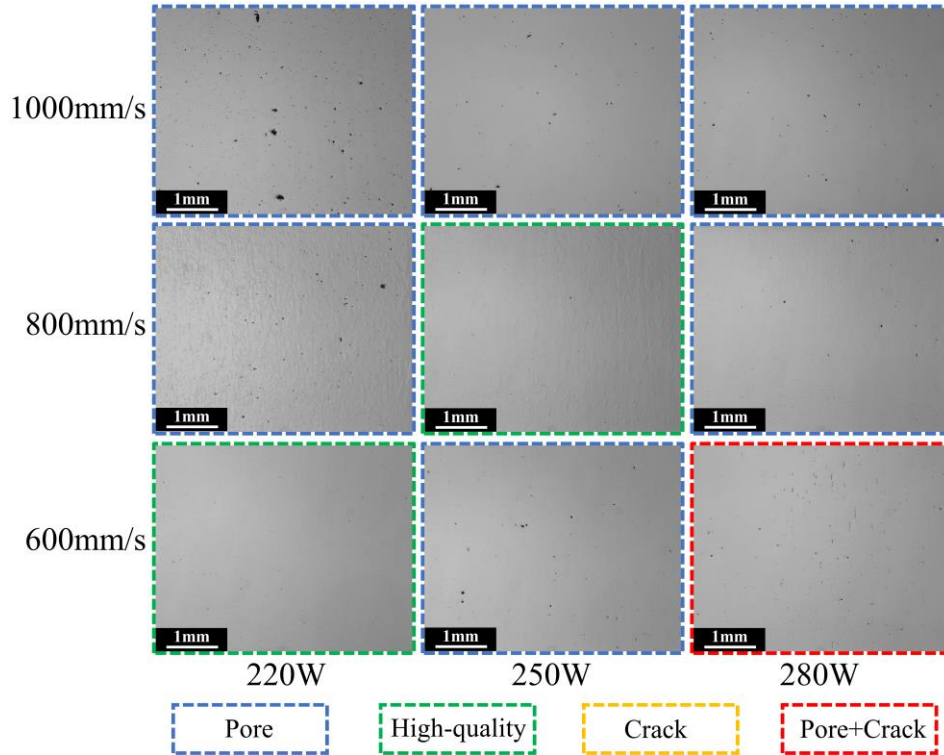
Figure 8.3. OM images of the polished surfaces of the APed alloy fabricated by LPBF showing the defects under the pulsed-wave mode (laser frequency 5 kHz, duty ratio 70 %) with different laser powers and scan speeds.

8.2.2. Single track and surface roughness

Surface ripples going in the opposite direction to laser beam have been commonly observed in the welding process [1]. A similar chevron-shaped welded morphology is also visible in the CWed track, as shown in Figure 8.4 (a). This is attributed to the Marangoni convection in the melt pool during the LPBF process. As aforementioned in Section 5.3.1, the Marangoni convection occurs when the molten liquid flows from the region with low surface tension to the region with high surface tension in the melt pool, driven by the thermal-capillary force. The gradient of surface tension to temperature $d\gamma/dT$ determines the direction of the Marangoni convection. $d\gamma/dT$ is normally a negative value, indicating that high temperatures result in lower surface tensions. In the

melt pool formed by a Gaussian-profile beam, the temperature of the melt pool centre is higher than that in the edge areas, therefore the Marangoni convection's direction is outward from the melt pool's centre [2]. A considerably large amount of molten liquid dragged by the Marangoni force flows to the rear of the melt pool, thus forming lamellar ripples on the top surfaces of the previously fabricated pools. The track has a straight and continuous profile (red block), i.e., with almost uniform width along the whole laser path, as shown in the view at high magnification in Figure 8.4 (c), and the average width is 100.7 ± 2.5 μm. Figure 8.4 (e) presents the reconstruction profile of the printed top surface of the CWed sample. Clear traces of laser scanning paths are visible, and the corresponding surface roughness is 16.0 ± 1.2 μm. The track morphology under the pulsed-wave mode differs from the CWed track, as shown in Figure 8.4 (b). The traces of laser radiation spot (melt pool profile generated during a single pulse time) can be visualised on the substrate under the pulsed-wave mode, leading to a continuously nodular track (yellow outline) in Figure 8.4 (d). The overlapping ratio (spot overlapping area/spot area) of the spots is ~ 1:4. The spot length is the distance between the centres of the adjacent laser radiation spots, indicated by Figure 8.4 (d)'s insert picture, which can reflect the distance that the laser beam moves while it is off in a single cycle, calculated as:

$$D_s = \frac{1}{f}(1-\delta)v \qquad\qquad \text{Equation 8.1}$$

where f is the frequency, δ is the duty ratio, and v is the scan speed. On this basis, D_s is calculated to be 48 μm, consistent with the measured result (47.3 ± 1.7 μm) from the optical image. The average width is 73.3 μm with a high standard deviation (9.7 μm)

236

attributed to the low overlapping ratio between the spots. Figure 8.4 (f) displays the

three-dimensional (3D) surface topography of the printed top surface of the PWed

sample. The surface exhibits a poor quality with a roughness of 21.4 ± 2.8 µm compared

to the CWed sample. As a result, it is difficult to identify the laser scanning path on the

reconstruction surface.
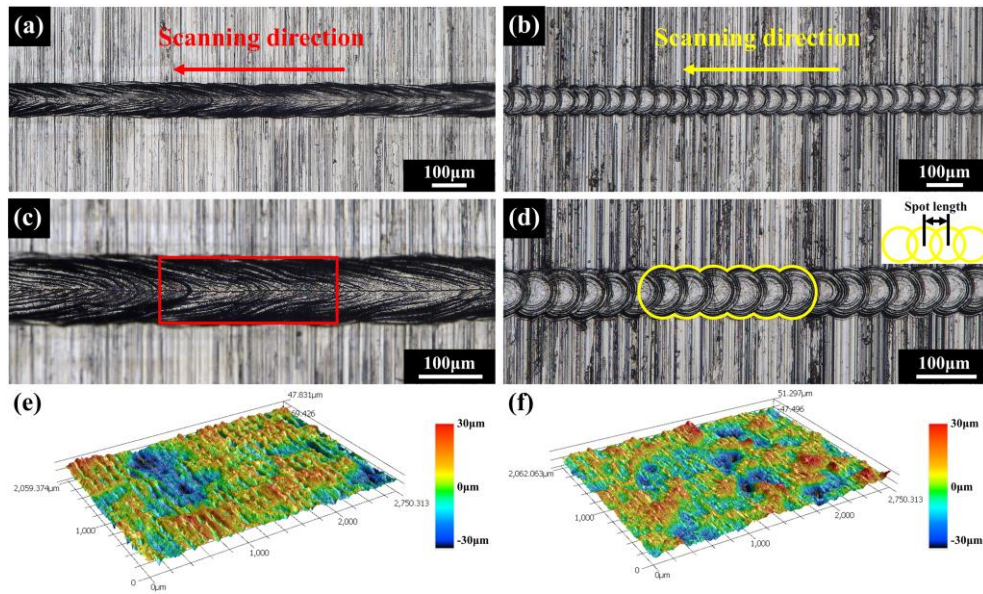
Figure 8.4. OM images of the single tracks on the substrate under (a) continuous-wave and (b) pulsed-wave modes, (c) and (d) are the views at high magnification of (a) and (b), inserted figure in (d) demonstrates the definition of spot distance, 3D reconstruction profiles of the printed top surfaces for the (e) CWed and (f) PWed samples using laser scan confocal microscope (LSCM).

8.2.3. Microstructure

Figure 8.5 shows the grain structure observed by electron backscattered diffraction

(EBSD) in the building direction for the CWed and PWed samples, respectively. The

columnar grains grow in parallel to the building direction and cross multiple layers in

the microstructure due to the highly directional laser-induced temperature gradients

during the LPBF's solidification process, as shown in Figures 8.5 (a) and 8.5 (b). The

columnar grains in the PWed sample are finer than the CWed sample, leading to different grain size distribution between the 2 samples, as shown in Figure 8.5 (c). The columnar grains are surrounded by a large number of fine grains for both conditions. For the CWed sample, most of the grains are smaller than 30 μm with a total fraction of 74.8 %, while the grains greater than 90 μm are 3.3 %, corresponding to these epitaxial grains along the building direction. Compared with the grain size distribution in the CWed sample, the application of the pulsed-wave mode dose not qualitatively change the distribution pattern, but the fraction of the fine grains with smaller than 30 μm increases to 85.6 %, while fewer grains are greater than 90 μm (0.5 %) compared to the CWed sample. As a result, the average grain size is smaller for the PWed sample (13.1 ± 0.9 μm) than that for the CWed sample (23.7 ± 1.0 μm).

Figure 8.6 shows the misorientation distribution images obtained by the EBSD measurements for the CWed and PWed samples, indicating a significant difference in the misorientation angle distribution of grain boundaries between the CWed and PWed samples. The grain boundaries are categorised into 3 types in this investigation: low-misorientation angle grain boundary (LAGB, < 20º), medium-misorientation angle grain boundary (MAGB, 20º-40º) and high-misorientation angle grain boundary (HAGB, > 40º). The fraction of LAGBs is 55.2 % for the CWed sample and increases to 72.5 % for the PWed sample, as comparing Figure 8.6 (b) with Figure 8.6 (e). However, Figures 8.6 (c) and 8.6 (f) exhibit that the CWed sample contains more HAGBs than the PWed sample, i.e., the fractions are 15.3 % and 9.9 %, respectively.
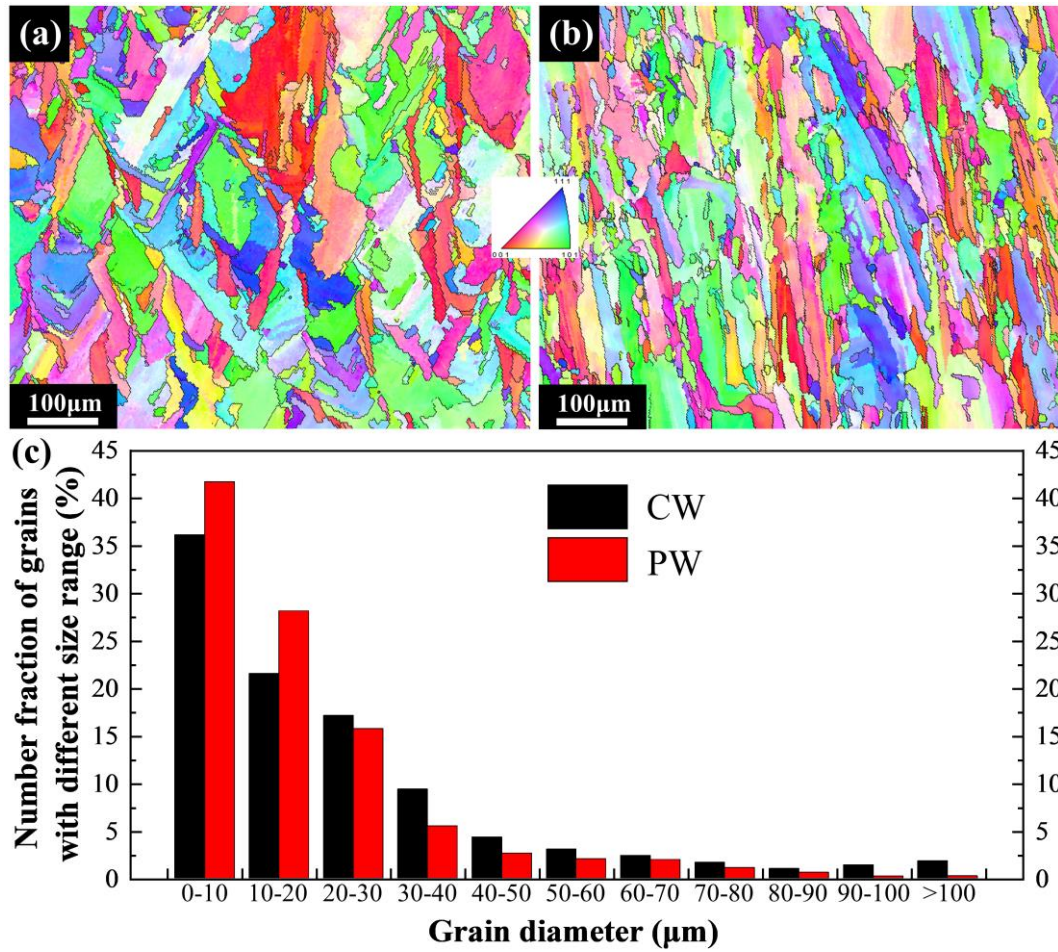
Figure 8.5. EBSD maps of the samples in the X-Z section showing the grain structures of the (a) CWed and (b) PWed samples and (c) grain size distribution.
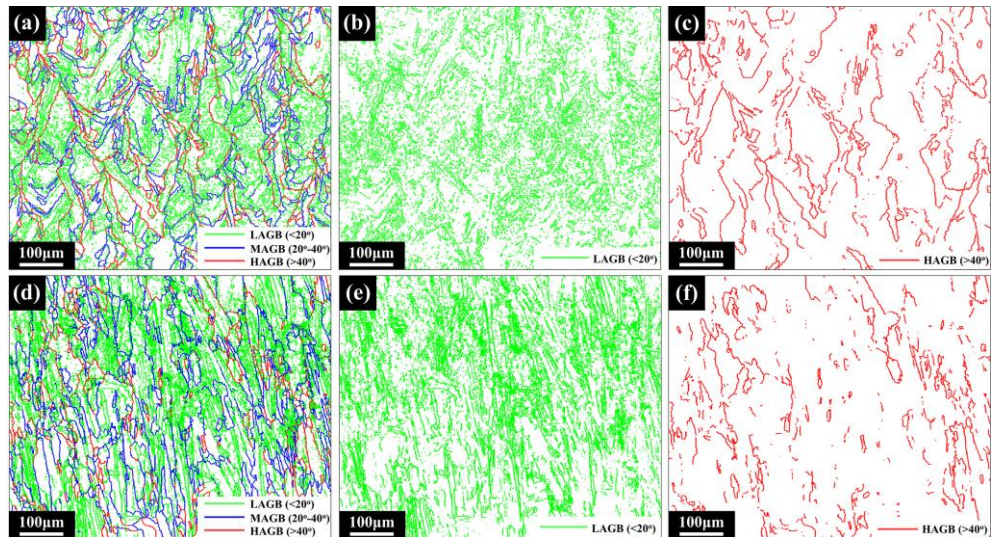

Figure 8.6. Misorientation distribution images based on the EBSD mapping showing (a, d) LAGBs, MAGBs and HAGBs, (b, e) extracted LAGBs from (a, d) and (c, f) extracted HAGBs from (a, d) for the CWed and PWed samples, respectively.

8.3. Discussions

8.3.1. Effects of pulsed-wave parameters on part quality

Figure 8.7 presents the profiles of the melt pools simulated by the Matlab R2016b software using the method described in Section 3.7.4. The parameters used in the calculation are the same as those in the experiment, as shown in Table 8.1. The shape of the melt pools appears similar to the single track in Figure 8.4 (d), i.e., a nodular track with adequate and inadequate overlaps between the laser spots. The laser frequency and the duty ratio have a great impact on the melt pool's dimensions and track continuity. It can be seen that the melt pools' width increases with the increase of the duty ratio while decreases with increasing the laser frequency. The time for the laser beam emitting in a single pulse directly decides the reaction time between the laser beam and the powder bed and further controls the melt pool's width, calculated as:

$$t_{on} = \frac{\delta}{f}$$
<div align="right">Equation 8.2</div>

where f is the laser frequency, and δ is the duty ratio. According to Equation 8.2, the time period for the laser beam emitting reduces with the decrease of the duty ratio and the increase of the laser frequency, implying the decreases of the energy input and the melt pool width in a single pulse. The distance between the laser spots decides the continuity of the laser track and further affects the printing quality. Equation 8.1 elucidates the relationship between the laser frequency, the duty ratio and the spot distance, implying that the spot distance increases with the decreases of the laser frequency and the duty ratio, consistent with Figure 8.7. Here, the track may lose its

continuity if the distance between spots is too large, inducing un-melt powders to trap in these big gaps and deteriorating the printing quality. The melt pool width increases while the spot distance decreases with increasing the duty ratio, favouring the continuity and the overlap of tracks. Therefore, high duty ratios always benefit the printing quality, as displayed in Figure 8.1. The increase of the laser frequency reduces the spot distance and thus induces a continuous track. But a relatively narrow melt pool is corresponding produced, which is unfavourable for the overlap between tracks. Therefore, Figure 8.1 shows that both considerably high and low laser frequencies adversely affect the printing quality. Thus, the PWed part achieved its best quality at the largest duty ratio, i.e., 70 % and a medium laser frequency, i.e., 5 kHz in the current experimental condition. It is worthy to note that the sample even cannot be fabricated under the conditions of low duty ratios and laser frequencies such as 30 % and 2 kHz due to low melt pool widths and large spot distances.
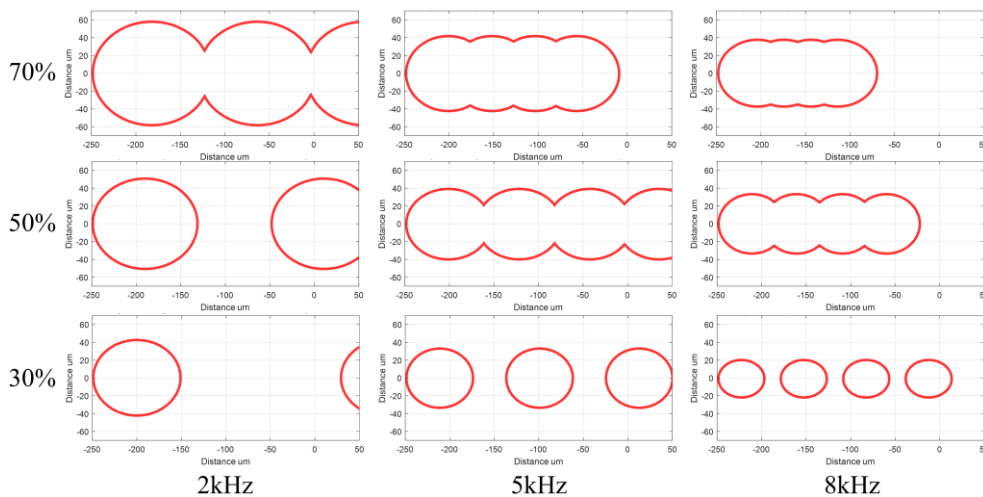

Figure 8.7. Profiles of the melt pools simulated by Matlab R2016b with different laser frequencies and duty ratios.

8.3.2. Effects of pulsed-wave mode on cracking development

As stated in Section 6.2.2.2, cracking during the LPBF process is expected to occur at the grain boundaries with high misorientation angles. ~ 60 % of cracks appeared at the grain boundaries with the misorientation angles between 40º and 60º. The PWed sample contains fewer HAGBs (> 40º) than the CWed sample but significantly more LAGBs, i.e., < 20º. Furthermore, there are more grain boundaries in the PWed sample compared to the CWed sample [3], and the average grain sizes are 13.1 ± 0.9 μm and 23.7 ± 1.0 μm, respectively. The application of the pulsed-wave laser beam, on the one hand, lowers the fraction of the cracking-susceptible HAGBs. On the other hand, for a limited element content, the increase of grain boundary areas leads to less segregation of the element onto unit grain boundary, i.e., the concentrations of some cracking-sensitive elements like Zr at grain boundaries are lower for the PWed sample than the CWed sample and finally induces less inclination of cracking [4]. The refinement of grains is considered to be the main contributor to the mitigation of cracking in the PWed sample.

Figure 8.8 shows the thermal history of the midpoint of the powder bed (P_2 in Figure 3.10) in the simulation domain under the continuous-wave and pulsed-wave modes using the method described in Section 3.7.3. The temperatures in the processed sample are generally higher under the continuous-wave mode than those under the pulsed-wave mode with the peak temperatures of 2885.1 ºC and 2331.3 ºC, respectively. For a given duty ratio at < 100 %, less energy density is inputted in the powder bed using the pulsed-wave mode due to the discontinuous radiation of the laser beam, thus

relatively lower temperatures are obtained in the PWed melt pool than the CWed one. In more detail, as depicted in the curves of heating (cooling) rate, the curves transfer from positive to negative, i.e., the thermal condition changes from heating to cooling when the laser beam moves away from P_2. Meanwhile, the application of the pulsed-wave mode can enhance the cooling process, and the corresponding maximum cooling rate (the minimum dT/dt) is 3.6×10^7 °C/s, higher than that under the continuous-wave mode (1.6×10^7 °C/s). Therefore, a finer microstructure is attained in the PWed sample [5, 6], as shown in Figures 8.5 (a) and 8.5 (b).
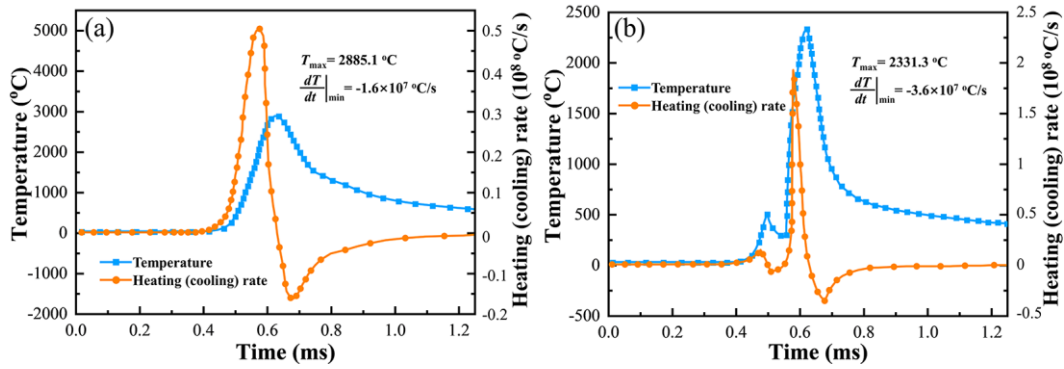
Figure 8.8. Calculated thermal history (temperature profiles, heating and cooling rates) versus time of P_2 under the (a) continuous-wave and (b) pulsed-wave modes.

8.3.3. Effects of pulsed-wave mode on pore formation

Detailed observation shows 2 categories of pores in the PWed sample, i.e., the irregular-morphology pores with un-melted powders (red dotted line) and the near-spherical pores (yellow dotted line), as shown in Figures 8.9 (a) and 8.9 (b), respectively. The pores with an irregular-morphology are primarily attributed to the lack of fusion and have the sizes ranging from 50 μm to 100 μm. While the sizes of the near-spherical pores are normally smaller than 20 μm. This kind of pores arises from gas evolved from

the powders or trapped within the melt pool during solidification in the LPBF process [7].

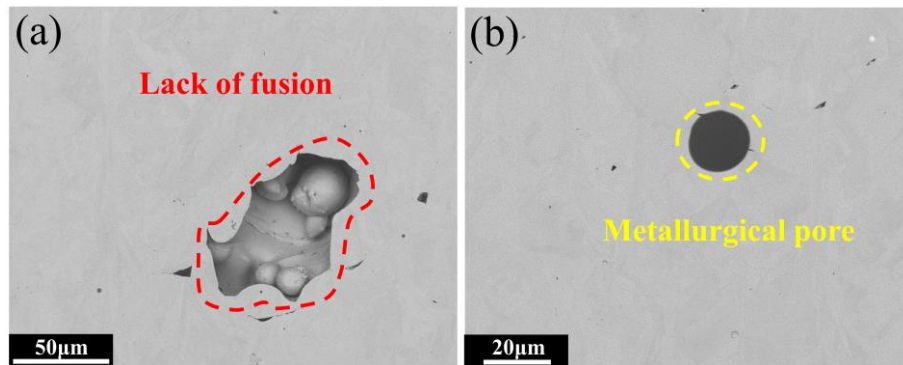**Figure 8.9. Scanning electron microscope (SEM) morphologies of the pores attributed to (a) lack of fusion and (b) metallurgical pore in the PWed sample.**

As the laser beam travels discontinuously in each cycle under the pulsed-wave mode, a non-uniform width along the length direction of track is induced. A trend of Rayleigh instability is accordingly enhanced with a fluctuating track, as depicted in Section 5.2.1. As mentioned in Section 4.2.1.2, during the LPBF process, the molten track is described as a liquid cylinder with a diameter of D and a length of λ. If $\lambda/D > \pi$, the track will fluctuate as a sinusoidal wave in width. This is the Rayleigh instability and consistent with the observation of the PWed track, as shown in Figure 8.4 (d). With the aggravation of the unstable condition, the track will break up into small droplets to reduce surface energy in the worst case [8]. It induces wave troughs and crests along the laser beam path by the fluctuation as the Rayleigh instability occurs. A strong metallurgical bonding generates once the 2 wave crests belonging to adjacent tracks overlap. However, a big void appears as a pocket morphology and contains several un-melted powders as 2 wave troughs adjoint, leading to pores generating due to the lack of fusion in the PWed sample, as depicted in Figure 8.10 (b). Compared with the pulsed-wave mode, the CWed track is straight and stable, as shown in Figures 8.4 (c) and 8.10

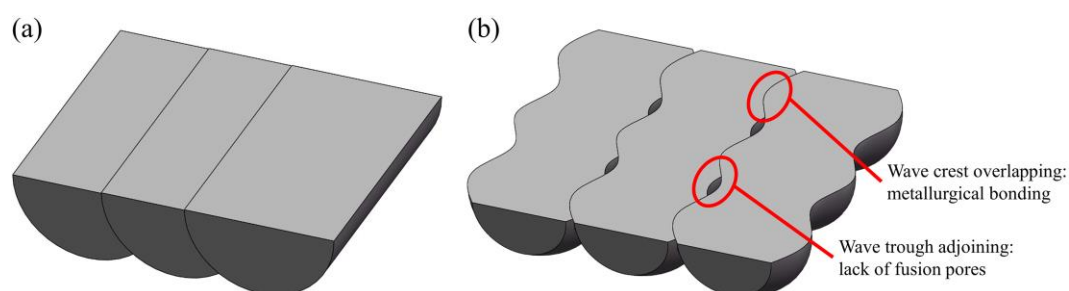(a). This ensures adequate overlapping between the tracks, thus effectively avoiding the pore formation.

Figure 8.10. Schematic diagrams showing the overlapping of the tracks under the (a) continuous-wave and (b) pulsed-wave modes.

Another type of pores, namely metallurgical pores, are observed in the PWed sample. This type of pores is ascribed to the residual bubble in the melt pool during solidification. Viscosity is a temperature-dependent thermophysical property and negatively correlated with temperature. Due to the continuous radiation of the laser beam under the continuous-wave mode, higher temperatures are obtained in the melt pool compared to that under the pulsed-wave mode, as demonstrated in Figure 8.8. Therefore, the molten liquid has a relatively high viscosity under the pulsed-wave mode, where the flow velocity of the molten liquid accordingly reduces. Ding et al. [9] also suggested that the pulsed-wave laser beam led to a lower fluid flow velocity than that under the continuous-wave mode by numerical analysis. Then, there are fewer opportunities for the bubbles within the melt pool to escape through the melt surface [7], favouring the formation of residual metallurgical pores in the PWed sample.

8.4. Summaries

Increasing the duty ratio can increase the melt pool's width and decrease the spot distance, which favours the continuity and the overlapping of tracks and leads to a high

printing quality. High laser frequencies decrease the spot distance and lead to continuous tracks, however, a relatively narrow melt pool is obtainable. Thus, both considerably high and low laser frequencies have an adverse effect on the printing quality.

The application of the pulsed-wave mode can eliminate cracking in the LPBFed IN738LC alloy, primarily ascribed to the refined microstructure induced by higher cooling rates based on the simulation results. On the one hand, the fraction of the cracking-susceptible HAGBs is reduced. On the other hand, the concentrations of element contents per unit grain boundary decrease due to more grain boundaries, and the segregations of the elements which cause cracking such as Zr are supposed to be removed.

Since the laser beam travels discontinuously in each cycle under the pulsed-wave mode, the trend of Rayleigh instability is accordingly enhanced with a fluctuating track, and the lack of fusion occurs due to powders trapping between tracks. Moreover, it attains a relatively low operating temperature under the pulsed-wave mode, and the molten liquid has a relatively high viscosity, where the flow velocity of the molten liquid is small. Here, it provides fewer opportunities for the bubbles within the melt pool to escape through the melt surface, favouring the formation of residual metallurgical pores. Therefore, more pores form in the PWed sample compared to the continuous-wave mode.

8.5. References

[1] Zhou X., Wang D., Liu X., Zhang D., Qu S., Ma J., London G., Shen Z., Liu, W., 3D-imaging of selective laser melting defects in a Co-Cr-Mo alloy by synchrotron radiation micro-CT, Acta Mater. 98 (2015) 1-16.

[2] Guo C., Li S., Shi S., Li X., Hu X., Zhu Q., Ward R. M., Effect of processing parameters on surface roughness, porosity and cracking of as-built IN738LC parts fabricated by laser powder bed fusion, J. Mater. Process. Technol. 285 (2020) 116788.

[3] Han Q., Gu, Y., Setchi R., Lacan F., Johnston R., Evans S. L., Yang S, Additive manufacturing of high-strength crack-free Ni-based Hastelloy X superalloy, Addit. Manuf. 30 (2019) 100919.

[4] Cloots M., Uggowitzer P. J., Wegener K. (2016). Investigations on the microstructure and crack formation of IN738LC samples processed by selective laser melting using Gaussian and doughnut profiles. Materials & Design, 89, 770-784.

[5] Li S., Xiao H., Liu K., Xiao W., Li Y., Han X., Mazumder J., Song L, Melt-pool motion, temperature variation and dendritic morphology of Inconel 718 during pulsed- and continuous-wave laser additive manufacturing: A comparative study, Mater. Des. 119 (2017) 351-360.

[6] Muñiz-Lerma J. A., Tian Y., Wang X., Gauvin R., Brochu M., Microstructure evolution of Inconel 738 fabricated by pulsed laser powder bed fusion, Progress in Addit. Manuf. 4 (2019) 97-107.

[7] Xia M., Gu D., Yu G., Dai D., Chen H., Shi Q., Porosity evolution and its thermodynamic mechanism of randomly packed powder-bed during selective laser melting of Inconel 718 alloy, Int. J. Mach. Tools Manuf. 116 (2017) 96-106.

[8] Guo C., Xu Z., Zhou Y., Shi S., Li G., Lu H., Zhu Q., Ward R. M. (2021). Single-track investigation of IN738LC superalloy fabricated by laser powder bed fusion: Track morphology, bead characteristics and part quality. Journal of Materials Processing Technology, 290, 117000.

[9] Ding X., Wan, L., Wang, S., Comparison study of numerical analysis for heat transfer and fluid flow under two different laser scan parttern during selective laser melting, Optik 127(22) (2016) 10898-10907.

Chapter 9 Conclusion and Future Work

9.1. Introduction

This chapter summarises the main findings presented in this study and the recommendations for future works.

9.2. Overall conclusions

9.2.1. Effects of processing parameters on printing qualities

This research investigates the effects of laser power, scan speed and hatch spacing on surface roughness, porosity and crack density of the Inconel 738 LC (IN738LC) superalloy fabricated by the laser powder bed fusion (LPBF) process. Some key findings are summarised as follows:

- Surface roughness increases with the increase of the scan speed and decreases with the increase of the laser power. Both extremely small and extremely large hatch spacings lead to high surface roughness.

- The pores can be divided into 2 categories, i.e., lack of fusion and keyhole pore according to the sizes and the morphologies.

- Crack density increases with the decrease of the hatch spacing and the scan speed and decreases with the decrease of the laser power.

- Regression analysis demonstrates that both extremely high and extremely low volume energy densities (VEDs) lead to high surface roughness and porosity, and crack density has a linear relationship with the VED. Moderate VED is optimal in

terms of mechanical properties.

- In addition, compared with the pores, the cracks cannot be entirely eliminated using the parameter control method, thus some other approaches need to conduct in solving the cracking in IN738LC during LPBF, which will be mentioned in the latter chapters.

9.2.2. Single-track behaviour and pore formation mechanism

Single-track experiments are performed to investigate the relationship between the track morphology, the bead characteristics and the printed part quality of IN738LC processed by LPBF. Key findings are summarised as follows:

- Continuous (stable) tracks appear at high energy input densities. When the energy input density is low, the track fluctuates and tends to break up into metallic droplets.

- Bead width and depth increase with the increase of the laser power and decrease with the increase of the scan speed. Bead height is independent of the processing parameters. Contact angle decreases with the increase of the energy input density.

- If the solidification time is less than the spread time, the molten droplet will solidify before it spreads out on the basic block, and then the balling correspondingly forms.

- When the deposited energy is ~ 50 times greater than the enthalpy for melting, the bead changes from the conduction mode to the keyhole mode.

- Both extremely high and low energy densities lead to high porosity in the bulk samples due to the keyhole pores and the lack of fusion.

9.2.3. Microstructures and crack formation mechanism

This research studies the microstructures in the as-printed (APed) and heat-treated (HTed) conditions and the cracking behaviour in the APed condition of the IN738LC alloy processed by LPBF. Key findings are summarised as follows:

- The main phases in the APed IN738LC alloy are γ/γ' and MC-type carbides. While 2 groups of precipitates, i.e., coarse (primary) γ' precipitates with an average size of ~ 400 nm and fine (secondary) precipitates with an average size of ~ 50 nm, are visible after heat treatment.

- Both parts in the APed and HTed conditions exhibit a strong cube texture dominated by a preferential alignment of <100>.

- During the rapid heating and cooling processes in the LPBF process, Zr segregates at grain boundaries, reducing the solidus in these regions, and solidification cracks occur due to the remaining liquid at the last stage of solidification under thermal stress.

- Cracking tends to occur at the grain boundaries with high misorientation angles.

9.2.4. Y_2O_3 decoration and cracking mitigation

Adding Y_2O_3 nanoparticles into IN738LC is studied to mitigate the cracking in IN738LC during the LPBF process. This research investigates the effects of Y_2O_3 nanoparticles on the printing quality, the microstructures and the resulting properties (tensile properties and oxidation resistance). Key findings are summarised as follows:

- The process window is significantly enlarged with the addition of 0.05 wt% Y_2O_3

nanoparticles into IN738LC for the crack-free condition during LPBF. When the Y_2O_3 additions increase to 0.2 wt% and 0.6 wt%, an adverse effect on the cracking resistance is observed.

- Well-dispersed $Y_4Al_2O_9$ particles form in the Y_2O_3-containing alloy, and Zr is found enriched in these particles, leading to less segregation of Zr at grain boundaries and eliminating the cracks. However, excessive $Y_4Al_2O_9$ particles formed in the inter-dendrite regions impair the bonding strength between the dendrites, leading to high crack densities.

- The grain structure is significantly coarsened by the addition of Y_2O_3 nanoparticles. Thus, the tensile strength at 850 ºC is improved by incorporating 0.05 wt% Y_2O_3 nanoparticles. When the additional amounts are 0.2 wt% and 0.6 wt%, however, the tensile strength is significantly reduced.

- Adding 0.05 wt% Y_2O_3 improves the oxidation resistance. Nevertheless, further additions to 0.2 wt% and 0.6 wt% Y_2O_3 increase the oxidation rate.

- The main oxidation products are Al_2O_3, Cr_2O_3, NiO, $NiCr_2O_4$ and $CoCr_2O_4$. It finds that the addition of sufficient Y_2O_3 causes the oxide scale to be dominated by Cr-rich oxides, Al_2O_3 sublayer is found to be suppressed into the jagged regions in the parent alloy.

9.2.5. Pulsed-wave laser beam and cracking mitigation

This research investigates the mitigation of cracking in IN738LC by the pulsed-wave mode during LPBF. Key findings are summarised as follows:

- The melt pool width increases and the spot distance decreases with the increase of the duty ratio, both of which favour producing the parts with high quality. The increase of the laser frequency reduces the spot distance and induces a continuous track, while it leads to a relatively narrow melt pool at high laser frequencies. Thus, both extremely high and extremely low laser frequencies have an adverse effect on the printing quality.

- The pulsed-wave mode can effectively eliminate the cracking in the LPBFed IN738LC alloy, while more pores form compared to the continuous-wave mode.

- The elimination of cracking in the pulsed-wave LPBFed (PWed) sample is primarily ascribed to the refined microstructure induced by the high cooling rate under the pulsed-wave laser beam.

- Lack of fusion and metallurgical pore attributed to the Rayleigh instability and the residual bubbles, respectively, lead to high porosity in the PWed sample.

9.3. Proposed future works

The defect formation mechanisms and some elimination methods in the nickel-based superalloy IN738LC during LPBF are investigated in this research. Below the future works are proposed:

- Grain structure and residual stress are more susceptible to the scan strategy compared to other parameters. Therefore, it is necessary to investigate the detailed effects of the scan strategy on microstructure, cracking behaviour and material properties.

- The residual stress in the APed IN738LC samples must be measured directly to evaluate the effects of processing parameters, e.g., the blind hole and Vickers micro-indentation methods are proposed to be used.

- The original microstructure of the APed IN738LC sample differs from cast alloy, thus a new heat treatment method for the alloy fabricated by LPBF needs to be optimised to reach good material properties.

- Since the Y_2O_3 addition amounts are at such a low level, it is worth investigating deeply in the latter research the effects of Y_2O_3 on the thermal diffusion as well as the grain structure during such a rapid cooling process. In addition, a high-temperature creep test is suggested to be carried out to judge the effects of the grain coarsening attributed to the Y_2O_3 addition on creep property.

- Due to high temperature gradients induced by the LPBF process, microstructures vary apparently between the parallel and vertical sections of printed parts. Therefore, the anisotropy of material properties should be studied.

- Structural components with a defect-free condition should be fabricated to assess the feasibility and universality of the methods obtained in this research to eliminate defects. And these structural components should be tested in the real service environment if the conditions permit.